1986

Atomic And Molecular Photoelectron Spectroscopy Studies Using Synchrotron Radiation

Brian Wayne Yates

CANADIAN THESES

THÈSES CANADIENNES

NOTICE

The quality of this microfiche is heavily dependent upon the quality of the original thesis submitted for microfilming. Every effort has been made to ensure the highest quality of reproduction possible.

If pages are missing, contact the university which granted the degree.

Some pages may have indistinct print especially if the original pages were typed with a poor typewriter ribbon or if the university sent us an inferior photocopy.

Previously copyrighted materials (journal articles, published tests, etc.) are not filmed.

Reproduction in full or in part of this film is governed by the Canadian Copyright Act, R.S.C. 1970, c. C-30.

AVIS

La qualité de cette microfiche dépend grandement de la qualité de la thèse soumise au microfilmage. Nous avons tout fait pour assurer une qualité supérieure de reproduction.

S'il manque des pages, veuillez communiquer avec l'université qui a conféré le grade.

La qualité d'impression de certaines pages peut laisser à désirer, surtout si les pages originales ont été dactylographiées à l'aide d'un ruban usé ou si l'université nous a fait parvenir une photocopie de qualité inférieure.

Les documents qui font déjà l'objet d'un droit d'auteur (articles de revue, examens publiés, etc.) ne sont pas microfilmés.

La reproduction, même partielle, de ce microfilm est soumise à la Loi canadienne sur le droit d'auteur, SRC 1970, c. C-30.

THIS DISSERTATION HAS BEEN MICROFILMED EXACTLY AS RECEIVED

LA THÈSE A ÉTÉ MICROFILMÉE TELLE QUE NOUS L'AVONS REÇUE

NL-339 (r 86/06)

Canada

ATOMIC AND MOLECULAR PHOTOELECTRON SPECTROSCOPY STUDIES USING SYNCHROTRON RADIATION

by

Brian Wayne Yates

Department of Chemistry

Submitted in partial fulfillment

of the requirements for the degree of

Doctor of Philosophy

Faculty of Graduate Studies

The University of Western Ontario

London, Ontario

February, 1986

ISBN 0-315-29494-9

ABSTRACT

Using photons from the Canadian Synchrotron Radiation Facility (CSRF) at the Tantalus electron storage ring, gas phase photoelectron spectra of the Xe $4d_{3/2,5/2}$ core level, and the valence orbitals of CF_4, SiF_4, CF_3I, and XeF_2 have been obtained as a function of photon energy. Branching ratios have been determined from these spectra and converted to partial cross sections, where possible. Theoretical branching ratios and partial cross sections obtained from MS-Xα calculations, are compared with experiment for the molecular cases. These atomic and molecular systems were studied in order to further our understanding of shape resonances and many-body effects in photoionization.

The Xe $4d_{5/2}$:$4d_{3/2}$ spin-orbit branching ratio has been accurately determined from 74 to 150 eV photon energy. There is good qualitative agreement between the values and the latest relativistic random-phase approximation (RRPA) calculations of Cheng and Johnson. However, the experimental minimum region is not as deep or as pronounced as in the RRPA calculation, and is shifted 3 eV to higher kinetic energy. It is proposed that these deviations arise from the neglect of relaxation effects during photoionization.

Valence orbital branching ratios for CF_4, SiF_4, and CF_3I have been obtained from 21 to ~100 eV photon energy. In general, the agreement between experiment and the MS-Xα results is good. For SiF_4, we have been able to confirm the orbital assignment on a cross section basis as $1t_1 < 5t_2 < 1e < 4t_2 < 5a_1$, in order of increasing binding energy. In contrast to the CF_4 results which show little structure, five shape resonances are predicted at 3, 7, 13, 23, and 35 eV kinetic energies. While the predicted resonance positions at 23 and 35 eV are in good agreement with experiment, the low energy resonances are in poorer agreement. Similarly, two shape resonances at 15 and 17 eV kinetic energies are predicted for CF_3I. Although much of the behavior of CF_3I is very similar to CF_4, weak shape resonances at ~13 eV kinetic energy have been observed on the 3e, 2e, and 1e orbitals. Intershell correlation effects in CF_3I have been found to occur above the I 4d edge on the I 5p lone pair orbital (4e).

Similarly, valence orbital branching ratios have been obtained for XeF_2 from 21 to 50 eV photon energy. A number of strong resonances are predicted and observed, in spite of the apparent lack of appropriate valence virtual orbitals and the long bond distance. The observed resonance positions are usually in reasonable agreement with theory.

ACKNOWLEDGEMENTS

I would like to thank my research supervisor, Dr. G.M. Bancroft, for his enthusiasm, insight, and ideas, which made this work possible over the last several years.

Special thanks are due to John Tse, who managed to educate the author as to the importance of quantum mechanics and theoretical calculations in general. I am deeply grateful for his help in "setting up" the multiple scattering Xα program of J.W. Davenport on the NRC computer system, during a very productive and informative three week stay with him in Ottawa. I would also like to thank John for teaching me much that I know about the Xα method, and for explaining many confusing aspects of the Xα and MS-Xα programs to me. His very sound scientific advice, friendship and help in guiding my research are greatly appreciated.

I am deeply grateful to Leighton Coatsworth for explaining the mysteries of vacuum technology to me, and for designing much of the experimental apparatus. Without his expert technical advice on vacuum, electronics, and computer interfacing, the synchrotron project would simply have never gotten off the ground. I am indebted to him for the use of his peak fitting program used extensively in this thesis, and for the numerous discussions we had

involving the algorithms used therein. I would specially like to thank I. Schmidt for his technical assistance and excellent machining jobs that were required to build the experimental chamber.

I thank fellow chemistry graduate students John Tse, Jim Brown, Duncan Bristow, David Creber, Gilles Jean, Emmanuel Pellach, Jim Metson, Tammy Chan, Jo-Ann Forrest, Ralph Jonasson, Margaret Hyland, Ian Muir, Lisa Dignard-Bailey, and Brenda Addison for their help and friendship.

I also wish to thank the assistance of the staff at the University of Wisconsin storage ring (Tantalus), particularly Roger Otte, Dick Fasking and Ed Rowe. My research effort on the Canadian Synchrotron Radiation Facility (CSRF) there, benefited greatly from the help given to me by Kim Tan. I would like to thank the "ring people" who made my stays in Wisconsin pleasant ones, namely Cliff Olson, Franco Cerrina, John Joyce, Dave O'Neill, Eric Jensen, Dave Wieliczka, Don Mueller ("Mr. Turkey"), Tom Miller, Al Shapiro (Al #1), Al Wachs (Al #2), Mike Kelly, Tim Whitley, Bob Daniels, Al Arko, Rich DiDio, Tom Carlson, Manfred Krause, Agneta Svensson, Candida, and of course "Jim Beam".

Apart from the chemistry and physics communities I would like to thank my parents, who have been very supportive throughout this work and to whom this thesis is dedicated.

My research efforts have been supported by the Natural Sciences and Engineering Research Council (NSERC) of Canada and the University of Western Ontario. I am very grateful to the National Research Council (NRC) of Canada and the University of Western Ontario for funding CSRF from its inception.

TABLE OF CONTENTS

LIST OF TABLES

LIST OF FIGURES

CHAPTER 1

INTRODUCTION

1.1.1 Introduction

The interaction of electromagnetic radiation with matter is complex, resulting in many important fields of study. In photoelectron spectroscopy, the photoelectric effect is the primary process involved. It is a one-step process:

$$M(\Psi_i) + h\nu \longrightarrow M^+(\Psi_j^+) + e^- , \qquad (1.1.1\text{-}1)$$

where M represents a neutral atom or molecule which absorbs a photon of light ($h\nu$), h is Planck's constant, and M^+ is the ion formed. The resulting photoelectron (e^-) emerges with a specific kinetic energy, which is the experimental observable in photoelectron spectroscopy.

For historical reasons, work in this field has been divided arbitrarily into two regions, depending on the photon source used. Photoelectron spectroscopy using X-ray radiation is commonly referred to as XPS (X-ray Photoelectron Spectroscopy) or ESCA (Electron Spectroscopy for Chemical Analysis). The most commonly used photon sources in the X-ray region are Mg Kα (1253.6 eV) and Al Kα (1486.6 eV). This was pioneered by K. Siegbahn and his coworkers at Uppsala, who developed an improved beta-ray

spectrometer to measure core electrons.[1] The historical development of ESCA can be found in the two monographs of Siegbahn et al.[2-3] If the photon source is close to the ultraviolet region (≤ 60 eV photon energy), the method is referred to as UPS (Ultraviolet Photoelectron Spectroscopy). This field mainly utilizes the ultraviolet radiation produced from the discharge of Ne (Ne Iα, 16.8476 eV) or He (He Iα, 21.2175 eV; He IIα, 40.8136 eV) gases. This technique was developed by Turner and his associates, who used it to study the outer valence shells of gas-phase molecules.[4] Numerous review articles[5-9] and books[10-15] exist describing these two fields of photoelectron spectroscopy. With the introduction of synchrotron radiation as a photon source,[16] the two fields are merging together.

In a photoelectron experiment, a monochromatic beam of photons with energy $h\nu$ is crossed with a target gas. As shown in equation 1.1.1-1, the target atom or molecule is initially in the neutral ground state Ψ_0. Some of the target molecules absorb a photon, ejecting an electron in the process and leaving the molecule in the jth ionic state (Ψ_j^+). The kinetic energy of the ejected electron is given from energy conservation principles[17-19] in Einstein's photoelectric equation:[20]

$$h\nu = I(j) + E_K(j) + E_{recoil} , \qquad (1.1.1-2)$$

where $h\nu$ is the photon energy, $I(j)$ is the ionization

energy (or potential) for production of the jth ionic state, $E_k(j)$ is the photoelectron kinetic energy associated with production of the jth ionic state, and E_{recoil} is the recoil energy of the absorbing molecule. It can be shown that the recoil energy is, in most cases, negligibly small in the measurements (i.e. $E_{recoil} \leq 0.1$ eV).[18] Therefore, equation 1.1.1-2 can be simplified to,

$$h\nu = I(j) + E_k(j) , \qquad (1.1.1\text{-}3)$$

where the ionization energy I(j) is given by,

$$I(j) = E_f^+(j) - E_i . \qquad (1.1.1\text{-}4)$$

The ionization energy I(j) is the energy difference between the total energies of the jth final ionic state ($E_f^+(j)$) and the initial neutral ground state (E_i). Since the total energies of the initial and final states may be calculated using a Hartree-Fock method, theoretical ionization energies may be estimated.

Using Koopmans' theorem,[21] the ionization energy may be equated to the binding energy of the electron:

$$I(j) = E_b(j) = - \epsilon_j , \qquad (1.1.1\text{-}5)$$

where ϵ_j is the eigenvalue of the jth orbital of the ground state. The binding energy $E_b(j)$ in Koopmans' approximation, is the energy required to completely remove the jth orbital electron to infinity, and assumes no readjustment of the other electrons in the atom or

molecule. The other electrons are assumed to remain frozen in their original orbitals. Koopmans' theorem basically yields a "one-electron" picture of photoionization, based on the orbitals and eigenvalues of the initial ground state. This picture is approximate since orbital relaxation does occur in photoionization.

Combining equations 1.1.1-5 and 1.1.1-3 yields,

$$h\nu = E_b(j) + E_k(j) \quad (1.1.1\text{-}6)$$

For gaseous samples, equation 1.1.1-6 holds since the binding energy $E_b(j)$ is referenced to vacuum level. Calibration of the measured kinetic energies $E_k(j)$ is accomplished usually by introducing a rare gas whose binding energies are known. For solid samples, however, the spectrometer work function ($\phi_{spectrometer}$) must be included in equation 1.1.1-6, since the initial and final states are then referenced to their Fermi levels.

The observable quantity in photoelectron spectroscopy is the photoelectron kinetic energy $E_k(j)$ of the ejected electron from the target atom or molecule. Ordinarily in a photoionization experiment, all energetically allowed ionic states are produced ($E_b(j) < h\nu$). From equation 1.1.1-6, this implies that the electrons ejected must be kinetic energy analyzed over the range $0 \leq E_k(j) \leq h\nu$, and their intensities determined by counting. A photoelectron spectrum consists of a series of peaks at characteristic binding energies, with binding

energy plotted generally on the x-axis and electron intensity on the y-axis. Assuming that the photon beam is monochromatic and of known energy $h\nu$, equation 1.1.1-6 can be used to relate the observed kinetic energies $E_k(j)$ to binding energies $E_b(j)$. Peaks observed in the photoelectron spectrum may be related in the one-electron picture to orbitals of the ground state.

The binding energies $E_b(j)$ can be readily determined from the photoelectron spectrum collected at a single photon energy. The photoionization process, however, is inherently photon energy-dependent. For example, peak intensities in a photoelectron spectrum may vary dramatically over a small photon energy range. The differential cross section for a randomly oriented target (e.g. gas-phase experiment) by partially linearly polarized light can be expressed in the electric dipole approximation as,[16]

$$\frac{d\sigma(h\nu,\Omega)}{d\Omega} = \frac{\sigma(h\nu)}{4\pi}\{1-\frac{\beta(h\nu)}{4}[(3\cos^2\theta_z-1)-3p(h\nu)(\cos^2\theta_x-\cos^2\theta_y)]\} \quad (1.1.1\text{-}7)$$

, where σ is the angle-integrated partial cross section, β is the asymmetry parameter, p is the light polarization, and the angles θ_x, θ_y, and θ_z are the angles between the direction of the ejected electron and the x-, y-, and z-axes, respectively. A more detailed discussion of equation 1.1.1-7 occurs later in section 2.5.2. The observable parameters $\sigma(h\nu)$ and $\beta(h\nu)$ are functions of the

photon energy $h\nu$ and depend on the squares of the dipole-matrix elements. In addition to this, the asymmetry parameter $\beta(h\nu)$ depends on the signs of the matrix elements and the relative phases of the outgoing waves.[22] A tuneable light source such as synchrotron radiation is ideal for studying these two parameters as a function of photon energy. Measurements of these parameters allows one to probe the photoionization dynamics of the target atom or molecule.

Following a description of the experimental apparatus and methods used in Chapter 2, Chapter 3 of this thesis investigates the many-electron effect known as intershell coupling or correlation. The atomic Xe 4d spin-orbit branching ratio was measured using synchrotron radiation over the photon energy range of 74 to 150 eV, and compared to the latest relativistic random-phase approximation (RRPA) calculation of Cheng and Johnson.[23] Experimentally a pronounced minimum occurs in the branching ratio at ~84 eV photon energy. The good qualitative agreement with the RRPA results strongly suggests that intershell correlation between the 4d inner shell and the outer 5s and 5p valence shells is important for Xe during photoionization near threshold. Amusia[24] has found this effect to occur similarly for Kr between the 3d inner shell and the outer valence shells, and between the 3d inner shell of Zn and the outer 4s valence shell. Although these calculations take into account many of the important

electron-electron correlation effects, coupling between the various photoionization channels (i.e. intershell correlation) and spin-orbit interaction, Wendin[25] has recently shown that relaxation effects can be very important in the threshold region. Evidence is then presented for the molecule CF_3I, which suggests that interchannel correlation can be observed also in molecular cases. A strong maximum occurring in the branching ratio of the highest occupied MO (HOMO) at ~90 eV photon energy is thought to be due to interchannel correlation between the HOMO (predominantly I 5p in character) and the I 4d inner shell.

The second part of this thesis is devoted to the study of valence band partial cross sections ($\sigma(h\nu)$) or branching ratios for several molecular cases, using synchrotron radiation as a tuneable photon source. The experimental results obtained are discussed in comparison with theoretical multiple scattering $X\alpha$ calculations (MS-$X\alpha$) in Chapters 4-5. Extensive reviews of the multiple scattering $X\alpha$ method can be found in refefences 26-28. The merit of this method in predicting both $\sigma(h\nu)$ and $\beta(h\nu)$ value trends as a function of photon energy has been established in several recent studies.[29-33] The molecules of carbon tetrafluoride (CF_4, T_d symmetry), trifluoroiodomethane (CF_3I, C_{3v} symmetry), silicon tetrafluoride (SiF_4, T_d symmetry) and xenon difluoride (XeF_2, $D_{\infty h}$ symmetry) were run using the Canadian

Synchrotron Radiation Facility (CSRF) situated on the Tantalus electron storage ring. These molecules were chosen firstly for their simplicity, so that theoretical calculations could be performed on them. This was an important consideration since photoionization studies currently require close interaction between theory and experiment. The molecular series of CF_4, CF_3I, and SiF_4 was chosen secondly, to investigate the photoionization effects of substituting an iodine atom for a fluorine substituent, or replacing the central carbon atom with a silicon atom from the next row.

Thirdly, these molecules were investigated for the presence of shape resonances in their photoionization continua, since it was felt that these highly fluorinated molecules would be likely candidates for such features. A shape resonance is a quasibound state embedded in the continuum, in which the excited electron is temporarily trapped by the molecular potential barrier before tunneling through and escaping. The excellent review by Dehmer[34] summarizes progress which has been made over the past ten years in understanding shape resonances in molecular systems. Interest in shape resonant phenomena stems firstly from the observation that they appear to be present in an increasing number of molecules. In fact, with the exception of hydride molecules, they appear to occur in varying degrees in most other molecules. Secondly, the predominantly one-electron localized nature of these

resonances has lent itself readily to theoretical treatment.[35-37] The MS-Xα method first developed by Dill and Dehmer[35] and applied initially to molecular N_2, has been extended to more complicated molecules like NO, O_2, CO, SF_6, CO_2, BF_3, CCl_4, HI, $SiCl_4$, and C_2H_4, by Davenport,[26] Wallace,[27] Grimm,[31,38,45,46] Dehmer,[39] and others.[40-42] One of the advantages of the multiple scattering technique is that the continuum final states are no more difficult to obtain than the bound states, and computations are far less costly than most other methods. Although the MS-Xα method stresses the scattering aspect of the problem, Langhoff[43] has been able to show using the Stieltjes-Tchebycheff moment-theory (STMT) that these shape resonances are intimately connected with virtual valence orbitals of the molecule. Recently, Robin[44] has discussed these shape resonances in terms of a double-well potential, which he feels is caused by the required orthogonality of the final continuum state to the initial state of the molecule.

The experimental results obtained for CF_4, CF_3I, SiF_4, and XeF_2 will be compared to theoretical MS-Xα results, in order to investigate the dynamics of photoelectron ejection from small molecules. Where it is possible, these results will be related to the experimental or theoretical results of other groups for similar molecular systems. Several novel effects, including shape resonances and intershell correlation, will be discussed for these molecules.

1.2.1 References

1. K. Siegbahn and K. Edvarson, Nucl. Phys. 1, 137 (1956).
2. K. Siegbahn, C. Nordling, G. Johansson, J. Hedman, P.F. Heden, K. Hamrin, U. Gelius, T. Bergmark, L.O. Werme, R. Manne, and Y. Baer, "ESCA Applied to Free Molecules", (American Elsevier, New York, 1969).
3. K. Siegbahn, C. Nordling, A. Fahlman, R. Nordberg, K. Hamrin, J. Hedman, G. Johansson, T. Bergmark, S.-E. Karlsson, I. Lindgren, and B. Lindberg, "ESCA - Atomic, Molecular, and Solid State Structure Studied by Means of Electron Spectroscopy", (Almqvist & Wiksells Boktryckeri AB, Uppsala, 1967).
4. D.W. Turner, C. Baker, A.D. Baker, and C.R. Brundle, "Molecular Photoelectron Spectroscopy", (Wiley-Interscience, London, 1970).
5. D.M. Hercules, Anal. Chem. 42, 20A (1970).
6. D.M. Hercules, Anal. Chem. 44, 1[illegible]R (1974).
7. D.M. Hercules and J.C. Carver, Anal. Chem. 46, 133R (1974).
8. K. Siegbahn, D. Hammond, H. Fellner-Feldegg, and E.F. Barnett, Science 176, 245 (1972).
9. D.W. Turner, Phil. Trans. Roy. Soc. Lond. A 268, 7 (1970).
10. J.H.D. Eland, "Photoelectron Spectroscopy", (Wiley-Halsted, New York, 1974).
11. T.A. Carlson, "Photoelectron and Auger Spectroscopy", (Plenum, New York, 1975).

12. R.E. Ballard, "Photoelectron Spectroscopy and Molecular Orbital Theory", (Adam Hilger, Bristol, 1978).

13. J.W. Rabalais, "Principles of Ultraviolet Photoelectron Spectroscopy", (Wiley-Interscience, New York, 1977).

14. "X-ray Photoelectron Spectroscopy", edited by T.A. Carlson, Benchmark papers in Physical Chemistry and Chemical Physics, Vol. 2, (Dowden, Hutchinson & Ross, Stroudsburg, Pennsylvania, 1978).

15. "Electron Spectroscopy: Theory, Techniques and Applications", Vol. 1-3, edited by C.R. Brundle and A.D. Baker, (Academic Press, New York, 1977).

16. M.O. Krause, "Synchrotron Radiation Research", edited by H. Winick and S. Doniach, (Plenum, New York, 1980), p. 101.

17. R.E. Ballard, "Photoelectron Spectroscopy and Molecular Orbital Theory", (Adam Hilger, Bristol, 1978), p. 2.

18. K. Siegbahn, C. Nordling, A. Fahlman, R. Nordberg, K. Hamrin, J. Hedman, G. Johansson, T. Bergmark, S.-E. Karlsson, I. Lindgren, and B. Lindberg, "ESCA - Atomic, Molecular, and Solid State Structure Studied by Means of Electron Spectroscopy", (Almqvist & Wiksells Boktryckeri AB, Uppsala, 1967), p. 35.

19. D.K. Creber, Ph.D. Thesis, University of Western Ontario (1979).

20. A. Einstein, Ann. Phys. 17, 132 (1905).

21. T. Koopmans, Physica 1, 104 (1934).

22. S.H. Southworth, Ph.D. Thesis, University of California, Berkeley (1982).

23. K.T. Cheng and W.R. Johnson, Phys. Rev. A 28, 2820 (1983).

24. M. Ya. Amusia, V.K. Ivanov, N.A. Cherepkov, and L.V. Chernysheva, Sov. Phys.-JETP 39, 752 (1974).

25. G. Wendin, "Photoionization and Other Probes of Many-Electron Interactions", edited by F.J. Wuilleumier, (Plenum Press, New York, 1976), p. 61.

26. J.W. Davenport, Ph.D. Thesis, University of Pennsylvania (1976).

27. R.S. Wallace, Ph.D. Thesis, Boston University Graduate School (1980).

28. J.W. Davenport, Int. J. Quantum Chem. Symp. 11, 89 (1977).

29. H.J. Levinson, T. Gustafsson, and P. Soven, Phys. Rev. A 19, 1089 (1979).

30. J.L. Dehmer, A.C. Parr, S. Wallace, and D. Dill, Phys. Rev. A 26, 3283 (1982).

31. T.A. Carlson, M.O. Krause, F.A. Grimm, P.R. Keller, and J.W. Taylor, J. Chem. Phys. 77, 5340 (1982).

32. J.L. Dehmer, A.C. Parr, S.H. Southworth, and D.M.P. Holland, Phys. Rev. A 30, 1783 (1984).

33. T.A. Carlson, A. Fahlman, W.A. Svensson, M.O. Krause, T.A. Whitley, F.A. Grimm, M.N. Piancastelli, and J.W. Taylor, J. Chem. Phys. 81, 3828 (1984).

34. J.L. Dehmer, "Resonances in Electron-Molecule Scattering, van der Waals Complexes, and Reactive Chemical Dynamics", edited by D.G. Truhlar, American Chemical Society Symposium Series 263, (American Chemical Society, Washington, D.C., 1984), p. 139.

35. D. Dill and J.L. Dehmer, J. Chem. Phys. 61, 692 (1974).

36. P.W. Langhoff, "Electron-Molecule and Photon-Molecule Collisions", edited by T.N. Rescigno, V. McKoy, and B. Schneider, (Plenum, New York, 1979), p. 183.

37. R.R. Lucchese and V. McKoy, Phys. Rev. A 24, 770 (1981).

38. F.A. Grimm, Chem. Phys. 81, 315 (1983).

39. J.L. Dehmer, A.C. Parr, S.H. Southworth, and D.M.P. Holland, Phys. Rev. A 30, 1783 (1984).

40. J. Kreile, A. Schweig, and W. Thiel, Chem. Phys. Lett. 100, 351 (1983).

41. D.J. Bristow, G.M. Bancroft, and J.S. Tse, Chem. Phys. 75, 263 (1983).

42. J.R. Swanson, D. Dill, and J.L. Dehmer, J. Chem. Phys. 75, 619 (1981).

43. P.W. Langhoff, "Resonances in Electron-Molecule Scattering, van der Waals Complexes, and Reactive Chemical Dynamics", edited by D.G. Truhlar, American Chemical Society Symposium Series 263, (American Chemical Society, Washington, D.C., 1984), p. 113.

44. M.B. Robin, Chem. Phys. Lett. 119, 33 (1985).

45. T.A. Carlson, A. Fahlman, M.O. Krause, P.R. Keller, J.W. Taylor, T. Whitley, and F.A. Grimm, J. Chem. Phys. 80, 3521 (1984).

46. T.A. Carlson, A. Fahlman, M.O. Krause, T.A. Whitley, F.A. Grimm, M.N. Piancastelli, and J.W. Taylor, J. Chem. Phys. 84, 641 (1986).

CHAPTER 2

EXPERIMENTAL

2.1.1 Introduction

Gas-phase photoelectron spectroscopy generally requires that a photon source be linked to an experimental apparatus capable of producing a gaseous sample, and an electron energy analyzer. Monochromatized synchrotron radiation was used as a photon source, gases were delivered basically in the form of an effusive gas jet using a multicapillary array, and the electrons produced from the interaction with the radiation were kinetic energy analyzed using an electron lens-hemispherical analyzer system. Since the instrumental aspects and techniques used in the experiments described in this dissertation have been described previously,[1-5] this chapter will merely review the major experimental aspects involved in the method.

All of the experiments were performed at the Canadian Synchrotron Radiation Facility (CSRF)[1,2] at Tantalus I, an electron storage ring operated by the University of Wisconsin at Stoughton, Wisconsin. CSRF is a national facility owned by NRC (Canada) and was funded in 1979 by the Natural Sciences and Engineering Research Council of Canada and the University of Western Ontario. Although CSRF was designed for the newly constructed

1 GeV Aladdin storage ring, this project was delayed seriously enough that the beamline was assembled instead on beam port 4 of Tantalus. Typical experimental "runs" lasted for approximately two months (three times a year), with eight hours of useable "beam time" per day. Since beam time is a valuable commodity, experiments were carefully planned to maximize the quality and quantity of data collected. As a consequence of the constraints imposed by the limited beam time, long hours of data analysis or alteration of the experimental setup were endured during the time period when the beam was turned off at night.

2.2.1 General Description of CSRF Beamline

The Canadian Synchrotron Radiation Facility (CSRF) consists of seven major components, labelled (1)-(7) in Figure 2.2.1-1. These sections are the "front end" of the beamline, (1); the M_0 mirror box for horizontal focussing, (2); the monochromator pumping chamber, (3); the Mark IV Grasshopper monochromator,[1,6] (4); the refocussing mirror chamber, (5); the differential pumping system, (6); and the experimental chamber used to collect gas-phase photoelectron spectra, (7). Various pumps located on sections (1)-(6) are labelled (a) to (h), while other miscellaneous beamline equipment are labelled (A) to (T). It is important to realize that Figure 2.2.1-1 is a proposed description of CSRF on Aladdin, for which all of the equipment was designed. Since the beamlines at

Figure 2.2.1-1

Scale diagram of the Canadian Synchrotron Radiation Facility (CSRF). The numbers refer to the major sections of the beamline: 1. cooled shutter and fixed aperture; 2. M_0 mirror chamber for horizontal focussing; 3. monochromator pumping chamber; 4. Mark IV "Grasshopper" monochromator; 5. refocussing mirror chamber; 6. differential pumping chamber; 7. experimental chamber. The small letters shown (a-h) refer to where major pumps are located, while capital letters (A-T) refer to other beamline equipment.

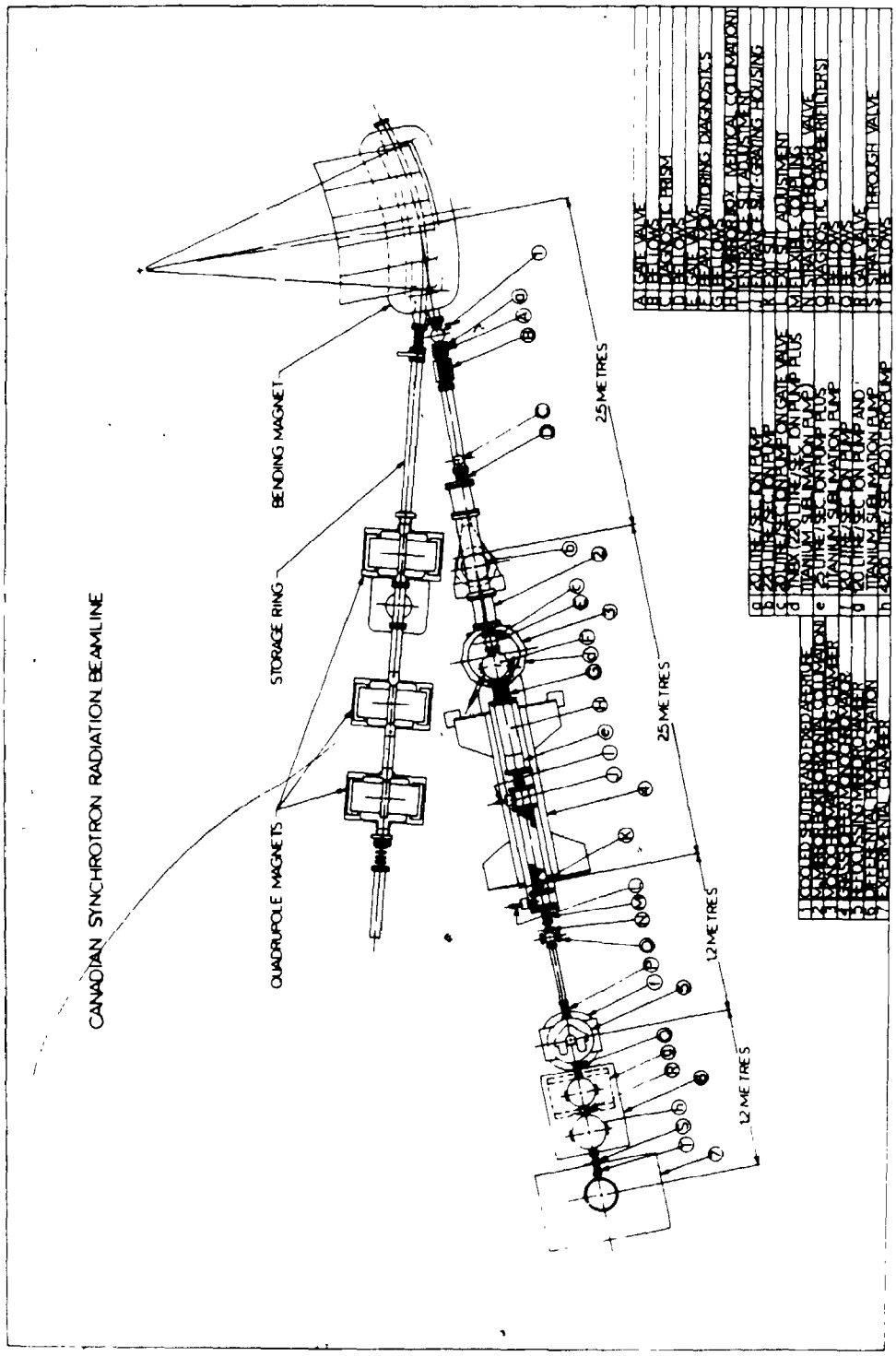
CANADIAN SYNCHROTRON RADIATION BEAMLINE
BENDING MAGNET
STORAGE RING
QUADRUPOLE MAGNETS
25 METRES
25 METRES
12 METRES
12 METRES

Tantalus are approximately five inches lower than Aladdin, a few modifications to the beamline were necessary. Most importantly, an additional mirror was installed 0.5 meters from the exit slit of the monochromator (K) to reflect the photon beam up a couple of inches. The "front end" of the beamline at Tantalus is also slightly different from the Aladdin version. It consists of a viton sealed straight-through valve, followed by the pumping station (a). A more detailed description of the CSRF beamline on Tantalus may be found in reference 2. A general discussion of some of the more important components in the beamline will now be undertaken.

2.3.1 Properties of Synchrotron Radiation

The properties of synchrotron radiation from an electron storage ring have been generally reviewed by Winick,[7] Kunz,[8] and numerous other authors.[9-13] The application of synchrotron radiation to various scientific fields has also been discussed at length in the literature.[14-18] In the operation of the Tantalus I electron storage ring, electrons are first injected from a microtron into the storage ring at an energy of 45 MeV. The electron beam circulates at about 99.9999% of the speed of light inside a stainless steel chamber, which has been evacuated into the low 10^{-10} torr pressure region. Eight bending magnets and four quadrupole magnets confine the electron beam to a closed orbit inside the vacuum chamber.

Once sufficient electron beam current is circulating (~40-200 mA), injection ceases and the energy of the electrons is raised to 240 MeV by increasing the magnetic field in the bending magnets. A radio frequency accelerating cavity operating at ~32 MHz restores the energy that the electrons lose to synchrotron radiation. Electrons circulating in the storage ring are not spread over the entire orbit but occur in a single bunch. Normally the bunch length is ~1 m and the bunch period is ~31 ns. Although a useable beam can be stored for ~4 hours before reinjection, the beam decays over this period due to electron scattering by gas molecules still present in the vacuum chamber. With a 150 mA beam, a typical half-life ($t_{\frac{1}{2}}$) is ~2 hours.

The circulating electron beam becomes a source of electromagnetic radiation as a result of the centripetal acceleration the beam undergoes in the magnetic field regions of the dipole bending magnets. The fundamental equations describing the emission of synchrotron radiation can be found in the modern textbook on electrodynamics by Jackson.[19] Due to the extremely relativistic velocity of the circulating electrons, the radiation emitted in the dipole bending magnet regions is beamed in a narrow cone in the direction of the velocity vector. An observer looking into a beam port would see a short pulse of radiation that would appear like a rather small point-like source.

Briefly, the electromagnetic radiation emitted by Tantalus I is a moderately intense continuum source from the visible to soft X-ray energy regions. In addition, the radiation is time structured and elliptically polarized.[20,21] Although these last two factors can be employed to advantage in certain lifetime and absorption measurement experiments, they were not used in this fashion in the basic photoelectron measurements undertaken in this research. The critical wavelength (λ_c)[18] for Tantalus I is 257 Å (48.2 eV), which is near the maximum of the continuum. A more useful parameter is the wavelength at which the continuum actually maximizes (λ_p),[18] which for Tantalus I is ~108 Å (~115 eV). At photon energies larger than that equivalent to λ_p the photon intensity falls off nearly exponentially, but with useable intensity down to ~$\lambda_c/4$ (~64 Å or ~193 eV for Tantalus I).

2.4.1 Mark IV "Grasshopper" Monochromator

After leaving the electron storage ring, the synchrotron radiation is first focussed by the M_0 mirror box. The M_0 mirror collects 14 mrad of horizontal synchrotron radiation at 2° grazing incidence, and focusses the photon beam horizontally in a 1:1 distance fashion onto the exit slit of the monochromator. The 1 meter long M_0 mirror consists of a gold coated piece of float glass bent to the appropriate curvature.

After the M_0 mirror the photon beam enters the Mark IV "Grasshopper" grazing incidence monochromator shown in

Figure 2.4.1-1, where it first grazes the spherical M_1 mirror at 1°. This can be seen in Figure 2.4.1-2 which shows the monochromator in both zero order and a position corresponding to some wavelength λ. Note that for the purpose of clarity the angles have been exaggerated in the diagram. A 1 m Rowland circle geometry (radius) formed by the "Grasshopper" legs is used in scanning the monochromator, which yields a constant exit beam direction ($\Psi = 2°$). The M_1 mirror serves to focus the beam vertically onto a Codling type entrance slit S_1, consisting of a mirror-slit combination. The M_1 mirror achieves an average demagnification in the vertical direction of 8:1, and consists of a 30 cm long fused silica mirror with a radius of 52.7 meters. The mirror-slit combination at S_1 guides the incoming photon beam to the grating G, which disperses the wavelength of interest through the exit slit. An adjustable entrance slit is accomplished by a slit jaw and its image in a gold coated plane mirror. The grating is mounted on the arm S_1G, which ensures that both the plane mirror and the grating lie on the Rowland circle geometry. A toggle mechanism[22] is used within vacuum to rotate the entrance slit-mirror at half the angular velocity of the grating.

During scanning, the elements M_1, S_1 and G translate parallel to the incoming photon beam. The parallel motion (about 460 mm total) is provided with precision by a linear air bearing referenced to a ground granite slab. The air

bearing is driven by a stepping motor coupled to a ball lead screw, both of which are external to vacuum. A Measur-matic variable speed driver controls the stepping motor. This driver outputs 12,800 steps per revolution of the stepping motor, resulting in very small photon energy increments and thus allowing very high resolution work to be done. Photon energy increments of ~0.004 eV are obtainable at 100 eV photon energy.

The main pumping for the monochromator is done in the separation chamber by a Perkin Elmer Ultek TNB-X, which consists of a 200 ℓ/s ion pump and titanium sublimator. A long transfer tube not shown in Figure 2.4.1-1 connects the separation chamber at the front to the exit slit, in order to add additional pumping capacity to the exit slit region. A smaller 25 ℓ/s ion pump is mounted close to the grating region in order to improve the vacuum in this region. Typically a vacuum of ~2 x 10^{-10} torr was achieved in the separation chamber, while ~5 x 10^{-10} torr was more characteristic of the grating chamber. The pressure in the grating chamber was sufficiently low that the average grating lifetime was ~1 year of almost constant use. For the atomic Xe work a 900 lines/mm original ruled grating from Hyperfine Inc. was used. For virtually all of the molecular systems studied after the initial Xe work, a 600 lines/mm holographic grating from JY Inc. was utilized. Although the resolution of the 600 lines/mm grating ($\Delta\lambda$ = 0.08 Å) was slightly worse than the

Figure 2.4.1-1

Block diagram of Mark IV "Grasshopper" monochromator.

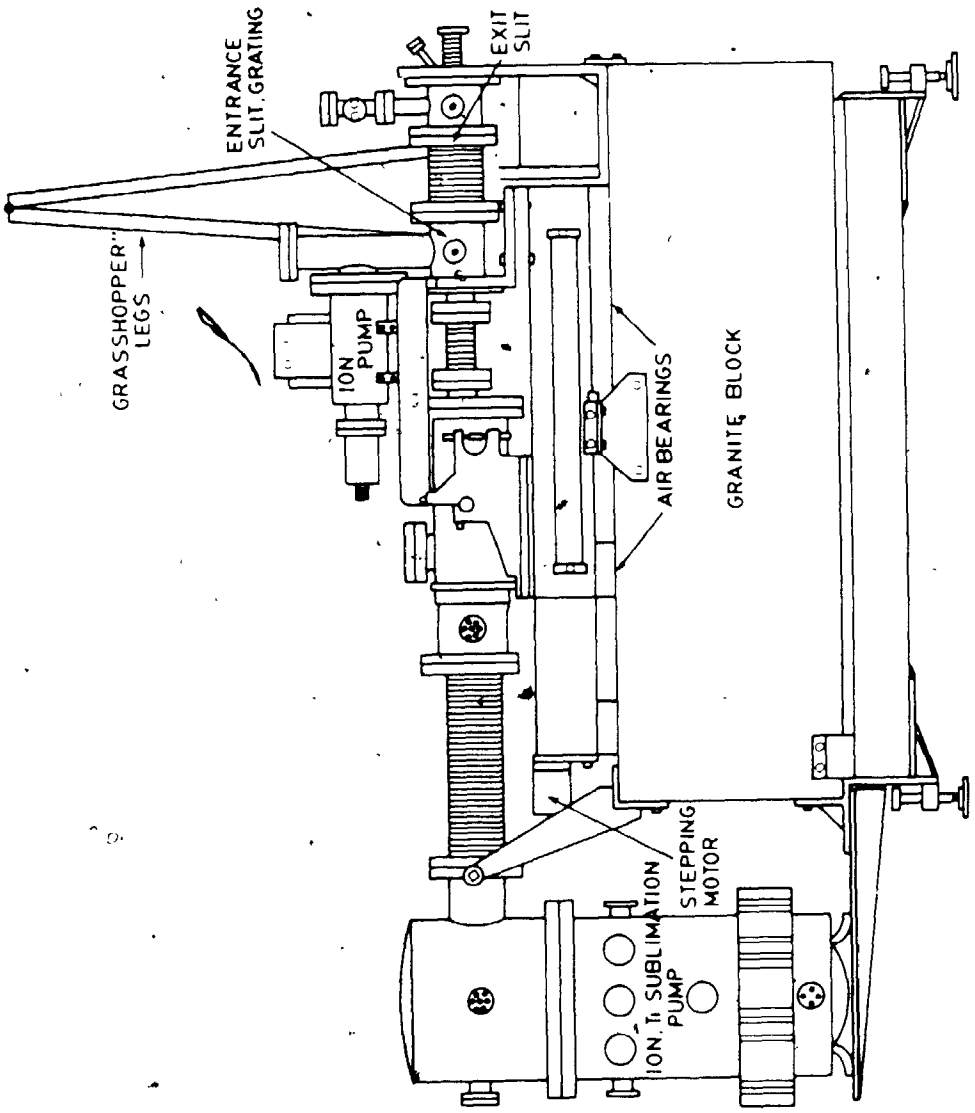
ENTRANCE SLIT, GRATING
EXIT SLIT
GRASSHOPPER LEGS
ION PUMP
AIR BEARINGS
GRANITE BLOCK
STEPPING MOTOR
ION, Ti SUBLIMATION PUMP

Figure 2.4.1-2

Optical elements and basic arrangement of the "Grasshopper" monochromator.[6] Angles are exaggerated, and two positions are shown, zero order and a wavelength λ.

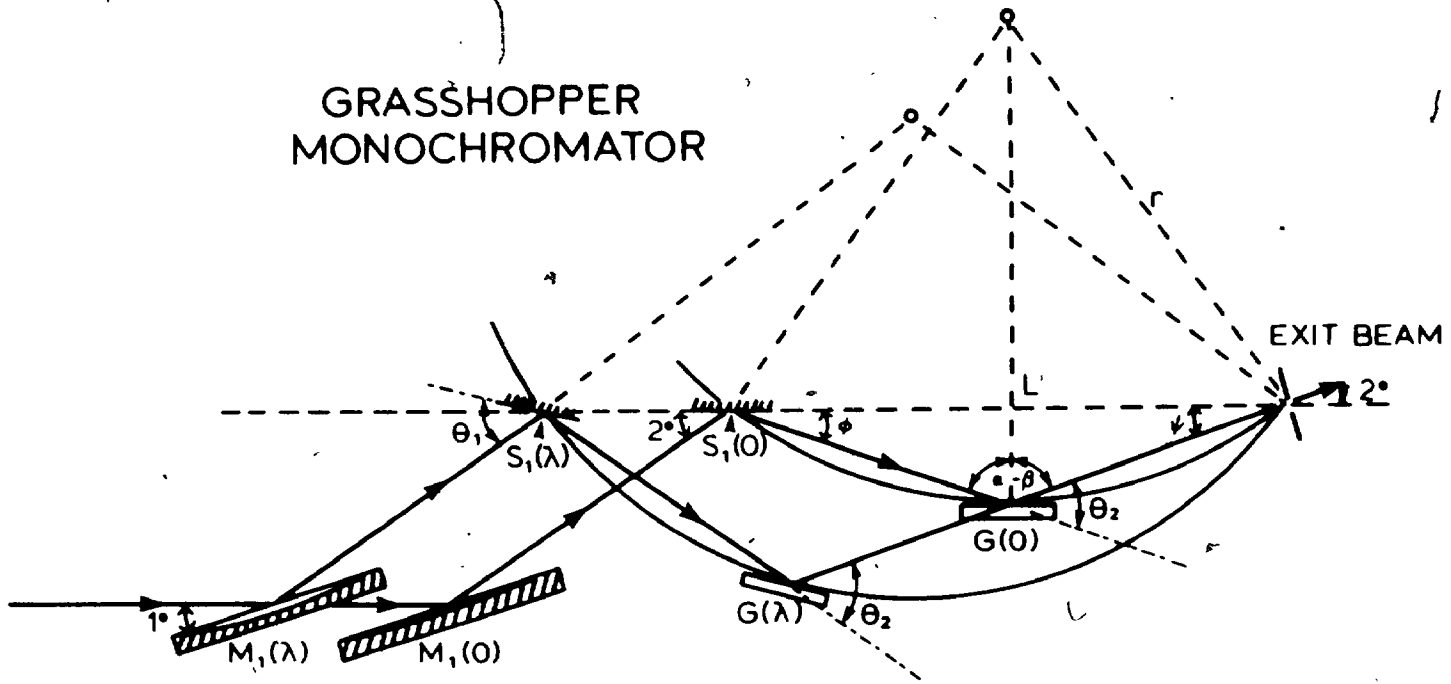
GRASSHOPPER
MONOCHROMATOR
EXIT BEAM
L
2°
θ₁
S₁(λ)
2°
S₁(0)
φ
α
-β
θ₂
G(0)
1°
M₁(λ)
M₁(0)
G(λ)
θ₂

900 lines/mm grating ($\Delta\lambda$ = 0.06 Å), it had the advantage that lower photon energies down to ~21 eV (instead of ~32 eV) were then obtainable.

2.4.2 Monochromator Scan Equation

An equation of scan for the monochromator can be derived with reference to the angles and distances shown in Figure 2.4.1-2. If we let D be the displacement of the grating carriage from the zero order position, L be the distance between entrance and exit slits, and L_0 be the value of L at zero order, then

$$D = L - L_0. \qquad (2.4.2\text{-}1)$$

Let r be the radius of the Rowland circle and R = 2r be the radius of curvature of the grating (2 m). Since R is a diameter of the Rowland circle, the constant plane mirror-grating distance $S_1G = R\cos\alpha$. Both the angle of incidence α (88°) and the exit beam angle Ψ ($\Psi = 90° - \alpha = 2°$) are constants. However, the angles θ_1, and θ_2 are functions of the wavelength λ. From the law of sines, it can be shown that

$$\sin\theta_2 = \frac{L}{2r} = \frac{L}{R}. \qquad (2.4.2\text{-}2)$$

Using the relationship $\theta_2 = 180° - (\alpha - \beta)$, and the first order grating equation[23]

$$\lambda = d(\sin\alpha + \sin\beta), \qquad (2.4.2\text{-}3)$$

where d is the constant groove separation of the grating, equation 2.4.2-2 can be solved for L in terms of λ:

$$L = R \sin[(180°-\alpha) + \sin^{-1}(\frac{\lambda}{d} - \sin\alpha)] . \quad (2.4.2-4)$$

The inverse relationship for λ in terms of L is

$$\lambda = d\{\sin\alpha + \sin[\sin^{-1}\left[\frac{L}{R}\right] - (180°-\alpha)]\} . \quad (2.4.2-5)$$

A Heidenhain linear encoder reads and displays the grating carriage displacement D, where normally the encoder readout is set to zero at zero order. At zero order D = 0 and λ = 0, so that from equation (2.4.2-4),

$$L_0 = R \sin(180°-2\alpha) = R \sin 2\alpha . \quad (2.4.2-6)$$

Equations 2.4.2-1, 2.4.2-6, 2.4.2-4 and 2.4.2-5 define the important operating equations for the monochromator.

In order to calibrate the monochromator, absorption spectra of several known absorption edges were measured. The absorption edge positions used for the energy calibration[24,25] are shown in Table 2.4.2-1. A nonlinear least squares program was written to determine the optimum α and R constant values of equation 2.4.2-5. The FORTRAN program was developed on a PDP-11/23 computer with 28K words of program memory. Using an iterative Gauss-Newton procedure,[26] this program obtains a least squares fit from the measured monochromator displacements (D) of the selected absorption edges and their corresponding

Table 2.4.2-1

Absorption Edge Positions Used for Energy Calibration

Absorption Edge	Energy (eV) Literature	From Least Squares Fit
Al L_3 edge	72.71[a]	72.74
Al L_2 edge	73.15[a]	73.18
2nd order of Al L_3 edge	36.355	36.354
LaF_3: $4d^{10}(^1S_o) \rightarrow 4d^9 4f^1(^3P_1)$[b]	97.5[c]	97.51
LaF_3: $4d^{10}(^1S_o) \rightarrow 4d^9 4f^1(^3D_1)$[b]	102.0[c]	101.97
2nd order of the above transition	51.0	50.96

a) From reference 24.

b) From reference 25.

c) C.G. Olson, Private Communication, 1981.

literature energy values. This calibration process must be repeated occasionally, or whenever a grating is changed. Shown in Table 2.4.2-1 are the results from a 600 lines/mm grating, where the agreement between the literature and fitted values is always better than 0.05 eV. One of the advantages of using absorption spectra for calibration is that this depends specifically on the photon beam and monochromator. The procedure is independent of any possible error contributions from the electron lens-analyzer system.

2.5.1 Experimental and Differential Pumping Chambers

The diverging photon beam from the exit slit of the monochromator is refocussed in the double refocussing mirror chamber from Baker Engineering (Figure 2.1.1-1,5) to the center of the experimental chamber (Figure 2.5.1-1,A). In doing so, the photon beam passes through a two-stage differential pumping section (Figure 2.1.1-1,6), and a high-vacuum gate value (Figure 2.5.1-1,B) with a rectangular light guide mounted in vacuum. The differential pumping section consists of two chambers; one pumped by a 120 ℓ/s ion pump and titanium sublimation pump, and the other pumped by a 4200 ℓ/s cryopump. Regeneration of the cryopump was necessary only every couple of months, even with heavy gas usage in the experimental chamber. The light guide (1 mm x 10 mm x 190 mm long) was surrounded by a graphite-coated Cu tube, which served to support the glass capillary and prevent electrical charging of the

glass. Approximately five orders of magnitude differential pumping result from the glass capillary tube. Typically the differential pumping chamber and light guide allow the beamline to operate at a pressure of ~2 x 10^{-10} torr, when the gas pressure in the experimental chamber is (1-2) x 10^{-5} torr.

The sample chamber (A) and combined lens-analyzer system (C) shown in Figure 2.5.1-1 were purchased commercially from Leybold-Heraeus. The spherical sample chamber (126 mm radius) is internally shielded from magnetic fields to less than 20 mG, using conetic material. The experimental chamber is pumped from below with a 500 ℓ/s turbopump from Balzers. The Leybold LHS-11 combined lens-analyzer system (Figure 2.5.1-1,C) is mounted at the magic angle ($\theta_x = \theta_y = \theta_z = 54.7°$, Figure 2.5.2-1) so that the measured electron intensities can be directly related to photoionization cross sections. The magic angle geometry will be discussed in more detail in section 2.5.2. Additional pumping on the lens is supplied by a 110 ℓ/s Balzers turbopump.

The gas probe is mounted on an XYZ manipulator (Figure 2.5.1-1,D) in order that the resulting gas jet could be adjusted optimally for maximum electron count rate with respect to the incoming photon beam. Gas is leaked in to the gas probe using a Varian Associates leak valve, then introduced to the sample chamber in the form of a collimated gas jet using a stainless steel multicapillary

array with ~20 μ diameter holes. Typical gas backing pressures in the gas probe, as measured by a MKS Inc. Baratron capacitance manometer, were in the 8-12 torr region. Unlike typical effusive gas sources, multicapillary arrays yield a non-cosine angular emission of the gas,[27] that results in a substantially more peaked intensity distribution about the center axis.[28-31] For a given backing pressure, a higher gas number density therefore results in the interaction region. The collimated gas jet is directed onto a CTI-21 cold head operating at 15 K (Figure 2.5.1-1,E). With a backing pressure of 8-12 torr, the ball pressure was typically (1-2) x 10^{-5} torr. The estimated pressure of ~10^{-4} torr in the interaction region is low enough to avoid scattering cross section problems.

Solid compounds can also be run in the gas phase using this basic gas probe. A solid state probe can be slid through an O-ring, placing a small teflon cylinder containing the solid directly behind the multicapillary array. The sample container and solid probe are in thermal contact with a Cu cylinder surrounding it, which has an ARi 700 watt BXX electric heater coiled about it. The temperature is controlled manually using a variac hooked up to the electric heater, and displayed using an Omega Model 4001 temperature controller/display.

The Leybold LHS-11 lens section consists of a multi-element lens system. It is designed to collect

electrons over a solid angle and specifically focus electrons of a desired kinetic energy E_k on an entrance slit leading to the analyzer section. By sweeping the kinetic energy E_k, a photoelectron spectrum is generated. The lens-analyzer system was operated in constant pass energy mode, where the analyzer resolution contribution is constant ($\Delta E_{Analyzer}$ = constant) and therefore independent of the kinetic energy. In this mode of operation, electrons with the selected kinetic energy E_k are appropriately accelerated/retarded, so that upon entering the analyzer section they have a kinetic energy corresponding to the selected pass energy (E_{pass}). Although some of the high resolution Xe work was done at 25 eV pass energy, the majority of the experimental data was collected using 50 eV pass energy. Increasing the pass energy results in poorer resolution, but has the advantage of higher electron intensities.

A hemispherical analyzer (mean radius $\bar{r}$ = 126 mm) is used finally to focus electrons of energy E_{pass} onto a Galileo Electro-Optics Corporation channeltron electron multiplier (Model 4028). One of the advantages of running in constant pass energy mode is that the detector efficiency is constant for a given pass energy, and therefore independent of the electron kinetic energy E_k.

The channeltron is linked to a specially designed detection electronics unit just outside vacuum. This unit basically consists of a LeCroy MVL100

Figure 2.5.1-1

Schematic diagram (top view) of the photoelectron spectrometer: A, experimental chamber; B, gate valve; C, Leybold-Heraeus combined lens and analyzer system (LHS-11); D, XYZ manipulator for gas probe; E, CTI cryopump gas trap; F, antimagnetic view port, and G, nude ionization gauge.

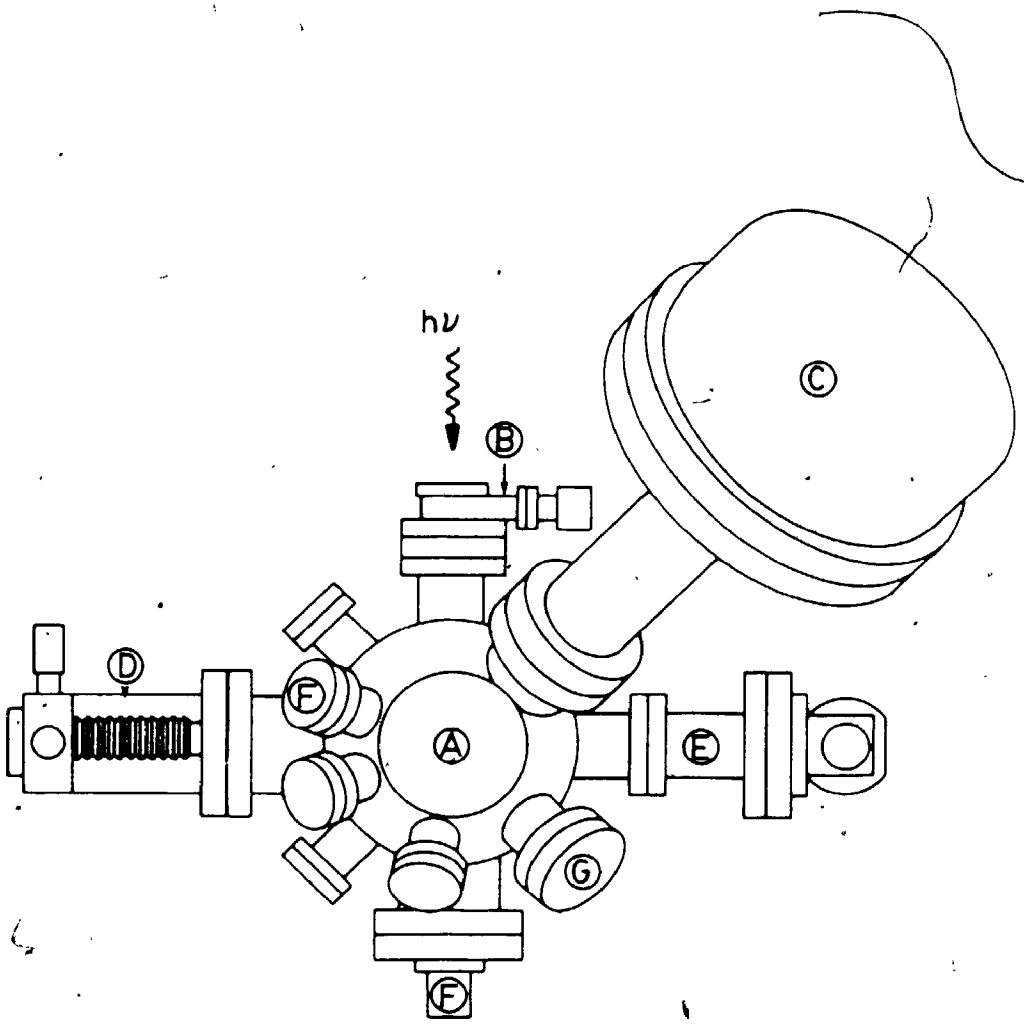
hν
B
C
D
F
A
E
G
F

amplifier-discriminator and a Motorola MC10128L chip. The LeCroy MVL100 chip amplifies the output pulses from the channeltron, generating an ECL pulse if this pulse exceeds the threshold voltage value. The Motorola MC10128L circuit takes the fast ECL output from the LeCroy MVL100 and converts it to a TTL output. This TTL level output is routed into a homemade counter unit, which is interfaced to a Digital Equipment Corporation PDP-11/23 computer which controls the spectrometer. It was discovered early on that the amplifier-discriminator chip from LeCroy was extremely sensitive to external RF noise and ground loops. Since our count rates are inherently low ($\leq 10^2$ Hz), this unit had to be totally redesigned to virtually prevent RF noise from entering and affecting the circuitry inside.

2.5.2 Photoionization Cross Section

The differential photoionization cross section at a particular photon energy $h\nu$ is defined as the number of electrons $N_{electron}$ ejected per unit time into the solid angle $d\Omega$ about Ω, divided by the number of photons $N_{h\nu}$ per unit area per unit time:[32]

$$d\sigma(h\nu,\Omega) = \frac{N_{electron}\, d\Omega}{N_{h\nu}} . \qquad (2.5.2\text{-}1)$$

This ratio has the dimensions of area. A typical total photoionization cross section obtained by integrating over all solid angles, is ~(0.1 - 100) megabarns (1 Mb = 10^{-18} cm^2). Since $N_{electron}$ is simply the (ejection) transition

probability $P_{fi}(h\nu)$ between the initial bound state i and the final state f (bound or continuum), equation 2.5.2-1 can be rewritten as,

$$d\sigma(h\nu,\Omega) = \frac{P_{fi}(h\nu)}{N_{h\nu}}\, d\Omega \quad . \qquad (2.5.2\text{-}2)$$

Using Fermi's golden rule, the transition probability $P_{fi}(h\nu)$ per unit time may be related to the square of the matrix element between the initial and final states and the dipole moment operator. Such a derivation[33] yields in the electric dipole approximation the following length form,

$$d\sigma \propto |\langle f|\sum_j \hat{A}\cdot\vec{r}_j|i\rangle|^2\, d\Omega \quad , \qquad (2.5.2\text{-}3)$$

where $\hat{A}$ is the unit polarization vector of the incident photon beam and $\vec{r}_j$ the position vector of the jth electron. Usually expressions like equation 2.5.2-3 are written in terms of the differential $d\sigma/d\Omega$. This is misleading however, since $d\sigma/d\Omega$ is not the derivative of the integrated or total cross section σ with respect to the solid angle $d\Omega$, but the infinitesimal cross section in the sold angle $d\Omega$ near Ω. Although the surface integral shown in equation 2.5.2-4 defines the integrated cross section σ, it can be alternatively thought of as a definition of $d\sigma/d\Omega$:

$$\sigma \equiv \int d\Omega \left[\frac{d\sigma}{d\Omega}\right] \quad . \qquad (2.5.2\text{-}4)$$

As predicted by theory[11] and verified experimentally,[34] synchrotron radiation is completely elliptically polarized. A differential cross section expression has been derived by Schmidt[20] for photoionization by elliptically polarized light. Schmidt derived the formula[20] for a randomly oriented target, assuming the dipole approximation. Samson and Starace[35] were able to derive an equivalent expression for partially linearly polarized light, even though elliptically polarized light differs from partially linearly polarized light by the presence of circularly polarized light. This results from the fact that the circularly polarized light content of elliptically polarized light does not change the angular distribution.[35-37]

Referring to Figure 2.5.2-1, the z-axis is defined by the direction of the photon beam, the x-axis lies in the synchrotron plane, and the angles, θ_x, θ_y, and θ_z are the angles between the direction of the emitted electron and the x-, y-, and z-axes, respectively. Following the derivation of Samson and Starace[35] for partially linearly polarized light, one may treat this as being equivalent to two incoherent linearly polarized beams vibrating along the orthogonal x- and y-axes. Letting I_x and I_y represent the photon intensities along the x- and y-axes, the polarization p may be defined as $p = (I_x - I_y)/(I_x + I_y)$. For partially linearly polarized light and a randomly oriented target, the differential cross section $d\sigma/d\Omega$ in

Figure 2.5.2-1

A photon beam travelling in the z-direction interacts with a molecule at the origin of the xyz axes. A photoelectron is ejected with the direction cosines cos θ_x, cos θ_y, and cos θ_z.

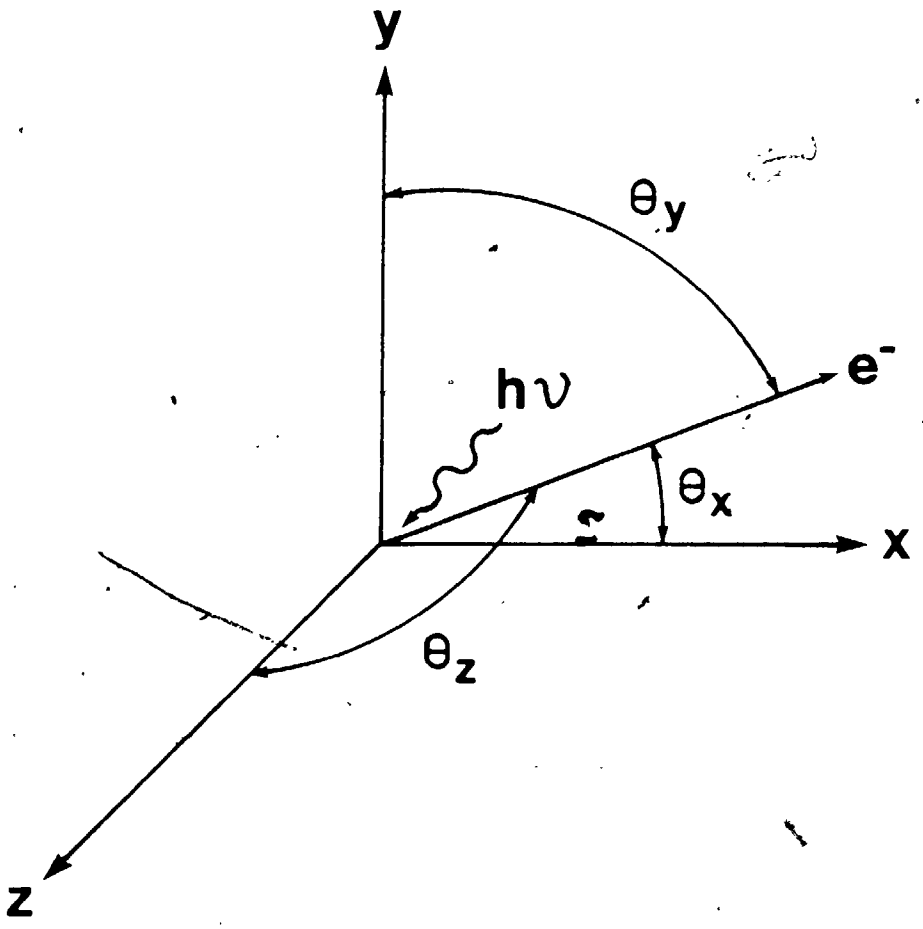
y
θy
e⁻
hν
θx
x
θz
z

the dipole approximation is,[35,38-39]

$$\frac{d\sigma(h\nu,\Omega)}{d\Omega} = \frac{\sigma(h\nu)}{4\pi}\{1-\frac{\beta(h\nu)}{4}[(3\cos^2\theta_z-1)-3p(h\nu)(\cos^2\theta_x-\cos^2\theta_y)]\} \quad (2.5.2\text{-}5)$$

, where σ is the angle-integrated partial cross section and β is the asymmetry parameter. In order that the cross section be positive, it can be readily shown that the asymmetry parameter must satisfy the inequality $-1 \leq \beta \leq 2$.

As shown in equation 2.5.2-5, the total cross section σ, the asymmetry parameter β, and the light polarization p are functions of the photon energy $h\nu$. From a theoretical point of view, the two observables σ and β are of primary interest. Whereas the total cross section σ depends solely on the transition matrix elements $\langle\psi_f|\sum_j \hat{A}\cdot\vec{r}_j|\psi_i\rangle$, the asymmetry parameter β depends in addition on the phase shifts δ_l of the outgoing waves.[40] In other words, measurement of σ yields information about the bound and continuum states ψ_f, while measurement of β contains further information about the phase shifts. Although it is possible to measure both σ and β by measuring the photoelectron spectra at as few as two angles,[41] this requires that the entire detection system be rotatable. Due to the prohibitive cost and impracticality of rotating the very large LHS-11 lens-analyzer system, it was decided that the electron detector should be mounted in

a fixed position at the magic angle configuration of $\theta_x = \theta_y = \theta_z = 54.7°$.

In this magic angle configuration, equation 2.5.2-5 reduces considerably to,

$$\left.\frac{d\sigma(h\nu,\Omega)}{d\Omega}\right|_{\theta_x=\theta_y=\theta_z=54.7°} = \frac{\sigma(h\nu)}{4\pi} \quad (2.5.2\text{-}6)$$

The advantage of mounting the detection system at the magic angle configuration is that the photoelectron spectra measured are independent of β and p and directly proportional to the total cross section σ. The disadvantage is that one sacrifices all knowledge about the asymmetry parameter β. Samson[42] has also used this particular configuration and shown further that equation 2.5.2-6 holds no matter how large the solid angle observed by the detector.

2.6.1 Data Acquisition System

A Digital Equipment Corporation (DEC) PDP-11/23 minicomputer was selected for the data collection, reduction and control of the experiment. The PDP-11/23 is a 16-bit minicomputer, with an extensive instruction set and good execution speed. The RT-11 foreground/background operating system (Version 3B) from DEC was used exclusively in all of the software developed. Other major DEC utilities used were the FORTRAN compiler, MACRO-11 assembler, LINK linking loader and TECO editor. While the

majority of the software developed was written in the high-level language FORTRAN because of the versatility, a small number of subroutines were written in MACRO-11 assembly language. Assembly language was used instead of FORTRAN whenever speed was critical, for interrupt-driven routines, or whenever the task could be coded more easily in assembly language (e.g. bit manipulation). The hardware and software aspects of the data acquisition system will now be briefly described.

2.6.2 Hardware

A block diagram of the photoelectron spectrosocopy data acquisition system is shown in Figure 2.6.2-1. The PDP-11/23 minicomputer has 28K words (1K = 1024 words; 1 word = 16 bits) of "lower" memory, which is used for program and data storage, and storage of the RT-11 operating system. An additional 32K words of "upper" memory is used exclusively for data storage of the collected photoelectron spectra. A dual double density RX02 disk drive from DEC supplies 1 Mbyte (1 byte = 8 bits) of program and data storage. A DEC VT105 graphics terminal is used to display the spectra being collected and allow the user to enter program commands. In addition to this console terminal a DEC LA36 (decwriter II) terminal is also connected to the DEC DLV11-J asynchronous serial interface, and used for hard copy listings. A Hewlett-Packard 7225A plotter is connected to the DEC IBV11-A IEEE instrument bus interface, providing for hard copy spectral plots.

Figure 2.6.2-1

Block diagram of photoelectron spectroscopy data acquisition system.

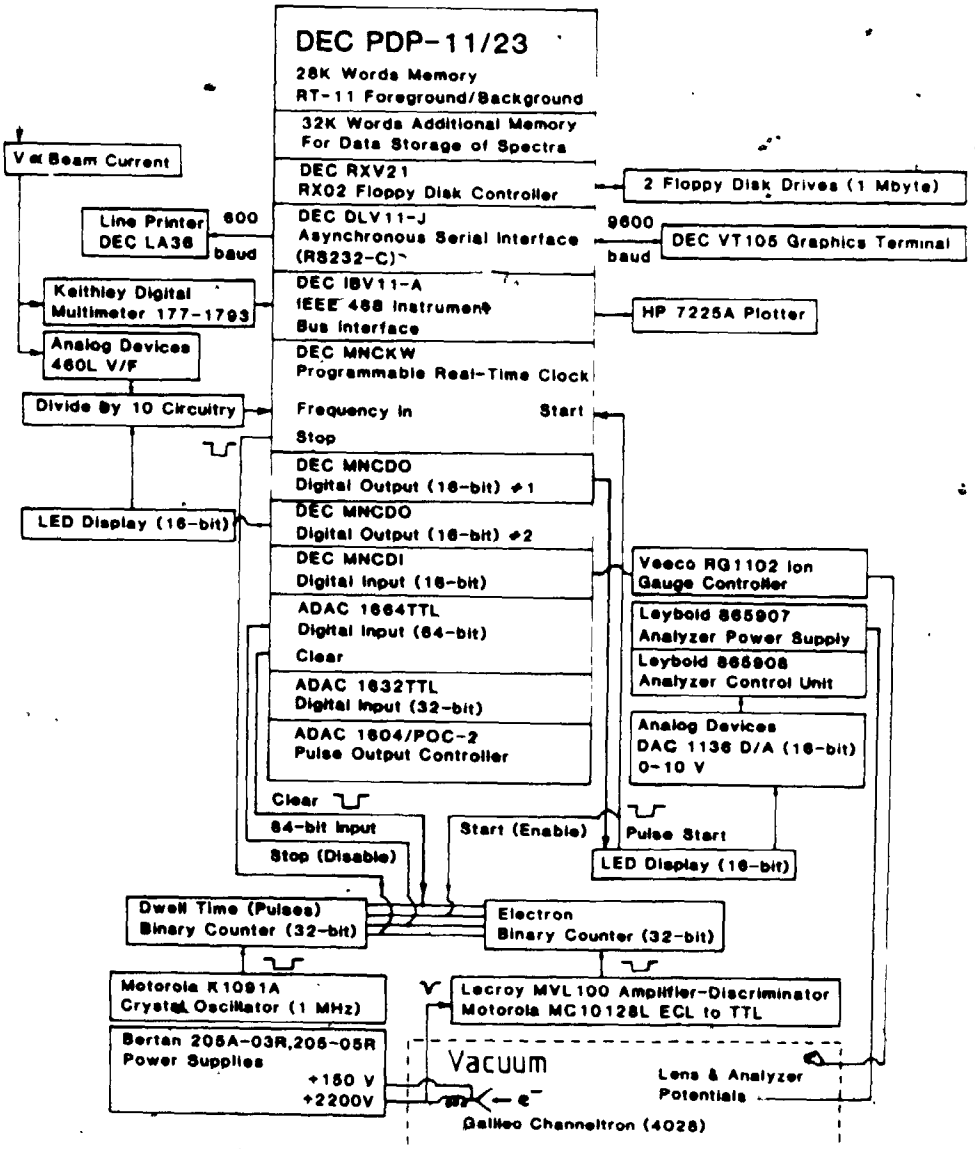
DEC PDP-11/23
28K Words Memory
RT-11 Foreground/Background
32K Words Additional Memory
For Data Storage of Spectra
DEC RXV21
RX02 Floppy Disk Controller
2 Floppy Disk Drives (1 Mbyte)
DEC DLV11-J
Asynchronous Serial Interface
(RS232-C)
600 baud
Line Printer
DEC LA36
9600 baud
DEC VT105 Graphics Terminal
DEC IBV11-A
IEEE 488 Instrument
Bus Interface
HP 7225A Plotter
DEC MNCKW
Programmable Real-Time Clock
Frequency In
Start
Stop
DEC MNCDO
Digital Output (16-bit) #1
DEC MNCDO
Digital Output (16-bit) #2
DEC MNCDI
Digital Input (16-bit)
ADAC 1664TTL
Digital Input (64-bit)
Clear
ADAC 1632TTL
Digital Input (32-bit)
ADAC 1604/POC-2
Pulse Output Controller
Beam Current
Keithley Digital
Multimeter 177-1793
Analog Devices
460L V/F
Divide By 10 Circuitry
LED Display (16-bit)
Veeco RG1102 Ion
Gauge Controller
Leybold 865907
Analyzer Power Supply
Leybold 865908
Analyzer Control Unit
Analog Devices
DAC 1136 D/A (16-bit)
0-10 V
Clear
64-bit Input
Stop (Disable)
Start (Enable)
Pulse Start
LED Display (16-bit)
Dwell Time (Pulses)
Binary Counter (32-bit)
Electron
Binary Counter (32-bit)
Motorola R1091A
Crystal Oscillator (1 MHz)
Lecroy MVL100 Amplifier-Discriminator
Motorola MC10128L ECL to TTL
Bertan 205A-03R,205-05R
Power Supplies
+150 V
+2200V
Vacuum
e⁻
Lens & Analyzer
Potentials
Galileo Channeltron (4028)

A brief description of the data collection process will now be undertaken. Let us make the assumption that a photoelectron spectrum consisting of N data points is currently being initiated, and that the data point to be first collected corresponds to a kinetic energy E_K. The control, multiscanning and data collection processes are carried out with a program called PES (Photoelectron Spectroscopy) and the PDP-11/23 minicomputer. An "appropriate" binary bit pattern corresponding to E_K is written by the 11/23 CPU into the first DEC 16-bit digital output module. This bit pattern is fed into an Analog Devices DAC 1136 16-bit D/A convertor, which supplies the Leybold electronic units (865907 & 865908) with a specific voltage between 0-10 V DC. This input voltage corresponds to the desired electron kinetic energy in a linear fashion. A bit pattern consisting of all 1's generates an analog signal of 10 V, corresponding to 100% full scale of the kinetic energy range. The kinetic energy range is selected manually on the Leybold analyzer control unit. Likewise, a bit pattern of all 0's generates an analogous signal of 0 V, corresponding to 0% full scale of the kinetic energy range, or E_K = 0 eV. From the one kinetic energy sweep voltage, the Leybold analyzer power supply (865907) generates all the remaining voltages required to run the Leybold LHS-11 lens-analyzer system inside vacuum.

The DEC MNCKW programmable real-time clock is used to control the time period over which electron counts in

the 32-bit binary counter are allowed to accumulate. Instead of a fixed dwell time period for each kinetic energy E_K in the sweep, electron counts are allowed to accumulate until a fixed number of pulses are received by the clock. If the frequency of the pulses is proportional to the instantaneous photon flux, then this technique can be used to give the same statistics (i.e. same number of photons) per channel. This frequency is generated at Tantalus by running a voltage proportional to the storage ring beam current, into an Analog devices 460L V/F convertor. Since the real-time clock cannot accept TTL pulse trains exceeding ~0.5 MHz, this frequency is divided by an appropriate power of 10 to ensure this does not happen. The power of 10 actually used in the division is software controlled with the second 16-bit digital output from DEC. Typical dwell times per channel were ~0.25 seconds. This results in data collection times per individual scan from ~(1-4) minutes, depending on the storage ring beam current and the number of data points in the spectrum (N). This technique very accurately accounts for the small decrease in photon flux between channels, due to beam current decay. The dwell time per channel (approximate only) was purposefully kept small however, in order that the results be independent of such effects as slight pressure fluctuations or electronic drift with time.

Once the lens and analyzer voltages inside vacuum have settled sufficiently to their proper values, a "start"

pulse generated from the 16-bit LED display unit initiates the real-time clock operation and enables both 32-bit counters. A 1 MHz frequency generated by a Motorola K1091A crystal oscillator is fed into one of these counters, so that the actual dwell time for a particular channel can be calculated, if so desired. The other 32-bit counter is fed a frequency proportional to the rate at which electrons strike the channeltron detector. As discussed previously in section 2.5.1, output pulses generated by electrons striking the Galileo Electro-Optics channeltron (Model 4028) are amplified and discriminated by a commercially available amplifier-discriminator unit (LeCroy MVL100). These pulses are converted from ECL to TTL level using the Motorola MC10128L chip, whereupon the pulses are fed directly into a fast 32-bit binary counter. Both 32-bit counters implement fast Schottky TTL logic, using eight 4-bit synchronous counters (Texas Instrument SN74LS161) in series.

Both counters remain enabled until a predetermined number of pulses (which is constant) have been counted by the real-time clock. At this point the clock generates a "stop" pulse which disables both of the 32-bit counters from counting, and initiates a computer software interrupt. The interrupt causes the PDP-11/23 to momentarily read the contents of these two counters using the 64-bit digital input from ADAC (1664TTL), and store these two numbers in the additional 32K words of "upper"

memory. A "clear" pulse generated after reading both counters by the 64-bit digital input module, is used to clear the counters to zero. Following this, the kinetic energy of the next channel is selected via software, and the entire procedure repeated until an individual scan of N channels has been collected. The software program PES displays the spectrum being collected on the DEC VT105 terminal, updating the graphics display in an asynchronous and independent manner of the actual data collection. Typically a spectrum is multiscanned ≥ 20 times, in order to minimize the effects of small drifts and fluctuations, and to statistically average the results. At the beginning and end of each individual scan, the experimental chamber pressure is read in from the VEECO RG1102 ion gauge controller using the 16-bit digital input from DEC, and stored in memory. In addition the initial and final storage ring beam currents for each individual scan are read in from the Keithley digital multimeter (model 177-1793), using the IEEE 488 bus. At the end of the multiscanning process, the spectrum is permanently saved on floppy disk. A data listing and plot are usually generated at this point on the line printer (DEC LA36) and HP 7225A plotter, respectively.

2.6.3 Software

The data acquisition software to control this experiment is termed PES (for Photoelectron Spectroscopy). A basic design philosophy was adopted which ensured that

the system was as simple as possible to use for the new user, and that the software was "modular" and extremely "readable". These last two design criteria are extremely important when software modifications (present or future) are necessary. "Modularity" was achieved by writing specific operations or tasks as concise, independent subroutines. This feature allowed the program to be heavily overlayed in its execution structure. Even with this overlayed organization, the program fills virtually the entire "lower" memory segment. The "upper" 32K words of memory are reserved exclusively for the storage of spectra. "Readability" was accomplished by writing the majority of these subroutines in the high level language FORTRAN, and documenting them with informative comments. The remaining subroutines were written in MACRO-11 assembly language, since for the most part they perform interrupt handling functions or extensive bit manipulation.

The user communicates with the data acquisition software using a series of "commands", typed on the DEC VT105 console terminal. Commands use the following command structure: < command character >< argument(s) >. The arguments required depend on the function selected, but most commands require the user to supply the region of interest. The data area located in the "upper" 32K of memory is organized into 10 regions of interest (1-10), with each region comprised of up to 465 32-bit channels. The command character consists of a single button on the

keyboard, which is indicative of the operation to be performed. The main program accepts commands entered by the user from the terminal, then invoking the appropriate subroutine to process it. This is accomplished using a single "polling" mode loop[43] in the main program, that continuously checks to see if any commands have been entered. A brief description of these commands is given in Table 2.6.3-1.

A photoelectron spectrum is collected typically using the following sequence of commands. The user first enters the R (Region) command to specify which region this spectrum will be stored in. Upon entering this command, a blank spectrum is initially drawn on the VT105 graphics terminal. The scan parameters are then defined by invoking the U (Update) command and following the "menu" then displayed on the terminal. Such information as the desired photon energy, the number of scans required, initial and final binding (or kinetic) energies of the scan, channel ΔE, approximate dwell time per channel, and general spectrum comments are entered and defined at this point. The L (Label) command is then usually executed, in order that various experimental conditions (e.g. lens voltage settings) may be defined. Data collection is then initiated simply with the G (Go) command. During the multiscanning process which ensues, the data acquisition program asynchronously updates the spectrum on the terminal. The user may readily determine intensities,

splittings or binding/kinetic energies of spectral features using the various cursor commands (eg. ↑, ↓ , →, ←, PF1 key, PF2 key). Upon completion the spectrum is saved automatically on floppy disk, whereupon program control is returned to the main program "polling" mode loop once again. A hard copy of the spectrum collected may be generated readily on the HP 7225A plotter, using the P (Plot) command.

Table 2.6.3-1

PES Commands

Command Character	Description
A	Abort data acquisition and return to RT-11 Monitor.
D	Calculate the monochromator displacement (mm) given a photon energy (eV).
E	Calculate the photon energy (eV) given the monochromator displacement (mm).
G	Go. The command initiates multiscanning of the regions of interest specified.
H	Halts the current scan immediately.
I	The specified file containing a previously collected spectrum is input from disk and stored in the requested region of interest.
L	This command allows the user to input various experimental conditions, in order to label the spectra.
P	Plot the specified region of interest on the HP 7225A plotter.
R	Display region of interest specified on the VT105 graphics terminal.
S	Stop data collection at the end of the current scan.
U	This command allows the user to update the scan parameters in the region of interest currently being displayed.

Table 2.6.3-1 (continued): PES Commands

Command Character	Description
↑	Y-axis scale is decreased by 2, and the spectrum redrawn.[a]
↓	Y-axis scale is increased by 2, and the spectrum redrawn.[a]
→	Currently "active" cursor is moved right.[a]
←	Currently "active" cursor is moved left.[a]
PF1 key	Switches "active" cursor selection between the left and right cursors.[a]
PF2 key	Switches the "active" cursor left/right movement between 1 and 10 channels.[a]

a) These commands refer specifically to the VT105 terminal display.

2.7.1 References

1. K.H. Tan, G.M. Bancroft, L.L. Coatsworth, and B.W. Yates, Can. J. Phys. 60, 131 (1982).
2. K.H. Tan, P.C. Cheng, G.M. Bancroft, and J.Wm. McGowan, Can. J. Spectrosc. 29, 134 (1984).
3. B.W. Yates, K.H. Tan, L.L. Coatsworth, and G.M. Bancroft, Phys. Rev. A 31, 1529 (1985).
4. B.W. Yates, K.H. Tan, G.M. Bancroft, L.L. Coatsworth, and J.S. Tse, J. Chem. Phys. 83, 4906 (1985).
5. B.W. Yates, K.H. Tan, G.M. Bancroft, L.L. Coatsworth, J.S. Tse, and G.J. Schrobilgen, J. Chem. Phys., in press.
6. F.C. Brown, R.Z. Bachrach, and N. Lien, Nucl. Instrum. Methods 152, 73 (1978).
7. H. Winick, "Synchrotron Radiation Research", edited by H. Winick and S. Doniach (Plenum, New York, 1980).
8. C. Kunz, "Synchrotron Radiation Techniques and Applications", edited by C. Kunz (Springer-Verlag, New York, 1979), p. 1.
9. J. Schwinger, Phys. Rev. 75, 1912 (1949).
10. D.H. Tomboulian and P.L. Hartman, Phys. Rev. 102, 1423 (1956).
11. A.A. Sokolov and I.M. Ternov, Sov. Phys. - JETP 4, 396 (1957).
12. D.H. Tomboulian and D.E. Bedo, J. Appl. Phys. 29, 804 (1958).

13. K. Codling and R.P. Madden, J. Appl. Phys. 36, 380 (1965).

14. G. P. Williams, Vacuum 32, 333 (1982).

15. K.O. Hodgson and S. Doniach, Chem. Eng. News, Aug. 21, 26 (1978).

16. D.E. Eastman and F.J. Himpsel, Physics Today, May, 64 (1981).

17. K. Codling, Physica Scripta 9, 247 (1974).

18. K. Codling, Rep. Prog. Phys. 36, 541 (1973).

19. J.D. Jackson, "Classical Electrodynamics" (John Wiley, 1975).

20. V. Schmidt, Phys. Lett. 45A, 63 (1973).

21. F. Wuilleumier and M.O. Krause, J. Electron Spectrosc. Relat. Phenom. 5, 921 (1974).

22. F.C. Brown, R.Z. Bachrach, and N. Lien, Nucl. Instrum. Methods 152, 73 (1978).

23. J.A.R. Samson, "Techniques of Vacuum Ultraviolet Spectroscopy", (Pied Publications, Lincoln, Nebraska, 1967), p. 10,

24. C. Gahwiller and F.C. Brown, Phys. Rev. B 2, 1918 (1970).

25. S. Suzuki, T. Ishii, and T. Sagawa, J. Phys. Soc. Jpn. 38, 156 (1975).

26. R.I. Jennrich and P.F. Sampson, Technometrics 10, 63 (1968).

27. R.H. Jones, D.R. Olander, and V.R. Kruger, J. Appl. Phys. 40, 4641 (1969).

28. D.R. Olander, J. Appl. Phys. 40, 4650 (1969).

29. J. Deckers and J.B. Fenn, Rev. Sci. Instr. 34, 96 (1963).

30. J.C. Johnson, A.T. Stair, Jr., J.L. Pritchard, J. Appl. Phys. 37, 1551 (1966).

31. J.A. Giordmaine and T.C. Wang, J. Appl. Phys. 31, 463 (1960).

32. H.A. Bethe and E.E. Saltpeter, "Quantum Mechanics of One- and Two-electron Systems", (Springer-Verlag, Berlin, 1957).

33. R.S. Wallace, Ph.D. Thesis, Boston University (1980).

34. P. Joos, Phys. Rev. Lett. 4, 558 (1960).

35. J.A.R. Samson and A.F. Starace, J. Phys. B 8, 1806 (1975).

36. M. Peshkin, Adv. Chem. Phys. 18, 1 (1970).

37. V.L. Jacobs, J. Phys. B 5, 2257 (1972).

38. L. Karlsson, L. Mattson, R. Jadrny, K. Siegbahn, and K. Thimm, Phys. Lett. 58A, 381 (1976).

39. M.O. Krause, "Synchrotron Radiation Research", edited by H. Winick and S. Doniach (Plenum, New York, 1980), p. 101.

40. J. Cooper and R.N. Zare, "Lectures in Theoretical Physics", Vol. XI-C, edited by S. Gettman, K. Mahanthajyra, and W. Brittin (Gordon and Breach, New York, 1969), p. 317.

41. T.A. Carlson, A. Fahlman, M.O. Krause, P.R. Keller, J.W. Taylor, T. Whitley, and F.A. Grimm, J. Chem. Phys. 80, 3521 (1984).

42. J.A.R. Samson, Phil. Trans. Roy. Soc. London A 268, 141 (1970).

43. R.H. Eckhouse, Jr. and L.R. Morris, "Minicomputer Systems Organization, Programming, and Applications (PDP-11)", (Prentice-Hall, Englewood Cliffs, New Jersey, 1979), p. 236.

CHAPTER 3

ELECTRON CORRELATION EFFECTS IN Xe AND CF_3I

3.1.1 Introduction

For some time electron correlation has been recognized to be of crucial importance in understanding atomic and molecular systems. Lowdin[1] in 1959 defined correlation energy as

$$E_{exact} = E_{HF} + E_{correlation} , \qquad (3.1.1\text{-}1)$$

where E_{HF} is the Hartree-Fock energy and E_{exact} is the exact nonrelativistic energy. The Hartree-Fock energy of an atomic or molecular system is not as low, in other words, as the true or "exact" energy. The Hartree-Fock approximation is a form of central-field approximation,[2] where each electron moves within a field determined by the average field of the remaining electrons. The average field of the (N-1) electrons is represented by the Coulomb and exchange operators.[3] The Hartree-Fock method deals with electron-electron interactions only in an average way, rather than instantaneous interactions between electrons ($1/r_{ij}$). Since electrons repel each other, their motions are correlated with each other in order that they may keep out of each other's way. Improvement of the Hartree-Fock

wavefunction can be accomplished by introducing instantaneous electron correlation into the wavefunction.

In actual fact, the Hartree-Fock wavefunction does have some instantaneous electron correlation built into it. Since a single Slater determinant is used in this method, the Hartree-Fock wavefunction automatically satisfies the antisymmetry requirement of the Pauli exclusion principle. As a result, the positions of electrons with parallel spin are automatically correlated to prevent them from occupying the same spatial coordinates, but has no effect on electrons with opposite spin. This is often referred to as a Fermi (or exchange) hole,[4] which surrounds each electron in a Hartree-Fock wavefunction. The Fermi hole merely indicates a region of space where the probability of finding an electron with the same spin is very small. The Coulomb operator accounts for the Coulomb repulsion which electrons experience in their motions, preventing two electrons of arbitrary spin from approaching too close to one another. In an analogous fashion, all electrons in the Hartree-Fock approximation are surrounded by a Coulomb hole. The error incurred for electrons with parallel spin is smaller than that for opposite spin, due to the inclusion of some instantaneous electron correlation by the Pauli exclusion principle for the parallel spin case. The major source of error in the Hartree-Fock approximation is primarily due to the

inadequate instantaneous electron correlation amongst electrons of opposite spin.

A great deal of evidence has been accumulated in recent years which illustrates the importance of both electron correlation[5-8] and relativistic effects[9-13] in the photoionization process. The availability of synchrotron radiation has played an important role in furthering our understanding of many-body effects in atoms and molecules. These correlations are most evident during photoionization near threshold,[9,14-16] where the kinetic energy of the outgoing electron is low. It has been discovered by comparing experimental photoionization cross sections (σ) and asymmetry parameters (β) with theoretical values calculated using the independent electron approximation, that many-electron effects are quite important. From photoionization cross section and asymmetry parameter measurements made using synchrotron radiation of the 3p valence orbital of Ar[8,17-19] and the Xe 5s, 5p and 4d orbitals,[8,9,11-13,20-27] it has been clearly established that electron correlation effects are important. While independent electron calculations based on the central-field or Hartree-Fock approximation have failed to account for some of the features in the experimental partial cross sections and asymmetry parameters, relativistic many-body calculations have generally given better agreement.[8,20,24,28]

Historically, one of the first atomic cases to be studied in detail for electron correlation was the rare gas Xe. Initially the inner 4d shell of Xe drew most of the experimental and theoretical attention because of the interesting structure that arose in the photoabsorption spectrum above the 4d thresholds. A giant resonancelike structure was observed in the photoabsorption spectrum,[29] maximizing at about 30 eV kinetic energy above the 4d thresholds and extending over a range of ~60 eV. The feature was a dramatic departure from the typical hydrogenlike behaviour, which is typified by a sharp increase at the absorption edge followed by a smooth monotonic decrease with increasing photon energy. The current explanation for the delayed onset of this giant resonancelike structure, is essentially the same as that given originally by Cooper.[30] The large maximum present in the photoabsorption spectrum is caused by the ϵf continuum channels, via the transition $4d \rightarrow \epsilon f$. The high angular momentum of f orbitals ($l = 3$) results in a double-well potential, with an inner well separated from the outer one by a potential barrier.[30,31] At low kinetic energies, the ϵf continuum wave penetrates very little through the potential barrier into the inner well area, where the 4d orbitals are localized. The resulting overlap between the ϵf continuum wave and the 4d orbitals is small, yielding a small cross section near threshold. As the energy increases, eventually the ϵf continuum wave penetrates the

potential barrier and overlaps strongly with the 4d orbitals. This leads to a dramatic increase in the photoionization cross section, giving rise to the delayed resonancelike structure in the photoabsorption spectrum.

In a single-electron picture, the Xe 5s partial cross section should decrease monotonically above the 4d ionization thresholds.[32-34] Likewise, the Xe 5p partial cross section should very slowly increase in a smooth monotonic fashion from the 4d ionization thresholds to at least a photon energy of 128 eV.[32] The slow increase predicted for the Xe 5p partial cross section is due to the 5p → εd Cooper minimum which occurs near the 4d ionization thresholds.[11,32] In fact, the 5s and 5p partial cross sections are both enhanced experimentally above the 4d ionization thresholds, showing delayed maxima which strongly mimic that found in the 4d partial cross section.[23,25] These maxima in the 5s and 5p partial cross sections are due to electron correlation effects between the 5s, 5p and 4d shells. This intershell correlation was predicted theoretically by Amusia et al.[32-34] using the many-body random phase approximation with exchange (RPAE). These calculations included most of the important electron correlations, some of which are shown using Feynman and pictorial diagrams in Figure 3.1.1-1. It should be noted that in these Feynman diagrams, a wiggly line represents a photon, a dashed line represents a Coulombic interaction, time increases in the upward-going direction, and a hole is

drawn as a particle moving backward in time.[36] Figure 3.1.1-1(a) shows a photon being absorbed by an atom, and an electron from the $n\ell$ subshell being directly ejected. If $n_0 \neq n_1$, Figure 3.1.1-1(b) represents interchannel correlation. In this interaction an electron is first photoexcited out of the $n_0\ell_0$ subshell, whereupon it interacts with an electron in a different subshell ($n_1\ell_1$). This interaction is such that the electron in the $n_1\ell_1$ subshell is ionized, and the electron initially photoexcited is scattered back into the original $n_0\ell_0$ subshell. This process can be thought of alternatively as interchannel scattering.[7] Intrachannel correlation is analogous to interchannel correlation, except that the scattering process occurs in the same subshell (i.e. $n_0 = n_1$) (Figure 3.1.1-1(b)).

In order to probe a little more deeply into such electron correlation effects, we decided that a more careful study of the atomic Xe 4d spin-orbit branching ratio would be useful, especially since the previous experimental results are in poor agreement with one another (section 3.3.1). In order to extend our knowledge of such effects to a new molecular case (and different Z), the valence band and I 4d spin-orbit branching ratios were determined for trifluoroiodomethane (CF_3I) (section 3.3.2). The results obtained are discussed in comparison with available theoretical calculations in section 3.3.

Figure 3.1.1-1

Feynman diagrams (top) and pictorial diagrams (bottom) for the following interactions: (a) direct photoionization following absorption of a photon; (b) interchannel correlation ($n_0 \neq n_1$), intrachannel correlation ($n_0 = n_1$) following absorption of a photon; (c) absorption of a photon by a virtual double-excited state.

hν
e⁻
nl
(a)
nl
ε'l'
hν
e⁻
n₀l₀
n₁l₁
(b)
n₀l₀
n₁l₁
ε'l'
ε''l''
hν
e⁻
nl
nl
e⁻
(c)
nl
ε'l'
nl
ε'l'

3 2 1 Experimental

High purity Xe gas (Research grade, 99 995%) was obtained commercially from Matheson. Trifluoroiodomethane (CF_3I) was purchased from PCR Research Chemicals Inc , and like the Xe gas was used without further purification Gas phase photoelectron spectra of Xe and CF_3I were obtained with photons from the Canadian Synchrotron Radiation Facility (CSRF)[37-39] at Tantalus I, an electron storage ring operated by the University of Wisconsin at Stoughton, Wisconsin. A Leybold-Heraeus LHS-11 photoelectron spectrometer was used in conjunction with a multicapillary array gas probe to collect the spectra. The LHS-11 lens-analyzer system is mounted at the magic angle, so that the photoelectron intensities are independent of the asymmetry parameter β and the light polarization p.[40] For the Xe 4d spin-orbit branching ratio, a 900 lines/mm original ruled grating from Hyperfine Inc. was used. A 600 lines/mm holographic grating from JY Inc. was used in the Mark IV Grasshopper monochromator to collect valence band spectra of CF_3I, limiting the minimum photon energy to ~21 eV. The Canadian beamline (CSRF), experimental arrangement, and data acquisition system have been described eleswhere in the literature[37-39] and in Chapter 2 of this thesis.

For the Xe 4d branching ratio study, at least two Xe 4d spectra were recorded every 2 eV from 74 to 150 eV photon energies using a 50 eV electron analyzer pass energy

(0.4 eV electron resolution). The monochromator resolution ranged from 1.2 Å monochromator band pass below 130 eV photon energy to 0.9 Å above this, resulting in total linewidths varying between 0.8 eV at 80 eV photon energy to 1.6 eV at 150 eV photon energy. Depending on the ring current (40-200 mA) these conditions resulted in count rates of several hundred counts per second for photon energies up to 110 eV, but only a few tens of counts per second by 150 eV photon energy. A few higher resolution spectra were obtained down to 0.17 Å monochromator band pass and 25 eV electron analyzer pass energy (0.2 eV electron resolution). Valence band spectra of CF_3I were obtained at ~1.7 Å monochromator band width, and 50 eV electron analyzer pass energy (0.4 eV electron resolution) from 21 to 110 eV photon energy. The transmission function of the electron spectrometer has been found to be constant to within 20% for kinetic energies between 2-60 eV.[39,41] This was based on an intensity analysis of Kr Auger peaks in this region, and the very good agreement down to ~2 eV kinetic energy between our partial cross sections for CF_4[42] (Chapter 4) and previously published results of Carlson et al.[43] The use of high pass energies (e.g. 50 eV) reduces substantially the kinetic energy dependence of the transmission function.[44] Backing pressures of ~8-10 torr were used for these two gases, resulting in a background pressure in the experimental chamber of ~(1-2) x 10^{-5} torr, and an estimated pressure of ~10^{-4} torr[44] in the

interaction region. The pressure in the interaction region was found to be low enough that scattering cross section losses at low kinetic energies were not a problem.[45]

All photoelectron spectra were computer-fitted using an iterative procedure described previously.[46] Voigt functions simulated by a linear combination of Lorentzian-Gaussian line shapes and a linear baseline are used in this fitting procedure. The Xe $4d_{3/2,5/2}$ peak positions were constrained to differ by the high resolution spin-orbit splitting of 1.979 ± 0.007 eV (Figure 3.3.1-3). In addition to this, the linewidths and line shapes were constrained to be the same for the two spin-orbit peaks. Although a slight linewidth difference was noted at high resolution (Figure 3.3.1-3) for the two peaks (see section 3.3.1 for a discussion of this), this difference is negligible at the poorer resolution of 50 eV pass energy, where all the Xe 4d branching ratio spectra were taken. Auger peaks were heavily constrained for < 110 eV photon energies using their known positions, linewidths, line shapes, and relative areas from "clean" Auger spectra at similar photon energies.

Valence band branching ratios were determined for CF_3I over the entire photon energy range selected, using the peak areas (A_i) and the branching ratio definition ($BR_i \equiv A_i/\Sigma A_i$ Valence). Due to overlap of some of the photoelectron bands in CF_3I, branching ratios representing contributions from two molecular orbitals could only be

determined sometimes. The weak and broad F 2s orbitals were neglected in this branching ratio determination. Unfortunately, the total photoionization cross section is not known for CF_3I in the photon energy range of 21-110 eV, so the measured branching ratios could not be converted to partial cross sections.

3.3 Results and Discussion

3.3.1 Xe 4d Linewidths and the $4d_{5/2}$:$4d_{3/2}$ Branching Ratio

Photoionization of closed p and d shells of atoms produces two final states of the ion, once the photon energy is above the second photoionization threshold. Spin-orbit splitting of an $n\ell$ subshell produces the two spin-orbit components $j = \ell \pm 1/2$, which differ in energy. For example, for a closed p shell, $^2P_{1/2}$ and $^2P_{3/2}$ ionic states are formed. Likewise, $^2D_{3/2}$ and $^2D_{5/2}$ states of the ion are formed for a closed d shell. The branching ratio for a closed p or d shell is simply the ratio of the probabilities of forming these two final states from photoionization, for a given photon energy. This ratio can be determined from a photoelectron spectrum, by taking the area ratio of the two peaks (i.e. electron intensity) corresponding to these two final states. From an experimental point of view, branching ratio determinations can be made more readily than absolute determinations of the individual partial cross sections, due to the relative nature of the measurement. In either case however, high

resolution is generally required to resolve the spin-orbit components. Since the branching ratio is sensitive to electron correlation and relativistic effects that affect the two components dissimilarly, such measurements can be used to probe for these effects in the photoionization process.

In the absence of any relativistic or many-body effects, the branching ratio should have the statistical value of $(\ell + 1)/\ell$. Branching ratio measurements have been reported by several investigators for p and d shells in solids and gases,[25,47-62,107] which show deviations from the statistical value. This is especially true close to threshold. Most of these studies have dealt with the Ar 3p, I 5p (of HI, CH_3I), Xe 5p, Xe 4d, the (n - 1)d subshells of Zn, Cd and Hg (n = 4 → 6), In 4d, Sn 4d, Pb 5d, and Bi 5d spin-orbit doublets. In addition, considerable theoretical progress[8,15,20,24,28,50,54,63-71] has also been made to explain these observed deviations. Calculations ranging from single-particle relativistic Dirac-Slater to the sophisticated many-body relativistic random-phase approx- imation (RRPA) incorporating electron correlation effects, have been carried out on some of these systems. Deviations from the statistical value reflect either the slight difference in the kinetic energies of the outgoing electrons of the two spin-orbit states (they differ by the spin-orbit splitting), or spatial differences in the initial state wavefunctions $|\ \ell - 1/2\ \rangle$ and $|\ \ell + 1/2\ \rangle$.[48,63]

In the last decade, several gas phase photoelectron measurements using synchrotron radiation[25,61,72] and line sources[24] have shown that the Xe $4d_{5/2}$:$4d_{3/2}$ branching ratio (BR) varies greatly from the statistical 1.5:1 value between 70 eV and 200 eV photon energies. A very recent Auger study,[73] also demonstrates that the I_{N_5OO}/I_{N_4OO} Auger intensity ratio agrees semiquantitatively with the corresponding photoelectron branching ratios. Several theoretical calculations of the preceding branching ratios have been performed,[20,28,63,74] ranging from the single-particle Dirac-Fock (DF) calculations[74] to the relativistic random-phase approximation (RRPA) calculations[20,28] with some electron correlation.

Despite all previous work, there is still not quantitative agreement between theory and experiment in this relatively simple atomic system. The agreement between the various experimental branching ratios, both at individual photon energies and for the overall trends with photon energy, is not particularly good for three reasons. First, the rather low intensity of the spectra[24,25,61,72] result in quoted standard deviations of $\geq$ 0.07 for most measurements. Secondly, it appears that strongly overlapping $N_{4,5}OO$ Auger peaks below photon energies of 110 eV were not quantitatively accounted for. The Auger contribution can often be quite significant, as demonstrated recently by Riedel et al. for the valence band 3p states in cleaved Si(111).[75] Thirdly, some of the

measurements were not made at the magic angle of 54.7°, causing the branching ratio to have a β dependence.[24] Even when the Auger and β problems are not important (for example, for magic angle measurements at 94 eV photon energy), the measured BR varied from 1.58 (Reference 25) to 1.42 (Reference 72).

The theoretical branching ratio curves are also rather sensitive to the theoretical approximations made[24] (e.g. coupling, basis function set quality, core relaxation effects); and although the previous experimental data[24] is in very rough qualitative agreement with the RRPA theoretical curve,[28] the agreement is not good enough for quantitative comparison.

In order to investigate more accurately this important atomic test case, the Xe $4d_{5/2}$-$4d_{3/2}$ branching ratio was carefully measured at the magic angle using the Canadian Synchrotron Radiation Facility (CSRF), from 74 to 150 eV photon energies. A high-resolution Xe 4d spectrum was also collected to aid in this determination (full width at half maximum (FWHM) for $4d_{5/2}$ = 0.262 eV). The interferring $N_{4,5}OO$ Auger peaks were corrected for quantitatively by computer-fitting all of the Xe 4d spectra.

A typical medium resolution spectrum of the Xe 4d and $N_{4,5}OO$ Auger peaks is shown in Figure 3.3.1-1 for 150 μm slits ($\Delta\lambda$ = 0.9 Å) and 50 eV electron analyzer pass energy (~0.4 eV electron resolution). Apart from the low kinetic energy region, the background is very low, and the

Figure 3.3.1-1

Xe 4d and $N_{4,5}OO$ Auger spectrum taken at a photon energy of 94 eV, with 150 μm slits ($\Delta\lambda$ = 0.9 Å), and 50 eV electron analyzer pass energy (0.4 eV electron resolution). The Auger peaks are numbered according to Reference 76.

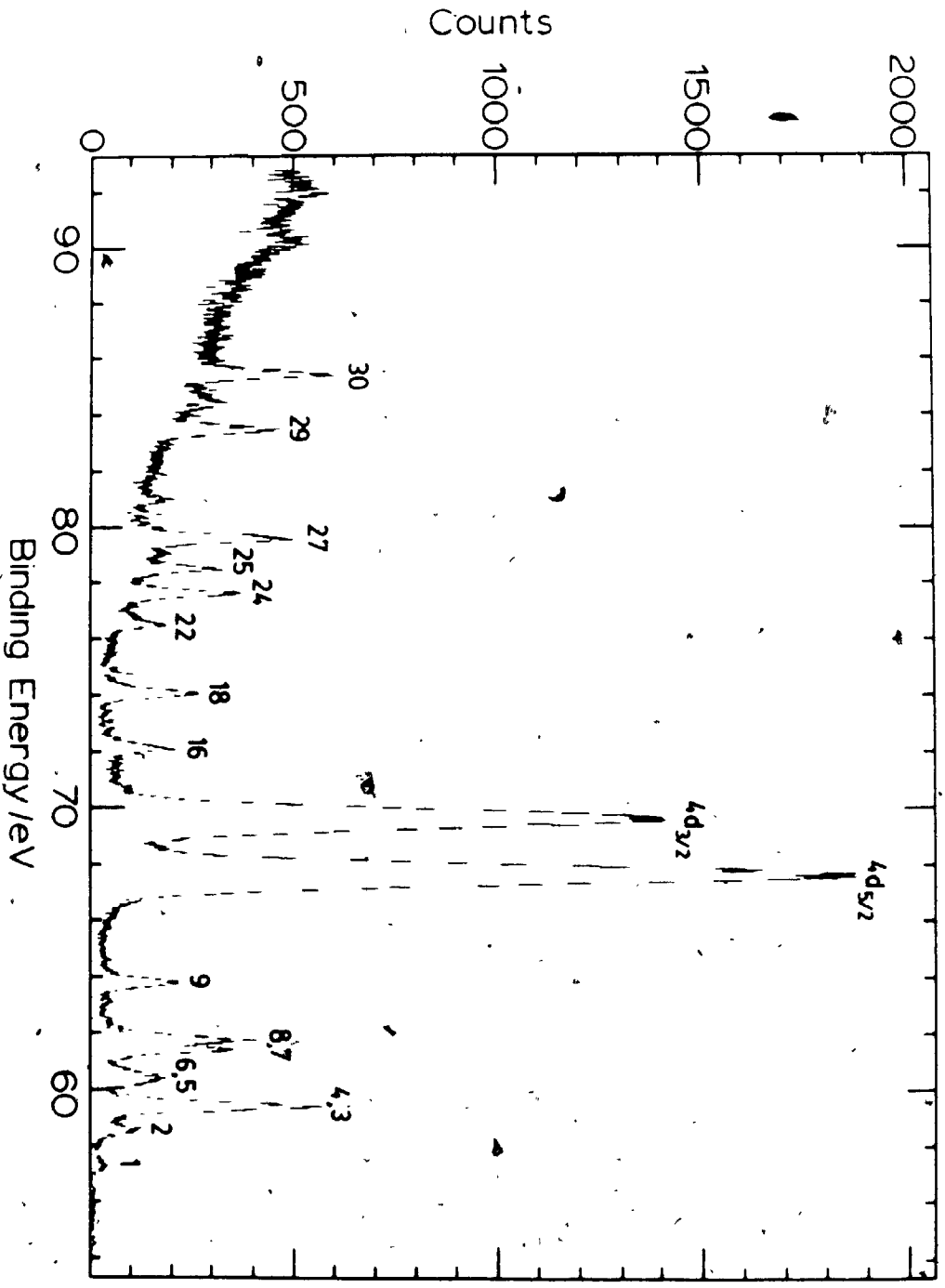
Counts
0
500
1000
1500
2000
90
80
70
60
Binding Energy/eV
30
29
27
25
24
22
18
16
4d3/2
4d5/2
9
8,7
6,5
4,3
2
1

linewidths of the Xe 4d and Auger lines are 0.83 and ~0.4 eV, respectively. The Auger peaks are numbered according to Reference 76, and as can be readily seen, they have considerable intensity relative to the Xe 4d spin-orbit components. To examine the overall beamline and photoelectron resolution in more detail, we obtained the Xe $4d_{5/2}$ linewidths at 50 μm slits ($\Delta\lambda$ = 0.3 Å) and different pass energies (Figure 3.3.1-2), and recorded a high-resolution Xe 4d spectrum at 30 μm slits ($\Delta\lambda$ = 1.7 Å) and 25 eV electron analyzer pass energy (Figure 3.3.1-3). The measured spin-orbit splitting of 1.979 ± 0.007 eV is in good agreement with previous experimental results.[77] The three data points in Figure 3.3.1-2 were fit by least squares to a straight line, and extrapolation to zero pass energy yields the photon plus lifetime resolution of 0.235 eV. This value, while probably a lower limit due to the linear extrapolation, is in surprisingly good agreement with the theoretical photon plus lifetime resolution with a 900 lines/mm grating of 0.233 eV for 30 μm slits.

The Xe $4d_{5/2}$ linewidth of 0.262 ± 0.009 eV (Figure 3.3.1-3) appears to be the smallest gas-phase core-level width yet observed using monochromatized photon sources. Comparable core-level gas-phase linewidths have been published recently by Gelius et al.[78] using a monochromatized Al Kα source. Also of interest is the slightly larger linewidth of the $4d_{3/2}$ component of 0.289 ± 0.012 eV. Since the instrumental (photon plus electron)

Figure 3.3.1-2

Xe $4d_{5/2}$ full width at half maximum (FWHM) taken at 93 eV photon energy versus electron analyzer pass energy, for 50 μm slits ($\Delta\lambda$ = 0.3 Å). The line results from a linear least-squares fit to the three data points. The theoretical monochromator resolution plus the lifetime linewidth (0.233 eV) is denoted by an asterisk on the y-axis.

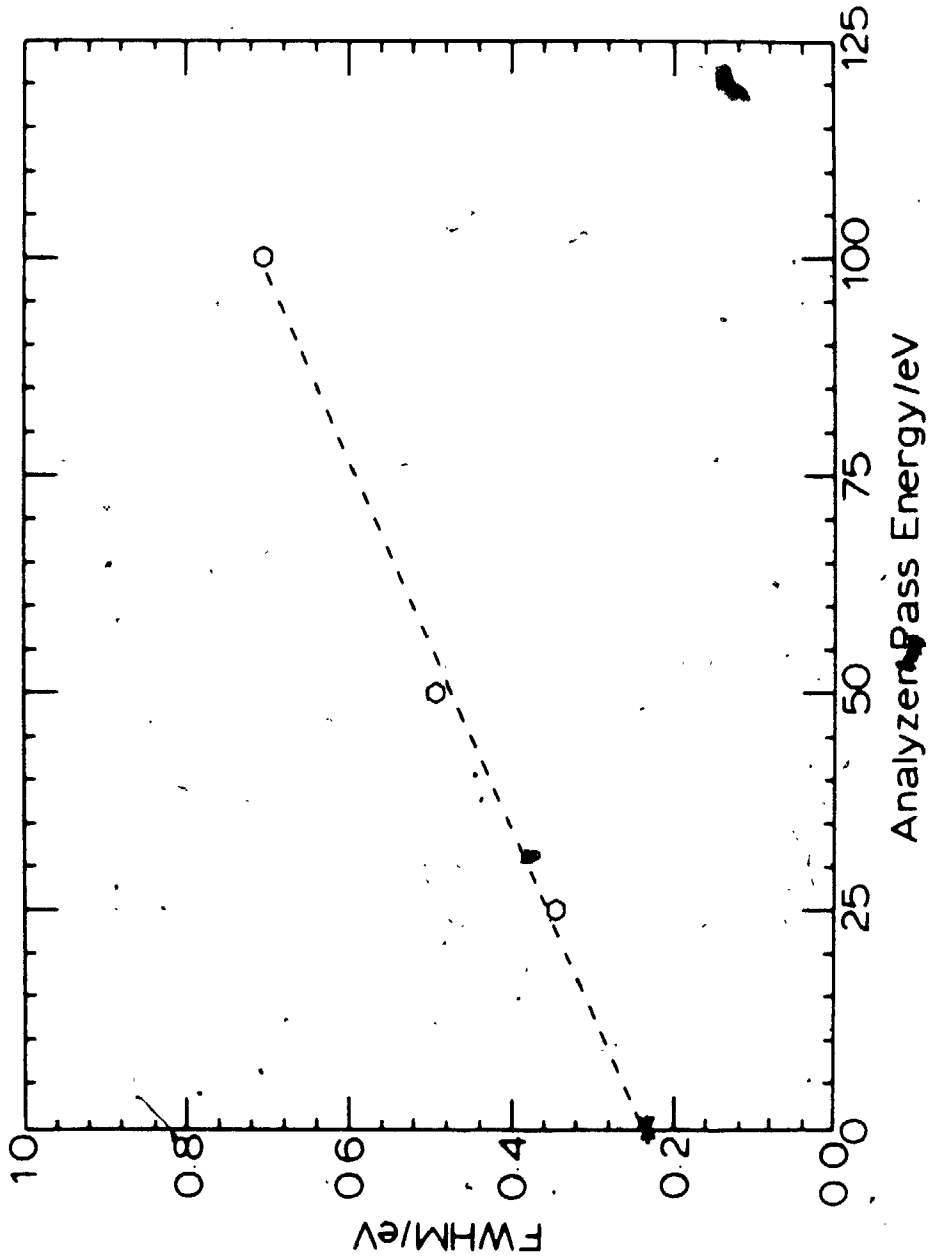
FWHM/eV
0.0
0.2
0.4
0.6
0.8
1.0
Analyzer Pass Energy/eV
0
25
50
75
100
125

Figure 3.3.1-3

Xe 4d spectrum taken with 94 eV photon energy, with 30 μm slits ($\Delta\lambda$ = 0.17 A), and 25 eV electron analyzer pass energy (0.2 eV electron resolution). This multiscanned spectrum took close to 3 hours to accumulate. The FWHM for the two spin-orbit components are given in the figure. The measured spin-orbit splitting is 1.979 ± 0.007 eV. The small Auger peaks 10-14 are all less than 1% of the intensity of the 4d peaks. A fit including these Auger peaks made no difference to the 4d linewidths.

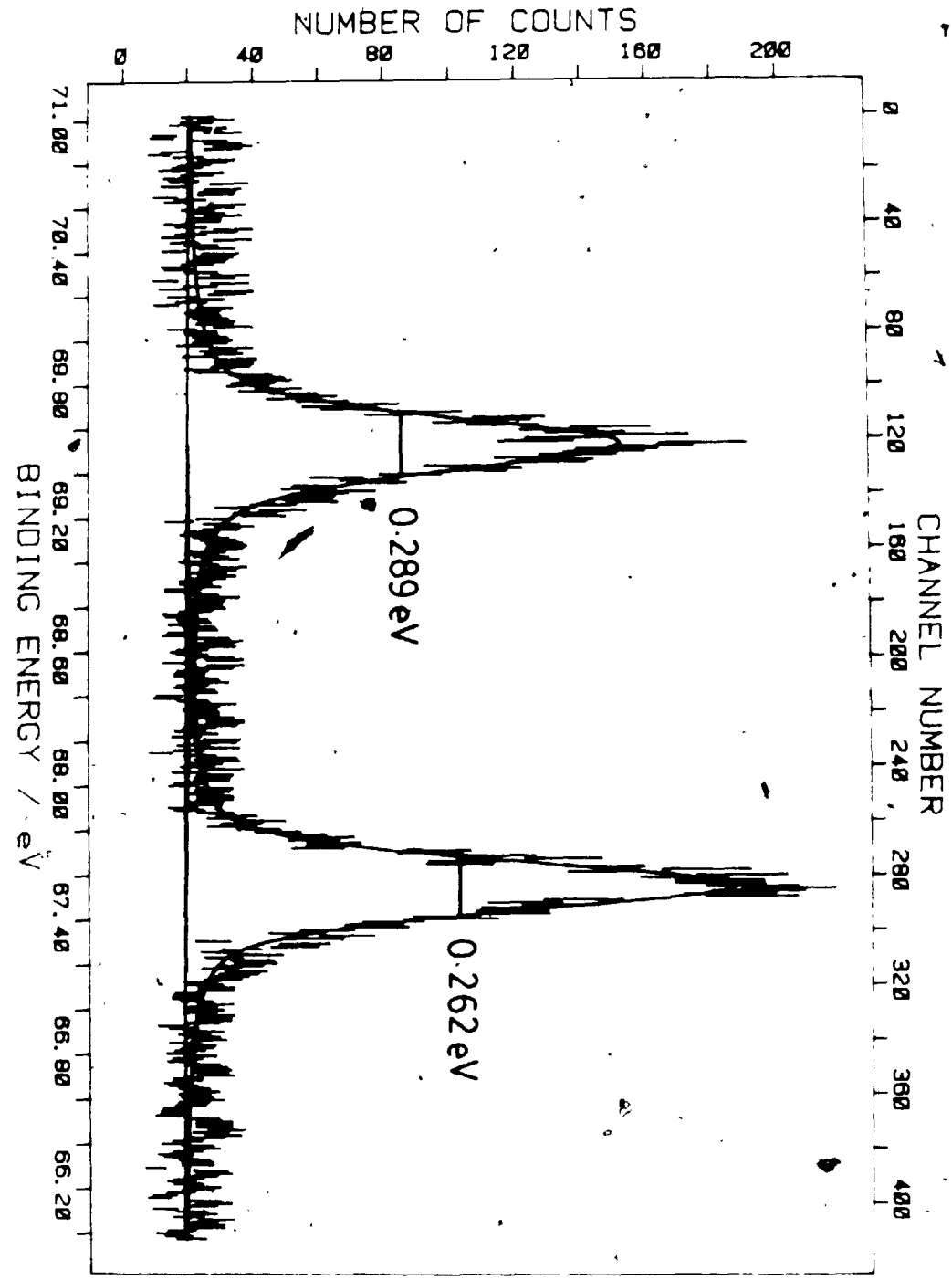
NUMBER OF COUNTS
0
40
80
120
160
200
CHANNEL NUMBER
0
40
80
120
160
200
240
280
320
360
400
BINDING ENERGY / eV
71.00
70.40
69.80
69.20
68.60
68.00
67.40
66.80
66.20
0.289 eV
0.262 eV

contributions to the two spin-orbit components are constant, the $4d_{3/2}$ inherent hole state lifetime width must be significantly broader than the $4d_{5/2}$ lifetime width. King et al.[79] have measured the lifetime widths of Xe 4d hole states using high-resolution electron impact, and they suggest that the mean width of $4d_{5/2,3/2}$ hole states is 129 ± 8 meV, consistent with the approximate value of 100 meV evaluated by Keski-Rahkonen and Krause.[80] There is a definite hint in King's data that the $4d_{3/2}$ hole state width is larger than the $4d_{5/2}$ width by ~10 meV, but the quoted errors are larger than this difference. Using the approximate expression:

$$\Gamma^2_{total} = \Gamma^2_{hole\ state} + \Gamma^2_{experimental}\ , \qquad (3.3.1\text{-}1)$$

where

$$\Gamma^2_{experimental} = \Gamma^2_{photon} + \Gamma^2_{electron}\ , \qquad (3.3.1\text{-}2)$$

Γ_{photon} for 30 μm slits ($\Delta\lambda$ = 0.17 Å) is 0.12 eV, and $\Gamma_{electron}$ = 0.20 eV for 25 eV electron analyzer pass energy ($E/\Delta E \sim 125$). Using these values, $\Gamma_{experimental}$ is then 0.23 eV. Using equation 3.3.1-1 and the experimental Γ_{total} values for the two spin-orbit components, the $4d_{5/2}$ and $4d_{3/2}$ hole state widths are ~120 and ~170 meV, respectively. Using the Voigt formula given by Keski-Rahkonen and Krause[81] to obtain more accurate values,

the $4d_{5/2}$ and $4d_{3/2}$ hole state widths are still quite different but significantly smaller - 54 and 100 meV, respectively. The errors on these numbers are ~20 meV

Differences in widths of spin-orbit components have been seen recently in the solid state on the 4f levels of Hf, Ta, and W.[82,83] The larger $4f_{5/2}$ width has been attributed to an $N_6N_7O_{4,5}$ Coster-Kronig decay which reduces the lifetime of the $4f_{5/2}$ core hole state relative to the $4f_{7/2}$ core hole state. Such a mechanism cannot be responsible for the differences observed here for Xe in the gas phase, however, and further theoretical work is required.

Turning now to branching ratios, a typical spectrum of the Xe 4d level at 80 eV photon energy (Figure 3.3.1-4) illustrates the problem of obtaining accurate branching ratio values when there are overlapping Auger lines. If the Xe $4d_{5/2,3/2}$ lines are fitted without including Auger peak 29, a BR of 1.13 results; when the Auger peak is properly fitted, a BR of 1.30 results. Differences of at least 0.2 in the branching ratio can arise with small shifts in Auger peaks relative to the 4d peaks. Many of the large discrepancies apparent in the literature for the Xe 4d BR can be attributed to neglect of these Auger peaks. Correction without computer fitting of the data is very difficult indeed.

The standard deviations from the computer fits on the BR values are ± 0.02 to ± 0.05 for most of the

Figure 3.3.1-4

Xe 4d spectrum taken at 80 eV photon energy, 200 μm slits ($\Delta\lambda$ = 1.2 Å), and 50 eV electron analyzer pass energy (0.4 eV electron resolution). Note the significant contribution of Auger peak 29 to the $4d_{3/2}$ peak. Inclusion of the weak Auger peak 28 (not shown) on the low binding energy edge of the $4d_{5/2}$ peak, makes no significant difference to the Xe $4d_{5/2}$:$4d_{3/2}$ branching ratio.

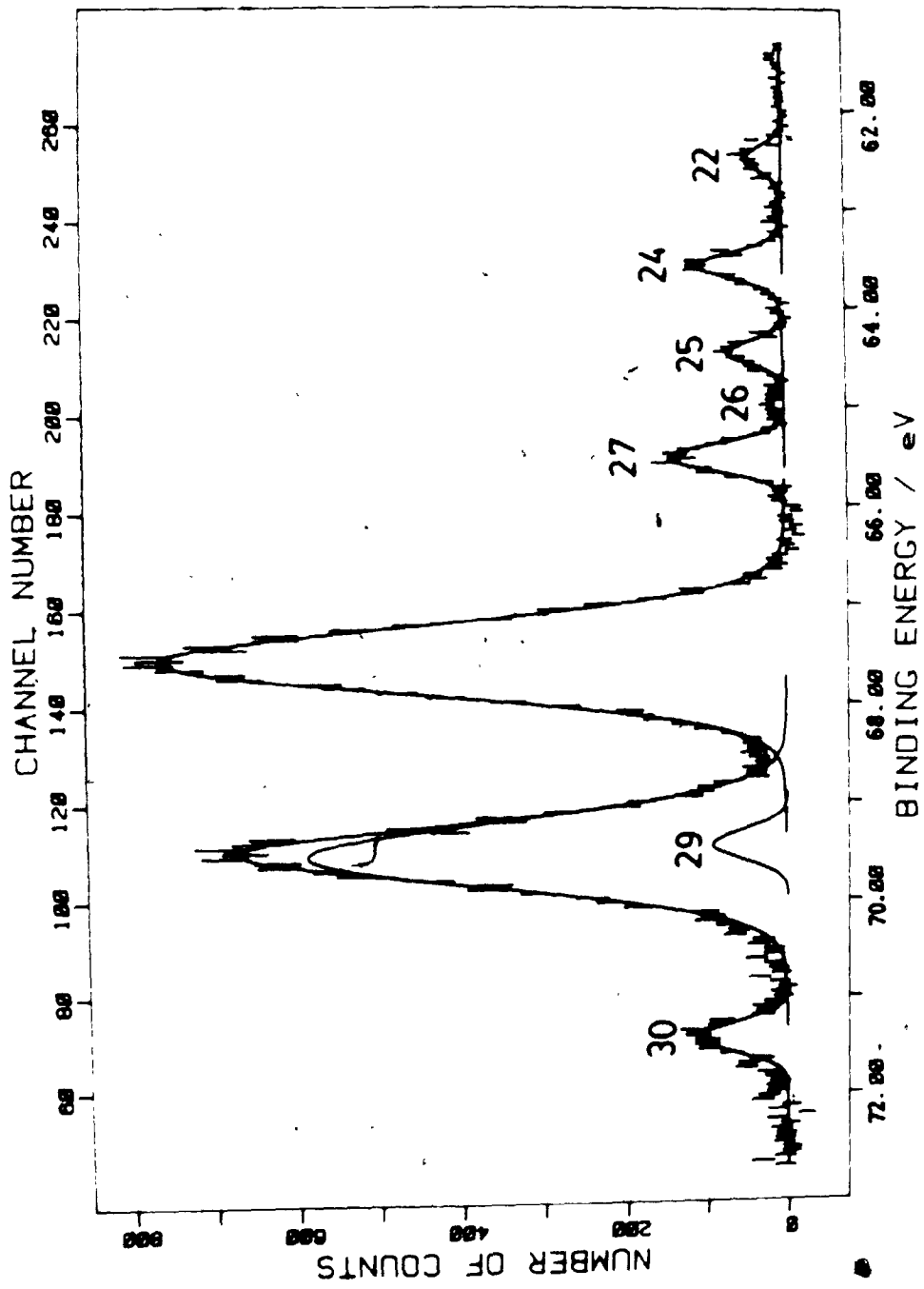
CHANNEL NUMBER
NUMBER OF COUNTS
BINDING ENERGY / eV
22
24
25
26
27
29
30

individual spectra. The question which arises, is whether these errors are really realistic? Using the statistical treatment outlined in Topping[84] and Clark et al.,[85] the two independent expressions for the standard error of the mean for the branching ratios can be evaluated:

$$\alpha_1^2 = \left[\sum_{j=1}^{n} \frac{1}{S_j^2} \right]^{-1} \qquad (3.3.1\text{-}3)$$

and

$$\alpha_e^2 = \frac{\alpha_1^2}{n-1} \left[\sum_{j=1}^{n} \frac{(X_j - \bar{X})^2}{S_j^2} \right] \qquad (3.3.1\text{-}4)$$

where α_1 is a function of the internal consistency and α_e is a function of the external consistency of the observations. S_j is the associated standard deviation for the branching ratios obtained from the computed spectra (Table 3.3.1-1). Snedecor's F test ($F = Z^{\pm 2}$, where $Z = \alpha_e/\alpha_1$) was used to check that α_1^2 and α_e^2 could reasonably be expected to be estimates of the same variance. The weighted means α_e, α_1, and Z are given in Table 3.3.1-1 for a number of spectra at two different photon energies. In all cases, the Z values are statistically acceptable, indicating that our standard

Table 3.3.1-1

Reproducibility of Branching Ratio (BR)

Photon Energy (ev)	BR	(S)	$\overline{BR}$	α_1	α_e	Z
120	1.323	(0.045)	1.293	0.014	0.007	0.50
	1.293	(0.024)				
	1.288	(0.021)				
110	1.338	(0.031)	1.326	0.015	0.007	0.47
	1.334	(0.035)				
	1.308	(0.027)				
	1.333	(0.032)				

deviations are indeed realistic and that any nonrandom effects are not influencing our spectra and the BR values.

The branching ratio versus photon energy plot is given in Figures 3.3.1-5(a),(b) along with the latest theoretical relativistic random-phase approximation (RRPA) results of Cheng and Johnson.[20] Their calculation was done in intermediate coupling using six interacting channels ($4d_{3/2} \rightarrow p_{1/2}, p_{3/2}, f_{5/2}; 4d_{5/2} \rightarrow p_{3/2}, f_{5/2}, f_{7/2}$). Our results[39] are in good qualitative agreement with the RRPA results, and not in agreement with the earlier Dirac-Fock (DF) results using jj coupling which are far too large above 100 eV photon energy.[74] The Dirac-Slater calculations of Desclaux[24,28,72] are in better agreement with experiment than the DF results, but the predicted minimum at > 90 eV is at least 6 eV too high, and the experimental data between 130-150 eV shows only a monotonic decrease whereas the DS calculations predict a strong increase in this region. Most of our BR values are significantly smaller than those obtained earlier (see for example, Figure 2, Reference 24), many of which were reported to be very close to the statistical value of 1.5. From 98 to 146 eV our BR falls very slowly and monotonically (Figure 3.3.1-5(a)). The agreement with RRPA in this region is rather good, although it should be noted that the experimental data is consistently a little lower than the theoretical curve. This suggests that further electron correlation must be included in the RRPA

Figure 3.3.1-5

Xe $4d_{5/2}$:$4d_{3/2}$ branching ratio (BR) as a function of photon energy, (a) from 80 to 150 eV; (b) from 74 to 150 eV. The error bars given are the larger of α_1 or α_e. The dashed line is a visual fit to the experimental data; the solid line is the latest RRPA theoretical results of Cheng and Johnson (Reference 20).

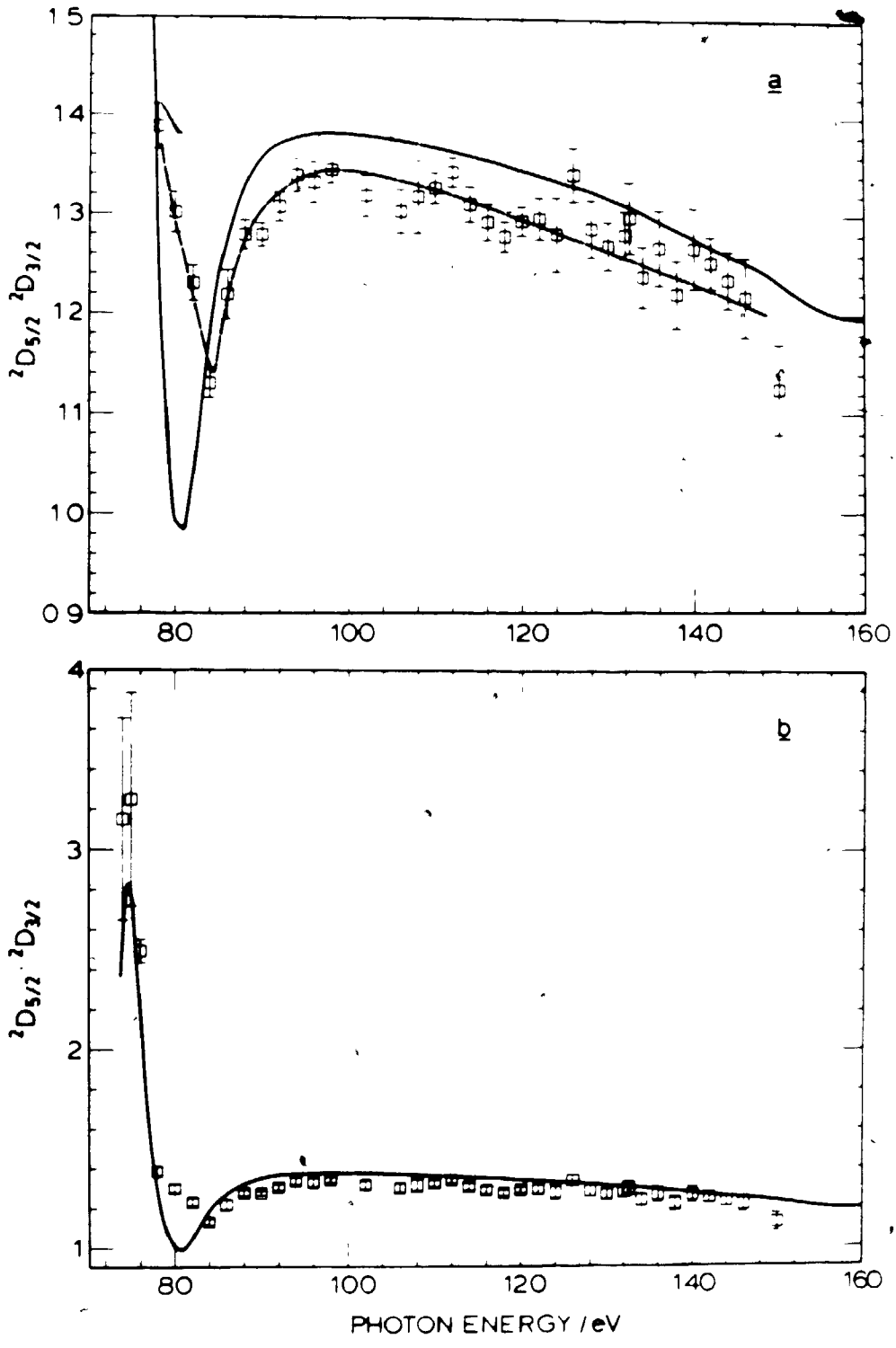
a
b
$^2D_{5/2}$ $^2D_{3/2}$
PHOTON ENERGY / eV

calculations. Johnson and Radojevic[28] have suggested that this might be accomplished by including intrashell and intershell correlation of the 4d shell with the 4s, 4p, 5s and 5p shells. Unfortunately, since this suggestion was put forth, calculations including some or all of these additional channels have not appeared.

To within the quoted errors, good agreement also occurs for the lower photon energies of 74-78 eV (Figure 3.3.1-5(b)). The largest deviations occur around the minimum region between 80 and 86 eV where electron correlation effects are strongest. The experimental minimum occurs at 84 eV photon energy, 3 eV higher than that predicted by the RRPA calculations. Furthermore, the experimental minimum region is not as deep or as pronounced as in the RRPA calculation, and has a definite asymmetric profile. Including coupling with other subshells might partially account for some of these differences. After publication of our Xe 4d branching ratio in the literature,[39] we became aware of a similar study by Schmidt.[86] Overall the agreement between the two studies is excellent, with their branching ratio minimum occurring a little lower at 82 eV photon energy. The only noticeable discrepancy occurs close to threshold, where our branching ratios begin to fall and appear to be in better agreement with the RRPA predictions in this region.

As can be readily seen in Figure 3.3.1-5, the branching ratio minimum region around 80 to 84 eV photon

energy is not reproduced very well by the RRPA calculations. The theoretical minimum region appears to be far too deep and shifted by ~3 eV to lower photon energy. A similar type of discrepancy has been noted recently for the σ and β values around the Xe 5s Cooper minimum.[12,26] Fahlman et al.[12] and Dehrenbach and Schmidt[26] discovered a considerable and rather surprising discrepancy in the region of the Cooper minimum between the experimental data and RRPA calculations of Johnson and Cheng.[8] The theoretical dip in β is far too deep (by close to 1 unit of β) and shifted by ~1 eV to lower photon energy.[12] The RRPA calculations[68] give good agreement for the Xe 5s cross section in the Cooper minimum region, but overestimates it at higher photon energies.[12] Obviously, important correlation effects of some sort are not being correctly accounted for in these calculations.

As Johnson and Cheng[8] have pointed out previously, the largest discrepancies between experiment and RRPA theoretical results in general occurs near threshold. They further suggest that these discrepancies can be traced to strong correlation effects between the outgoing electron of low kinetic energy and the residual ion which are not properly accounted for. In other words, the RRPA calculations currently ignore all relaxation effects, assuming a frozen core instead. Although the framework by which relaxation effects may be included in such calculations has been discussed by Wendin[87] and Amusia,[88]

only a few exploratory calculations have been made. Wendin has performed random-phase approximation with exchange (RPAE) calculations on atomic Ba and La,[87] both with and without relaxation, and found that including relaxation effects improved substantially the agreement with experiment near threshold. Carter and Kelly[70] have similarly performed a many-body perturbation theory (MBPT) calculation on the Cd 4d subshell including relaxation effects. They found that relaxation reduces the maximum in the Cd 4d cross section in better agreement with experiment, and that the maximum position was shifted significantly by several eV to higher photon energy. As Wendin has pointed out,[87] relaxation effects can shift ionization thresholds and deform the shape of the cross section near the threshold, so that simply introducing experimental binding energies into the RPA equations can be very bad when the photoionization cross section is quite peaked near threshold. Inclusion of double excitations accounting for relaxation of the frozen core, correlation satellites (shakeup or shakeoff), and Auger transitions is undoubtedly necessary in the threshold region of the Xe 4d. Some of the important double excitation mechanisms are displayed using Feynman diagrams in Figure 3.3.1[illegible]. Since the core-hole attracts surrounding electron density in the relaxation process and the outgoing electron repels electron density, the electron density is distorted around both the electron and the hole. This affects the field in

which the photoelectron moves. Figure 3.3.1-6(a) shows photoionization with correlation satellites (shakeup/shakeoff) for the case i = j, or Auger types of processes (i ≠ j). Figure 3.3.1-6(b) illustrates photoionization with inelastic scattering of the outgoing electron, which yields another electron in the process.

Finally, it is interesting to note that our BR value at 150 eV photon energy (1.125 ± 0.045) is significantly below that predicted theoretically. Southworth et al.[73] have also obtained very low I_{N_5OO}/I_{N_4OO} Auger ratios in this region (0.96 ± 0.14 at 155 eV, and 1.09 ± 0.18 at 162 eV). Unfortunately the errors in both measurements are rather large because of the low photon intensity and small cross sections as one approaches the 4d Cooper minimum at these energies. This apparent change may be due to the onset of the $4p_{1/2}$ ionization threshold (145.51 eV),[89] which by analogy with the Kr 4p ionization should reach its maximum cross section at 5-10 eV above threshold.[68] This effect is very similar to the decrease noted by Wertheim[90] in the Se $3d_{5/2}$:$3d_{3/2}$ BR when ionizing the Se $2p_{1/2}$ level exactly at threshold (binding energy is 1476 eV) with Al Kα. An electron in the Se $2p_{1/2}$ level is resonantly excited by an Al Kα photon from $2p_{1/2} \rightarrow 4d_{3/2}$ (initially unoccupied), followed by a $3d_{3/2}$ electron filling the $2p_{1/2}$ hole via $3d_{3/2} \rightarrow 2p_{1/2}$ and the initially excited electron now in the $4d_{3/2}$ level being ionized. Overall a single electron is observed and a hole is created

Figure 3.3.1-6

Feynman diagrams for the following double excitation processes: (a) photoionization with correlation satellites (i = j, sometimes also referred to as shakeup/shakeoff) or Auger types of processes (i ≠ j); (b) photoionization with inelastic scattering of the photoelectron, yielding another electron.

(a)
(b)

in the $3d_{3/2}$ level. Since this process represents an additional process to the direct one of ionizing an electron from the $3d_{3/2}$ level, this will lead to a higher partial cross section for the 3/2 component and therefore a lower $3d_{5/2}:3d_{3/2}$ branching ratio. Clearly, more accurate experimental measurements are required in this region to confirm this effect.

3.3.2 Intershell Correlation Effects in Trifluoroiodomethane (CF_3I)

Numerous photoabsorption and photoelectron studies of Xe (see section 3.3.1) have established that electron correlation effects are important in understanding the dynamics of photoionization in the N and O shells of Xe above the 4d threshold. This was accomplished through comparison of experimental results to theoretical calculations ranging from single-particle to the more sophisticated relativistic many-body type. As a result of these studies and more recent developments in the field,[91,92] these observed effects are believed not to be a peculiarity of Xe (Z = 54), but a general property of other elements around Xe with similar Z.[20,93] This hypothesis is supported by photoabsorption measurements done on atomic or molecular systems containing Te (Z = 52),[94] I (Z = 53),[91,92,95-99] and Cs (Z = 55),[97,100,101] where broad resonances similar to Xe are observed above their respective 4d thresholds. In this series a decrease in the

maximum position of ~5 eV kinetic energy has been observed (40 (Te), 35 (I), 30 (Xe), 25 (Cs) eV kinetic energy above threshold). These broad photoabsorption maxima have been interpreted similarly as delayed 4d → εf transitions, in an analogous fashion to Xe. For Z < 54 (Xe), the centrifugal barrier is higher than that present in Xe.[20,91-93] A higher kinetic energy in the continuum εf wavefunction is therefore required to overcome this barrier, accounting for the larger kinetic energy delay in these broad resonances for Z < 54. In order to investigate the Z dependence of electron correlation effects, the iodine atom (Z = 53) in the molecular environment of trifluoroiodomethane (CF_3I) was selected.

Valence band photoelectron spectra of CF_3I taken at ~35, 41, and 80 eV photon energies are shown in Figure 3.3.2-1. The spectrum at 41 eV photon energy is very similar in quality and resolution to that obtained earlier with a He II source.[102] The spin-orbit split peaks labelled as the 4e molecular orbital (MO) is mainly due to the I 5p lone pair electrons, while the peak labelled as the $4a_1$ MO is predominantly due to the C-I bonding molecular orbital.[102] As can be readily seen in these three spectra (Figure 3.3.2-1), a large change in the relative intensity of these two peaks is evident. At 21.2 eV photon energy, photoionization from the 4e MO is much more probable than from the $4a_1$ MO; but this decreases rapidly thereafter until at 41 eV photon energy, it is less

Figure 3.3.2-1

Photoelectron spectra of the valence band of CF_3I taken with monochromatized synchrotron radiation at 35.15, 41, and 80 eV photon energies. The molecular orbital assignment is given in the bottom plot. Some second order contamination of the I 4d levels is present in the 35.15 and 41 eV photon energy spectra.

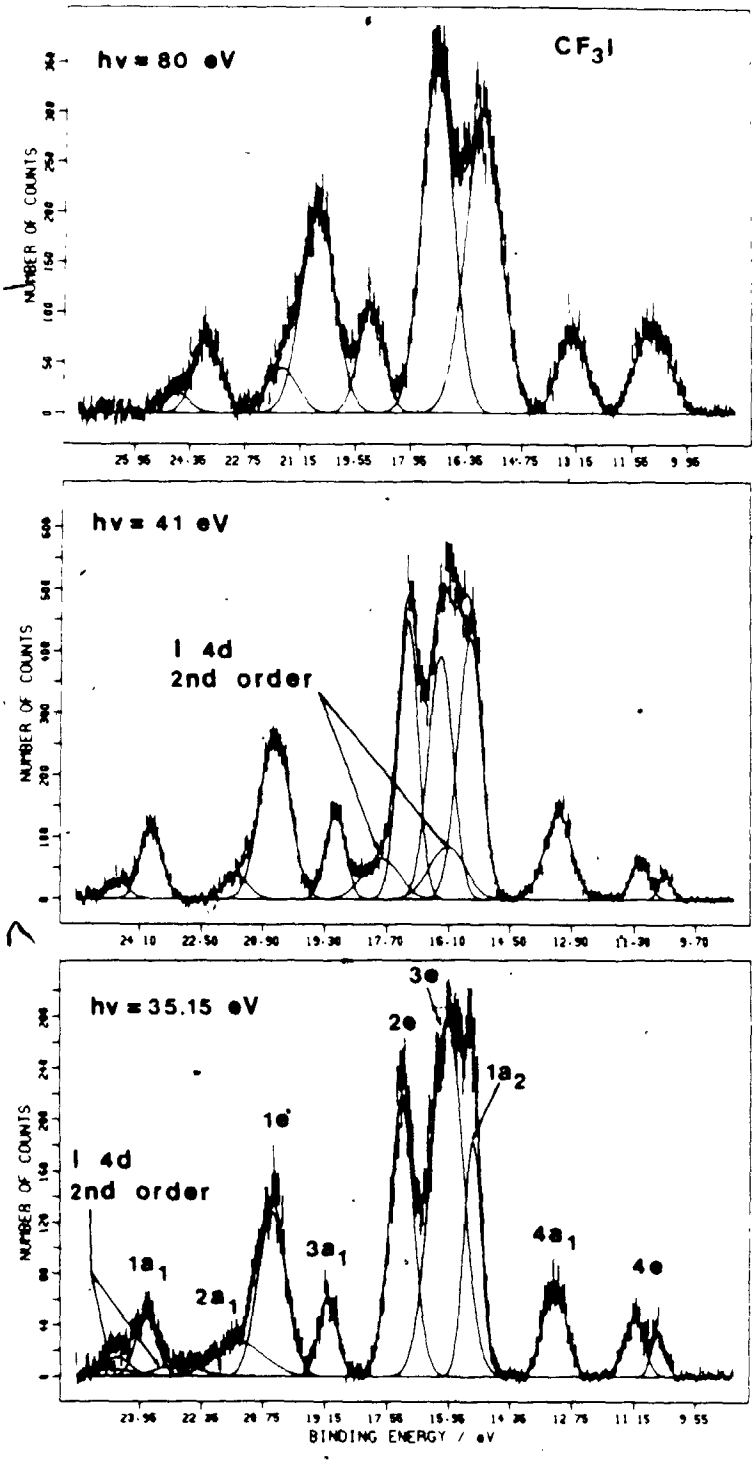
hv = 80 eV
CF_3I
NUMBER OF COUNTS
hv = 41 eV
I 4d
2nd order
hv = 35.15 eV
3e
2e
1e
$1a_2$
I 4d
2nd order
$1a_1$
$2a_1$
$3a_1$
$4a_1$
4e
BINDING ENERGY / eV

probable relative to the $4a_1$ MO. This relative decrease continues to ~60 eV photon energy where the probability of photoionizing an electron from the 4e MO increases rapidly relative to that of the $4a_1$ MO, maximizing somewhere between 80 and 90 eV photon energy. At ≥100 eV photon energy, photoionization from the 4e MO becomes less probable than the $4a_1$ MO once again.

This large change in the relative intensity of the spin-orbit split peaks (4e MO) follows the I 4d cross section rather closely. The I $4d_{5/2}$ peak has a binding energy of 57.8 ± 0.3 eV and a spin-orbit splitting of 1.70 ± 0.05 eV (Figure 3.3.2-2); and like the Xe 4d level in Xe,[25] the I 4d cross section increases to a maximum approximately 30-35 eV above threshold.[91,92,95,98] Figure 3.3.2-2 shows that at 81 eV photon energy, the I 4d cross section in CF_3I is about an order of magnitude larger than the valence band partial cross sections. Using the Xe analogy, the enhancement of the I 5p lone pairs (4e MO) in CF_3I above the I 4d threshold is due to interchannel correlation between the I 5p and 4d subshells (Figure 3.1.1-1(b)). A number of recent solid state studies have shown similar intensity enhancements in the valence band on scanning through a core level,[14,103-106] but such enhancements have only recently been characterized in the gas phase.[107,111] The above many-body effect should be a generally important mechanism for enhancing valence band intensities at known core level energies, when the cross

Figure 3.3.2-2

Photoelectron spectrum of CF_3I taken at 81 eV photon energy. Note the valence band region at ~10-25 eV binding energies, the weak F 2s peaks at ~40 eV binding energy, the intense I 4d spin-orbit peaks at ~60 eV binding energy, and the I $N_{4,5}VV$ Auger peaks in the same region.

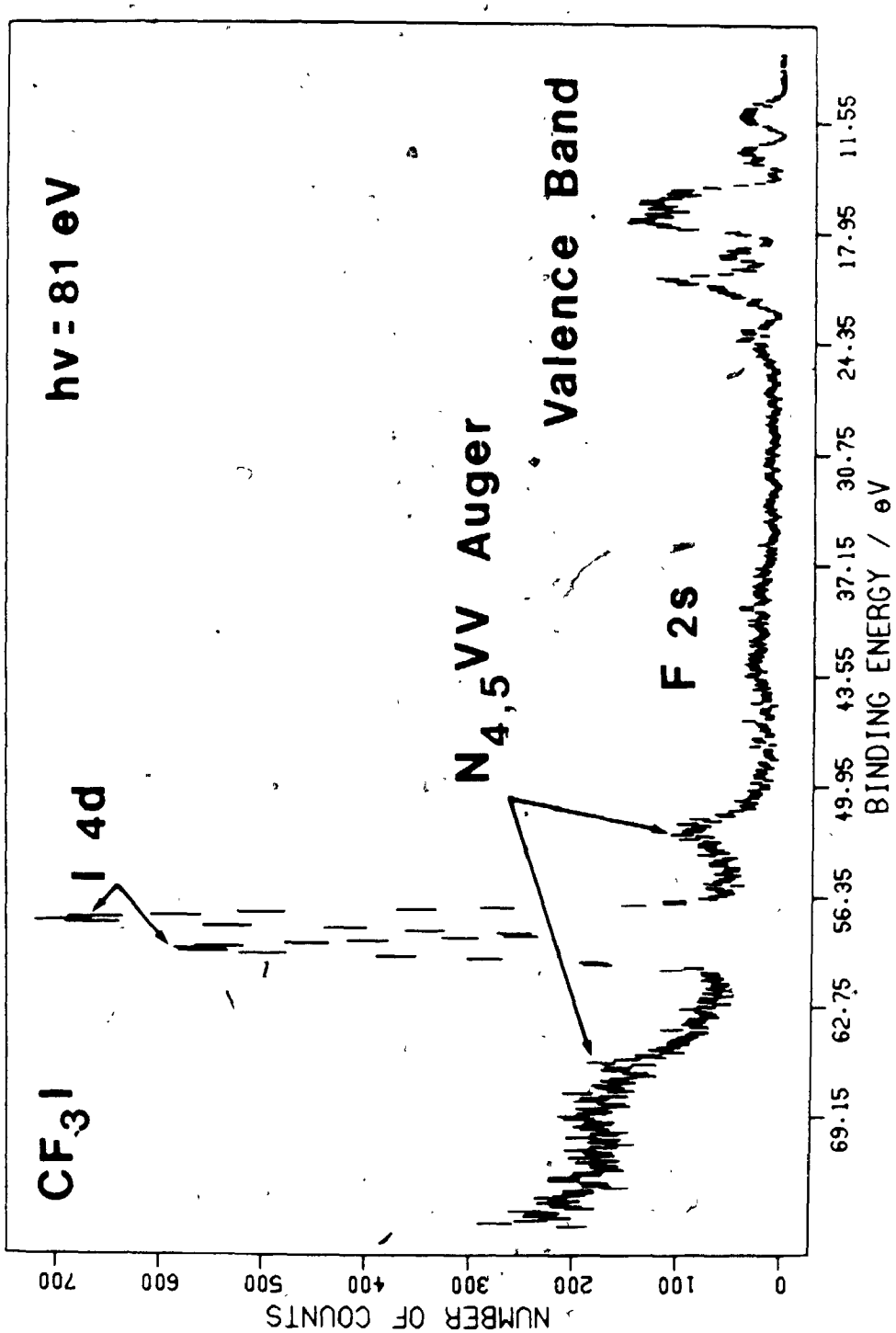
hv = 81 eV
CF3I
I 4d
N4,5VV Auger
Valence Band
F 2s
NUMBER OF COUNTS
0
100
200
300
400
500
600
700
69.15
62.75
56.35
49.95
43.55
37.15
30.75
24.35
17.95
11.55
BINDING ENERGY / eV

section of the core level is large compared with valence band cross sections. Although the limitations to this are currently not known, this effect might be very useful for molecular orbital assignments. For example, the photon energy could be tuned to a known intense core level (e.g. (n - 1)d) to enhance the intensity of the valence molecular orbital with the largest atomic np character. Obviously further experimental work is required to determine exactly how general intershell correlation is.

The enhancement of the I 5p lone pairs (4e MO) in CF_3I has been made more quantitative by determining the valence band branching ratios from 21 eV to 110 eV photon energy. These measured branching ratios could not be converted to partial cross sections, unfortunately, since the total photoionization cross section has not been measured in this energy range. In Figure 3.3.2-3 is shown the theoretical MS-Xα branching ratio and partial cross section, and experimental branching ratio for the I 5p lone pairs (4e MO) of CF_3I. A complete analysis of the remaining molecular orbitals of CF_3I, and a comparison to CF_4 will be pursued later on in Chapter 4. Details of the theoretical MS-Xα calculations done on CF_3I may also be found in Chapter 4.

Turning to the theoretical partial cross section of the 4e MO of CF_3I (Figure 3.3.2-3), we find a simple monotonic decrease in σ, with no minimum. This behaviour is very similar to the MS-Xα results obtained by

Figure 3.3.2-3

Experimental and theoretical MS-Xα (solid lines) results for the photoionization of the 4e orbital (predominantly I 5p lone pairs) of CF_3I. The upper and bottom plots give the σ and branching ratio, respectively.

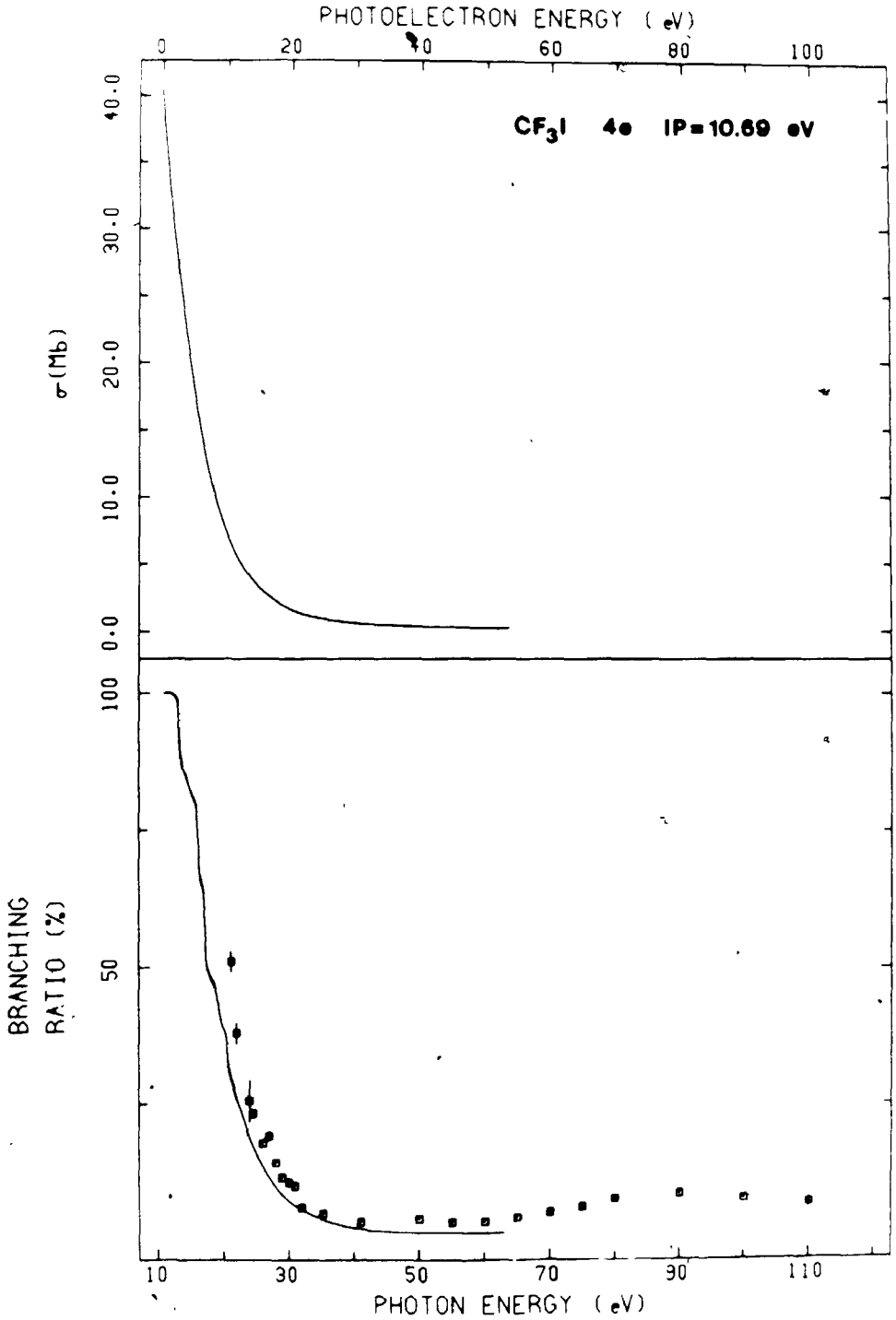
PHOTOELECTRON ENERGY (eV)
0
20
40
60
80
100
CF_3I 4e IP=10.69 eV
σ(Mb)
40.0
30.0
20.0
10.0
0.0
100
50
BRANCHING RATIO (%)
10
30
50
70
90
110
PHOTON ENERGY (eV)

Carlson et al.[107] on the I 5p lone pairs of HI ($1\ ^2\Pi$), where σ decreases monotonically from threshold to ~110 eV photon energy and also shows no minimum. While the agreement for this partial cross section in HI is quite good between experiment and theory (MS-Xα) up until ~60 eV photon energy,[107] a broad maximum centered at ~81 eV photon energy is observed instead of the predicted monotonic decrease. Likewise, a broad maximum centered at ~84 eV photon energy occurs in their partial cross section data for the I 5p lone pairs of CH_3I ($1\ ^2E$).[107] A similar broad maximum centered at ~90 eV photon energy can be found for CF_3I in the 4e branching ratio.

For the asymmetry parameter β, one finds that although the agreement between experiment and theory is generally good for the I 5p lone pairs in HI below ~60 eV photon energy (~45 eV kinetic energy), above this very large discrepancies between the two occur.[107] An almost identical asymmetry parameter has been observed by these authors for CH_3I.[107] In fact both of these β curves are similar in shape and magnitude to the Xe 5p asymmetry parameter,[5,11] although in Xe discrepancies between single-particle Hartree-Slater calculations and experiment occur above ~70 eV photon energy. It is interesting to note that these discrepancies in σ and β for these compounds between experiment and single-particle calculations, occur just above their respective 4d thresholds for I or Xe. These discrepancies are also

virtually coincident with their Cooper minima (HI, CH_3I:~45 eV; Xe:~53 ev).[107-109] These deviations do not arise explicitly however, because of these Cooper minima. Single-particle MS-Xα calculations have given, for example, good agreement both above and below the Cooper minima in HCl and HBr.[110] Since the discrepancies occur in the region of 4d electron excitation, this points instead to intershell electron correlations between the I 5p and I 4d subshells being important in these molecules,[112] as in the atomic Xe case. Above the Xe 4d threshold, theoretical agreement with experiment for the Xe 5p asymmetry parameter was only obtained[11] with the many-body RRPA calculations of Johnson et al.,[8,16] which included correlations between the 5p, 5s and 4d subshells. The maximum observed in the 4e branching ratio of CF_3I at ~90 eV photon energy is furthermore in good agreement with the I 4d cross section maxima measured for I_2 (~93 eV photon energy)[98] and CH_3I (~85 eV photon energy).[91]

The I 4d spin-orbit branching ratio (BR) was determined for CF_3I from 66 eV to 110 eV photon energy, as shown in Figure 3.3.2-4. A typical computer-fitted spectrum of the I 4d level of CF_3I at 78 eV photon energy can be found in Figure 3.3.2-5. The $4d_{5/2}$:$4d_{3/2}$ BR drops quickly from ~2.1 at 66 eV photon energy to values clearly less than the statistical value of 1.5 above 72 eV photon energy. At photon energies ≥90 eV, the BR appears to be very slowly dropping, with values close to ~1.33. A

Figure 3.3.2-4

I $4d_{5/2}$:$4d_{3/2}$ branching ratio (BR) as a function of photon energy, from 66 to 110 eV. The solid line is a visual fit to the experimental data.

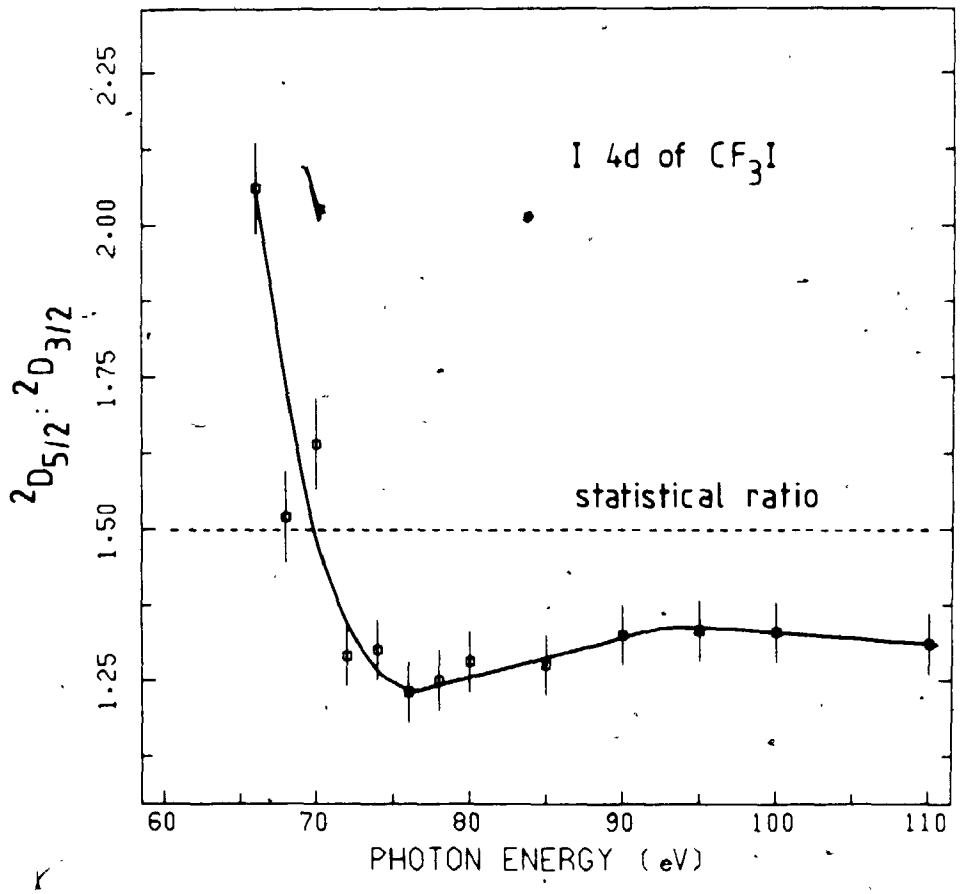
I 4d of CF_3I
statistical ratio
$^2D_{5/2}:{}^2D_{3/2}$
2·25
2·00
1·75
1·50
1·25
60
70
80
90
100
110
PHOTON ENERGY (eV)

Figure 3.3.2-5

I 4d photoelectron spectrum of CF_3I taken at 78 eV photon energy, with a band pass of ~1.7 Å and 50 eV electron analyzer pass energy (0.4 eV electron resolution).

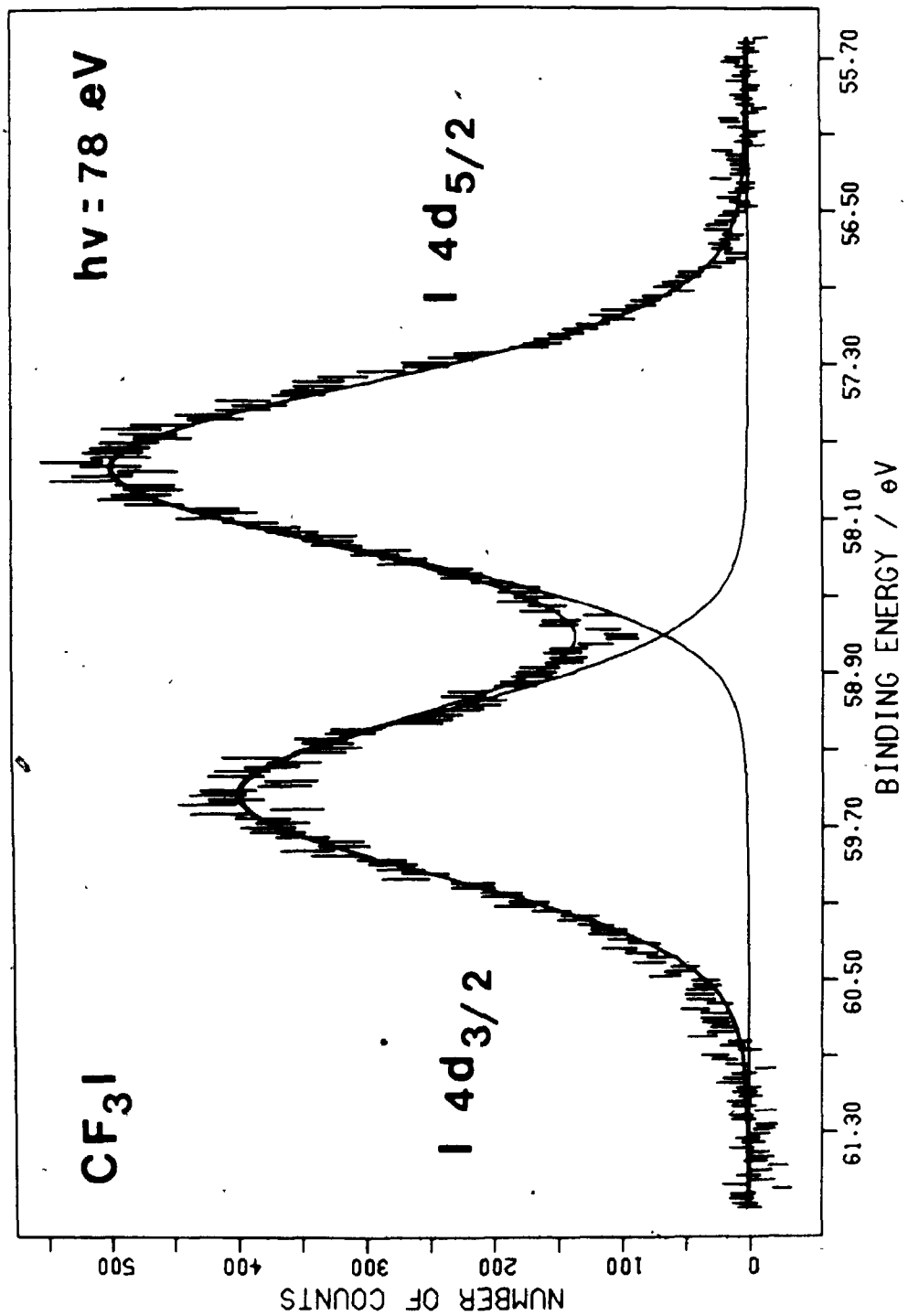
hν = 78 eV
CF3I
I 4d5/2
I 4d3/2
NUMBER OF COUNTS
0
100
200
300
400
500
61.30
60.50
59.70
58.90
58.10
57.30
56.50
55.70
BINDING ENERGY / eV

shallow minimum occurs at ~76 eV photon energy (~16 eV kinetic energy). Lindle et al.[91] found that the I 4d spin-orbit BR in CH_3I dropped monotonically above threshold to the statistical value, although these conclusions seemed to have been drawn from three roughly statistical values between 73 and 105 eV photon energy. The general shape in Figure 3.3.2-4 is very similar to that found for the Xe 4d spin-orbit BR (Figure 3.3.1-5), except that the I 4d BR minimum is more shallow than for Xe and occurs at ~2 eV higher kinetic energy. Above 90 eV photon energy, the I and Xe 4d BR's are very similar in both behaviour and magnitude.

3.4.1 References

1. P.-O. Lowdin, Adv. Chem. Phys. 2, 207 (1959).
2. C.F. Fischer, "The Hartree-Fock Method for Atoms", (Wiley-Interscience, New York, 1977).
3. M. Weissbluth, "Atoms and Molecules", (Academic Press, New York, 1978).
4. I.N. Levine, "Quantum Chemistry", (Allyn and Bacon, Boston, 1970).
5. M.O. Krause, "Synchrotron Radiation Research", edited by H. Winick and S. Doniach (Plenum, New York, 1980), p. 101.
6. V. Schmidt, Appl. Optics 19, 4080 (1980).
7. A.F. Starace, Appl. Optics 19, 4051 (1980).
8. W.R. Johnson and K.T. Cheng, Phys. Rev. A 20, 978 (1979).
9. W.R. Johnson and K.T. Cheng, Phys. Rev. Lett. 40, 1167 (1978).
10. W.R. Johnson, C.D. Lin, K.T. Cheng, and C.M. Lee, Physica Scripta 21, 409 (1980).
11. M.O. Krause, T.A. Carlson, and P.R. Woodruff, Phys. Rev. A 24, 1374 (1981).
12. A. Fahlman, T.A. Carlson, and M.O. Krause, Phys. Rev. Lett. 50, 1114 (1983).
13. M.G. White, S.H. Southworth, P. Kobrin, E.D. Poliakoff, R.A. Rosenberg, and D.A. Shirley, Phys. Rev. Lett. 43, 1661 (1979).

14. T. Miller and T.-C. Chiang, Phys. Rev. B 29, 1121 (1984).

15. B.R. Tambe, W. Ong, and S.T. Manson, Phys. Rev. A 23, 799 (1981).

16. W.R. Johnson and C.D. Lin, Phys. Rev. A 20, 964 (1979).

17. M.Y. Adam, F. Wuilleumier, N. Sandner, S. Krummacher, V. Schmidt, and W. Mehlhorn, Jpn. J. Appl. Phys. 17, 170 (1978).

18. R.G. Houlgate, J.B. West, K. Codling, and G.V. Marr, J. Electron Spectrosc. Relat. Phenom. 9, 205 (1976).

19. T.N. Chang, Phys. Rev. A 18, 1448 (1978).

20. K.T. Cheng and W.R. Johnson, Phys. Rev. A 28, 2820 (1983).

21. G. Wendin, Phys. Lett. 37A, 445 (1971).

22. T. Gustafsson, Chem. Phys. Lett. 51, 383 (1977).

23. J.B. West, P.R. Woodruff, K. Codling, and R.G. Houlgate, J. Phys. B 9, 407 (1976).

24. M.S. Banna, M.O. Krause, and F. Wuilleumier, J. Phys. B 12, L125 (1979).

25. S.P. Shannon, K. Codling, and J.B. West, J. Phys. B 10, 825 (1977).

26. H. Derenbach and V. Schmidt, J. Phys. B 16, L337 (1983).

27. A. Fahlman, M.O. Krause, and T.A. Carlson, J. Phys. B 17, L217 (1984).

28. W.R. Johnson and V. Radojević, J. Phys. B 11, L773 (1978).

29. D.L. Ederer, Phys. Rev. Lett. 13, 760 (1964).

30. J.W. Cooper, Phys. Rev. Lett. 13, 762 (1964).

31. M.B. Robin, Chem. Phys. Lett. 119, 33 (1985).

32. M. Ya. Amusia, V.K. Ivanov, N.A. Cherepkov, and L.V. Chernysheva, Sov. Phys.-JETP 39, 752 (1974).

33. M. Ya. Amusia, L.V. Chernysheva, and V.K. Ivanov, Phys. Lett. 43A, 243 (1973).

34. M. Ya. Amusia, V.K. Ivanov, N.A. Cherepkov, and L.V. Chernysheva, Phys. Lett. 40A, 361 (1972).

35. M.Y. Adam, Ph.D. Thesis, University of Orsay, France (1978).

36. R.D. Mattuck, "A guide to Feynman diagrams in the many-body problem", (McGraw-Hill, New York, 1976), p. 18.

37. K.H. Tan, G.M. Bancroft, L.L. Coatsworth, and B.W. Yates, Can. J. Phys. 60, 131 (1982).

38. K.H. Tan, P.C. Cheng, G.M. Bancroft, and J.Wm. McGowan, Can. J. Spectrosc. 29, 134 (1984).

39. B.W. Yates, K.H. Tan, L.L. Coatsworth, and G.M. Bancroft, Phys. Rev. A 31, 1529 (1985).

40. J.A.R. Samson, Philos. Trans. Roy. Soc. London A 268, 141 (1970).

41. S. Aksela, K.H. Tan, G.M. Bancroft, H. Aksela, B.W. Yates, and L.L. Coatsworth, Phys. Rev. A 32, 1219 (1985).

42. B.W. Yates, K.H. Tan, G.M. Bancroft, L.L. Coatsworth, and J.S. Tse, J. Chem. Phys. 83, 4906 (1985).

43. T.A. Carlson, A. Fahlman, W.A. Svensson, M.O. Krause, T.A. Whitley, F.A. Grimm, M.N. Piancastelli, J.W. Taylor, J. Chem. Phys. 81, 3828 (1984).

44. E.W. Plummer, T. Gustafsson, W. Gudat, and D.E. Eastman, Phys. Rev. A 15, 2339 (1977).

45. F. Wuilleumier, M.Y. Adam, P. Dhez, N. Sandner, V. Schmidt, and W. Mehlhorn, Phys. Rev. A 16, 646 (1977).

46. G.M. Bancroft, I. Adams, L.L. Coatsworth, C.D. Bennewitz, J.D. Brown, and W.D. Westwood, Anal. Chem. 47, 586 (1975).

47. G.M. Bancroft, W. Gudat, and D.E. Eastman, Phys. Rev. B 17, 4499 (1978).

48. G. Margaritondo, J.E. Rowe, and S.B. Christman, Phys. Rev. B. 19, 2850 (1979).

49. G. Margaritondo, F. Cerrina, G.P. Williams, and G.J. Lapeyre, J. Vac. Sci. Technol. 16, 507 (1979).

50. T.E.H. Walker, J. Berkowitz, J.L. Dehmer, and J.T. Waber, Phys. Rev. Lett. 31, 678 (1973).

51. N.G. Stoffel and G. Margaritondo, Phys. Lett. 75A, 319 (1980).

52. P.H. Kobrin, P.A. Heimann, H.G. Kerkhoff, D.W. Lindle, C.M. Truesdale, T.A. Ferrett, U. Becker, and D.A. Shirley, Phys. Rev. A 27, 3031 (1983).

53. A. Ron, Y.S. Kim, and R.H. Pratt, Phys. Rev. A 24, 1260 (1981).

54. F. Wuilleumier, M.Y. Adam, P. Dhez, N. Sandner, V. Schmidt, and W. Mehlhorn, Phys. Rev. A 16, 646 (1977).

55. J.L. Dehmer and J. Berkowitz, Phys. Rev. A 10, 484 (1974).

56. S. Svensson, N. Mårtensson, E. Basilier, P.Å. Malmquist, U. Gelius, and K. Siegbahn, J. Electron Spectrosc. Relat. Phenom. 9, 51 (1976).

57. D.R. Williams, R.T. Poole, J.G. Jenkin, J. Liesegang, and R.C.G. Leckey, J. Electron Spectrosc. Relat. Phenom. 9, 11 (1976).

58. S. Suzer, P.R. Hilton, N.S. Hush, and S. Nordholm, J. Electron Spectrosc. Relat. Phenom. 12, 357 (1977).

59. J.E. Rowe and G. Margaritondo, Phys. Lett. 57A, 314 (1976).

60. J.W. Rabalais and T.P. Debies, J. Electron Spectrosc. Relat. Phenom. 5, 847 (1974).

61. M.Y. Adam, F. Wuilleumier, S. Krummacher, N. Sandner, V. Schmidt, and W. Mehlhorn, J. Electron Spectrosc. Relat. Phenom. 15, 211 (1978).

62. P. Shannon and K. Codling, J. Phys. B 11, 1193 (1978).

63. T.E.H. Walker and J.T. Waber, J. Phys. B 7, 674 (1974).

64. J.H. Scofield, J. Electron Spectrosc. Relat. Phenom. 8, 129 (1976).

65. W. Ong and S.T. Manson, J. Phys. B 11, L163 (1978).

66. W. Ong and S.T. Manson, Phys. Rev. A 21, 842 (1980).

67. W.R. Johnson, V. Radojević, P. Deshmukh, and K.T. Cheng, Phys. Rev. A 25, 337 (1982).

68. K.-N. Huang, W.R. Johnson, and K.T. Cheng, At. Data Nucl. Data Tables 26, 33 (1981).

69. B.R. Tambe and S.T. Manson, Phys. Rev. A 30, 256 (1984).

70. S.L. Carter and H.P. Kelly, J. Phys. B 11, 2467 (1978).

71. W.R. Johnson and V. Radojević, Phys. Lett. 92A, 75 (1982).

72. F. Wuilleumier, M.Y. Adam, N. Sandner, V. Schmidt, W. Mehlhorn, and J.P. Desclaux, Proceedings of the 5th International Conference on VUV Radiation Physics, Montpellier, France, Extended Abstracts, Vol. 1, 41 (1977).

73. S. Southworth, V. Becker, C.M. Truesdale, P.H. Kobrin, D.W. Lindle, S. Owaki, and D.A. Shirley, Phys. Rev. A 28, 261 (1983).

74. W. Ong and S.T. Manson, Bull. Am. Phys. Soc. 23, 564 (1978).

75. R.A. Riedel, M. Turowski, and G. Margaritondo, Phys. Rev. Lett. 52, 1568 (1984).

76. L.O. Werme, T. Bergmark, and K. Siegbahn, Physica Scripta 6, 141 (1972).

77. G.M. Bancroft, P.A. Malmquist, S. Svensson, E. Basilier, U. Gelius, and K. Siegbahn, Inorg. Chem. 17, 1595 (1978).

78. U. Gelius, L. Asplund, E. Basilier, S. Hedman, K. Helenelund, and K. Siegbahn, Nucl. Instrum. Methods 229, 85 (1984).

79. G.C. King, M. Tronc, F.H. Read, and R.O. Bradford, J. Phys. B. 10, 2479 (1977).

80. O. Keski-Rahkonen and M.O. Krause, At. Data Nucl. Data Tables 14, 139 (1974).

81. O. Keski-Rahkonen and M.O. Krause, Phys. Rev. A 15, 959 (1977).

82. J.F. Van der Veen, F.J. Himpsel, and D.E. Eastman, Phys. Rev. B 25, 7388 (1982).

83. R. Nyholm and J. Schmidt-May, J. Phys. C 17, L113 (1984).

84. J. Topping, "Errors of Observation and Their Treatment", (The Institute of Physics and Physical Society, London, 1961).

85. M.G. Clark, G.M. Bancroft, and A.J. Stone, J. Chem. Phys. 47, 4250 (1967).

86. E. Schmidt, Ph.D. Thesis, University of Hamburg (1985).

87. G. Wendin, "Photoionization and Other Probes of Many-Electron Interactions", edited by F.J. Wuilleumier (Plenum, New York, 1976), p. 61.

88. M. Ya. Amusia, Appl. Opt. 19, 4042 (1980).

89. U. Gelius, J. Electron Spectrosc. Relat. Phenom. 5, 985 (1974).

90. G.K. Wertheim, J. Electron Spectrosc. Relat. Phenom. 33, 79 (1984).

91. D.W. Lindle, P.H. Kobrin, C.M. Truesdale, T.A. Ferrett, P.A. Heimann, H.G. Kerkhoff, U. Becker, and D.A. Shirley, Phys. Rev. A 30, 239 (1984).

92. D.W. Lindle, Ph.D. Thesis, University of California, Berkeley (1984).

93. K.T. Cheng and C.F. Fischer, Phys. Rev. A 28, 2811 (1983).

94. R.W. Woodruff and M.P. Givens, Phys. Rev. 97, 52 (1955).

95. G. O'Sullivan, J. Phys. B 15, L327 (1982).

96. M. Pettini, M. Mazzoni, and G.P. Tozzi, Phys. Lett. 82A, 168 (1981).

97. F.C. Brown, C. Gahwiller, and H. Fujita, Phys. Rev. B 2, 2126 (1970).

98. F.J. Comes, U. Neilsen, and W.H.E. Schwarz, J. Chem. Phys. 58, 2230 (1973).

99. A.P. Hitchcock and C.E. Brion, J. Electron Spectrosc. Relat. Phenom. 13, 219 (1978).

100. K. Radler and B. Sonntag, Chem. Phys. Lett. 39, 371 (1976).

101. H. Petersen, K. Radler, B. Sonntag, and R. Haensel, J. Phys. B 8, 31 (1975).

102. T. Cvitaš, H. Gusten, L. Klasinc, I. Novadj, and H. Vančik, Z. Naturforsch 33A, 1528 (1978).

103. M. Aono, T.-C. Chiang, F.J. Himpsel, and D.E. Eastman, Solid State Commun. 37, 471 (1981).

104. L.I. Johansson, J.W. Allen, T. Gustafsson, I. Lindau, and S.B.M. Hagstrom, Solid State Commun. 28, 53 (1978).

105. W. Lenth, F. Lutz, J. Barth, G. Kalkoffen, and C. Kunz, Phys. Rev. Lett. 41, 1185 (1978).

106. W. Gudat, S.F. Alvarado, and M. Campagna, Solid State Commun. 28, 943 (1978).

107. T.A. Carlson, A. Fahlman, M.O. Krause, P.R. Keller, J.W. Taylor, T. Whitley, and F.A. Grimm, J. Chem. Phys. 80, 3521 (1984).

108. S.T. Manson, J. Electron Spectrosc. Relat. Phenom. 1, 413 (1972/73).

109. S.T. Manson, Phys. Rev. A 31, 3698 (1985).

110. T.A. Carlson, A. Fahlman, M.O. Krause, T.A. Whitley, and F.A. Grimm, J. Chem. Phys. 81, 5389 (1984).

111. G.M. Bancroft, B.W. Yates, K.H. Tan, and L.L. Coatsworth, J. Chem. Soc., Chem. Commun., 1613 (1984).

112. H. Lefebvre-Brion, G. Raseev, and H. Le Rouzo, Chem. Phys. Lett. 123, 341 (1986).

CHAPTER 4

VALENCE BAND BRANCHING RATIOS AND SHAPE RESONANCES OF CF_4, SiF_4, AND CF_3I

4.1.1 Introduction

Remarkable progress has occurred in the last decade in characterizing various aspects of atomic and molecular photoionization dynamics. This has resulted from a strong interplay between experimentalists and theorists. The development of synchrotrons has given experimentalists access to a tuneable light source of large photon flux and allowed them to probe both valence and core levels, in a continuous fashion over large ranges in photon energy. These developments have allowed experimentalists to readily check theoretical predictions pertaining to the dynamics of photoionization. The excellent reviews by Dehmer[1] and Langhoff[2] summarize the experimental and theoretical progress made recently in this field.

One very important research area has been the measurement of branching ratios, partial cross sections (σ) and asymmetry parameters (β) as a function of photon energy for atomic and molecular systems in the gas phase. A large number of these systems have exhibited shape resonant features in these observables.[1] Shape resonances arise from quasibound states in which the photoelectron is

temporarily trapped by a potential barrier. The basic shape resonance mechanism is shown schematically in Figure 4.1.1-1. The electron is trapped at a particular resonance energy (E_r) by the potential barrier for a certain lifetime, before it may tunnel through and escape. The name "shape resonance" means that the resonance behavior is due to the "shape" of the potential. The presence of the potential barrier yields a double-well potential which tends to separate the wavefunction into inner- and outer-well wavefunctions. Shape resonances are initially localized in the inner well, being eigenfunctions of the potential well inside the barrier. Since shape resonances are localized in the inner well, they are essentially uncoupled from the outer well states and the external surroundings of the molecule. Due to this localized behavior, shape resonant behavior is not quenched in going from the gas phase to the solid state.

One of the earliest and most dramatic examples of molecular shape resonances was discovered in the photoabsorption spectra of the sulfur K- and L-shells of sulfur hexafluoride (SF_6).[3-8] The four shape resonances present in these spectra (of a_{1g}, t_{1u}, t_{2g}, and e_g symmetry) are very striking examples of how dramatically a potential barrier in the molecular potential can perturb the photoionization cross section. If one compares the sulfur $L_{2,3}$ edge of SF_6 to that of H_2S, one notices that they exhibit quite different behavior both below and above

Figure 4.1.1-1

Schematic diagram of a double-well potential arising from an attractive Coulombic potential ($\sim -1/r$) and repulsive centrifugal term ($\sim \ell(\ell+1)/r^2$). A quasibound state above vacuum level($V_{eff} = 0$) is shown in the inner well region trapped by the potential barrier.

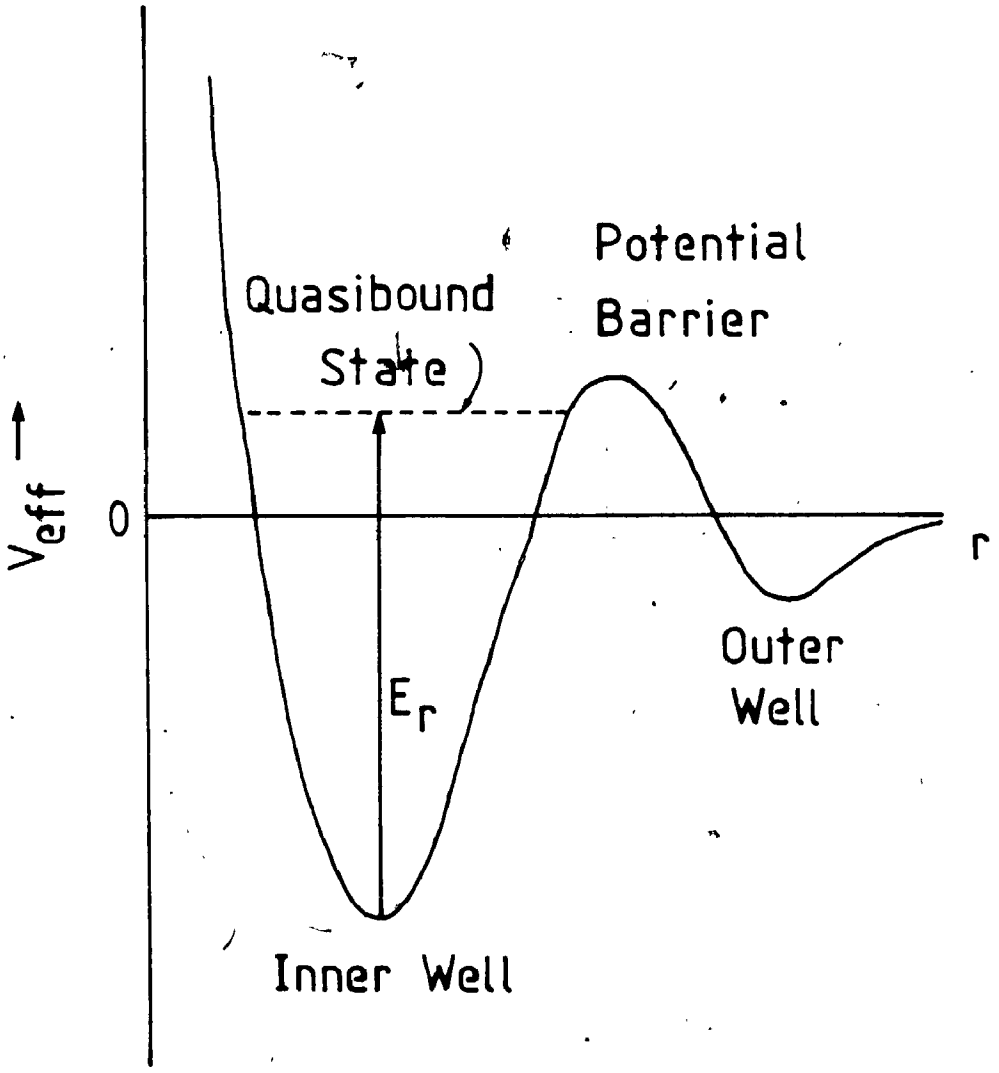
Potential
Barrier
Quasibound
State
V_{eff}
0
r
E_r
Outer
Well
Inner Well

the edge.[1] The H_2S spectrum can be considered as a normal reference spectrum, since it has been shown that hydrogen atoms generally do not give rise to shape resonance effects. The sulfur $L_{2,3}$ photoabsorption spectrum of H_2S displays a valence transition to a bound state, followed by transitions to Rydberg states which merge into a smooth and structureless continuum above the S 2p ionization potential. In SF_6 the sulfur 2p photoabsorption spectrum displays three intense and broad peaks. Whereas the first band lies below the S 2p ionization threshold, the other two bands actually lie well above. In addition, the Rydberg structure and continuum absorption spectrum is greatly reduced in strength about these three bands. Dehmer[4] interpreted this unusual oscillator strength redistribution as arising from a molecular potential barrier in SF_6. These three bands have been assigned as arising from shape resonances in the final continuum states of a_{1g}, t_{2g}, and e_g symmetry. An additional shape resonance in the final state of t_{1u} symmetry occurs in the sulfur 1s photoabsorption spectrum of SF_6.[6,7] Virtually identical shape-resonance features in photoabsorption and partial photoionization cross section results have been obtained in the gas phase and solid state,[5,9] illustrating that shape resonances appear to be strongly localized in the inner-well region of the molecule. The more current review by Dehmer et al.[10] summarizes very concisely the

central role SF_6 has played in the elucidation of shape-resonance effects in molecules.

The most dramatic shape resonance effects were initially discovered in molecules like SF_6, BF_3, and SiF_4, containing highly electronegative ligands.[4] At this point in time (~1972) it was not yet known what caused the potential barrier. Dehmer[4] suggested, however, that these potential barriers were due to electron repulsion in the vicinity of the electronegative atoms in the molecule. Three types of repulsive interactions with the photoelectron were identified by Dehmer:[4] (1) direct Coulomb interaction between the photoelectron and the electronegative atoms, (2) exchange interaction amongst these same electrons, and (3) forces arising from the requirement that the final state wavefunction be orthogonal to all occupied orbitals.[11] Later on, Dehmer and Dill[12] were able to show that centrifugal forces were primarily responsible for the intense shape resonances in the first row diatomics N_2, CO, and NO. Since then, all well-documented cases of shape resonances in molecular photoionization have been found to arise from potential barriers where centrifugal forces play a fundamental role. It has been found that centrifugal forces are primarily responsible for the strong shape resonances present in SF_6.[13]

The concept of a potential barrier is fundamental in understanding shape resonant phenomena. The barrier

arises from the superposition of an attractive Coulombic potential (~-1/r) and a repulsive centrifugal barrier (~$\ell(\ell+1)/r^2$). For an angular momentum $\ell \geq 1$, the effective potential V_{eff} (Figure 4.1.1-1) is given by,

$$V_{eff} \propto V_{Coulombic}(r) + \ell(\ell+1)/r^2 \ . \qquad (4.1.1\text{-}1)$$

Probably the most well-known and documented case which illustrates this centrifugal barrier contribution, occurs in the K-shell photoionization cross section of N_2. Dehmer and Dill[12] were able to show with multiple-scattering Xα (MS-Xα) cross section calculations on N_2, that the nonhydrogenic behavior observed experimentally[14,15] ~9 eV above the ionization threshold was due to a shape resonance in the σ_u channel. Furthermore, their calculations showed that this was caused by a centrifugal barrier acting specifically on the $\ell = 3$ angular momentum component of the σ_u continuum wavefunction. Although photoionization from the nitrogen K shell initially produces a p-wave photoelectron ($\ell = 1$) via a 1s → εp transition, the anisotropic molecular potential in N_2 scatters this outgoing wave into a range of angular momentum states for the allowed σ- and π-channels ($\Delta\lambda = 0, \pm 1$). Their calculations show that at resonance ($E = E_r$, ~11 eV kinetic energy) the $\ell = 3$ angular momentum of the σ_u final state wavefunction can overcome its centrifugal barrier, which allows it to penetrate strongly into the inner-well

region. At $E = E_r$ the inner well of N_2 can support a quasibound state, resulting in strong overlap with the initial states which also reside there. As a result of the barrier penetration over a narrow band of energies about E_r, a rapid increase in the eigenphase sum by ~π radians occurs.[16]

In order to gain a deeper understanding of shape resonances and the dynamics of photoionization in polyatomic molecules, the valence band branching ratios or partial cross sections of CF_4, SiF_4, CF_3I, and XeF_2 were measured in the gas phase using monochromatized synchrotron radiation. These polyatomic molecules were studied as a function of photon energy from ~21 eV to ~100 eV. Discussion of the XeF_2 results will be presented later on in Chapter 5. The results obtained for the cage-like CF_4, SiF_4, and CF_3I are discussed in this chapter, and compared with our theoretical MS-Xα results.

4.1.2 Molecular Cross Section Studies

Over the last two decades, many approximate theoretical methods have been developed to calculate atomic photoionization cross sections.[17,18] The agreement for atoms between theory and experiment is generally quantitative. In recent years theoreticians have gone beyond central field Hartree-Slater (HS) and Hartree-Fock (HF) calculations,[19-26] in an attempt to include electron-electron correlation effects. This has been

accomplished using configuration interaction (CI) in the initial state and final unbound continuum states,[27-29] R-matrix theory,[30] many-body perturbation theory (MBPT),[31,32] and the random phase approximation.[33,34] However, our understanding of photoionization in molecular systems is less satisfactory, since an equivalent theoretical treatment does not exist. The major difficulty in the molecular case is the computation of accurate continuum wavefunctions for an electron in the field of a molecular ion, and treatment of the multi-center potential.

Theoretical treatments of molecular photoionization usually disregard nuclear motion to a first approximation, assuming that the nuclei are fixed instead at their equilibrium positions. In addition to this, effects due to relativity, electron spin, electron correlation, and relaxation are generally ignored due to their additional complexity. Initially, the majority of the theoretical work approximated the final state ($\langle f|$) with a plane wave of the form,[35-38]

$$\langle f| = e^{i\vec{k}\cdot\vec{r}} , \qquad (4.1.2\text{-}1)$$

where $\vec{k}$ is the wave vector of the photoelectron. The plane-wave approximation basically ignores the influence of the molecular potential acting on the photoelectron, and is therefore independent of the molecular system. The most complete plane-wave (PW) and orthogonalized plane-wave

(OPW) calculations have been performed by Rabalais and coworkers[35-37] and Thiel et al.,[39-41] both of whom used Slater-type orbitals to represent the initial state. If one compares[42] the results of Rabalais et al.[37] for the $3\sigma_g$ level of N_2 with the experimental data, it is found that the plane wave gives very poor agreement for photon energies less than ~40 eV. The poor agreement here implies that the influence of the molecular potential on the ejected electron cannot simply be ignored at low kinetic energies. In an attempt to correct some of these problems, methods using one-center Coulomb potentials or one-center pseudopotentials have been developed.[43] The review by Thiel[43] discusses some of the various one-center potentials that have been used.

In contrast to these one-center potentials or total neglect of the potential, the multiple-scattering model[44] uses a multi-center potential of the muffin-tin variety. The molecular potential formed from this yields an accurate representation of the potential singularities at the nuclei, and shows the correct asymptotic behavior. Moreover, this is done without the introduction of time-consuming and costly multicenter integrals. The multiple-scattering technique was first applied to calculate bound-state molecular eigenvalues by Johnson and Smith.[45-52] The multiple-scattering method was extended to treat continuum electronic states of molecules by Dill and Dehmer,[44] who applied it to calculate core level cross

sections of N_2. The method has since been extended to more complex systems (e.g. CO_2, BF_3, SF_6, CF_4) by Davenport,[53,54] Thiel et al.,[43,55] Wallace et al.,[10,13] Grimm et al.,[56-61] Gustafsson et al.,[62-64] and others.[8,65-69] In general, photoionization cross-sections and asymmetry parameters calculated using the multiple-scattering technique compare well with experiment, and are clearly superior to those obtained using plane waves, Coulomb waves, or one-center pseudopotential functions.[43] The method has also been able to qualitatively reproduce shape resonance structure in molecules such as SF_6,[8,63,64] BF_3,[65] CF_4,[61] CCl_4,[57] SiF_4,[68] and $SiCl_4$.[127]

In the multiple-scattering model, the molecular space is partitioned into three different regions of potential energy, as shown in Figure 4.1.2-1. Since the details of this model have been discussed previously at length,[13,44,53] only a brief outline will be sketched here. In this scheme, each nuclei is surrounded by a spherical region of radius sufficiently large to include all atomic electron density. If the jth atomic region is denoted by I_j, then region I is merely the summation of these I_j (i.e. region I includes all of these atomic spheres). The atomic spheres can be either placed tangential to one another as shown, or overlapped slightly. Although the reasons are not fully understood, overlapping spheres generally leads to improvement in the bound state calculations.[70] Inside each of the atomic

Figure 4.1.2-1

Muffin-tin partitioning of the molecular potential for a heteronuclear diatomic molecule.

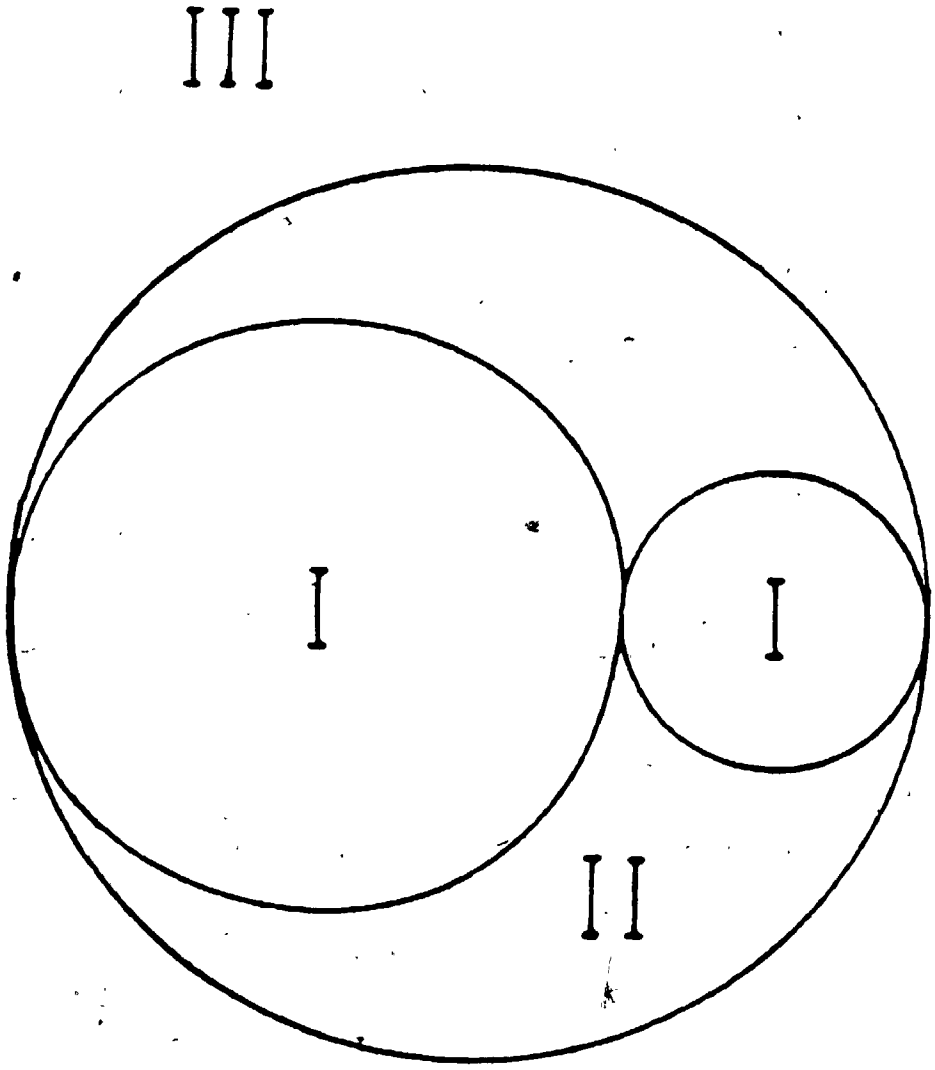

I : ATOMIC SPHERE

II : INTERSPHERE

III : OUTERSPHERE

regions Ij the potential is assumed to be spherically symmetrical, and approximated by the sum of the central model potential for the atom at site j and the spherically averaged contribution of all the other atomic sphere potentials to the jth site. Region II is usually referred to as the intersphere or interatomic region, and consists of the region between the atomic spheres (Region I) and the outersphere enclosing the entire molecule. The potential in region II is approximated by volume averaging the potentials in regions I and III to a constant. Since this approximation is admittedly rather crude, one generally attempts to minimize the volume in region II as much as possible. Scherz[71] has been able to show how this assumption may be relaxed somewhat in this region, in favor of a more general central potential. The outersphere or extramolecular region III is simply the region outside of the sphere which encloses the entire molecule. The spherically symmetric potential in region III is obtained by taking the sum of the monopole terms of the atomic sphere potentials (Region I), expanded about the origin of the outersphere.

Partitioning the molecule into different regions allows us to construct spherically symmetrical potentials in regions I and III. In each of these spherical regions, the Schrodinger equation is separable into radial and angular parts. As a result of this, the wavefunction of the molecule in these regions can be expanded in a rapidly

convergent series involving the product of the radial and angular parts.[13,44] The total electronic wavefunction in the multiple-scattering model is of the form,[44]

$$\Psi = (\sum_j \Psi_{I_j}) + \Psi_{II} + \Psi_{III} \qquad (4.1.2\text{-}2)$$

Each of the terms in equation 4.1.2-2 is the solution to the corresponding potential in the region in question, with the proviso that these solutions must satisfy the boundary conditions for that region. The boundary conditions require that the wavefunction and its first derivative be continuous at the sphere boundaries.

The actual molecular potential is determined in a self-consistent-field (SCF) manner. Using an initial estimate for the molecular potential, the one-electron Schrödinger equations (equation 4.1.2-3) are solved in each region.[13,46,72,73] When these solutions are matched at the sphere boundaries, a set of spin-orbitals u_i and associated eigenvalues ϵ_i are obtained. The one-electron Schrodinger equation (in Rydberg energy units),

$$[-\nabla_1^2 + V_N(1) + V_C(1) + V_{X\alpha}(1)]u_1(1) = \epsilon_i u_i(1) \ , \qquad (4.1.2\text{-}3)$$

$$\text{where} \quad V_{X\alpha}(1) = -6\alpha[(3/8\pi)\rho(1)]^{1/3} \ , \qquad (4.1.2\text{-}4)$$

must be solved in regions I, II, and III. Here $-\nabla_1^2$ is the kinetic energy (in Rydbergs), $V_N(1)$ is the attractive

nuclear-electron potential energy at position 1, $V_C(1)$ is the repulsive Coulomb contribution at position 1 arising from all electrons, $V_{X\alpha}(1)$ is the $X\alpha$ statistical approximation developed by Slater[46,48,72] to the exchange-correlation potential, $\rho(1)$ is the charge density at position 1 ($\rho(1) = \sum_i n_i u_i^* u_i$; n_i = occupation number of spin orbital u_i), and α is the variable scaling parameter. Since the photoelectron experiences a Coulombic potential at long range as a result of the remaining molecular ion, a Latter tail[74] is applied in photoionization applications to the potential in Region III, to ensure that the potential is indeed Coulombic as $r \to \infty$. The spin-orbitals obtained are then used to calculate the charge density ρ, from which a radial potential incorporating the nuclear and Coulomb potential contributions can be calculated for each spherical region. Adding the exchange-correlation potential $V_{X\alpha}$ to this and carrying out the averaging required by the muffin-tin potential, yields a new molecular potential. This procedure is then repeated to a certain tolerance, yielding a self-consistent-field or SCF molecular potential.

The general form of the differential photoionization cross section is:[53]

$$\frac{d\sigma}{d\Omega} = \frac{\alpha}{\pi}\frac{k}{\omega}\,|\langle f|\hat{A}\cdot\vec{p}|i\rangle|^2\, a_0^2, \qquad (4.1.2\text{-}5)$$

where α is the fine structure constant, a_0 is the Bohr radius, k is the magnitude of the wave vector of the photoelectron, $\hat{A}$ is a unit polarization vector of the incident photon beam of energy $\hbar\omega$, and $\vec{p}$ is the linear momentum operator. Equation 4.1.2-5 can be rewritten using the commutation relation $[H,\vec{p}] = i\hbar\vec{\nabla}V$, yielding

$$\frac{d\sigma}{d\Omega} = \frac{\alpha}{\pi}\frac{k}{\omega}\frac{1}{(\epsilon_f-\epsilon_i)^2}|\langle f|\hat{A}\cdot\vec{\nabla}V|i\rangle|^2 a_0^2, \qquad (4.1.2\text{-}6)$$

where ϵ_i and ϵ_f are the energy eigenvalues of the initial and final states. The dipole acceleration form is convenient for use with a muffin-tin potential, since the dipole matrix element in the intersphere region (constant potential region) reduces to evaluation of "surface terms" at the sphere boundaries,[13] since $\vec{\nabla}V = 0$ there. The problem of calculating photoionization cross sections involves defining the final state continuum wavefunction properly, and evaluating equation 4.1.2-6. The appropriate form of the continuum wavefunction and a discussion of the details of how the dipole matrix elements are evaluated in the multiple-scattering method have been discussed in detail by Wallace,[13] Dill and Dehmer,[44] and Davenport.[53]

4.2.1 Experimental

High purity CF_4 and SiF_4 (99.7%-99.99%) were obtained commercially from Matheson. Trifluoroiodomethane (CF_3I) was purchased from PCR Research Chemicals Inc., and

like the other two gases was used without further purification. Gas phase photoelectron spectra of CF_4, SiF_4, and CF_3I were obtained using photons from the Canadian Synchrotron Radiation Facility (CSRF) at the Tantalus I storage ring, with a Leybold-Heraeus LHS-11 photoelectron spectrometer mounted at the magic angle.[75,76] In this geometry, the photoelectron intensities are independent of β and the polarization of the incident radiation.[77] A 600 lines/mm holographic grating from JY Inc. was used in our Mark IV Grasshopper monochromator, limiting our minimum photon energy to 21 eV. The Canadian beamline (CSRF), experimental arrangement, and data acquisition have been described elsewhere in the literature[75,76] and in Chapter 2 of this thesis. Spectra of the valence regions of CF_4 and SiF_4 were recorded at 1.7 Å monochromator band width, and 50 eV electron analyzer pass energy (0.4 eV electron resolution) from 21 to 100 eV photon energy. Valence band spectra of CF_3I were collected at identical resolution, but from 21 to 110 eV photon energy. Representative spectra for both CF_4 and SiF_4 are shown in Figures 4.2.1-1,2 at 32, 45 and 60 eV photon energies, while those for CF_3I are shown in Figure 3.3.2-1 at ~35, 41, and 80 eV photon energies. As discussed in section 3.2.1, the transmission function of our electron spectrometer has been found to be constant to within 20% for kinetic energies between 2-60 eV,[76,78]

Figure 4.2.1-1

Photoelectron spectra of CF_4 at 32 eV, 45 eV, and 60 eV photon energies. The molecular orbital assignment is given in the bottom plot.

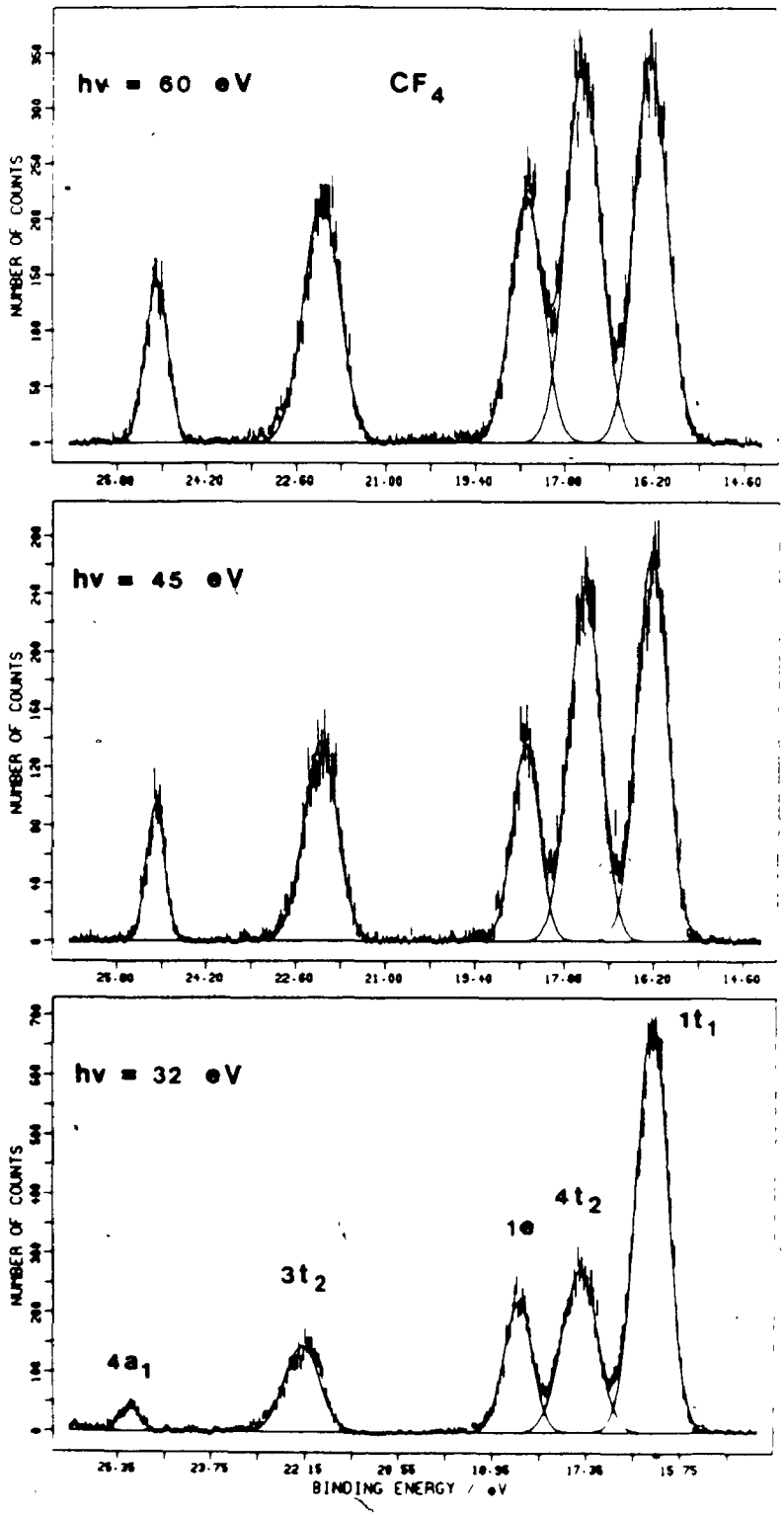
hv = 60 eV
CF4
hv = 45 eV
hv = 32 eV
1t1
4t2
1e
3t2
4a1
NUMBER OF COUNTS
BINDING ENERGY / eV

Figure 4.2.1-2

Photoelectron spectra of SiF_4 at 32 eV, 45 eV, and 60 eV photon energies. The molecular orbital assignment is given in the bottom plot.

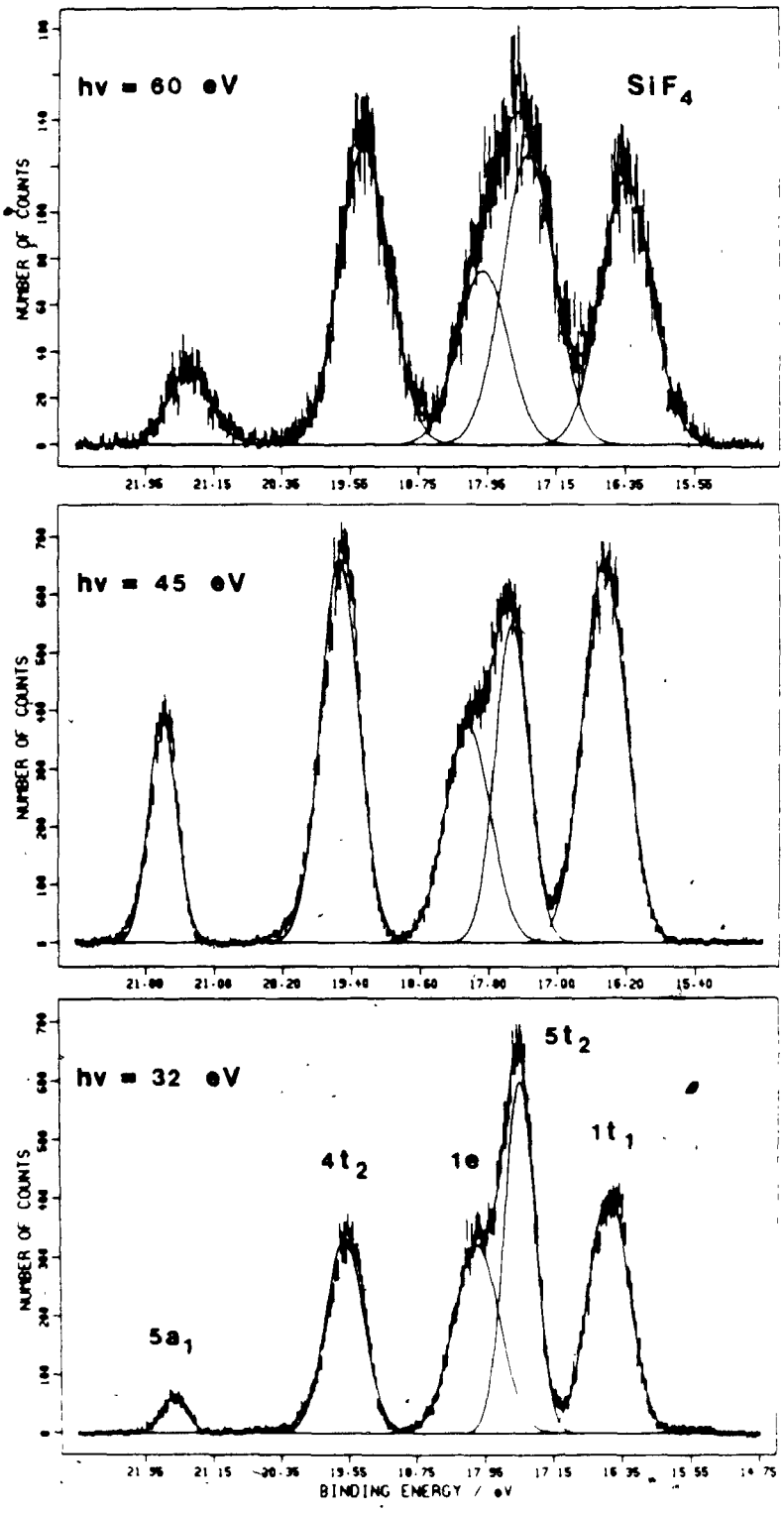
hv = 60 eV
SiF4
hv = 45 eV
hv = 32 eV
5t2
1t1
4t2
1e
5a1
NUMBER OF COUNTS
BINDING ENERGY / eV

enabling us to obtain branching ratios without intensity corrections.

All of the photoelectron spectra were computer-fitted with a Voigt function simulated by a linear combination of Lorentzian-Gaussian line shapes, using an iterative procedure described previously.[79] Valence band branching ratios were determined for these three systems over the entire photon energy range that photoelectron spectra were collected, using the peak areas (A_i) and the branching ratio definition ($BR_i = A_i/\Sigma A_{i\ Valence}$). For SiF_4, the second and third peaks ($5t_2$ and 1e, respectively, Figure 4.2.1-2) are only separated by 0.5 eV. Above ~50 eV photon energy, these two peaks are no longer adequately resolved (due to the increasing photon width contribution from the monochromator), so that only their total area can be accurately determined. Due to similar peak overlap problems in CF_3I, branching ratios representing contributions from two molecular orbitals could only be determined sometimes (e.g. $2a_1$ + 1e and 3e + $1a_2$). In all three cases, the weak and broad F 2s orbitals were neglected in the branching ratio determination. Even at 70 eV photon energy, neglect of the F 2s leads to an error in the branching ratio of less than ~11%. Unfortunately, total photoionization cross sections are not known for SiF_4 and CF_3I in this photon energy range, so the measured branching ratios could not be converted to partial cross sections. However, the total photoionization cross

sections of Lee et al.[80] for CF_4 and Carlson et al.[61] enabled us to convert the CF_4 branching ratios to partial cross sections.

4.3.1 Theory

Theoretical partial cross sections were obtained for the valence molecular orbitals of CF_4, SiF_4, and CF_3I as a function of photon energy, using the MS-Xα cross section program of Davenport.[44,53,54] The merit of this method in predicting both α and β value trends has been established in several recent studies.[10,57,61,64,65] The parameters employed in the calculation are shown in Table 4.3.1-1. The atomic exchange parameters α_{HF} were taken or interpolated from Schwarz.[81] A weighted average of the atomic exchange parameters based on the number of valence electrons was used for the outersphere and intersphere regions. Touching spheres were used for the CF_4 and SiF_4 calculations, with C-F and Si-F bond lengths of 1.323 Å and 1.552 Å, respectively.[82,83] Due to convergence problems in the SCF procedure for the ground state of CF_3I (touching spheres case), it was found necessary to enlarge the iodine sphere by ~17.7% to presumably enclose the electron density about it properly. As a result of this, the carbon and iodine spheres overlap in CF_3I. For CF_3I, C-F and C-I bond lengths of 1.3285 Å and 2.1438 Å were used.[84] Energy mesh sizes of 0.7, 1.1, and 1.4 eV were used in the calculations for CF_4, SiF_4, and CF_3I, respectively.

Table 4.3.1.1

Parameters Used in the MS-Xα Calculation

Region	X	Y	Z[a]	R[a]	α	Initial State ℓ_{max}	Final State ℓ_{max}
Outersphere	0.0	0.0	0.0	3.8141	0.74007	4	8
C	0.0	0.0	0.0	1.1861	0.75928	2	4
F_1	2.0413	0.0	1.4434	1.3140	0.73732	2	4
F_2	0.0	2.0413	-1.4434	1.3140	0.73732	2	4
F_3	-2.0413	0.0	1.4434	1.3140	0.73732	2	4
F_4	0.0	-2.0413	-1.4434	1.3140	0.73732	2	4
Outersphere	0.0	0.0	0.0	4.3455	0.73609	4	8
Si	0.0	0.0	0.0	1.5202	0.72751	2	4
F_1	2.3947	0.0	1.6933	1.4126	0.73732	2	4
F_2	0.0	2.3947	-1.6933	1.4126	0.73732	2	4
F_3	-2.3947	0.0	1.6933	1.4126	0.73732	2	4
F_4	0.0	-2.3947	-1.6933	1.4126	0.73732	2	4
Outersphere	-0.7428	-2.0975	0.0	5.1766	0.73192	4	7
C[b]	0.0	0.0	0.0	1.2048	0.75928	2	2
F_1	2.5105	0.0	0.0	1.3057	0.73732	2	2
F_2	-0.8380	1.1833	2.0495	1.3057	0.73732	2	2
F_3	-0.8380	1.1833	-2.0495	1.3057	0.73732	2	2
I[b]	-1.3523	-3.8188	0.0	3.3500	0.70007	2	3

a) Coordinates and sphere radii in a.u.
b) C and I spheres overlap in CF_3I.

The photoionization cross section and asymmetry parameter were calculated with the converged ground state SCF potential, modified with a Latter tail[135] to correct for large r behavior. In order to define the final state properly, the spherical harmonics were extended to higher azimuthal ℓ quantum numbers in the outersphere region, in particular. The choice of maximum ℓ values shown in Table 4.3.1-1 should provide convergence to better than a few percent. Previous studies have shown that the numerical results are sensitive to the completeness of the partial wave expansion of the continuum state.[66,85] Although the coordinates shown in Table 4.3.1-1 reflect the point group symmetry of the molecules CF_4, SiF_4, and CF_3I (namely T_d, T_d, and C_{3v}, respectively), the calculations were carried out for simplicity assuming only C_{2v}, C_{2v}, and C_s symmetry, respectively. All symmetry-allowed photoionization processes based on the dipolar selection rule were included in the calculation. The computer program of Davenport was modified by J.S. Tse to operate on the IBM 3081 computer at the computation center of the National Research Council of Canada.

4.4. Results and Discussion

4.4.1 Preamble

There have been a number of recent gas phase photoelectron studies of valence bands of polyatomic molecules using synchrotron radiation as the photon

source.[10,57,61,64,65,86-88] In these papers, valence band cross sections (σ) and/or angular distribution parameters (β) have been studied as a function of photon energy from threshold to ≈100 eV and usually compared with theoretical MS-Xα calculations. Shape resonances have been a major focus of many of these studies. Although these shape resonances can be a powerful aid in confirming the order of valence levels,[10,64,65,68] the understanding of the positions and intensities of these resonances is still very incomplete (see, e.g., a discussion of SF_6 results[65]).

Using monochromatized synchrotron radiation, we have recently obtained the gas phase valence band photoelectron spectra of a number of inorganic and organic molecules.[68,69,88] In this section, we report our detailed experimental and theoretical studies for SiF_4 and CF_3I. These results are compared and contrasted with those for the analog CF_4.[61]

SiF_4 is an excellent molecule for such a synchrotron study, for several reasons. First, we would expect intense shape resonances on the photoelectron valence peaks because intense shape resonances have been confirmed above the Si 2p edge in the absorption spectrum of SiF_4[89-91] and other silicon compounds.[4,92] There is still disagreement on the theoretical interpretation of the photoabsorption resonance features,[4,93-95] which should make the expectedly more complex valence band resonance features[65,91] of considerable theoretical interest. The most recent

assignment identifies the two resonant features at ~5 and ~22 eV above threshold[94,95] to mostly 2p → e(d) and 2p → t_2(d) channels respectively, as initially suggested by Dehmer.[4] These latest calculations, however, give fewer resonance features than in a previous theoretical study.[93] Furthermore, they fail to explain the A' shoulder in the Si 2p photoabsorption spectrum which was initially assigned to a 2p → a_1 channel.[93] Our second objective was to provide an unambiguous assignment of the valence band spectrum. The assignment of the five valence band peaks[96,97] of SiF_4 have been widely debated,[98] but more recent experimental[99-101] and theoretical results strongly favor the orbital assignment:[96] $1t_1 < 5t_2 < 1e < 4t_2 < 5a_1$, in order of increasing binding energy. Finally, a comparative study of the σ and β for SiF_4 and the close analog CF_4, should lead to a better understanding of the physical nature of the resonance features.

In addition to SiF_4, trifluoroiodomethane (CF_3I) was deemed to be a good candidate for study by synchrotron radiation. Only very recently was the He I and He II photoelectron spectra of this compound measured by Cvitaš et al.[102] This study found that the intensity of the iodine lone pair (4e) decreased, while the relative intensity of the fluorine lone pairs (3e + $1a_2$) relative to the C-I bonding molecular orbital ($4a_1$) increased in going from He I to He II radiation. To the best of our knowledge, this particular molecule has not been studied

using synchrotron radiation. However, related electron impact or synchrotron studies have been carried out on the C 1s, I 4d, and I 4p core levels in CH_3I.[103,104] Recently, Carlson et al.[87] measured the partial cross sections and angular distribution factors for ionization from the first three valence bands of CH_3I (forming the 1 ^2E, 1 ^2A, and 2 ^2E states), discussing their behavior in terms of the Cooper minimum. Unfortunately, theoretical calculations for CH_3I were not presented in this study. It is hoped that a comparative study of the partial cross section and branching ratio behavior for the valence band of CF_3I with the close analog CF_4, will lead to a better understanding of how ligand substitution (i.e. iodine for fluorine) and the resulting lowering of symmetry, affects the photoionization dynamics.

4.4.2 CF_4

Shortly after completion of our experimental work, experimental[61] and theoretical[105] σ and β were published for CF_4 by Carlson.[61] Our theoretical σ results are in quantitative agreement with those of Stephens et al.[105] However, our β values tend to be shifted significantly to lower values. The differences in theoretical β values are probably due to the larger ℓ values used in our calculation. It is well known that the asymmetry parameter β is much more sensitive than σ to the completeness of the partial wave expansion of the final state.[13]

It seems appropriate first to compare these experimental and theoretical σ and β values for CF_4. Our theoretical σ, branching ratio, and β values for the $1t_1$, $4t_2$, $1e$, $3t_2$, and $4a_1$ molecular orbitals of CF_4 are shown in Figures 4.4.2-(1-5). These can be compared directly with those of Carlson et al.[61] For the $1t_1$ orbital (majority F 2p lone pair), our theoretical and experimental σ values agree quantitatively with those given by Carlson (Table 4.4.2-1). Our theoretical β results, although in good qualitative agreement with the previous trend in β,[105] are shifted to lower values, e.g. by ~0.7 at a photon energy of 20 eV, to ~0.2 at 40 eV photon energy. Our theoretical β values are in considerably better agreement with experiment.[61] Similar trends are found for the $4t_2$ molecular orbital (majority F 2p lone pair). The theoretical and experimental σ values are once again in quantitative agreement with the published results[61] (Table 4.4.2-1). Our theoretical β values are again slightly lower than Stephens et al.,[105] giving slightly worse agreement with the experimental values up to ~30 eV photon energy, but slightly better agreement above 30 eV.

It is interesting to note that the theoretical and observed branching ratios are in much better agreement generally than are the theoretical and observed partial cross sections (Figures 4.4.2-(1,5)). This is due to the poor agreement between theoretical and observed total cross sections. For example, at 30 eV photon energy, the total

Figure 4.4.2-1

Experimental and theoretical MS-Xα (solid lines) results on the photoionization of the $1t_1$ orbital of CF_4. The upper plot gives the theoretical and experimental partial cross section in Mb, using the total cross section given by Carlson (Ref. 61). The lower energy scale is in terms of photon energy, while the upper scale gives the photoelectron kinetic energy. For a direct comparison of our σ values with those of Carlson (Ref. 61), see Table 4.4.2-1. The middle plot gives the theoretical and experimental branching ratios, while the bottom plot gives the theoretical β values.

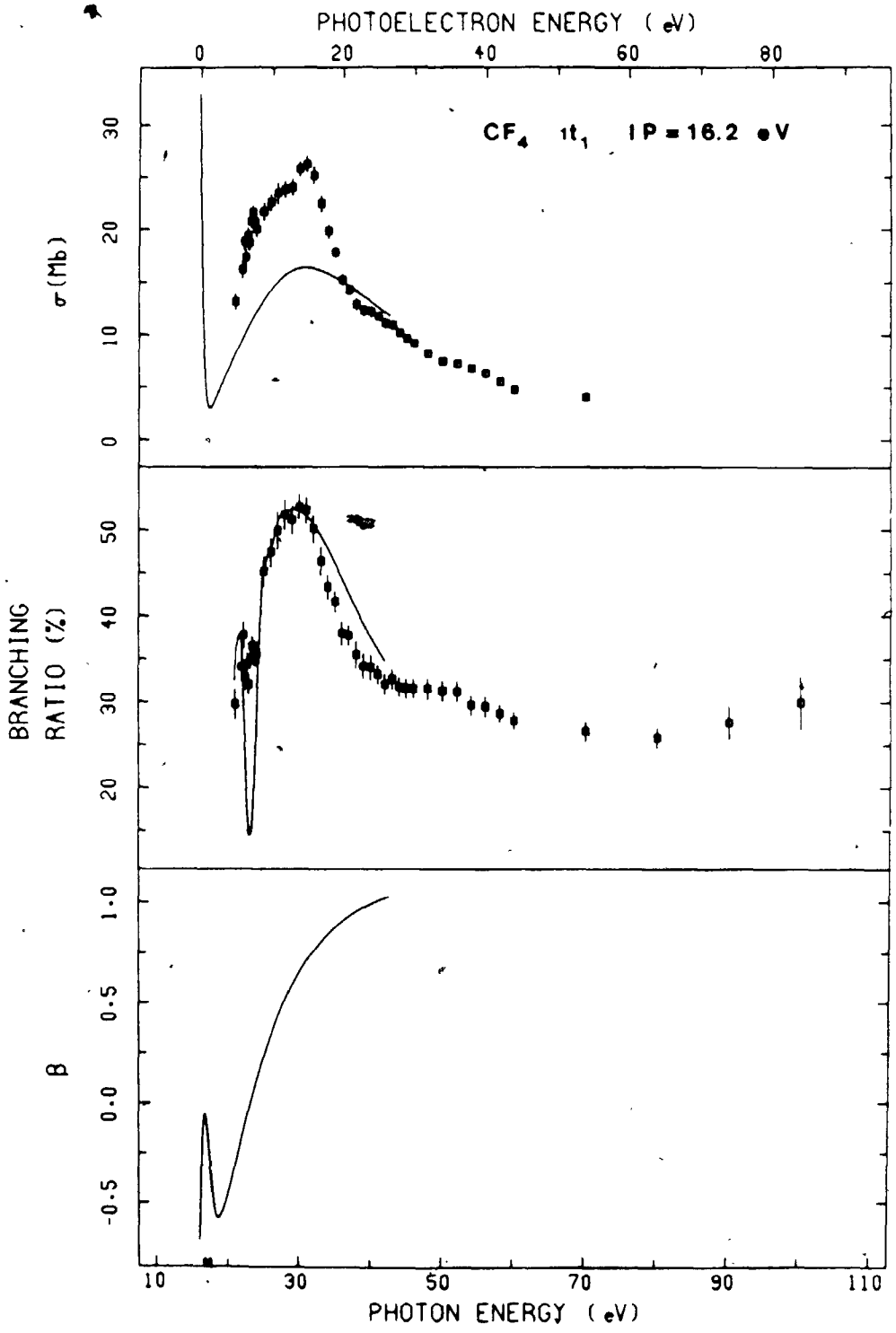
PHOTOELECTRON ENERGY (eV)
0
20
40
60
80
CF_4 $1t_1$ IP = 16.2 eV
σ(Mb)
0
10
20
30
BRANCHING RATIO (%)
20
30
40
50
β
-0.5
0.0
0.5
1.0
10
30
50
70
90
110
PHOTON ENERGY (eV)

Figure 4.4.2-2

Experimental and theoretical MS-Xα (solid lines) results on the photoionization of the $4t_2$ orbital of CF_4. For a direct comparison of our σ values with those of Carlson (Ref. 61), see Table 4.4.2-1. The upper, middle, and bottom plots give the σ, branching ratio, and β values, respectively.

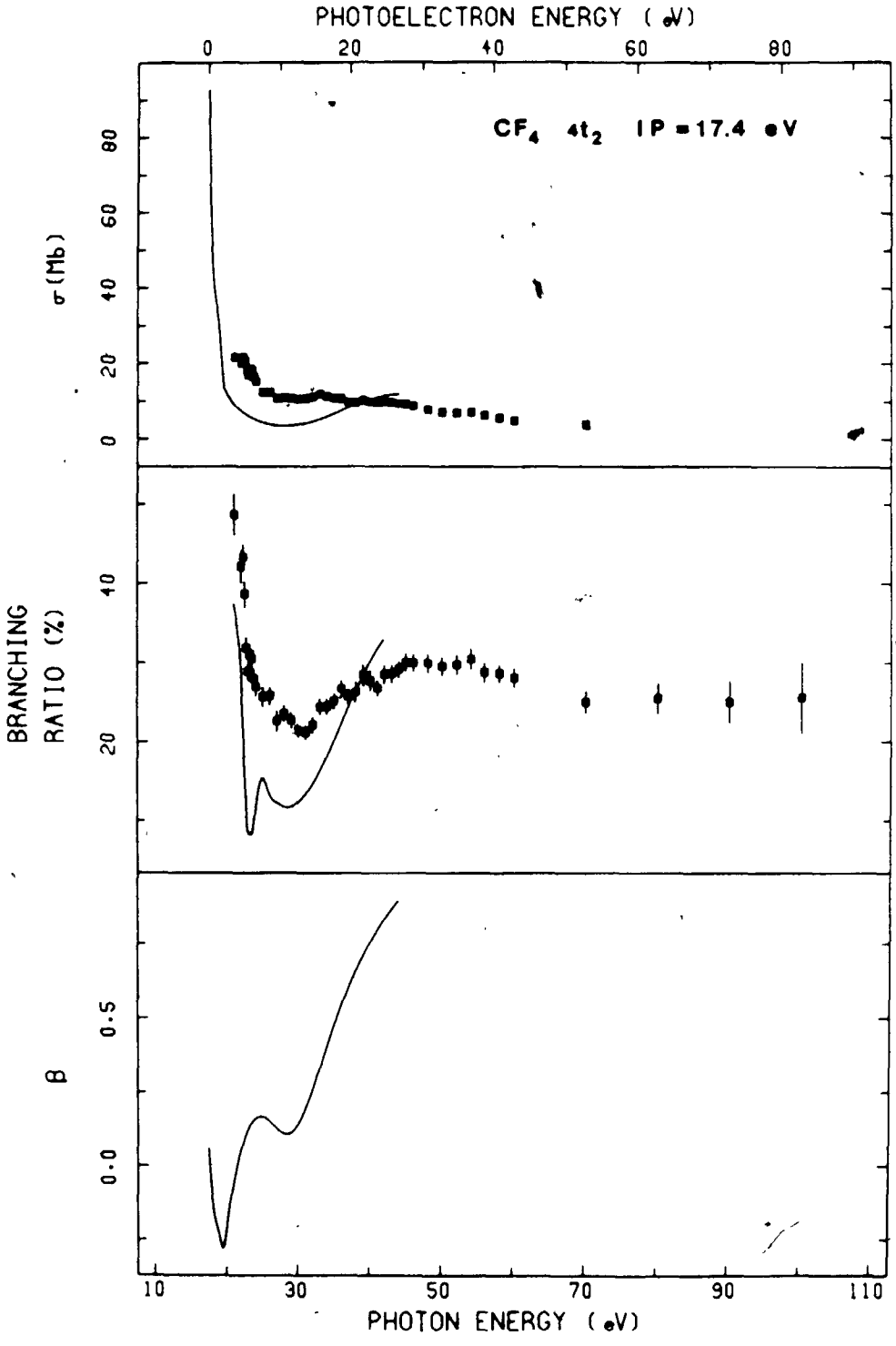
PHOTOELECTRON ENERGY (eV)
0
20
40
60
80
CF4 4t2 IP = 17.4 eV
σ (Mb)
0
20
40
60
80
BRANCHING RATIO (%)
20
40
β
0.0
0.5
10
30
50
70
90
110
PHOTON ENERGY (eV)

Figure 4.4.2-3

Experimental and theoretical MS-Xα (solid lines) results on the photoionization of the $1t_2$ orbital of CF_4. The upper, middle, and bottom plots give the σ, branching ratio, and β values, respectively.

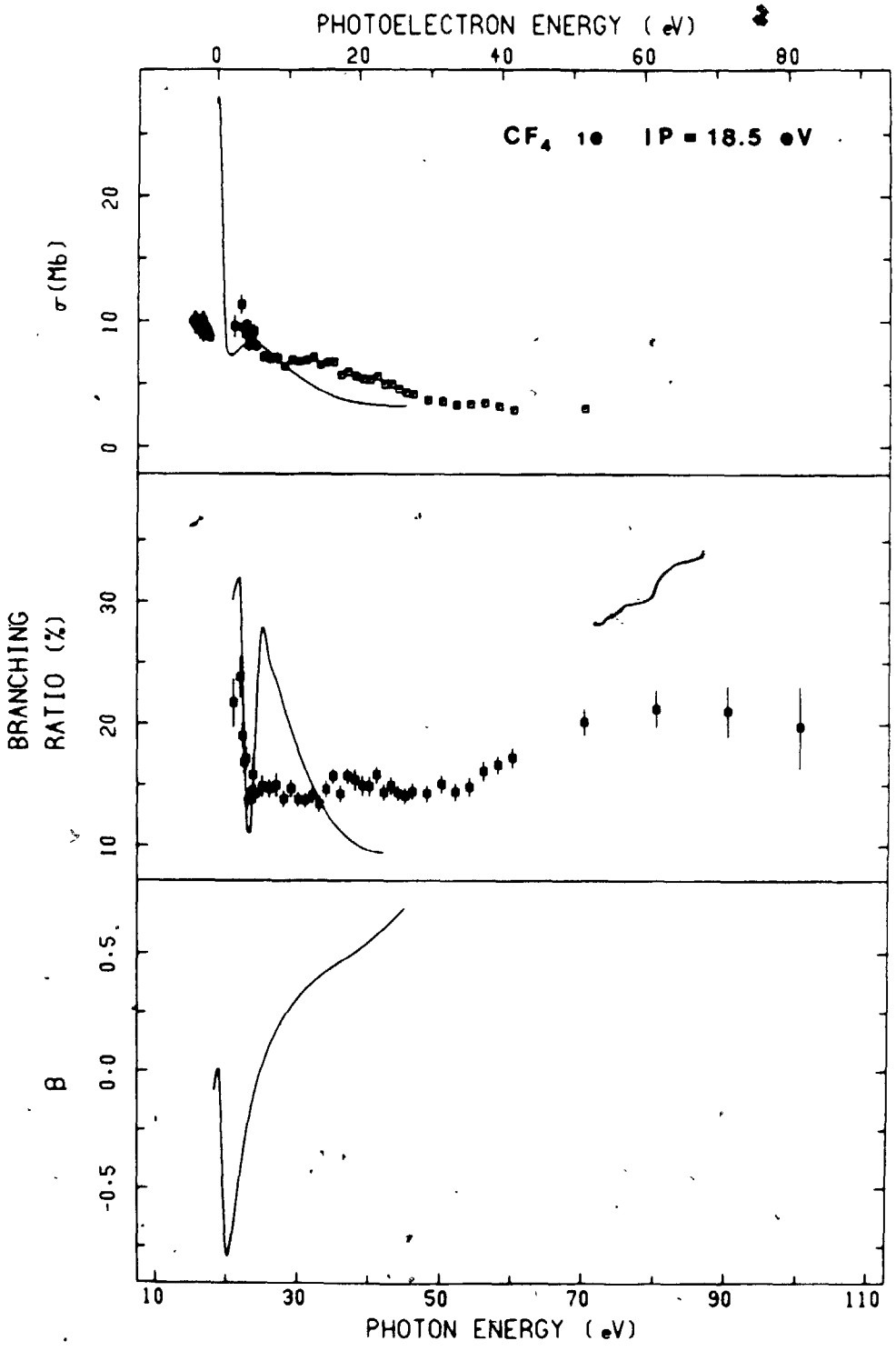
PHOTOELECTRON ENERGY (eV)
0
20
40
60
80
CF4 1e IP = 18.5 eV
σ(Mb)
20
10
0
BRANCHING RATIO (%)
30
20
10
β
0.5
0.0
-0.5
10
30
50
70
90
110
PHOTON ENERGY (eV)

Figure 4.4.2-4

Experimental and theoretical MS-Xα (solid lines) results on the photoionization of the $3t_2$ orbital of CF_4. The upper, middle, and bottom plots give the σ, branching ratio, and β values, respectively.

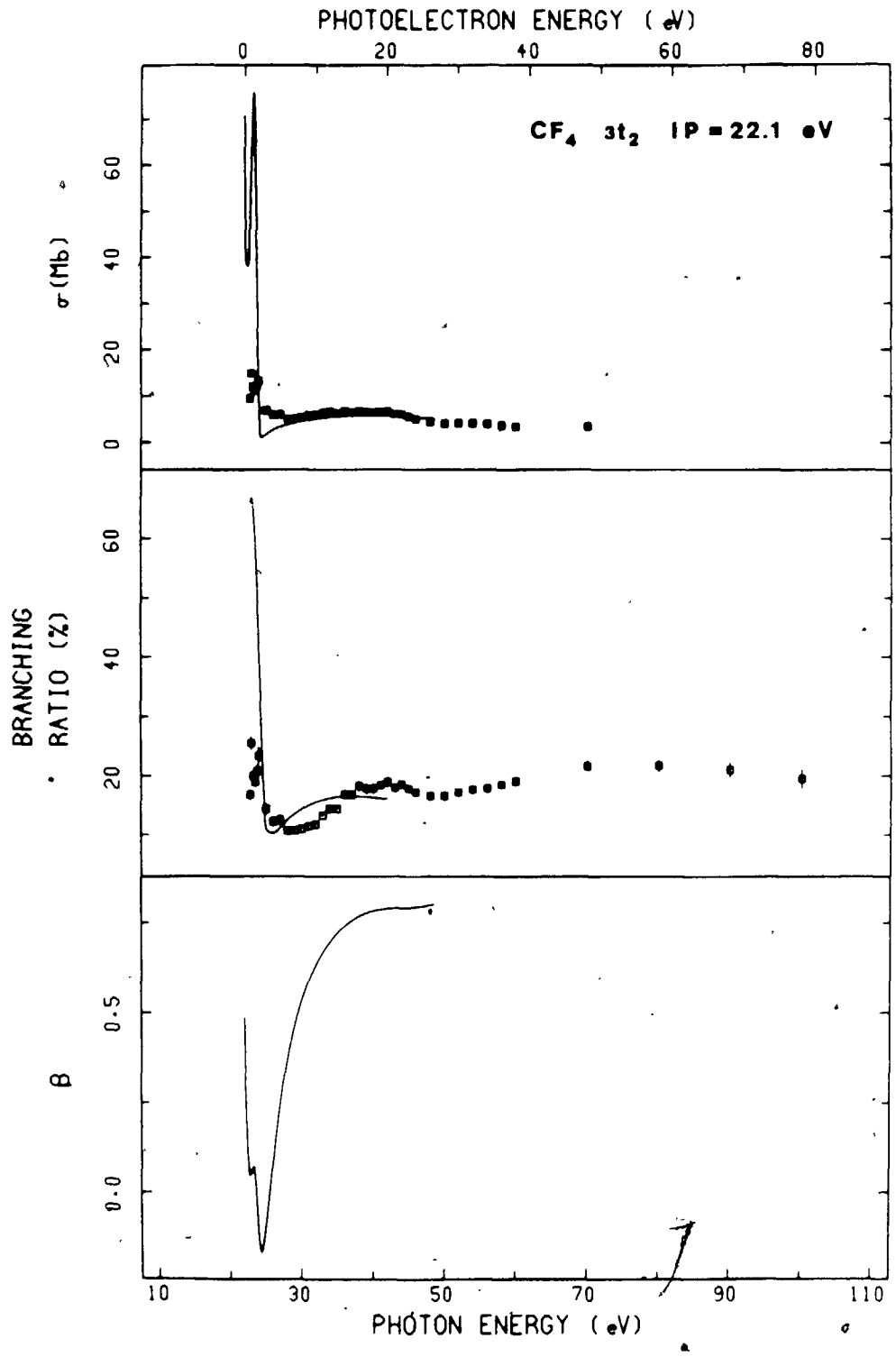
PHOTOELECTRON ENERGY (eV)
0
20
40
60
80
CF4 3t2 IP = 22.1 eV
σ(Mb)
0
20
40
60
BRANCHING RATIO (%)
0
20
40
60
β
0.0
0.5
10
30
50
70
90
110
PHOTON ENERGY (eV)

Figure 4.4.2-5

Experimental and theoretical MS-Xα (solid lines) results on the photoionization of the $4a_1$ orbital of CF_4. The upper, middle, and bottom plots give the σ, branching ratio, and β values, respectively.

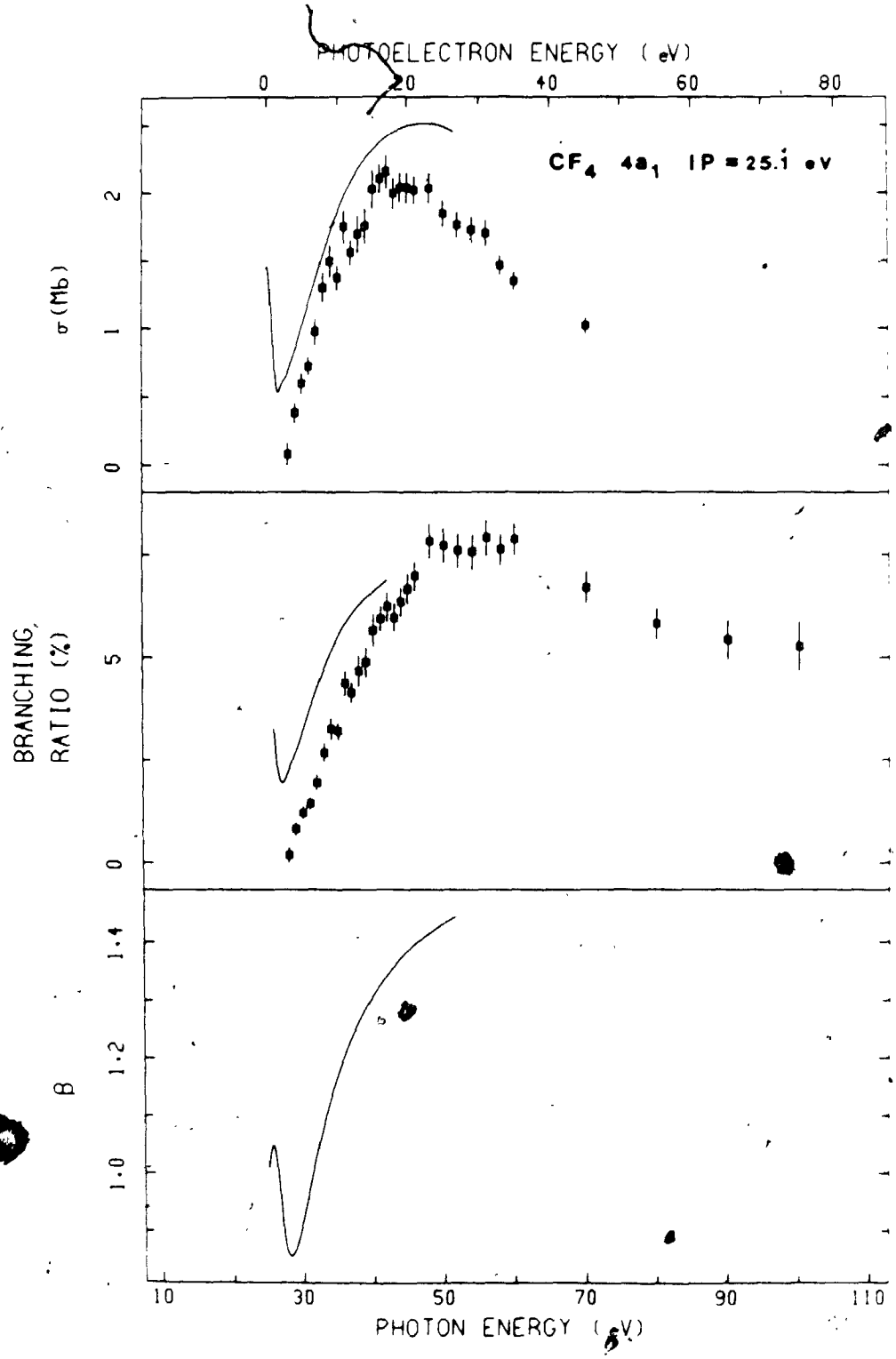
PHOTOELECTRON ENERGY (eV)
0
20
40
60
80
CF4 4a1 IP = 25.1 eV
σ (Mb)
2
1
0
BRANCHING RATIO (%)
5
0
β
1.4
1.2
1.0
10
30
50
70
90
110
PHOTON ENERGY (eV)

Table 4.4.2-1.

Experimental Partial Cross Sections for the $1t_1$ and $4t_2$ Molecular Orbitals of CF_4

	$1t_1$		$4t_2$	
hν(eV)	This work[a]	Ref. 61	This work[a]	Ref. 61
21.2	13.8±0.8	14.0±1.4	21.2±1.2	22.0±2.2
22	16.2±0.8	16.7±1.7	20.0±1.0	19.5±2.0
23	18.7±0.7	18.6±1.9	16.9±0.6	17.8±1.8
24	20.1±0.8	19.6±2.0	15.1±0.6	14.7±1.5
25	21.7±0.8	19.5±2.0	12.3±0.6	11.8±1.2
26	22.6±0.8	21.0±2.1	12.3±0.5	11.6±1.2
28	23.9±0.8	22.0±2.2	10.9±0.5	10.3±1.0
30	25.8±0.7	24.2±2.4	10.5±0.4	11.0±1.1
32	25.2±0.8	23.4±2.3	11.1±0.5	11.4±1.1
34	19.8±0.7	18.8±1.9	11.2±0.5	12.0±1.2
36	15.2±0.6	14.4±2.2	10.7±0.4	10.9±1.5
38	12.9±0.6	11.9±1.8	9.5±0.5	10.1±1.5
40	12.2±0.5	11.3±1.7	9.9±0.5	10.2±1.5
45	9.6±0.4	9.9±1.5	9.2±0.4	9.1±1.4
50	7.5±0.3	7.6±1.1	7.1±0.3	7.2±1.1
55	6.5±0.3	6.8±1.0	6.5±0.3	6.5±1.0
60	4.8±0.2	4.8±0.7	4.8±0.2	5.1±0.8
65	4.4±0.2	4.3±0.6	4.3±0.2	4.3±0.6
70	4.0±0.2	4.2±0.8	3.8±0.2	4.0±0.8

a) Using the total cross sections determined in Ref. 61.

theoretical cross section (31.0 Mb) is much lower than the experimental value (49.0 Mb),[61] and thus the theoretical $1t_1$ partial cross section is ~37% smaller than the experimental value.

For the three remaining molecular orbitals of 1e (majority F 2p lone pair), $3t_2$ (bonding), and $4a_1$ (bonding), our theoretical and experimental cross sections are in quantitative agreement with those published previously.[61,105] While our calculated β values are somewhat lower than Stephens et al.[105] for the 1e orbital, quantitative agreement was found for the $3t_2$ and $4a_1$ bonding orbitals. It is interesting to note that theoretical β values for the $4a_1$ orbital are only in qualitative agreement with experiment. The calculated β values are still much larger than the experimental values, by at least 0.5 units. A further discrepancy of ~5 eV occurs between the theoretical and experimental β value minima positions.

As reported by Carlson,[61] the MS-Xα method appears to give reasonable predictions regarding the overall behaviour of cross sections and β. The agreement for branching ratios is generally considerably better, as noted previously. In CF_4, very little structure was found in either σ or β, although experimental evidence seems to indicate a shape resonance at approximately 2-3 eV kinetic energy. As shall be discussed in section 4.4.3, this is in

sharp contrast to SiF_4, which exhibits shape resonances far into the continuum.

4.4.3 SiF_4

The theoretical σ values, theoretical and experimental branching ratios (BR), and theoretical β values for the first five valence photoelectron peaks of SiF_4 (Figure 4.2.1-2) are shown in Figures 4.4.3-(1-6). Unfortunately, the total photoionization cross section for SiF_4 is not known in this energy range, so that the experimental branching ratios could not be converted to partial cross sections. In order to facilitate the conversion when such data becomes available, the experimental branching ratios are presented in Table 4.4.3-1. Instead, the experimental branching ratios were compared against theoretical branching ratios, calculated from the theoretical partial cross sections. Since both of these branching ratios neglect the weak F 2s orbital cross section contribution, they are directly comparable. Comparison of the branching ratios instead of the partial cross sections has the advantage noted above; and also that it is independent of photodissociation effects, which can be spuriously introduced when correction is made to the photoabsorption data.

In general, there is rather good agreement between the theoretical and experimental branching ratios, at least as good agreement as for other molecules in the

Figure 4.4.3-1

Experimental and theoretical MS-Xa (solid lines) results on the photoionization of the $1t_1$ orbital of SiF_4. The upper, middle, and bottom plots give the σ, branching ratio, and β values, respectively. The predicted shape resonances are numbered in the upper plot of σ, while the observed shape resonances are numbered in the middle branching ratio plot (see the text and Table 4.4.3-2).

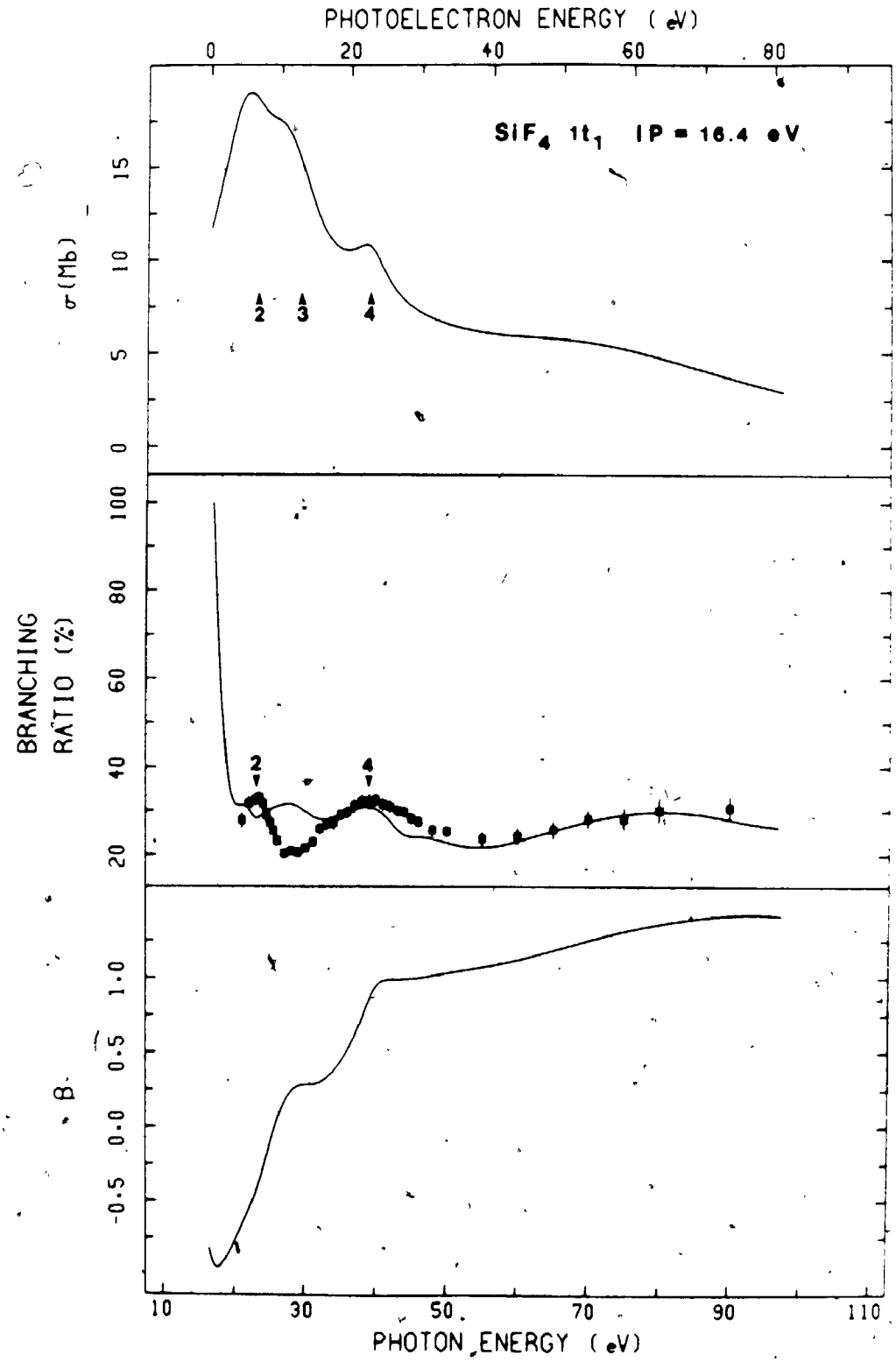
PHOTOELECTRON ENERGY (eV)
0
20
40
60
80
SiF4 1t1 IP = 16.4 eV
σ(Mb)
15
10
5
0
2
3
4
BRANCHING RATIO (%)
100
80
60
40
20
2
4
β
1.0
0.5
0.0
-0.5
10
30
50
70
90
110
PHOTON ENERGY (eV)

Figure 4.4.3-2

Experimental and theoretical MS-Xa (solid lines) results on the photoionization of the $5t_2$ orbital of SiF_4. The upper, middle, and bottom plots give the σ, branching ratio, and β values, respectively. The predicted shape resonances are numbered in the upper plot of σ, while the observed shape resonances are numbered in the middle branching ratio plot (see the text and Table 4.4.3-2).

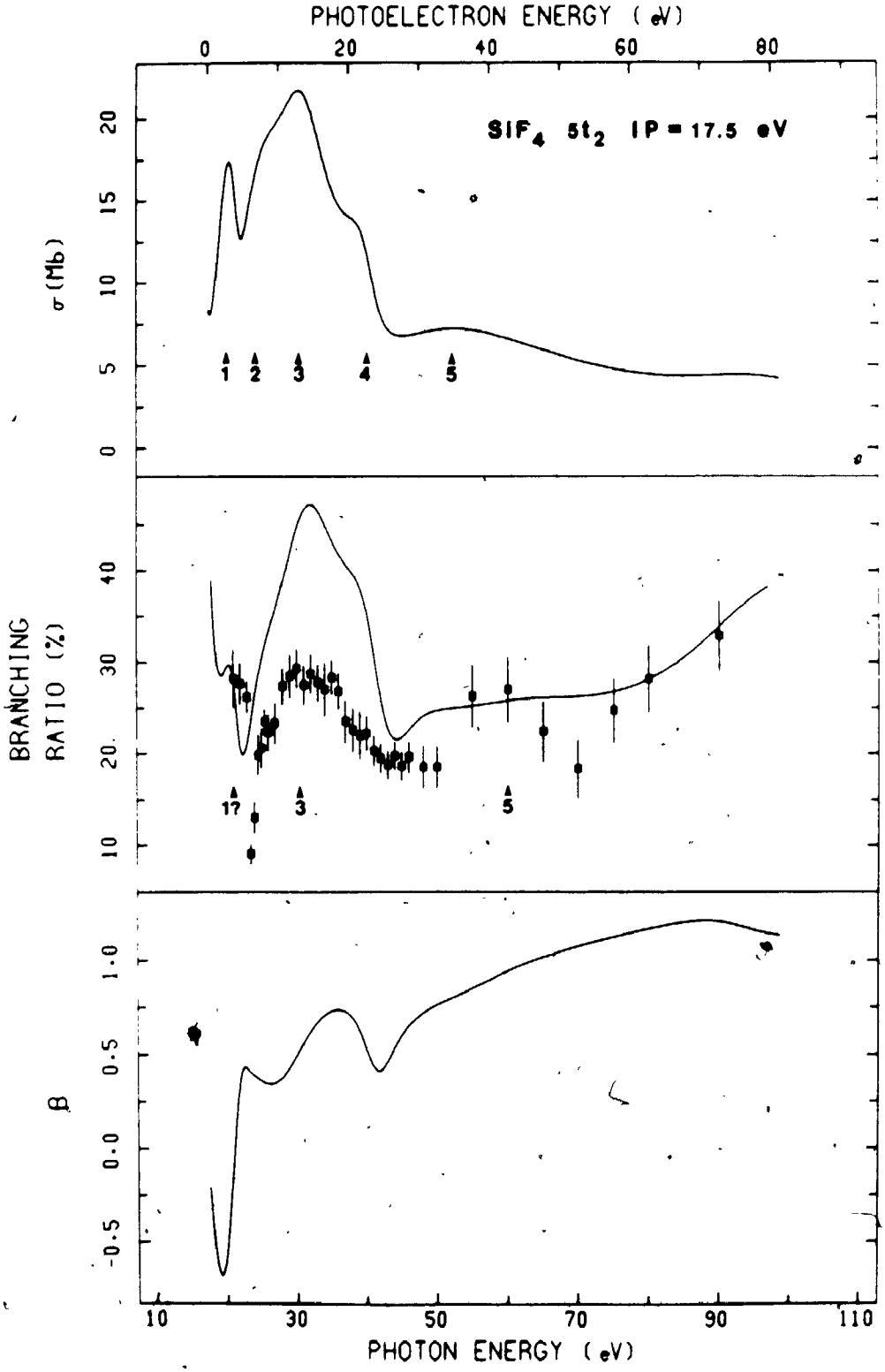
PHOTOELECTRON ENERGY (eV)
0
20
40
60
80
SIF4 5t2 IP = 17.5 eV
σ (Mb)
0
5
10
15
20
1
2
3
4
5
BRANCHING RATIO (%)
10
20
30
40
1?
3
5
β
-0.5
0.0
0.5
1.0
10
30
50
70
90
110
PHOTON ENERGY (eV)

Figure 4.4.3-3

Experimental and theoretical MS-Xa (solid lines) results on the photoionization of the 1e orbital of SiF_4. The upper, middle, and bottom plots give the σ, branching ratio, and β values, respectively. The predicted shape resonances are numbered in the upper plot of σ, while the observed shape resonances are numbered in the middle branching ratio plot (see the text and Table 4.4.3-2).

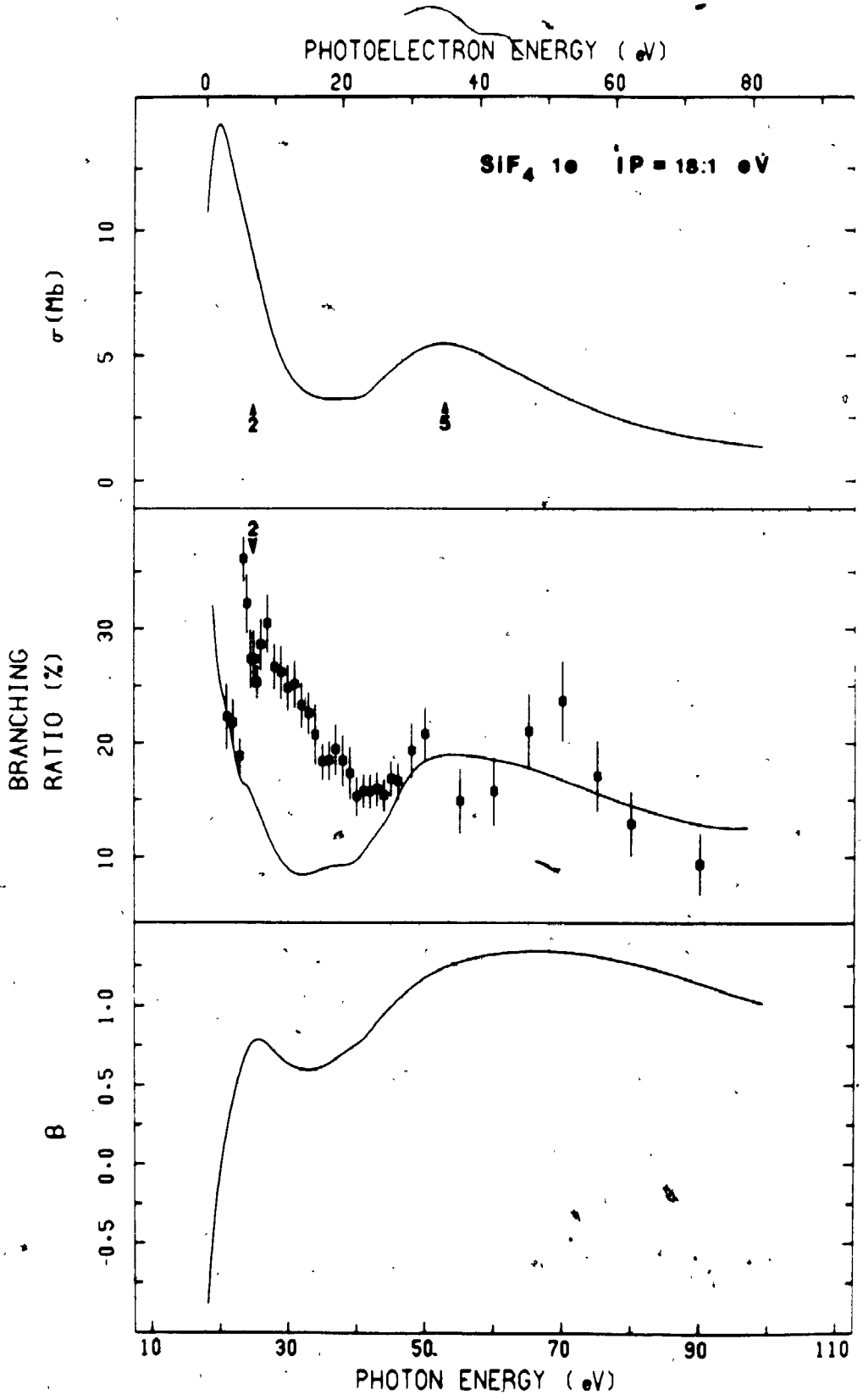
PHOTOELECTRON ENERGY (eV)
0
20
40
60
80
SiF4 1e IP = 18.1 eV
σ(Mb)
10
5
0
2
2
5
BRANCHING RATIO (%)
30
20
10
2
β
1.0
0.5
0.0
-0.5
10
30
50
70
90
110
PHOTON ENERGY (eV)

Figure 4.4.3-4

Experimental and theoretical MS-Xa (solid lines) results on the photoionization of the 1e and $5t_2$ orbitals of SiF_4. The upper, middle, and bottom plots give the σ, branching ratio, and β values, respectively. The predicted shape resonances are numbered in the upper plot of σ, while the observed shape resonances are numbered in the middle branching ratio plot (see the text and Table 4.4.3-2).

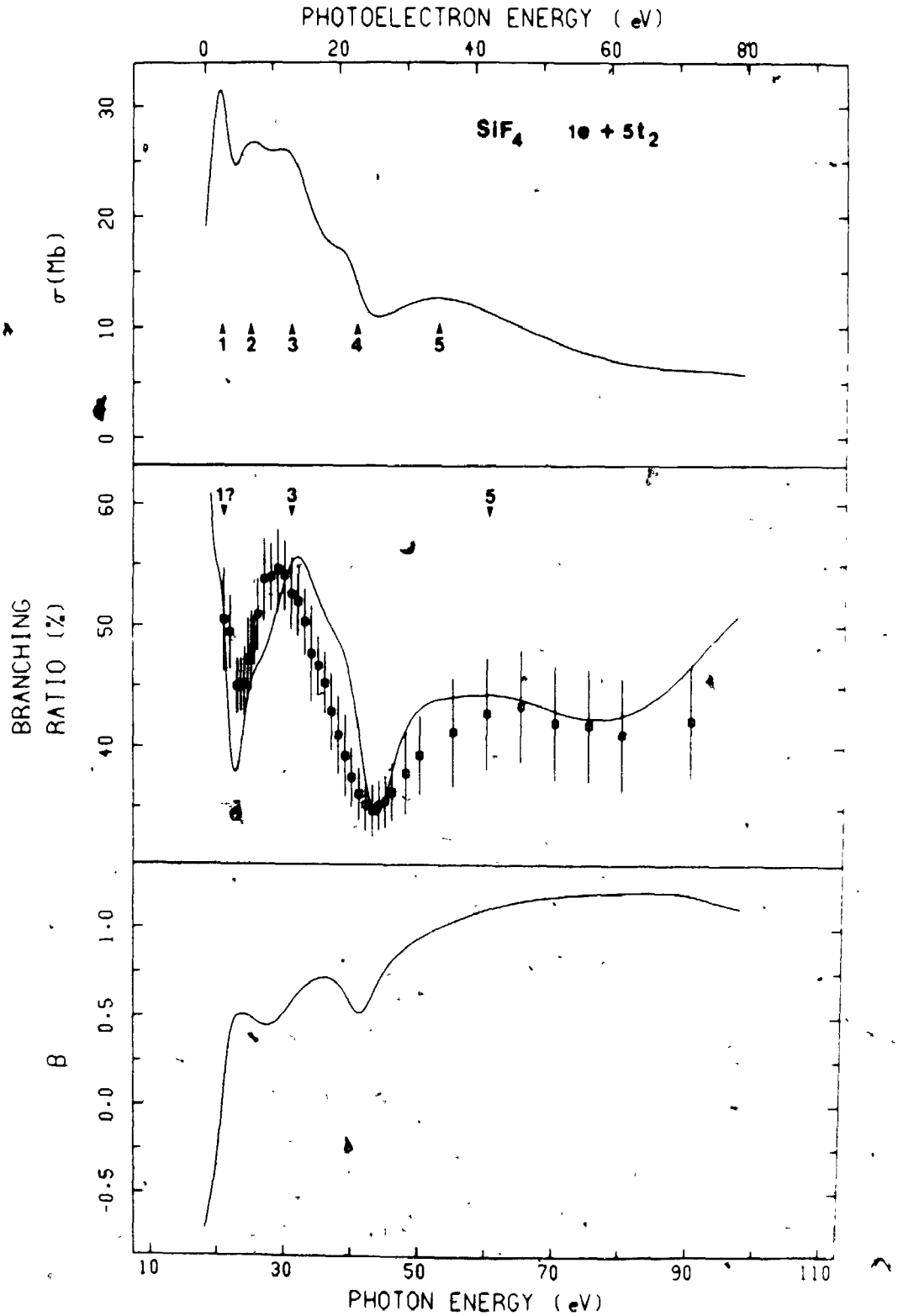
PHOTOELECTRON ENERGY (eV)
0
20
40
60
80
SiF4 1e + 5t2
σ(Mb)
30
20
10
0
1
2
3
4
5
BRANCHING RATIO (%)
60
50
40
1?
3
5
β
1.0
0.5
0.0
-0.5
10
30
50
70
90
110
PHOTON ENERGY (eV)

Figure 4.4.3-5

Experimental and theoretical MS-Xa (solid lines) results on the photoionization of the $4t_2$ orbital of SiF_4. The upper, middle, and bottom plots give the σ, branching ratio, and β values, respectively. The predicted shape resonances are numbered in the upper plot of σ, while the observed shape resonances are numbered in the middle branching ratio plot (see the text and Table 4.4.3-2).

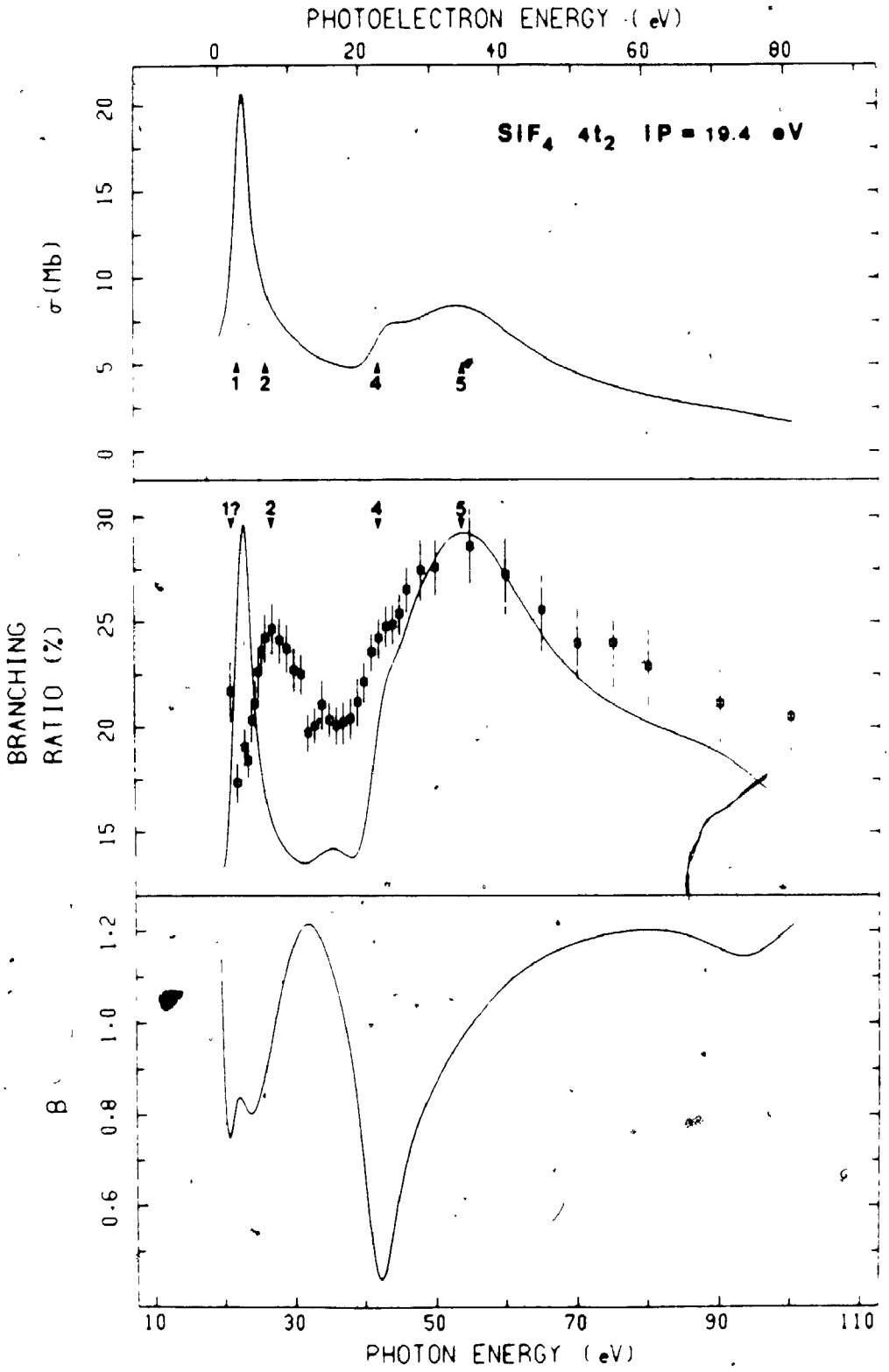
PHOTOELECTRON ENERGY (eV)
0
20
40
60
80
SiF4 4t2 IP = 19.4 eV
σ(Mb)
0
5
10
15
20
1
2
4
5
BRANCHING RATIO (%)
15
20
25
30
1?
2
4
5
β
0.6
0.8
1.0
1.2
10
30
50
70
90
110
PHOTON ENERGY (eV)

Figure 4.4.3-6

Experimental and theoretical MS-Xa (solid lines) results on the photoionization of the $5a_1$ orbital of SiF_4. The upper, middle, and bottom plots give the σ, branching ratio, and β values, respectively. The predicted shape resonances are numbered in the upper plot of σ, while the observed shape resonances are numbered in the middle branching ratio plot (see the text and Table 4.4.3-2).

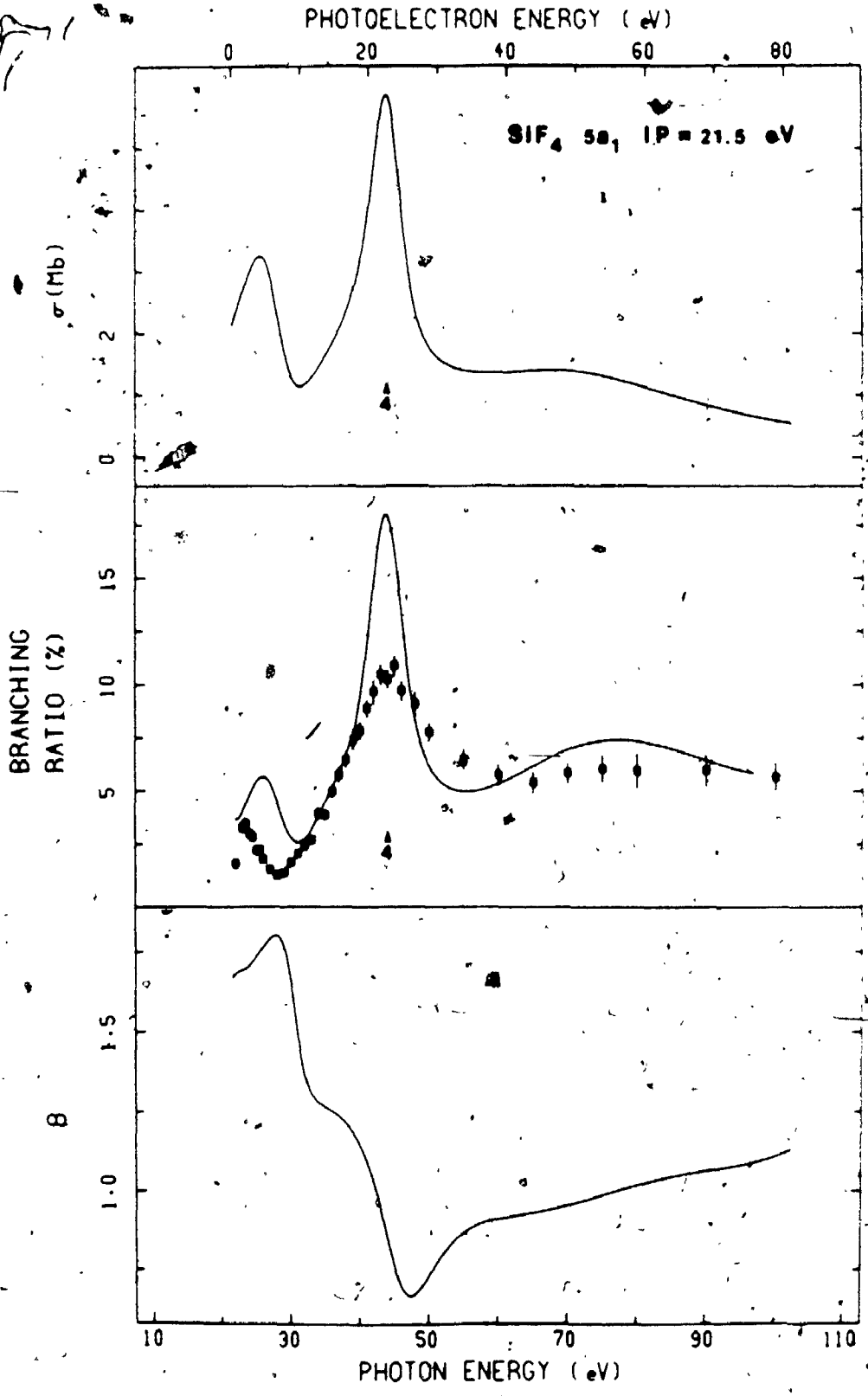
PHOTOELECTRON ENERGY (eV)
0
20
40
60
80
SiF4 5a1 I.P = 21.5 eV
σ(Mb)
2
0
BRANCHING RATIO (%)
15
10
5
β
1.5
1.0
10
30
50
70
90
110
PHOTON ENERGY (eV)

Table 4.4.3-1

Branching Ratios for Valence Orbitals of SiF_4 as a Function of Photon Energy

hν(eV)	$1t_1$ BR	$5t_2$ BR[a)]	1e BR[a)]	$4t_2$ BR	$5a_1$ BR
21.0	27.8±1.7	28.2±3.1	22.3±2.9	21.7±1.4	
22.0	31.7±1.5	27.7±2.2	21.8±2.1	17.4±1.0	1.6±0.2
23.0	32.7±1.4	26.2±1.7	18.8±1.5	19.1±0.9	3.3±0.3
23.5	33.0±1.3	9.0±1.1	36.1±1.9	18.4±0.8	3.5±0.3
24.0	31.6±1.5	13.0±1.8	32.2±2.6	20.3±1.0	3.0±0.3
24.5	28.9±1.4	19.9±2.2	27.3±2.6	21.1±1.1	2.8±0.2
25.0	27.2±1.4	20.6±2.2	27.3±2.5	22.6±1.2	2.2±0.2
25.5	25.4±0.9	23.5±1.4	25.3±1.4	23.6±0.9	2.2±0.2
26.0	23.1±1.1	22.3±2.0	28.6±2.2	24.2±1.1	1.8±0.2
27.0	20.3±1.0	23.3±2.3	30.4±2.5	24.7±1.2	1.3±0.2
28.0	20.9±1.0	27.4±2.0	26.6±2.0	24.1±1.1	1.0±0.1
29.0	20.5±1.0	28.5±2.4	26.2±2.3	23.7±1.2	1.2±0.1
30.0	21.5±1.0	29.3±2.1	24.8±2.0	22.7±1.0	1.6±0.2
31.0	22.8±1.0	27.5±2.1	25.1±2.0	22.5±1.0	2.0±0.2
32.0	25.9±1.2	28.7±2.1	23.3±1.9	19.8±0.9	2.4±0.2
33.0	26.9±1.2	27.7±2.0	22.6±1.9	20.1±0.9	2.7±0.2
34.0	27.3±1.5	27.0±3.0	20.7±2.7	21.1±1.2	3.9±0.3
35.0	29.1±1.1	28.3±1.9	18.3±1.6	20.4±0.8	3.9±0.2
36.0	29.7±1.3	26.8±2.0	18.4±1.7	20.1±0.9	5.0±0.3
37.0	31.1±1.5	23.5±2.4	19.4±2.2	20.2±1.1	5.8±0.4
38.0	32.1±1.5	22.6±2.4	18.4±2.2	20.4±1.0	6.5±0.4
39.0	32.1±1.7	21.9±2.5	17.3±2.3	21.2±1.2	7.4±0.5
40.0	32.5±1.4	22.2±1.9	15.3±1.7	22.2±1.0	7.8±0.4
41.0	31.4±1.2	20.3±1.6	15.8±1.5	23.6±0.9	8.9±0.4
42.0	30.9±1.2	19.5±1.6	15.7±1.5	24.3±1.0	9.7±0.6
43.0	30.0±1.2	18.8±1.6	16.0±1.5	24.8±1.0	10.5±0.5
44.0	29.7±1.1	19.8±1.5	15.4±1.4	24.9±1.0	10.2±0.5
45.0	28.2±1.1	18.6±1.6	16.9±1.5	25.4±1.0	10.9±0.5
46.0	27.5±1.1	19.6±1.7	16.6±1.6	26.6±1.1	9.7±0.5
48.0	25.6±1.4	18.5±2.3	19.3±2.4	27.5±1.5	9.1±0.6
50.0	25.3±1.3	18.5±2.3	20.8±2.4	27.6±1.3	7.8±0.5
55.0	23.7±1.6	26.3±3.5	14.9±2.8	28.6±1.8	6.5±0.5
60.0	24.2±1.8	27.0±3.6	15.8±3.0	27.3±1.9	5.8±0.5
65.0	25.7±2.0	22.4±3.3	21.0±3.2	25.6±2.0	5.4±0.5
70.0	28.2±1.9	18.4±3.2	23.7±3.5	24.0±1.7	5.8±0.5
75.0	28.2±2.5	24.7±3.5	17.1±3.1	24.0±2.1	6.0±0.7
80.0	30.1±2.7	28.2±3.7	12.9±2.8	22.9±1.9	5.9±0.8
90.0	30.7±2.7	32.8±3.9	9.4±2.7	21.1±1.9	6.0±0.8
100.0	30.3±2.8	12.2±3.2	31.4±3.6	20.5±1.7	5.7±0.7

a) As discussed in the text, the larger uncertainty of the experimental data at photon energies >50 eV is due to strong overlap of the $5t_2$ and 1e peaks. At such photon energies the use of their BR sum is more meaningful.

Table 4.4.3-2

Energies and Widths of Resonances from MS-Xa Calculations and Experiment[a] for SiF_4

MO	Transition	Resonance Number	MS Results[b] E_{phase}(eV)	Δ(Eigenphase Sum)	Resonance Width(eV)	E_{cross}(eV)	Experimental Results $E_{resonance}$(eV)	Resonance Width(eV)
$1t_1$	$1t_1 \rightarrow kt_2$	2	6.8w	0.28π[c]	5.3	d	7.1	~5
	$1t_1 \rightarrow ke$	3	12.9m	0.61π	8.3	10.5m	-	-
	$1t_1 \rightarrow kt_2$	4	22.6s	0.47π	5.9	22.1w	22.6	13
$5t_2$	$5t_2 \rightarrow ka_1$	1	2.7s	0.70π	2.4	3.3s	≤2?	-
	$5t_2 \rightarrow kt_2$	2	6.8w	0.28π[c]	5.3	7.4m	e	-
	$5t_2 \rightarrow ke$	3	12.9m	0.61π	8.3	13.1s	11.2	~9
	$5t_2 \rightarrow kt_2$	4	22.6s	0.47π	5.9	22.8w	e	-
	$5t_2 \rightarrow kt_2$	5	34.6w	~1π	~18	34.8w	42	~25
1e	$1e \rightarrow kt_2$	2	6.8w	0.28π[c]	5.3	d	~7	~7
	$1e \rightarrow kt_2$	5	34.6w	~1π	~18	34.8w	42	-
$4t_2$	$4t_2 \rightarrow ka_1$	1	2.7s	0.70π	2.4	3.3s	≤2?	-
	$4t_2 \rightarrow kt_2$	2	6.8w	0.28π[c]	5.3	d	7.6	7
	$4t_2 \rightarrow kt_2$	4	22.6s	0.47π	5.9	22.9w	22.6	8
	$4t_2 \rightarrow kt_2$	5	34.6w	~1π	~18	33.8m	35.6	~24
$5a_1$	$5a_1 \rightarrow kt_2$	4	22.6s	0.47π	5.9	21.8s	22.6	~14

a) See text for definitions.
b) Classification: strong (s), medium (m), weak (w).
c) Weak feature, borderline case.
d) Feature not intense enough to define a resonance energy.
e) Resonance may be present but probaly masked by the strong e channel resonance at 11.2 eV kinetic energy.

literature.[10,57,61,64,65,86-88] This agreement confirms the assignment of the valence peaks which appears to be generally accepted as $1t_1 < 5t_2 < 1e < 4t_2 < 5a_1$, in order of increasing binding energy. An earlier assignment[97] based on CNDO/2 calculations, $1t_1 < 5t_2 < 5a_1 < 1e < 4t_2$, can be ruled out rather quickly. From our results, it is evident that the $5a_1$ orbital must be the highest binding energy valence band orbital. As predicted by the MS-Xα calculations, the branching ratio (BR) for the fifth peak has a broad resonance feature near 23 eV kinetic energy, and is near 6% from 30 to 80 eV kinetic energy above threshold. In contrast, the third peak (which was assigned to $5a_1$ in the earlier assignment) has a very large BR near threshold, does not have the resonance feature near 23 eV kinetic energy, and is 15 ± 5% from 30 to 80 eV kinetic energy above threshold. Similarly, the rather rich and differing structure of the BR plots for different molecular orbitals puts the valence band assignment for SiF_4 on a very firm basis. The ordering of molecular orbitals in SiF_4 is identical to that found in CF_4.[61]

Before discussing the resonance features in more detail, a comparison of the theoretical cross section and β values of CF_4 and SiF_4, along with a general discussion of the SiF_4 results will be made. The first three molecular orbitals in both CF_4 and SiF_4 are basically F 2p lone-pair orbitals, and thus we could expect the σ and β values for both molecules to be similar. There certainly are

qualitative similarities, but the SiF_4 plots show much more structure. SiF_4 does not show a sharp resonance feature near threshold in the $1t_1$ cross section (Figure 4.4.3-1) as is predicted for CF_4. This feature may well be shifted to a bound state for SiF_4, as indicated by the minimum at threshold in β. This may be partially a consequence of the longer M-F bond length (M = C,Si) in SiF_4 than CF_4.[92] The broad maximum observed at a kinetic energy of ~14 eV in CF_4 is replaced by a more structured maximum in SiF_4 centered at ~7 eV kinetic energy, but the theoretical cross section maxima for both compounds is ~15 Mb before decreasing at higher kinetic energies. Similarly, the β values for both compounds are negative at threshold before rising rapidly to ~1 at higher kinetic energies. The theoretical minimum in β at about threshold in SiF_4 suggests that a shape resonance is indeed at, or below, threshold. The SiF_4 β value, while rising rapidly above threshold like CF_4, shows a very distinct minimum at about 13 eV kinetic energy, somewhat higher kinetic energy than the ~7 eV peak in σ. The agreement between the theoretical and experimental BR for SiF_4 is good, except that the experimental cross section maximum observed at 7.1 eV is theoretically not predicted by our calculation (see BR plot in Figure 4.4.3-1).

For the $5t_2$ orbital, the SiF_4 σ plot (Figure 4.4.3-2) shows much more structure than for the analogous $4t_2$ orbital in CF_4 (Figure 4.4.2-2). In particular, the

broad intense structured maximum between 5 and 25 eV kinetic energy in SiF_4, is not seen in the theoretical CF_4 calculations, although there is a broad weak maximum centered at about 18 eV kinetic energy in the observed CF_4 σ plot. Both the SiF_4 and CF_4 cross sections are about 5 Mb above 30 eV kinetic energy. Both β values show a sharp minimum at ~-0.5 just above threshold, and rise to ~+1 at higher kinetic energies. The SiF_4 theoretical values show two additional minima at ~10 and ~23 eV kinetic energy. These minima in β correspond to the theoretical σ maxima at ~13 and ~23 eV kinetic energy. For this orbital, the agreement between the observed and theoretical BR values is not quantitative, but the overall shapes of the two are certainly very similar. The sharp minimum at 5 eV kinetic energy, a broad maximum centered near 13 eV kinetic energy, and then another minimum at ~26 eV kinetic energy are reproduced fairly well by theory. The two weak shoulders in the theoretical σ plot at ~7 and ~23 eV kinetic energy cannot be readily discerned on the experimental data, but the broader width of the experimental maximum suggests the presence of two or more resonances. The larger uncertainty and scatter of the experimental data at photon energies of >50 eV is due to the strong overlap of the $5t_2$ peak with the 1e at higher photon energies.

For the 1e orbital, the maximum near threshold for SiF_4 (Figure 4.4.3-3) is not as intense or sharp as for CF_4 (Figure 4.4.2-3), but both cross sections decrease rapidly

above threshold, and are both ≤ 3 Mb at higher photon energies. In addition, a broad maximum at ~35 eV kinetic energy is present for SiF_4, but not for CF_4. Both β plots show a sharp increase above threshold with maximum values near +1 at higher kinetic energy. The SiF_4 plot shows a broad minimum in β near ~15 eV kinetic energy which does not seem to correspond to any feature in σ. The agreement between observed and calculated branching ratios is reasonable, but the theoretical BR curve is ~10% lower than the observed values and shifted somewhat to lower kinetic energy. The larger uncertainty and scatter at higher photon energies is once again due to the overlap of the 1e and $5t_2$ peaks.

The final two valence band peaks arise from the M-F (M = C, Si) bonding molecular orbitals. Therefore, differences in σ and β would be expected between SiF_4 and CF_4. On the contrary, the $4t_2$ (Figure 4.4.3-5) and $3t_2$ (Figure 4.4.2-4) σ and BR plots for SiF_4 and CF_4, respectively, do show similarities. Just above threshold, both σ plots show a rapid drop to ~5 Mb, followed by a weak broad maximum. In SiF_4, this maximum is structured, and shifted to higher kinetic energy, from ~16 eV in CF_4 to ~34 eV in SiF_4. The β values, however, for SiF_4 and CF_4 show dramatic differences. The magnitudes of the β values are very different, and two additional minima are seen for SiF_4 at ~5 and ~23 eV. The β minimum at ~5 eV has no visible associated maximum in σ, however a maximum in the branching

ratio does occur at 7.6 eV kinetic energy. The intense β minimum at 23 eV kinetic energy is associated with a rather weak maximum in σ at the same kinetic energy. The agreement between the theoretical and experimental BR for SiF_4 is quite reasonable at higher photon energies, but at lower energies the theoretical maximum at 3.3 eV kinetic energy is not observed experimentally and the observed maximum at 7.6 eV kinetic energy is not predicted theoretically (The 3.3 and 7.6 eV peaks do not correspond, as is discussed later.). The minimum at ~18 eV kinetic energy, the shoulder at ~24 eV kinetic energy, and the maximum at ~35 eV kinetic energy are all well reproduced in the experimental results.

For the remaining valence band a_1 orbitals, the σ and β plots differ greatly for SiF_4 and CF_4 (Figures 4.4.3-6 and 4.4.2-5, respectively). While the CF_4 σ value increases rapidly to ~2 Mb at 10 eV kinetic energy before levelling off, the SiF_4 plot shows a minimum at about 10 eV kinetic energy followed by an intense maximum (~6 Mb) at ~23 eV kinetic energy, before decreasing above 30 eV kinetic energy to ~1 Mb. These differences in σ are also apparent in the variation of β values. The cross section minimum for SiF_4 at ~10 eV kinetic energy (which is absent in CF_4) may be due to a molecular Cooper minimum for the Si 3s orbital (i.e. $3s \rightarrow \epsilon p$). Examination of the p-wave component contribution to the $5a_1$ theoretical cross section of SiF_4, shows a clear minimum at ~11 eV kinetic energy.

The Cooper minimum occurs experimentally at ~6.5 eV kinetic energy in the BR plot. The position of this molecular Cooper minimum occurs at ~6 eV higher kinetic energy than that calculated by Manson[106] for the atomic Si 3s orbital, which was done ignoring core relaxation and using Hartree-Slater (HS) central-field functions for the initial state. Similar effects have been seen for valence p orbitals in HCl, HI, and $SiCl_4$.[87,107,127]

The sharp minimum in β at ~26 eV kinetic energy is related to the intense maximum in σ at ~23 eV. In addition, the change in slope of β at ~12 eV kinetic energy signifies the molecular Cooper minimum for the Si 3s orbital. In contrast, the CF_4 β plot has no structure apart from a minimum at ~2 eV (theoretical) or 7 eV (experimental) and is qualitatively very similar in shape to the theoretical β plots of the $1t_1$, 1e, and $3t_2$ CF_4 orbitals. The experimental and theoretical BR for SiF_4 (Figure 4.4.3-6) are in good overall agreement, although the theoretical maximum at 4 eV is shifted to ~2 eV, and the theoretical resonance at 23 eV is more intense and narrower than the experimental.

A detailed analysis of the maxima in the cross sections of SiF_4 will now be made in terms of shape resonances. As discussed in section 4.1.1, a shape resonance is a quasibound state embedded in the continuum, in which the excited electron is temporarily trapped by the molecular potential barrier.[4] The electron eventually

tunnels through the barrier and escapes, giving rise to a Breit-Wigner-type maximum[108] in the cross section.

In contrast to CF_4 which only shows shape resonances within 2-3 eV kinetic energy above threshold, the MS-Xα calculations for SiF_4 show a total of five shape resonances in the exit channels from 2.7-34.6 eV kinetic energy, and many of these are observed in the branching ratios (Table 4.4.3-2). The shape resonances are predicted to occur at 2.7 (a_1 exit channel), 6.8 (t_2 channel), 12.9 (e channel), 22.6 (t_2 channel) and 34.6 eV kinetic energy (t_2 channel) above threshold. They are numbered 1-5, respectively, both in Table 4.4.3-2 and on the cross section plots (Figures 4.4.3-(1-6). The eigenphase sums verify that these features are indeed shape resonances. These features meet the two resonance criteria of Kreile et al.[55] (namely that the eigenphase sum changes by $\geq 0.3\pi$ over an energy range $\Delta E \leq 6$ eV, and $|E_{cross}-E_{phase}| < 4$ eV), although the t_2 exit channel at 6.8 eV kinetic energy is a weak borderline case. The resonance energy E_{phase} shown in Table 4.4.3-2 is merely the inflection point in the plot of the appropriate channel eigenphase sum versus photoelectron kinetic energy. The resonances are classified rather subjectively as being weak (w), medium (m), or strong resonances (s), based on the plots of the respective exit channel cross sections (E_{cross} in Table 4.4.3-2) or eigenphase sums versus photoelectron kinetic energy (E_{phase} in Table 4.4.3-2).

For the highest occupied molecular orbital $1t_1$ of SiF_4, three shape resonances are predicted from an analysis of the partial cross section behavior; a t_2 channel resonance at 6.8 eV, an e channel resonance at 12.9 eV, and a t_2 channel resonance at 22.6 eV kinetic energy. As can be clearly seen in Figure 4.4.3-1, only two maxima are clearly discernible in the experimental BR. The experimental BR maximum at 22.6 eV kinetic energy is in exact agreement with the theoretical, so the assignment of t_2 exit channel here is reasonable. Since no resonance is predicted or observed for this orbital in the t_2 exit channel at 34.6 eV kinetic energy, the agreement above ~18 eV kinetic energy can be considered excellent. However agreement below this is much less satisfactory. Firstly, the e channel shape resonance predicted at 12.9 eV kinetic energy is not observed experimentally, as witnessed by the experimental BR minimum there. Secondly, the maximum observed in the BR at 7.1 eV kinetic energy is dipole allowed, but the theoretically predicted intensity is very small. The cause of this is unknown. The maximum is tentatively assigned to the t_2 exit channel at 6.8 eV kinetic energy, based on the close kinetic energy match. Unfortunately, the sharp increase in the theoretical BR close to threshold could not be verified, due to the restrictive low photon energy limit of ~21 eV with the monochromator used.

Since only two rather weak resonances are predicted to occur at 6.8 and 34.6 eV kinetic energy on the 1e orbital (Figure 4.4.3-3), we use both the more accurate sum of BR values (Figure 4.4.3-4) as well as the $5t_2$ BR to discuss the $5t_2$ cross section (Figure 4.4.3-2). The overall agreement for both orbitals is satisfactory. The experimental BR maximum at 11.2 eV kinetic energy is ~2.8 eV lower than the theoretical BR, and above 26 eV kinetic energy, the theoretical BR rises too rapidly (Figure 4.4.3-4). The predicted $5t_2$ orbital a_1 resonance (No. 1) at 3.3 eV kinetic energy could not be verified due to our low photon limit of ~21 eV. The experimental branching ratio values are rising however at ~21 eV photon energy which is at least consistent with this a_1 resonance. The large experimental BR maximum centered at 11.2 eV kinetic energy in both Figures 4.4.3-2 and 4.4.3-4 can be assigned to the 1e exit channel of the $5t_2$ orbital. The intensity and large width of this resonance probably masks the t_2 resonances at 6.8 and 22.6 eV kinetic energy. The broad maximum at ~42 eV kinetic energy in the experimental BR (Figure 4.4.3-4) can be assigned to the t_2 channel resonance predicted to occur at 34.6 eV kinetic energy on both the $5t_2$ and 1e orbitals. The discrepancy in this resonance position of ~7 eV is the largest found, but perhaps understandable considering the large width of this resonance, and the crude experimental photon energy mesh size of ~5 eV used in that region.

For the 1e orbital (Figure 4.4.3-3), the observed peak at 7 eV kinetic energy is probably the t_2 resonance seen also in the $1t_1$ orbital, but not predicted. The t_2 resonance at 35 eV is not well characterized experimentally because of the larger errors and scatter involved in fitting this higher energy region.

For the $4t_2$ bonding molecular orbital shown in Figure 4.4.3-5, the agreement above 20 eV kinetic energy between the experimental and theoretical BR is quite reasonable. Towards higher kinetic energies the theoretical BR falls off a little more rapidly than experiment. A shoulder is clearly discernible in the experimental BR plot at ~24 eV kinetic energy, while the maximum occurs at ~35.6 eV kinetic energy. These two features are assigned as t_2 resonances, since theoretically two t_2 resonances are predicted at 22.6 and 34.6 eV kinetic energy. The agreement at kinetic energies lower than this is poorer, however. Experimentally a maximum is observed in the BR at 7.6 eV kinetic energy, which is not predicted to have appreciable intensity. A situation almost identical to this was discussed previously for the $1t_1$ orbital. Although it is tempting to invoke a kinetic energy shift argument and attempt to assign this as either the e resonance or a_1 resonance, this is unreasonable for several reasons. First of all, a 1e resonance is not predicted for this orbital; and for the similar $1t_1$ orbital case, the a_1 resonance is dipole forbidden. Second, a

shift of the a_1 resonance to ~7 eV kinetic energy is not reasonable, because the $5t_2$ orbital (which also has an allowed a_1 resonance) shows a minimum at ~7 eV kinetic energy. This really only leaves the t_2 resonance at 6.8 eV kinetic energy. Again, the calculation does not predict any significant intensity for this resonance. Therefore, this maximum is tentatively assigned again to the t_2 resonance at 6.8 eV kinetic energy, making the assumption that the intensity of this resonance is seriously underestimated. The predicted a_1 resonance could not be verified near threshold. However, as for the $5t_2$ orbital, the increase in BR at 21 eV photon energy (1.6 eV kinetic energy) may be consistent with a resonance very near threshold.

In Figure 4.4.3-6 the experimental BR for the $5a_1$ bonding orbital shows two maxima at 2.1 and 22.6 eV kinetic energy. The analysis of this orbital is greatly simplified since all exit channels except t_2 are dipole forbidden. In general, the agreement over the entire photon energy range for the $5a_1$ orbital is very good. Analysis of the theoretical results for the first maximum at 2.1 eV kinetic energy indicates that this is a nonresonant feature in the cross section. Experimentally this maximum is shifted by ~2 eV to lower kinetic energy and is not quite as intense as theory predicts. The second maximum at 22.6 eV kinetic energy is in excellent agreement with the t_2 resonance predicted for this orbital at 22.6 eV kinetic energy. This

resonance position is higher by ~1.5 eV kinetic energy, but in basically good agreement with the resonance observed for SiF_4 in the photoabsorption data above the Si 2p edge[91,92] at 133 eV photon energy. The theoretical BR maximum here is narrower and more intense than experiment. In neglecting vibrational effects, the multiple scattering approach usually exaggerates the strengths of resonances and underestimates their widths.[111,112] A detailed analysis of the asymptotic partial waves shows that this t_2 resonance is due to resonant trapping by the molecular potential barrier of primarily p, d, and f components ($\ell = 1 \rightarrow 3$) of the continuum molecular wave function.

4.4.4 CF_3I

The valence band spectrum of trifluoroiodomethane (CF_3I) is shown in Figure 3.3.2-1 at ~35, 41, and 80 eV photon energies. Included at the bottom of Figure 3.3.2-1, is our final molecular orbital assignment of CF_3I. This assignment was based on our Xα-SW ground state calculation (transition state) for CF_3I, comparison of the experimental branching ratios with those calculated using the MS-Xα method, and comparison with the previous photoelectron assignment of CF_3I by Cvitaš et al.[102] With minor differences, our assignment of CF_3I agrees with that of Cvitaš et al.[102] The He I/He II photoelectron assignment of CF_3I by Cvitaš et al.[102] was largely based on the similarity of the photoelectron spectra of the series

CF_3X (X = Cl, Br, I) in the region between 15-25 eV binding energy. The similarity in this region was attributed as arising from the substituent (X) interacting very little with the electronic structure of the CF_3 moiety. In short, the assignment for CF_3I by Cvitaš et al.[102] was based on their previous assignment for CF_3Cl, which in turn was made on the basis of comparison of the photoelectron spectra of the chlorofluoromethanes (CF_3Cl, CF_2Cl_2, $CFCl_3$),[113] and correlations with the previous assignments of fluoromethanes and chloromethanes.[82,114] The recent analysis by Jadrny et al.[115] of vibrational structure present in the high resolution He I photoelectron spectrum of CF_3Cl, yields an assignment in agreement with that of Cvitaš et al.[113] An earlier assignment by Doucet et al.[116] of the first five bands of CF_3Cl is also in accord with that made by Cvitaš et al.,[113] and was discussed in relation to the vacuum UV absorption spectrum. Xα-SW transition-state calculations by Preston et al.[117] on the chlorofluoromethanes confirm very nicely the molecular orbital assignment by Cvitaš et al.[113] for CF_3Cl. Potts et al.[118] have recently measured the photoelectron asymmetry parameters for CF_3Cl and the other chlorofluoromethanes in the photon energy range of 18-80 eV, and were able to locate the molecular orbitals corresponding to the Cl 3s and F 2s orbitals.

The He I/He II investigation of CF_3I by Cvitaš et al.[102] does not give a totally satisfactory assignment of

the spectrum, however, since the I 5s level in this molecule is not accounted for. It is possible that this arose from their correlation of CF_3Cl with CF_4,[113] and from a failure to recognize that the Cl 3s orbital lies at significantly smaller binding energy (~26 eV binding energy[118]) than the F 2s orbitals (≈ 40 eV binding energy[118]).[119] According to the free atom binding energies tabulated by Lotz,[119] the I 5s level should lie around ~20.6 eV binding energy. As can be seen in Figure 3.3.2-1, a shoulder appears at ~21.5 ± 0.2 eV binding energy, to the left of the band assigned as arising from the 1e molecular orbital. This shoulder is most noticeable at photon energies close to ~35 eV, and has been assigned to the $2a_1$ molecular orbital. Our assignment for CF_3I is shown in Table 4.4.4-1, including the calculated charge distributions for each of the ground state valence molecular orbitals. For comparative purposes, the analogous results for CF_4 have also been included in this table. A transition-state calculation for the $2a_1$ MO places it at ~21.9 eV binding energy, in good agreement with the experimental position of this shoulder at 21.5 ± 0.2 eV binding energy.

It seems appropriate at this point to briefly discuss the electronic structure of CF_3I, based on the Xα-SW charge distributions shown in Table 4.4.4-1. The first two bands at 10.45 and 11.18 eV binding energy (Figure 3.3.2-1) correspond to removal of an electron from

Table 4.4.4-1

Calculated Charge Distribution for CF_3I and CF_4 Ground State Valence Molecular Orbitals[a),b)]

	MO	Experimental Energy (eV)	Outer	C	F	I	Inter
CF_3I	4e	10.45[c)] 11.18[c)]	4.2(p,d)	0.1(p,d)	1.1(p)	77.6(p)	17.0
	$4a_1$	13.25	1.9(p)	27.9(p,s)	18.0(p,$\bar{s}$,$\bar{d}$)	44.2(p,d,$\bar{s}$)	8.0
	$1a_2$	15.56	0.6(g,f)	0.0	80.5(p)	0.0	18.9
	3e	16.32	0.7(g,f,p)	0.3(d,p)	78.4(p)	0.3(p,d)	20.3
	2e	17.28	2.2(f,d,g,p)	0.7(p)	76.9(p)	0.1(d,p)	20.2
	$3a_1$	19.15	1.9(d,s)	1.0(p,s)	36.2(p)	49.7(s,p)	11.2
	1e	20.6	2.4(f,d,g)	15.9(p)	61.4(p,$\bar{s}$)	0.3(d,p)	20.0
	$2a_1$	21.5±0.2 (~21.9[d)])	1.1(p,f,d)	8.7(p,s)	29.4(p)	45.3(s,p,$\bar{d}$)	15.5
	$1a_1$	23.8	1.8(g,p,s)	20.8(s,$\bar{p}$)	52.2(p,s)	4.0(s,p,d)	21.3
CF_4	$1t_1$	16.2	3.0(f,g)	0.0	77.8(p)		19.2
	$4t_2$	17.4	4.8(p,g)	2.5(p,d)	73.1(p)		19.6
	1e	18.5	3.2(d)	0.2(d)	70.3(p)		26.3
	$3t_2$	22.1	3.8(d,f)	14.1(p)	57.1(p,s)		24.9
	$4a_1$	25.1	5.1(f,s,g)	18.6(s)	54.8(p,s)		21.5

a) Outer, Inter is the percentage charge of the outersphere and intersphere regions, respectively.

b) Spherical harmonic basis functions contributing to each sphere are shown in brackets, in order of decreasing importance. Contributions that represent ~(1-10%) are shown with a bar on top.

c) Ionization of the 4e MO yields the two states of $^2E_{1/2}$ (11.15 eV) and $^2E_{3/2}$ (10.45 eV), due to spin-orbit coupling. The center of gravity lies at 10.69 eV binding energy.

d) Estimated binding energy from a transition-state calculation on this orbital.

the 4e molecular orbital, which consists largely of I 5p lone pair electrons. The high iodine content of this degenerate MO leads to large interactions between electron spin and orbital angular momentum (i.e. spin-orbit coupling) upon photoionization. Removal of an electron from the filled 4e MO yields two electronic states having half integral total angular momentum, which must be treated using double groups.[120] Photoionization from the 4e MO thus gives rise to the spin-orbit $^2E_{3/2}$ (10.45 eV) and $^2E_{1/2}$ (11.18 eV) states. The next band at 13.25 eV binding energy ($4a_1$) corresponds to ionization from the C-I bonding orbital. Bonding in the $4a_1$ orbital occurs mainly via the overlap of the C $2p_z$ and I $5p_z$ atomic orbitals, although significant C 2s character is also involved. The next three bands at 15.56 eV ($1a_2$), 16.32 eV (3e), and 17.28 eV (2e) are associated with ionizations of the fluorine 2p lone pair electrons. Of these, the $1a_2$ molecular orbital has for symmetry reasons, strictly pure fluorine character.

The band centered at 19.2 eV ($3a_1$) and the shoulder located at ~21.5 ± 0.2 eV binding energy ($2a_1$), both contain significant F 2p and I 5s character (Table 4.4.4-1). The I 5s atomic orbital mixes significantly with the F 2p atomic orbitals, since they are close in energy. The $2a_1$ and $3a_1$ molecular orbitals are essentially the in-phase and out-of-phase combinations, respectively, of the F 2p and I 5s atomic orbitals. Although the I 5s is rather compact, it is delocalized in CF_3I into the $2a_1$ and

$3a_1$ MO's through symmetry. A similar case of delocalization occurs in CH_3I between the C 2s and I 5s atomic orbitals, for the $1a_1$ and $2a_1$ molecular orbitals.[121]

The two remaining bands at 20.6 eV and 23.8 eV binding energy are due to ionization from the 1e and $1a_1$ C-F bonding molecular orbitals, respectively. Bonding in the 1e MO arises from overlap of the C ($2p_x$, $2p_y$) with the F 2p atomic orbitals. The $1a_1$ molecular orbital accomplishes this bonding from the overlap of the C 2s and F 2p atomic orbitals. Ionization from the $1a_1$ MO yields an asymmetric peak shape, with a distinct shoulder occurring at ~0.9 ± 0.2 eV higher binding energy than the primary photoline. This additional feature on the $1a_1$ MO was not mentioned in the study by Cvitaš et al.,[102] but the He II spectrum published by this group was collected only up to ~24 eV binding energy, just short of this feature. This feature was probably masked in their study by the He^+ line at 24.587 eV binding energy,[122] which typically contaminates most He II spectra. Green's function calculations by Cambi et al.[123] on CHF_3 clearly show that the one-particle model of photoionization begins to break down at intermediate binding energies deeper than ~24 eV. In CHF_3, Cambi et al.[123] predict the $4a_1$ C-F bonding molecular orbital to be the first valence orbital for which some satellite structure should be observed. It seems likely that the satellite structure observed in CF_3I at higher binding energy above the $1a_1$ primary photoline

(analogous to $4a_1$ in CHF_3), is due to such a breakdown of the one-particle model for valence photoionization. In calculating the branching ratio for the $1a_1$ MO, this additional satellite area was therefore included with that of the primary photoline.

The theoretical and experimental branching ratios (BR), and theoretical partial cross sections (σ) for the first nine valence molecular orbitals of CF_3I are shown in Figures 4.4.4-(1-11). Due to overlap of the 3e and $1a_2$ bands, and the $2a_1$ and 1e bands, the sum of the two have been plotted instead (i.e. 3e + $1a_2$ (Figure 4.4.4-3), $2a_1$ + 1e (Figure 4.4.4-8)). For completeness, and to aid in the ensuing discussion, the theoretical partial cross sections and branching ratios for the $1a_2$, 3e, 1e, and $2a_1$ molecular orbitals have also been included (Figures 4.4.4-(4,5,9,10), respectively). The experimental branching ratios are also summarized in Table 4.4.4-2, so that partial cross sections may be obtained when the total photoionization cross section for CF_3I is determined.

A detailed analysis of the structure in the partial cross sections and branching ratios of CF_3I will now be undertaken, including a correlation with the CF_4 results. As discussed in section 4.4.3, CF_4 shows shape resonances only within 2-3 eV kinetic energy above threshold. At higher kinetic energies than this the eigenphase sums for CF_4 are without structure and slowly changing, accounting for the smooth behavior in each of the partial cross

Figure.4.4.4-1

Experimental and theoretical MS-Xα (solid lines) results are shown for the photoionization of the 4e orbital of CF_3I. The upper and bottom plots give the partial cross section σ, and branching ratio, respectively.

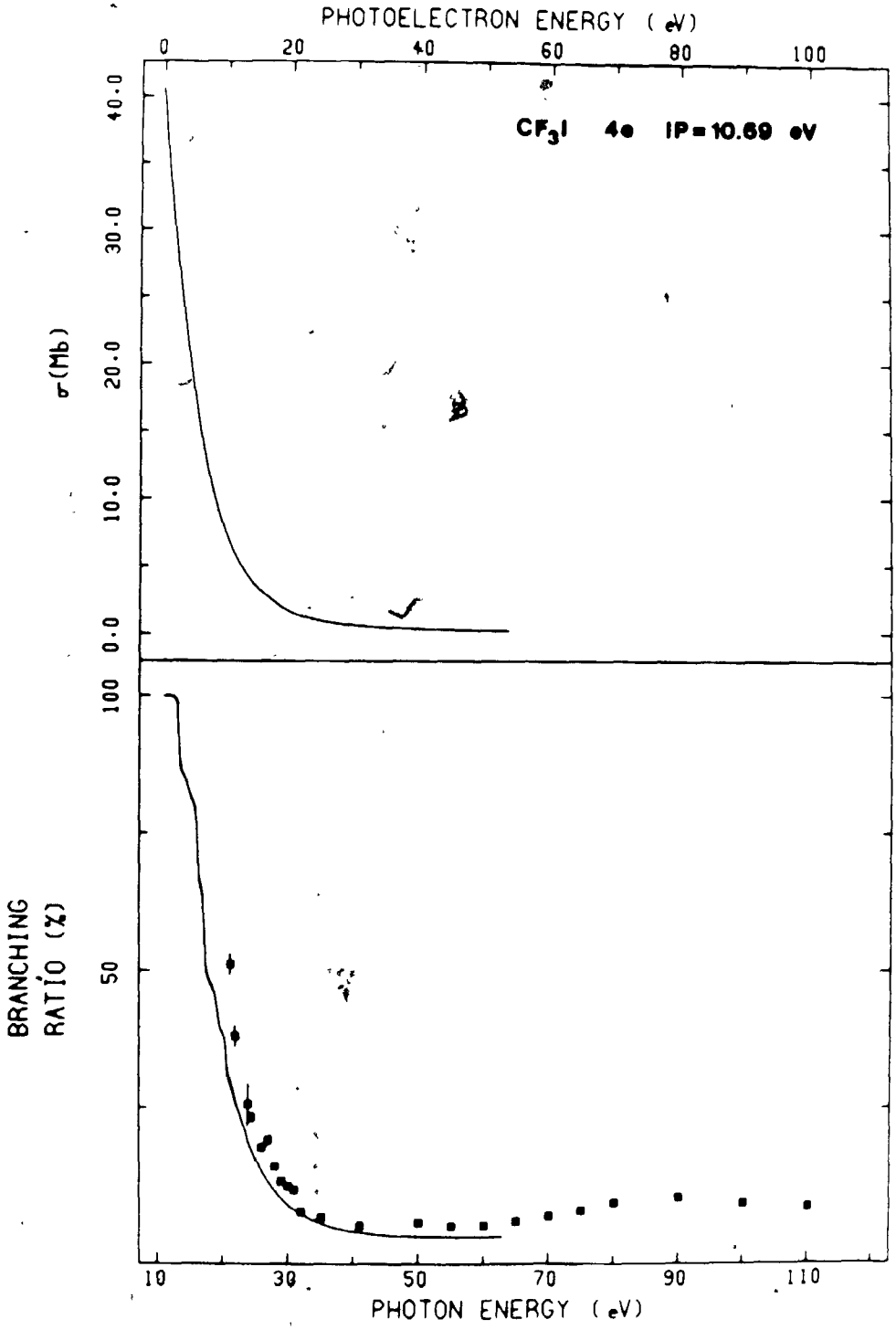
PHOTOELECTRON ENERGY (eV)
0
20
40
60
80
100
CF_3I 4e IP=10.69 eV
σ(Mb)
40.0
30.0
20.0
10.0
0.0
BRANCHING RATIO (%)
100
50
10
30
50
70
90
110
PHOTON ENERGY (eV)

Figure 4.4.4-2

Experimental and theoretical MS-Xα (solid lines) results are shown for the photoionization of the $4a_1$ orbital of CF_3I. The upper and bottom plots give the partial cross section σ, and branching ratio, respectively.

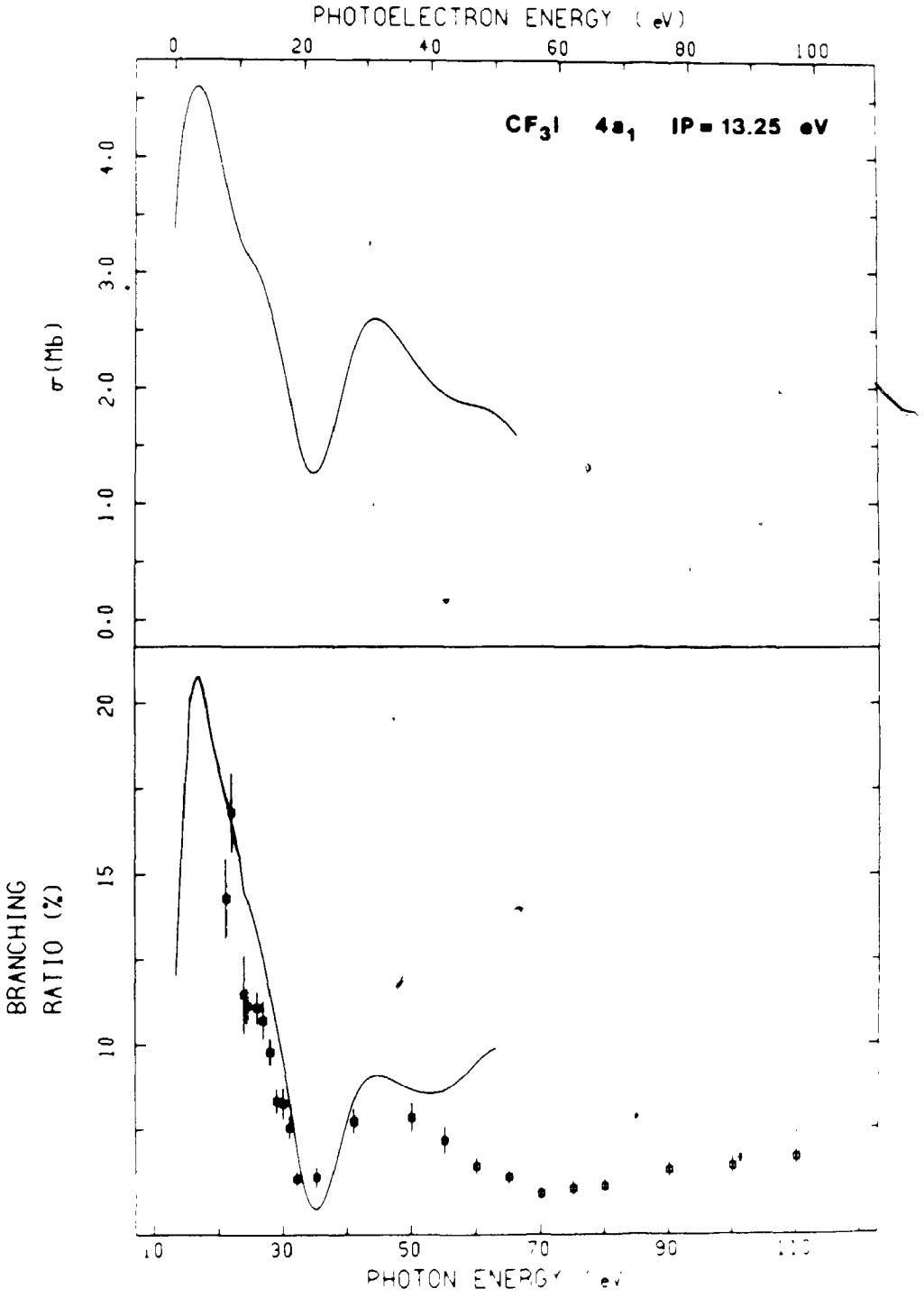
PHOTOELECTRON ENERGY (eV)
0
20
40
60
80
100
CF_3I $4a_1$ IP = 13.25 eV
σ(Mb)
4.0
3.0
2.0
1.0
0.0
BRANCHING RATIO (%)
20
15
10
30
50
70
90
PHOTON ENERGY (eV)

Figure 4.4.4-3

Experimental and theoretical MS-Xα (solid lines) results are shown for the photoionization of the 3e and $1a_2$ orbitals of CF_3I. The upper and bottom plots give the partial cross section σ, and branching ratio, respectively.

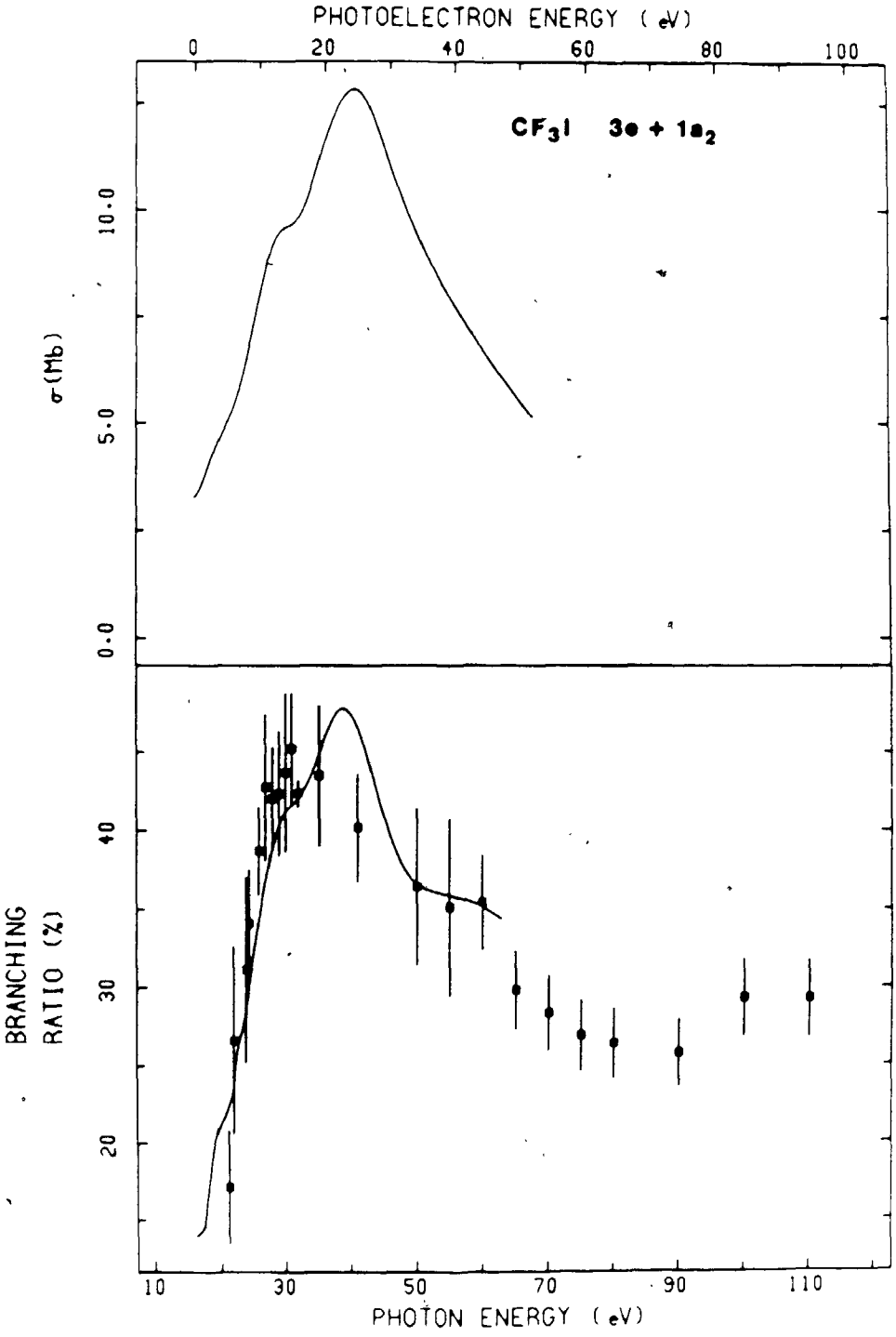
PHOTOELECTRON ENERGY (eV)
0
20
40
60
80
100
CF_3I $3e + 1a_2$
σ(Mb)
10.0
5.0
0.0
BRANCHING RATIO (%)
40
30
20
10
30
50
70
90
110
PHOTON ENERGY (eV)

Figure 4.4.4-4

Theoretical MS-Xα (solid lines) results are shown for the photoionization of the $1a_2$ orbital of CF_3I. The upper and bottom plots give the partial cross section σ, and theoretical branching ratio, respectively.

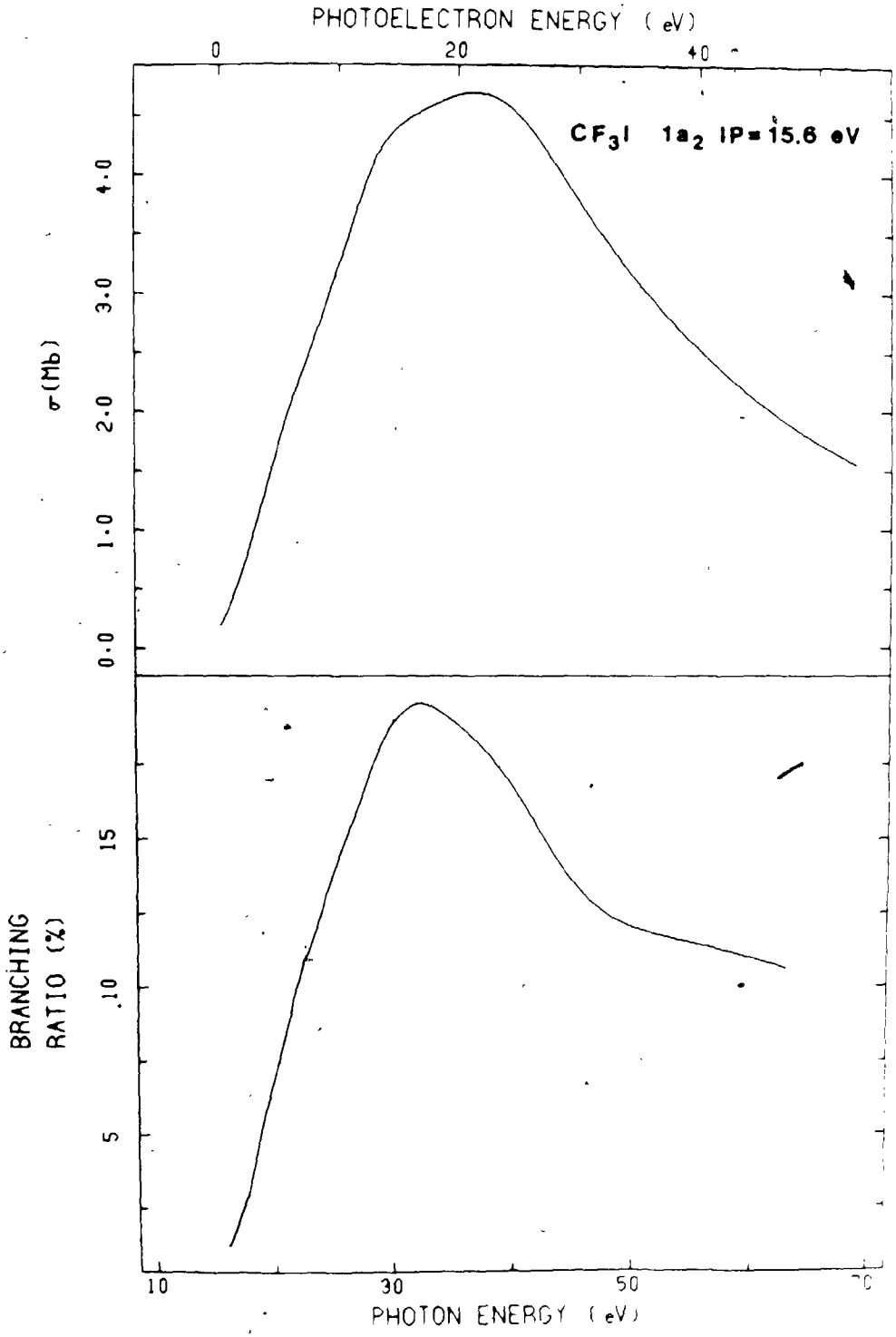
PHOTOELECTRON ENERGY (eV)
0
20
40
CF_3I $1a_2$ IP=15.6 eV
σ(Mb)
0.0
1.0
2.0
3.0
4.0
BRANCHING RATIO (%)
5
10
15
10
30
50
PHOTON ENERGY (eV)

Figure 4.4.4-5

Theoretical MS-Xα (solid lines) results are shown for the photoionization of the 3e orbital of CF_3I. The upper and bottom plots give the partial cross section σ, and theoretical branching ratio, respectively.

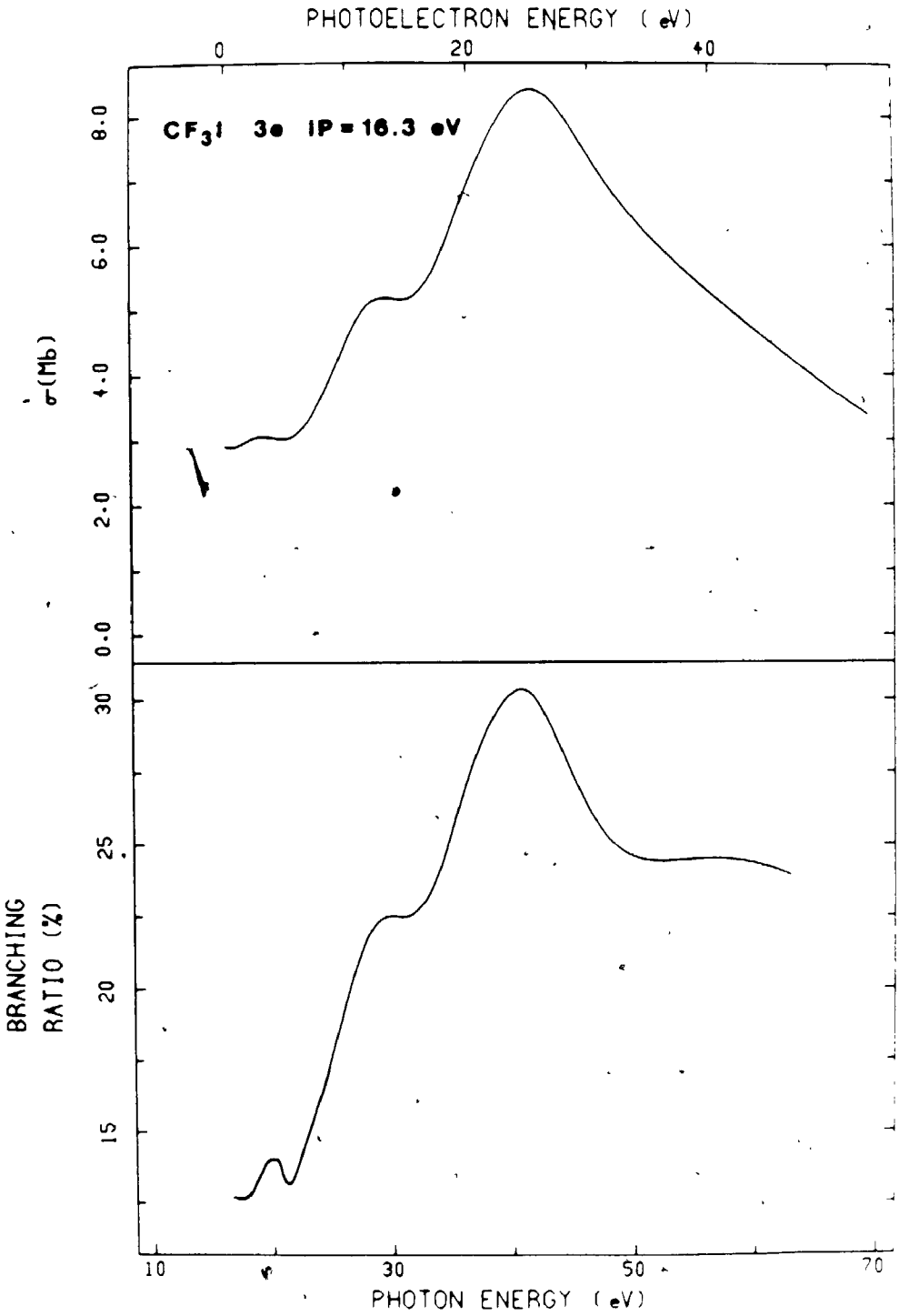
PHOTOELECTRON ENERGY (eV)
0
20
40
CF_3I 3e IP = 16.3 eV
σ(Mb)
8.0
6.0
4.0
2.0
0.0
BRANCHING RATIO (%)
30
25
20
15
10
30
50
70
PHOTON ENERGY (eV)

Figure 4.4.4-6

Experimental and theoretical MS-Xα (solid lines) results are shown for the photoionization of the 2e orbital of CF_3I. The upper and bottom plots give the partial cross section σ, and branching ratio, respectively.

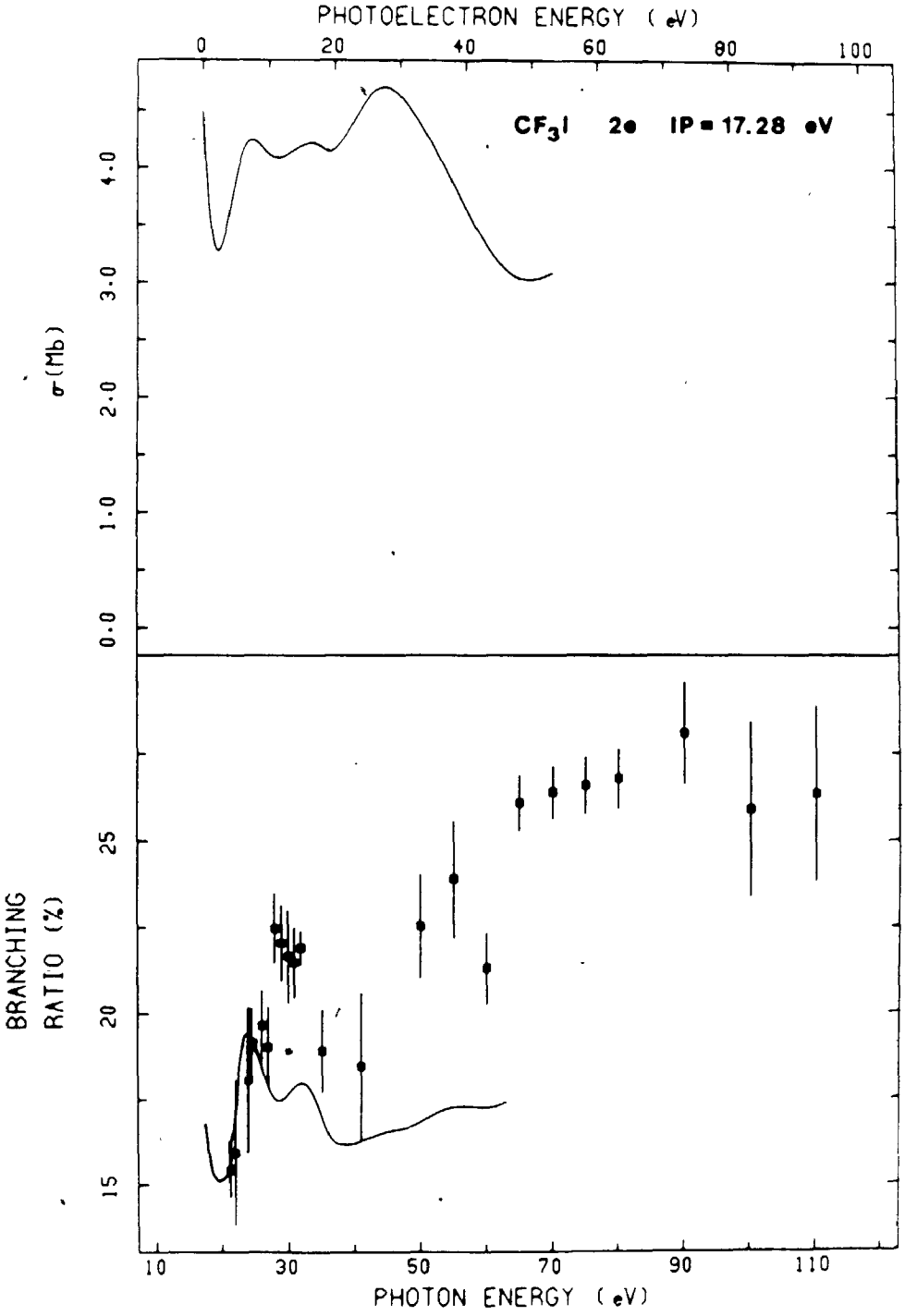
PHOTOELECTRON ENERGY (eV)
0
20
40
60
80
100
CF_3I 2e IP = 17.28 eV
σ(Mb)
0.0
1.0
2.0
3.0
4.0
BRANCHING RATIO (%)
15
20
25
10
30
50
70
90
110
PHOTON ENERGY (eV)

Figure 4.4.4-7

Experimental and theoretical MS-Xα (solid lines) results are shown for the photoionization of the $3a_1$ orbital of CF_3I. The upper and bottom plots give the partial cross section σ, and branching ratio, respectively.

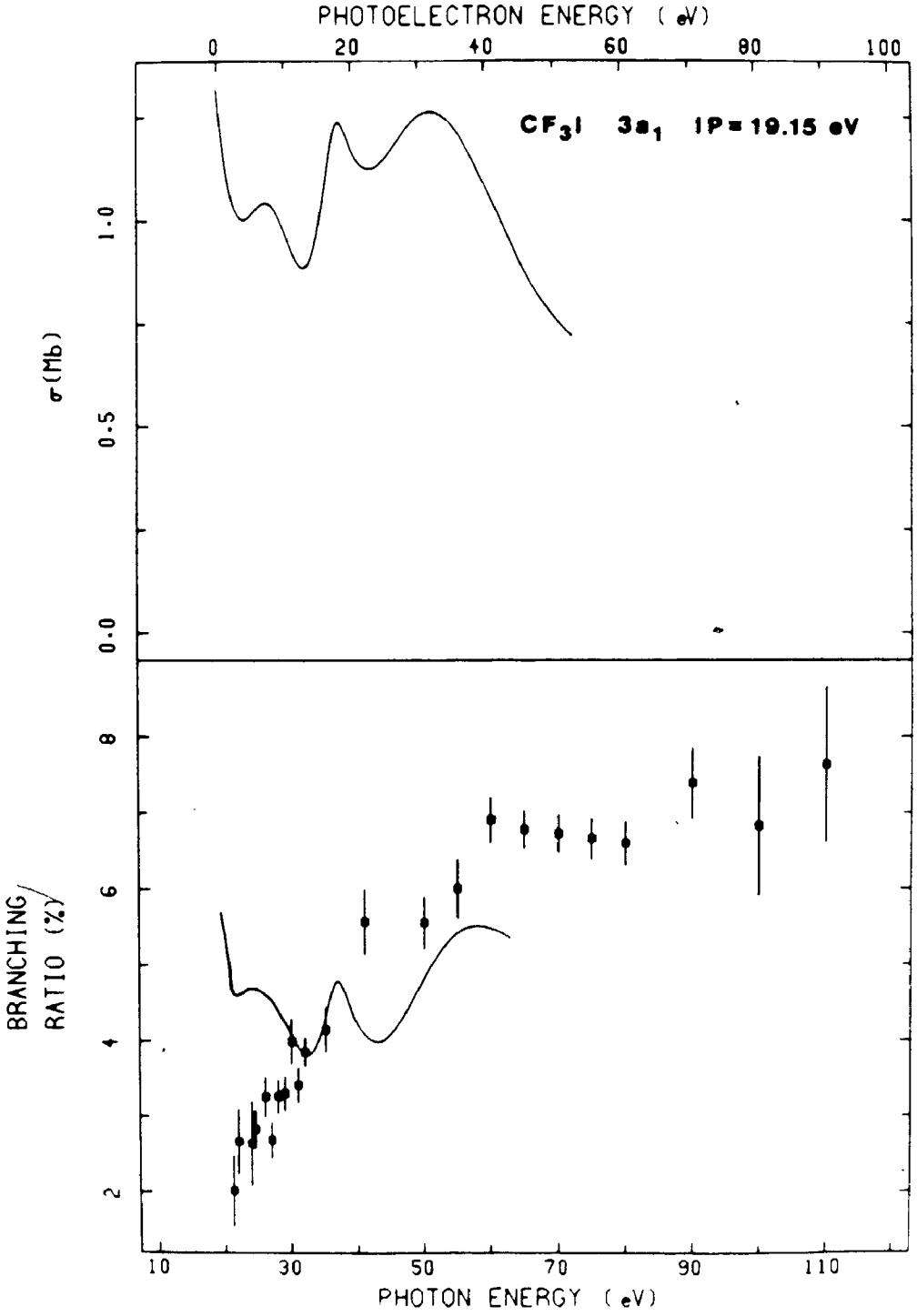
PHOTOELECTRON ENERGY (eV)
0
20
40
60
80
100
CF_3I $3a_1$ IP = 19.15 eV
σ(Mb)
1.0
0.5
0.0
BRANCHING RATIO (%)
8
6
4
2
10
30
50
70
90
110
PHOTON ENERGY (eV)

Figure 4.4.4-8

Experimental and theoretical MS-Xα (solid lines) results are shown for the photoionization of the $2a_1$ and 1e orbitals of CF_3I. The upper and bottom plots give the partial cross section σ, and branching ratio, respectively.

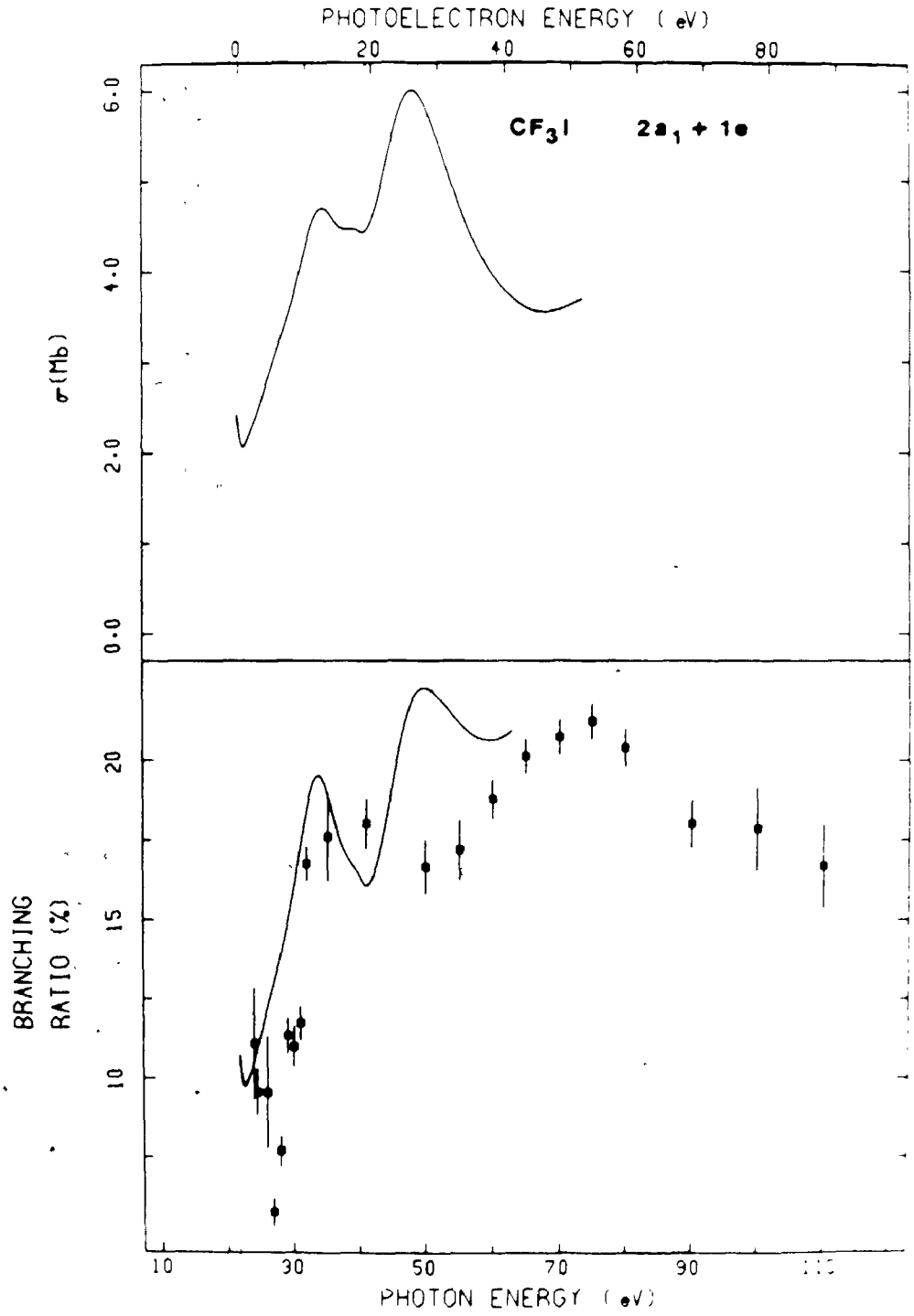
PHOTOELECTRON ENERGY (eV)
0
20
40
60
80
CF_3I $2a_1 + 1e$
σ(Mb)
6.0
4.0
2.0
0.0
BRANCHING RATIO (%)
20
15
10
10
30
50
70
90
PHOTON ENERGY (eV)

Figure 4.4.4-9

Theoretical MS-Xα (solid lines) results are shown for the photoionization of the 1e orbital of CF_3I. The upper and bottom plots give the partial cross section σ, and theoretical branching ratio, respectively.

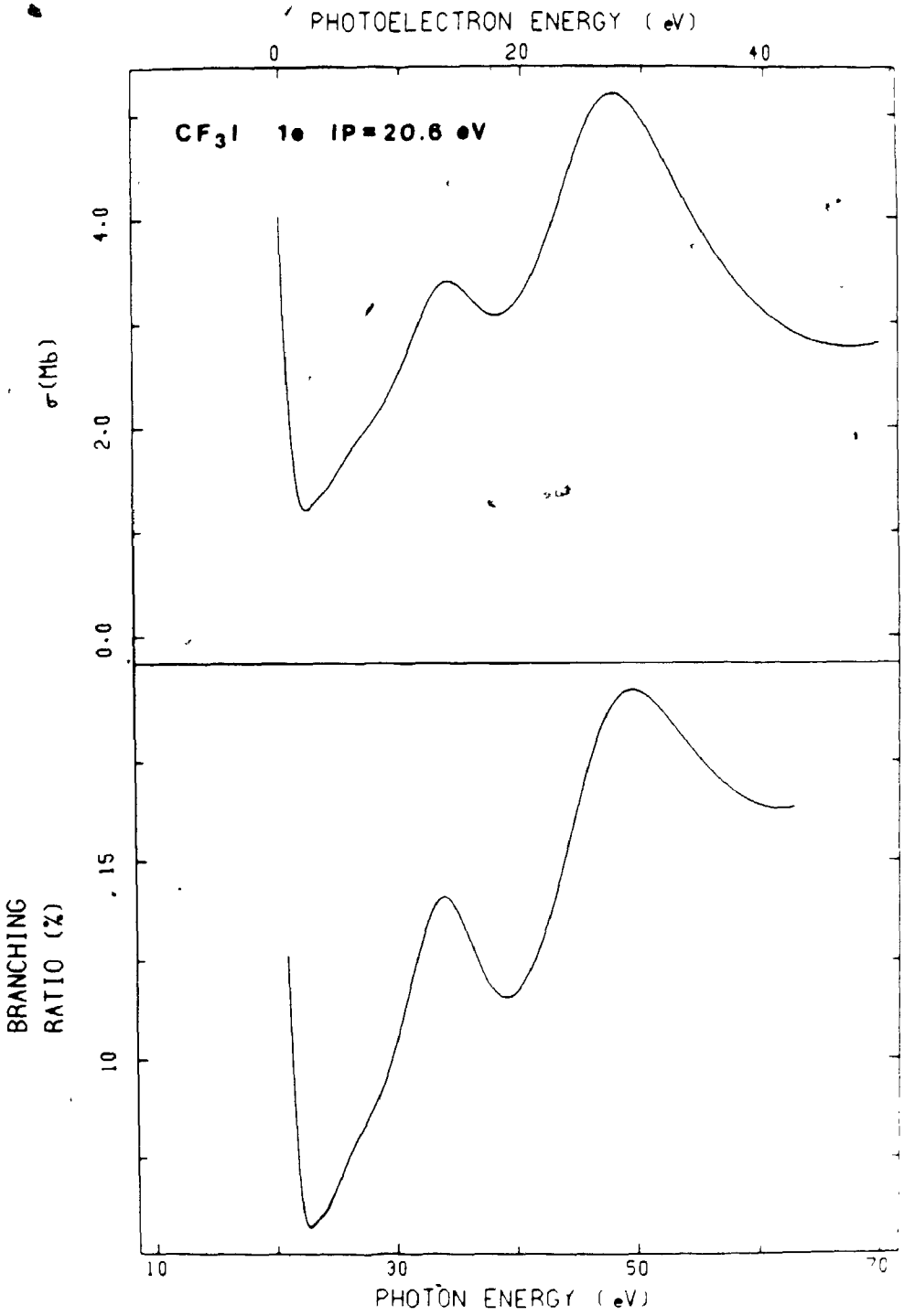
PHOTOELECTRON ENERGY (eV)
0
20
40
CF_3I 1e IP=20.6 eV
σ(Mb)
4.0
2.0
0.0
BRANCHING RATIO (%)
15
10
10
30
50
70
PHOTON ENERGY (eV)

Figure 4.4.4-10

Theoretical MS-Xα (solid lines) results are shown for the photoionization of the $2a_1$ orbital of CF_3I. The upper and bottom plots give the partial cross section σ, and theoretical branching ratio, respectively.

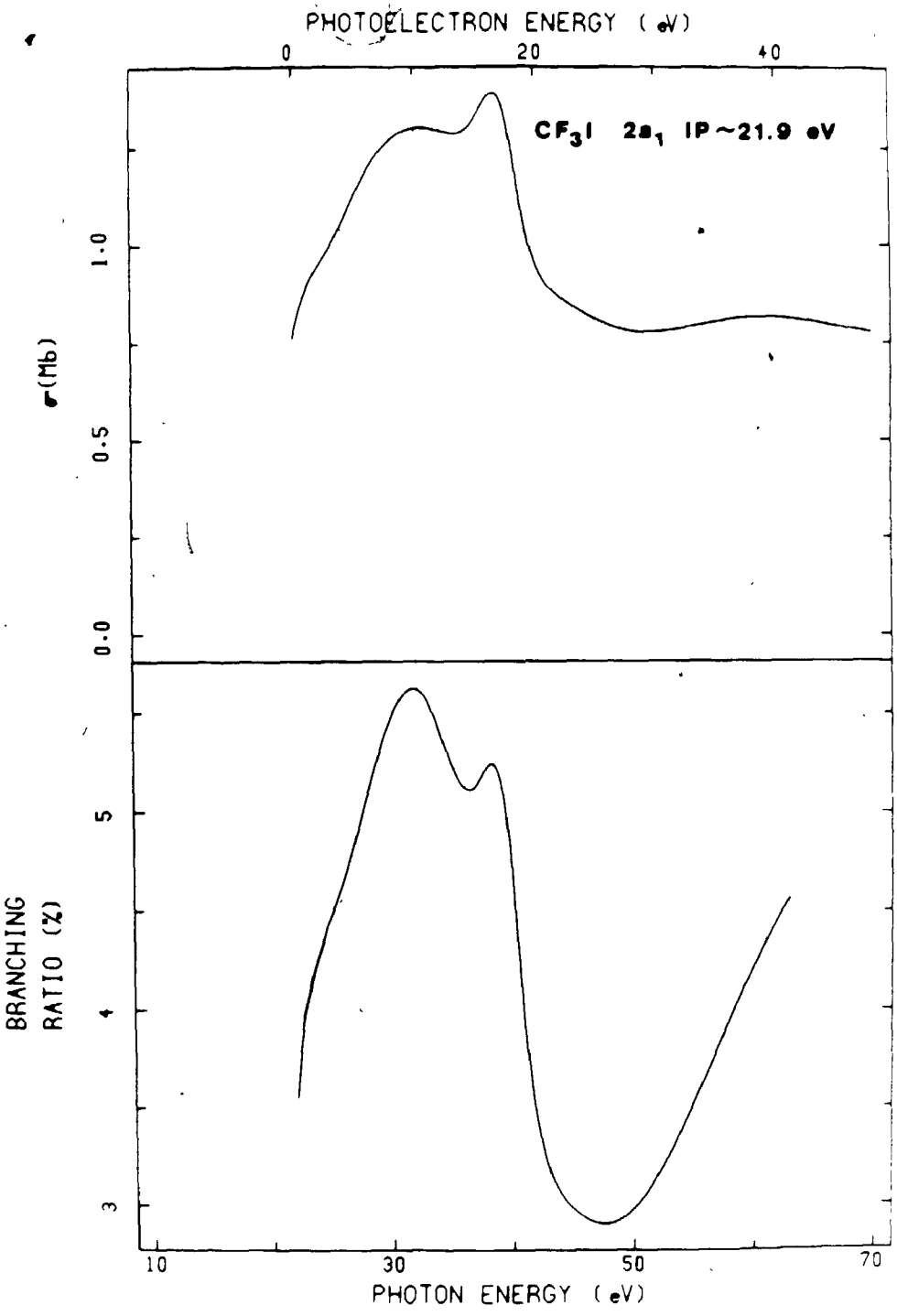
PHOTOELECTRON ENERGY (eV)
0
20
40
CF_3I $2a_1$ IP~21.9 eV
σ(Mb)
1.0
0.5
0.0
BRANCHING RATIO (%)
5
4
3
10
30
50
70
PHOTON ENERGY (eV)

Figure 4.4.4-11

Experimental and theoretical MS-Xα (solid lines) results are shown for the photoionization of the $1a_1$ orbital of CF_3I. The upper and bottom plots give the partial cross section σ, and branching ratio, respectively.

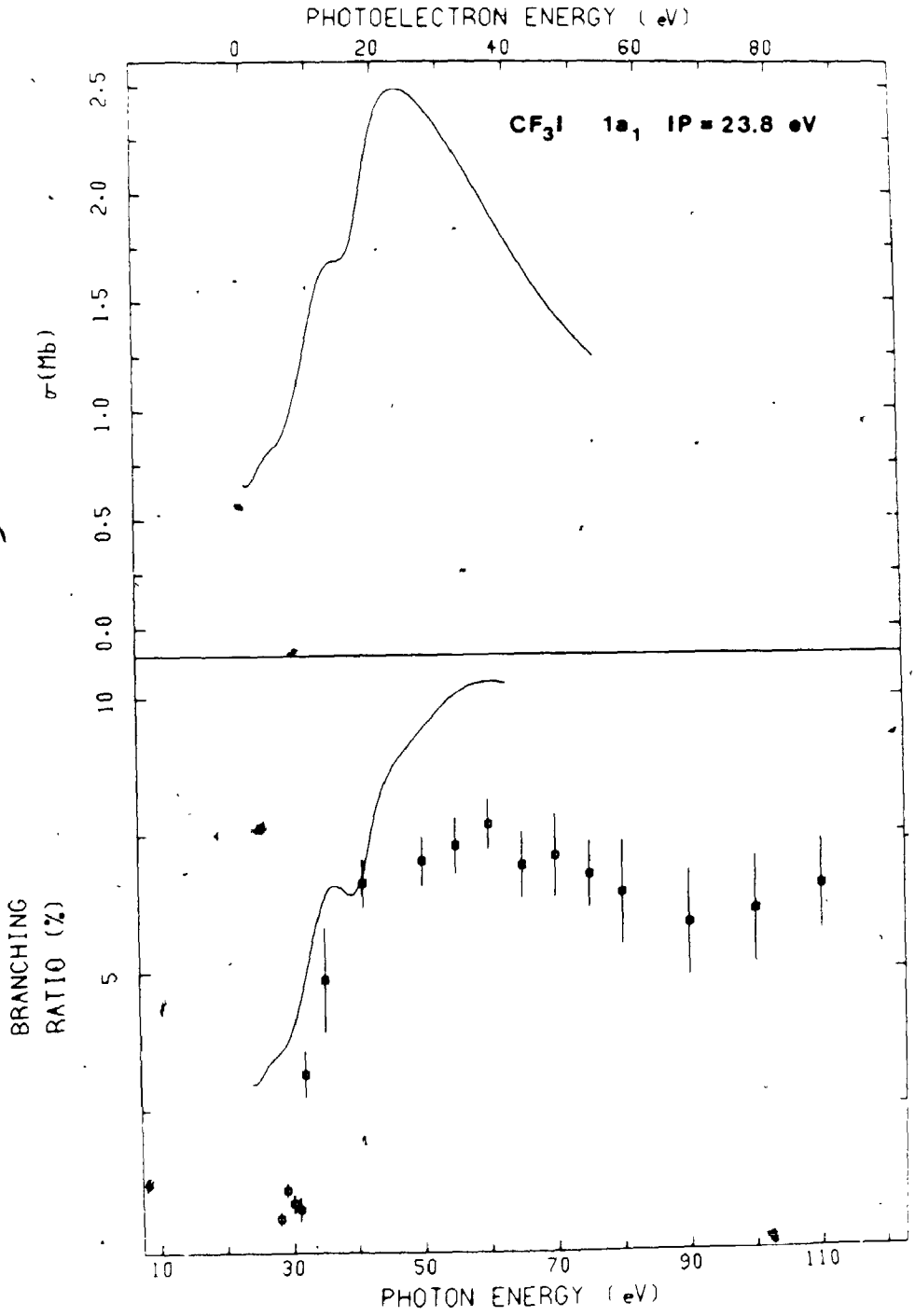
PHOTOELECTRON ENERGY (eV)
0
20
40
60
80
CF_3I $1a_1$ IP = 23.8 eV
σ(Mb)
0.0
0.5
1.0
1.5
2.0
2.5
BRANCHING RATIO (%)
5
10
10
30
50
70
90
110
PHOTON ENERGY (eV)

Table 4.4.4-2

Branching Ratios for Valence Orbitals of CF_3I as a Function of Photon Energy[a)]

hν (ev)	4e BR	$4a_1$ BR	$(3a_1 + 1a_2)$ BR	2e BR	$3a_1$ BR	$(2a_1 + 1e)$ BR	$1a_1$ BR
21.22	51.1±1.9	14.3±1.2	17.1±3.7	15.5±0.8	2.0±0.5		
22.0	38.0±2.0	16.8±1.2	26.6±6.0	15.9±2.1	2.7±0.4		
24.0	25.6±3.8	11.5±1.2	31.1±5.9	18.1±2.1	2.6±0.6	11.1±1.8	
24.5	23.2±0.9	11.1±0.5	34.1±3.5	19.2±1.0	2.8±0.3	9.5±0.7	
26.0	17.8±0.6	11.1±0.5	38.7±2.8	19.7±1.0	3.3±0.3	9.5±1.8	
27.0	19.1±0.8	10.7±0.6	42.8±4.7	19.0±1.2	2.7±0.2	5.7±0.5	
28.0	14.2±0.6	9.8±0.4	42.0±3.3	22.5±1.0	3.3±0.2	7.7±0.5	0.5±0.1
29.0	11.6±0.5	8.4±0.4	42.3±4.0	22.1±1.1	3.3±0.2	11.3±0.6	1.0±0.1
30.0	10.6±0.6	8.3±0.5	43.7±5.0	21.7±1.3	4.0±0.3	11.0±0.6	0.8±0.2
31.0	10.0±0.5	7.6±0.3	45.2±3.5	21.5±1.0	3.4±0.2	11.7±0.5	0.7±0.2
32.0	6.0±0.3	6.0±0.2	42.4±0.9	21.9±0.5	3.8±0.2	16.7±0.5	3.1±0.4
35.15	4.9±0.4	6.1±0.3	43.5±4.5	18.9±1.2	4.1±0.3	17.6±1.4	4.9±1.0
41.0	3.4±0.2	7.8±0.4	40.2±3.4	18.5±2.1	5.6±0.4	18.0±0.8	6.6±0.4
50.0	4.0±0.5	7.9±0.5	36.4±5.0	22.6±1.5	5.5±0.3	16.6±0.8	7.0±0.5
55.0	3.3±0.4	7.2±0.4	35.1±5.6	23.9±1.7	6.0±0.4	17.2±0.9	7.3±0.5
60.0	3.5±0.4	6.4±0.3	35.4±3.0	21.3±1.0	6.9±0.3	18.8±0.6	7.7±0.4
65.0	4.2±0.6	6.1±0.2	29.9±2.5	26.1±0.8	6.8±0.3	20.1±0.5	6.9±0.6
70.0	5.1±0.7	5.6±0.2	28.4±2.4	26.4±0.8	6.7±0.3	20.7±0.5	7.1±0.8
75.0	6.0±0.2	5.7±0.2	27.0±2.3	26.6±0.8	6.7±0.3	21.2±0.6	6.8±0.6
80.0	7.5±0.2	5.8±0.2	26.5±2.2	26.8±0.9	6.6±0.3	20.4±0.6	6.4±0.9
90.0	8.5±0.3	6.3±0.3	25.8±2.2	28.1±1.5	7.4±0.5	18.0±0.8	5.9±1.0
100.0	7.6±0.4	6.4±0.3	29.3±2.5	25.9±2.5	6.8±0.9	17.8±1.3	6.1±1.0
110.0	6.9±0.9	6.7±0.9	29.3±2.5	26.3±2.5	7.6±1.0	16.7±1.3	6.5±0.8

a) Above ~60 eV photon energy, the I 4d BR contributes significantly, and these will be required to convert BR to σ.

sections. In CF_3I, however, the eigenphase sum changes by ~π in the e and and a_1 continuum channels, at ~15.2 and ~17.2 eV kinetic energies, respectively. A summary of the theoretical MS-Xα eigenphase sum features in CF_3I is shown in Table 4.4.4-3. The kinetic energy positions labelled E_{phase} in Table 4.4.4-3 indicate possible shape resonance positions. In the framework of these calculations, these features in the eigenphase sum depend only on the final continuum state and not on the initial orbital.

The results for the highest occupied 4e molecular orbital of CF_3I are shown in Figure 4.4.4-1. According to the calculated charge distribution (Table 4.4.4-1), this molecular orbital consists largely of I 5p lone pair electrons. For both the partial cross section (σ) and branching ratio (BR), theory predicts a rapid monotonic decrease towards higher photon energy. Similar behavior has been observed experimentally for the I 5p lone pair orbitals of CH_3I and HI,[87] and moreover MS-Xα calculations for HI show this monotonic decrease occurs out to ~110 eV photon energy.[87] The theoretical BR is in excellent agreement with experiment up to ~60 eV photon energy, whereupon intershell correlation with the I 4d shell causes significant deviations from the predicted behavior of a monotonically decreasing function. The feature maximizing at ~90 eV photon energy in the branching ratio has been assigned to such intershell correlation, and discussed previously in section 3.3.2. It is interesting

Table 4.4.4-3

Theoretical MS-Xα Eigenphase Sum Features for CF_3I

Channel Symmetry	MS-Xα Results		
	E_{phase}(eV)[a]	Δ(Eigenphase Sum)[b]	Partial-Wave[c]
e	15.2	~π	1, 2, 4
a_1	17.2	~π	0, 3, 5

a) The resonance energy E_{phase} is given by the inflection point in the plot of the eigenphase sum versus photoelectron kinetic energy.
b) According to Krelle's[55] first resonance criteria, the eigenphase must change by ≥ 0.3π over an energy range ΔE ≤ 6 eV.
c) Predominant asymptotic partial-wave components are shown.

to note that the predominant asymptotic partial-wave components for the continuum state of this orbital, consists of s-, p-, and d-waves, with the largest contributions coming from the d-waves (ke channel) and the smallest from the s-waves. This is consistent with an atomic photoionization picture; namely that p → εd is the most intense transition, p → εp is dipole forbidden in the atomic case (but would be allowed in the molecular case), and p → εs is much less intense than the p → εd transition. This atomic-like photoionization behavior implies that the 4e MO is rather localized in nature.

Since the 4e MO differs greatly in orbital character from the $1t_1$ and $4t_2$ MO's of CF_4 (Table 4.4.4-1), a more meaningful correlation can be found by comparing the 4e MO of CF_3I to the $5\pi_u$ orbital in XeF_2 (Figure 5.4.1-1), since it also shows a similar monotonic decrease in σ and BR above ~20 eV photon energy. Although the $5\pi_u$ orbital does involve significant F 2p character, the fact remains that this MO largely involves the Xe 5p atomic orbitals. Both of these two orbitals have large 5p character of π-symmetry (the 4e MO of CF_3I has local π-symmetry about the C-I bond), and have very similar cross section behavior above ~20 eV photon energy.

In Figure 4.4.4-2 the theoretical BR for the $4a_1$ MO shows a pronounced decrease above threshold and a minimum at ~35 eV photon energy, in good agreement with experiment. As discussed previously, the $4a_1$ MO is the

C-I bonding orbital and involves primarily overlap of the C $2p_z$ and I $5p_z$ atomic orbitals. The rather slow increase in branching ratio from ~5.6% → ~6.7% which occurs above ~70 eV photon energy is due to the I 5p Cooper minimum at ~45 eV kinetic energy.[26,87,106] Since the $4a_1$ BR behavior simply increases slowly in this region and is different than the distinct maximum observed at ~90 eV photon energy for the 4e MO, it must be concluded that intershell correlation between the $4a_1$ orbital and 4d shell is not dominant in this MO. If this is true, then it seems that the intershell correlation effect is largest when the localized 4d core shell is interacting with a localized and atomic-like 5p orbital, as is the case with the 4e MO of CF_3I. On the other hand, the I $5p_z$ atomic orbital involved in the $4a_1$ C-I bonding MO is heavily mixed with C 2s and C $2p_z$, and delocalized over the entire C-I bond. This slow increase in branching ratio probably arises from the combination of weak intershell correlation and weak contributions from the I 5p Cooper minimum. Carlson et al.[87] have found that the C-I bonding MO of CH_3I does not show a distinct minimum in σ in this region, but that a shallow minimum in β does occur. This group has concluded that bonding orbitals involving halogen atoms show only weak effects of the Cooper minimum.[87]

From threshold to the minimum at ~35 eV photon energy, the predominant asymptotic partial-waves involved in the continuum states of the $4a_1$ MO are ℓ = 0, 1, and 2,

with the largest contribution from the d-waves. This is reminiscent of the behavior found for the 4e MO, which involves largely I 5p lone pair electrons. The sharp decrease observed in the $4a_1$ branching ratio from ~21 eV to ~35 eV photon energy arises from the large I $5p_z$ content of this MO. A slight perturbation of this monotonic behavior is predicted to occur at ~13 eV kinetic energy, due to a weak contribution from the e shape resonance (Table 4.4.4-3). By analogy to the 4e MO, whose cross section decreases monotonically above threshold, one would expect the I $5p_z$ content of the $4a_1$ MO to behave similarly with photon energy. The increase in cross section and BR above ~35 eV photon energy must be due to cross section contributions from the F 2p and C 2p atomic orbitals.

These conclusions are confirmed by the results of a "minimal" MS-Xα calculation that was done on CF_3I. Unlike the "extended" MS-Xα calculation reported in Table 4.3.1-1 and Figures 4.4.4-(1-11) for CF_3I, the minimal calculation restricted the carbon and fluorine spheres to $\ell \leq 1$ (s-, p-waves), and the iodine sphere to $\ell \leq 2$ (s-, p-, and d-waves), for both the ground state and continuum states. With the exception of the 4e and $4a_1$ MO's, the minimal calculation yielded cross sections that were without any of the structure given by the extended calculation, and that were approximately an order of magnitude smaller. From an atomic point of view this makes considerable sense, since the rest of the MO's involve primarily C 2p and F 2p atomic

orbitals. Exclusion of d-waves on the carbon and fluorine spheres effectively disallows the important $p \rightarrow \epsilon d$ process. It is interesting to note that the minimal calculation yielded monotonically decreasing cross sections for both the 4e and $4a_1$ MO's. The minimal 4e cross section differed very little from the extended calculation, verifying that contributions larger than d-waves are relatively unimportant for this case. The similarity of the minimal 4e and $4a_1$ cross sections is strong theoretical evidence that the decrease in the $4a_1$ cross section from threshold to ~35 eV photon energy, is indeed caused by the I $5p_z$ atomic orbital contribution to this MO.

In Figure 4.4.4-3 the combined results of the 3e and $1a_2$ molecular orbitals of CF_3I are shown. The theoretical branching ratios are in good agreement with experiment. The experimental BR rises rapidly above 21 eV photon energy, maximizing at ~30 eV photon energy (~14 eV kinetic energy). It is interesting to note that this maximum in the experimental BR occurs where a shoulder is predicted theoretically, with the theoretical BR maximum occurring some 9 eV higher kinetic energy at ~39 eV photon energy. The individual theoretical cross sections for the $1a_2$ and 3e MO's are shown in Figures 4.4.4-4 and 4.4.4-5, respectively. The basic behavior of their theoretical cross sections is very similar. The 3e theoretical cross section (Figure 4.4.4-5) shows evidence of a rather weak shape resonance in the ke channel (Table 4.4.4-3) at ~14 eV

kinetic energy, followed by a very broad structure which maximizes at ~26 eV kinetic energy above threshold. The behavior of the $1a_2$ theoretical cross section (Figure 4.4.4-4) is similar in that it shows a broad structure which maximizes at ~22 eV kinetic energy, with only the slightest hint of a shoulder around the region where the eigenphase sum changes in the ke continuum channel (15.2 eV kinetic energy). The maximum occurring at ~30 eV photon energy (~14 eV kinetic energy) in the branching ratio is tentatively assigned as arising from an e shape resonance on the 3e MO. The position of this feature (~14 eV kinetic energy) is in good agreement with the calculated value of 15.2 eV kinetic energy (Table 4.4.4-3).

The basic similarity (ignoring shape resonances) of the 3e and $1a_2$ MO's in CF_3I is a reflection of the fact that both of these MO's involve F 2p lone pair electrons. The σ and BR behavior of the $1a_2$ MO of CF_3I (Figure 4.4.4-4) correlates well with the $1t_1$ MO of CF_4 (Figure 4.4.2-1). Both of these molecular orbitals show a rather broad maximum feature in σ and BR. Correlation of the 3e MO of CF_3I is more complicated, since it is not clear if this should correlate with the $4t_2$ (Figure 4.4.2-2) or $1t_1$ MO (Figure 4.4.2-1) in CF_4 (i.e. both t_2 and t_1 split to yield an e symmetry in C_{3v} symmetry). The similarity of the 3e and $1a_2$ σ and BR shapes (ignoring shape resonances) seems to suggest the $1t_1$ MO of CF_4. In fact, the basic shape of the (3e + $1a_2$) σ and BR of CF_3I (Figure 4.4.4-3)

is quite similar to the $1t_1$ σ and BR of CF_4 (Figure 4.4.2-1), and very different than the $4t_2$ of CF_4 (Figure 4.4.2-2). This correlation is in agreement with that proposed by Potts et al.,[114] between CHF_3 and CF_4. Comparing partial cross sections and branching ratios between related molecules may prove to be an extremely useful way to actually verify proposed correlation schemes.

For the 2e MO of CF_3I (Figure 4.4.4-6), the theoretical cross section shows a weak e shape resonance feature at ~16.3 eV kinetic energy, followed by a broad structure which maximizes at ~27 eV kinetic energy. It is interesting to note that this double maximum feature occurs in the 1e (Figure 4.4.4-9), 2e (Figure 4.4.4-6), and 3e (Figure 4.4.4-5) MO's of CF_3I. As shown in Table 4.4.4-1, the 2e MO of CF_3I consists of F 2p lone pair electrons and should correlate with the 1e MO of CF_4 (Figure 4.4.2-3). The experimental BR of the 2e MO of CF_3I shows evidence of a maximum at ~29 eV photon energy (~12 eV kinetic energy), which we tentatively assign as arising from an e shape resonance (Table 4.4.4-3). It seems that the MS-Xα calculation is underestimating the strength of the e channel resonance which occurs in the 2e and 3e MO's. Overall, the agreement of theory with the experimental BR for the 2e MO of CF_3I is fair up to ~41 eV photon energy, where theory begins to underestimate the increase in branching ratio. The 1e MO of CF_4 (Figure 4.4.2-3) shows a very different behavior in the experimental BR (roughly

constant from 20-50 eV photon energy), and theory fairs just as poorly at predicting the experimental BR behavior. The experimental branching ratios for the 1e MO of CF_4 and the 2e MO of CF_3I have similar behavior though at higher photon energies (50-110 eV).

The results for the $3a_1$ MO of CF_3I are shown in Figure 4.4.4-7. The theoretical cross section shows an a_1 shape resonance feature at ~18 eV kinetic energy (Table 4.4.4-3), followed by a broad structure which maximizes at ~31 eV kinetic energy above threshold. The experimental BR shows little evidence of this a_1 resonance, showing instead a slow linear increase until ~60 eV photon energy. The theoretical BR deviates most strongly from experiment below ~30 eV photon energy. The $3a_1$ MO is related to the $2a_1$ MO in that they are the out-of-phase and in-phase combinations, respectively, of the F 2p and I 5s atomic orbitals. Both of these molecular orbitals have similar charge distributions and substantial I 5s character (Table 4.4.4-1). It is interesting to note the different theoretical cross section behavior predicted for the $2a_1$ MO (Figure 4.4.4-10). Instead of a decrease close to threshold, the $2a_1$ theoretical σ increases from threshold to ~10 eV kinetic energy. Like the $3a_1$ MO, the $2a_1$ theoretical σ shows an a_1 shape resonance feature at ~16.3 eV kinetic energy, followed by a sharp decrease thereafter.

With the exception of the a_1 shape resonance features, the theoretical σ and BR behavior of these two MO's is quite different, in spite of the fact that the charge distributions are very similar (Table 4.4.4-1). This difference in cross section behavior is undoubtedly due to the difference in ground state nodal properties which arise from this in-phase and out-of-phase mixing of the F 2p and I 5s atomic orbitals. This difference in ground state nodal properties allows the d-wave component of the continuum states to overlap constructively up to ~10 eV kinetic energy for the $2a_1$ MO, accounting for the increase in σ. Likewise, the node present in the $3a_1$ MO causes the d-wave component of the continuum states to overlap destructively in this region, causing σ to decrease. The sharp increase which occurs in the $2a_1$ cross section and which maximizes at ~32 eV photon energy, explains very nicely why the shoulder which appears at ~21.5 ± 0.2 eV binding energy (and assigned as the $2a_1$ MO, Figure 3.3.2-1) is most noticeable at ~35 eV photon energy.

The theoretical cross section for the 1e MO (Figure 4.4.4-9) shows the same double maximum behavior that the 2e and 3e MO's of CF_3I display, although the 1e differs in that it is a bonding orbital involving overlap of the C 2p and F 2p atomic orbitals. The maximum at ~13.6 eV kinetic energy is due to an e shape resonance, and is followed by a broad structure at ~28 eV kinetic energy. Analysis of the partial waves shows that this e resonance is due to

resonant trapping by the potential barrier of primarily d-wave components of the continuum molecular wave function, with some p-wave contribution. In the plot of $(2a_1 + 1e)$ shown in Figure 4.4.4-8, the theoretical σ is very similar in shape to that of the 1e. Fair agreement between theory and experiment occurs for the $(2a_1 + 1e)$ BR, although the theoretical BR plot appears to be compressed relative to the experimental. A shift of theory by ~3-4 eV to higher kinetic energy gives even better agreement. Theory reproduces the experimental double maximum behavior and minimum observed close to threshold fairly well, although the second experimental maximum is shifted to ~20 eV higher kinetic energy. It seems likely that the first maximum at ~35-41 eV photon energy arises as a result of the e shape resonance on the 1e MO, although smaller contributions from the a_1 resonance of the $2a_1$ MO are also possible. The experimental BR for the $3t_2$ MO of CF_4 (Figure 4.4.2-4) has a very similar double maximum behavior to that of the $(2a_1 + 1e)$ of CF_3I (Figure 4.4.4-8). This similarity is due to the fact that the bonding 1e MO of CF_3I correlates with the $3t_2$ bonding MO in CF_4.

Finally, the results for the $1a_1$ bonding molecular orbital of CF_3I are shown in Figure 4.4.4-11. The $1a_1$ MO is primarily a C-F bonding orbital (Table 4.4.4-1) involving overlap of the C 2s and F 2p atomic orbitals. The theoretical cross section of the $1a_1$ MO of CF_3I is very similar in shape and magnitude to the $4a_1$ C-F bonding MO of

CF_4 (Figure 4.4.2-5), with the exception of the weak e channel resonance that occurs at ~13 eV kinetic energy in the $1a_1$ MO. Both of these orbitals show a broad maximum in the theoretical cross section of ~2.5 Mb at ~23 eV kinetic energy. While the experimental BR for the $4a_1$ MO of CF_4 (Figure 4.4.2-5) increases in a roughly linear fashion up to ~50 eV photon energy, the $1a_1$ MO BR of CF_3I (Figure 4.4.4-11) deviates in slope from this trend at ~41 eV photon energy. This change in slope is accompanied by positive deviations of the threshold BR from experiment. The experimental BR for the $1a_1$ MO of CF_3I shows little evidence of the predicted e shape resonance at ~13 eV kinetic energy, but this is not surprising considering the extreme weakness of it.

4.5.1 Conclusions

Experimental branching ratios have been determined for the valence orbitals of CF_4, SiF_4, and CF_3I as a function of photon energy. In conjunction with this, multiple scattering $X\alpha$ calculations were performed on these compounds. The CF_4 results were compared to the previous CF_4 results of Carlson et al.,[61] and good agreement with both theory[105] and experiment[61] was found. A comparison between CF_4 and SiF_4 was undertaken first. The results reveal that although there are some qualitative similarities, SiF_4 has much more structure in σ, BR, and β. This was even found to be true for the first three

molecular orbitals in CF_4 and SiF_4, which are essentially F 2p lone pair in character for both compounds. Our observation seriously questions the general validity of the normal practice in MO assignment, of comparing the spectra of similar compounds at low photon energies (such as He I at 21.2 eV and He II at 40.8 eV). As can be readily seen in Figures 4.2.1-1 and 4.2.1-2, the first three molecular orbitals in CF_4 and SiF_4 have dramatically different intensities at 32 eV photon energy, even though their orbital characters are very similar. Although assignments based on comparison of He I/He II spectra are less likely to be incorrect than assignments based on one energy, serious errors can occur if a molecular orbital exhibits a strong shape resonance near either photon energy. This happens in SiF_4 on the $5a_1$ MO (see Figures 4.2.1-2 and 4.4.3-6), which exhibits a strong t_2 shape resonance near He II at ~44 eV photon energy.

The intensity differences found in comparing the first three molecular orbitals of CF_4 and SiF_4 must be due to changes in the molecular potential which scatters the outgoing electron. These changes are in turn partially caused by the differing radial nodal structures of the carbon and silicon valence s- and p-orbitals,[124] and the differing M-F bond lengths. Recently Sette et al.[125,126] showed that the resonance position is a sensitive function of the bond length. However, the work by Sette et al. has received strong criticism recently that their ideas may be

highly oversimplified. Although it is quite reasonable to expect that bond length plays a role in shape resonances, it appears that the role of bond length may not be as dominant as these authors claim. In addition, much of the structure in SiF_4 is probably due to the involvement of the Si 3d orbitals. Analysis of the results from our MS-Xα calculation shows that higher basis functions such as $\ell = 2,3$ are important for these resonances.

The generally good agreement for SiF_4 between the experimental BR and those calculated from the MS-Xα method confirms the assignment of the valence peaks on a cross section basis as $1t_1 < 5t_2 < 1e < 4t_2 < 5a_1$, in order of increasing binding energy. Poor agreement does occur, however, for the $1t_1$ and $5t_2$ molecular orbitals for kinetic energies less than ~12.9 eV. Although this is not currently understood, cases have been found where theoretically predicted resonances are observed in some orbital cases but absent in others.[65] Similar valence results have been obtained for $SiCl_4$ by Carlson et al.[127] Indeed, molecules such as CO_2, BF_3, SF_6, and SiF_4 pose a major challenge to our understanding of shape resonances in general, and further work is required. For SiF_4, future work should involve measuring β, and measuring the total photoionization cross section in order that cross sections may be obtained. A search close to threshold for the predicted a_1 resonance should be done on the $5t_2$ and $4t_2$ molecular orbitals of SiF_4.

In general, the theoretical cross sections and branching ratios for CF_3I are quite similar to those found in CF_4, if one excludes the I 5p lone pair orbital (4e) and the C-I bonding orbital ($4a_1$) of CF_3I. The agreement between theory and experiment is generally quite good, although deviations were found for the 2e' and $3a_1$ MO's. Rather weak shape resonances are predicted to occur in the e continuum channel on all the remaining MO's (except $2a_1$ and $3a_1$) and in the a_1 continuum channel for the $2a_1$ and $3a_1$ MO's. While no firm evidence was found to support the predicted weak a_1 shape resonances, the 3e, 2e, and 1e MO's of CF_3I do show evidence to suggest that they can support an e shape resonance. The e shape resonances involve trapping primarily of d-waves by the potential barrier. The fundamental question which arises, is why does CF_3I show this additional weak shape resonant behavior over CF_4?

The problem is a perplexing one, but it probably has to do with the perturbation that occurs in the molecular potential when one substitutes a fluorine atom by an iodine atom. Such a substitution obviously lowers the symmetry of the molecular potential. Lowering the molecular potential symmetry means that there may now be certain directions where the photoelectron experiences a potential barrier strong enough to support an additional shape resonance. This can be rephrased in terms of basis functions of the continuum state - lowering of the molecular potential symmetry may lead to certain important

partial waves in the continuum function experiencing a potential barrier (i.e. centrifugal barrier) strong enough to support an additional shape resonance. In CF_3I, these additional weak e shape resonances are caused by important d-wave contributions in the continuum function experiencing a potential barrier large enough now to support a quasi-bound d-state.

Analysis of the $4a_1$ and 4e branching ratios of CF_3I from ~50-110 eV photon energy, reveal that intershell correlation between the I 5p electrons and the I 4d shell occurs strongly only in the 4e MO. The weak BR increase in the $4a_1$ MO probably arises from a combination of weak intershell correlation and weak contributions from the I 5p Cooper minimum. Since the 4e MO consists of I 5p lone pair electrons, while the $4a_1$ MO has the I $5p_z$ electrons involved in bonding, the implication is that intershell correlation is strongest between the I 4d shell and a localized atomic I 5p orbital.

4.6.1 References

1. J.L. Dehmer, "Resonances in Electron-Molecule Scattering, van der Waals Complexes, and Reactive Chemical Dynamics", edited by D.G. Truhlar, American Chemical Society Symposium Series 263, (American Chemistry Society, Washington, D.C., 1984), p. 139.

2. P.W. Langhoff, "Resonances in Electron-Molecule Scattering, van der Waals Complexes, and Reactive Chemical Dynamics", edited by D.G. Truhlar, American Chemical Society Symposium Series 263, (American Chemistry Society, Washington, D.C., 1984), p. 113.

3. R.E. LaVilla and R.D. Deslattes, J. Chem. Phys. 44, 4399 (1966).

4. J.L. Dehmer, J. Chem. Phys. 56, 4496 (1972).

5. D. Blechschmidt, R. Haensel, E.E. Koch, U. Nielsen, and T. Sagawa, Chem. Phys. Lett. 14, 33 (1972).

6. R.E. LaVilla, J. Chem. Phys. 57, 899 (1972).

7. F.A. Gianturco, C. Guidotti, and U. Lamanna, J. Chem. Phys. 57, 840 (1972).

8. V.P. Sachenko, E.V. Polozhentsev, A.P. Kovtun, Yu. F. Migal, R.V. Vedrinski, and V.V. Kolesnikov, Phys. Lett. 48A, 169 (1974).

9. J.-H. Fock and E.E. Koch, Chem. Phys. 96, 125 (1985).

10. J.L. Dehmer, A.C. Parr, S. Wallace, and D. Dill, Phys. Rev. A 26, 3283 (1982).

11. D.Y. Smith, Phys. Rev. 137, A574 (1965).

12. J.L. Dehmer and D. Dill, Phys. Rev. Lett. 35, 213 (1975).

13. R.S. Wallace, Ph.D. Thesis, Boston University Graduate School (1980).

14. G.R. Wright, C.E. Brion, and M.J. van der Wiel, J. Electron Spectrosc. Relat. Phenom. 1, 457 (1972/73).

15. G.R. Wright and C.E. Brion, J. Electron Spectrosc. Relat. Phenom. 4, 313 (1974).

16. L.I. Schiff, "Quantum Mechanics", (McGraw-Hill, New York, 1968), p. 121.

17. S.T. Manson, "Photoemission in Solids I", edited by M. Cardona and L. Ley, Topics in Applied Physics, Volume 26 (Springer-Verlag, New York, 1978), p. 135.

18. S.T. Manson and D. Dill, "Electron Spectroscopy: Theory, Techniques and Applications", Vol. 2, edited by C.R. Brundle and A.D. Baker (Academic Press, New York, 1978), p. 158, and references therein.

19. J.W. Cooper, Phys. Rev. 128, 681 (1962).

20. S.T. Manson and J.W. Cooper, Phys. Rev. 165, 126 (1968).

21. S.T. Manson, Phys. Rev. A 3, 1260 (1971).

22. S.T. Manson, Phys. Rev. A 5, 668 (1972).

23. S.T. Manson, Phys. Rev. A 6, 1013 (1972).

24. J.W. Cooper and S.T. Manson, Phys. Rev. 177, 157 (1969).

25. D.J. Kennedy and S.T. Manson, Phys. Rev. A 5, 227 (1972).

26. S.T. Manson, J. Electron Spectrosc. Relat. Phenom. 1, 413 (1972/73).

27. A.W. Weiss, Adv. At. Molecular Phys. 9, 1 (1973).

28. U. Fano, Phys. Rev. 124, 1866 (1961).

29. F. Mies, Phys. Rev. 175, 164 (1968).

30. P.G. Burke and W.D. Robb, Adv. At. Molecular Phys. 11, 143 (1975).

31. H.P. Kelly, Phys. Rev. A 6, 1048 (1972).

32. G. Wendin, J. Phys. B 6, 42 (1973).

33. M. Ya. Amusia, N.A. Cherepkov, and L.V. Chernysheva, Sov. Phys.-JETP 33, 90 (1971).

34. G. Wendin, "Photoionization and Other Probes of Many-Electron Interactions", edited by F. Wuilleumier (Plenum, New York, 1976), p. 61.

35. J.W. Rabalais, "Principles of Ultraviolet Photoelectron Spectroscopy", (Wiley-Interscience, New York, 1977), p. 140.

36. F.O. Ellison, J. Chem. Phys. 61, 507 (1974).

37. J.W. Rabalais, T.P. Debies, J.L. Berkosky, J.J. Huang, and F.O. Ellison, J. Chem. Phys. 61, 516 (1974).

38. L.L. Lohr, Jr., and M.B. Robin, J. Am. Chem. Soc. 92, 7241 (1970).

39. W. Thiel and A. Schweig, Chem. Phys. Lett. 12, 49 (1971).

40. W. Thiel and A. Schweig, Chem. Phys. Lett. 16, 409 (1972).

41. A. Schweig and W. Thiel, Chem. Phys. Lett. 21, 541 (1973).

42. J.W. Davenport, Ph.D. Thesis, University of Pennsylvania (1976), p. 23.

43. W. Thiel, Chem. Phys. 57, 227 (1981), and references therein.

44. D. Dill and J.L. Dehmer, J. Chem. Phys. 61, 692 (1974).

45. K.H. Johnson, J. Chem. Phys. 45, 3085 (1966).

46. J.C. Slater and K.H. Johnson, Phys. Rev. B 5, 844 (1972).

47. K.H. Johnson, Int. J. Quantum Chem. Symp. 1, 361 (1967).

48. K.H. Johnson, "Advances in Quantum Chemistry", Volume 7, edited by P.-O. Löwdin, (Academic Press, New York, 1973), p. 143.

49. F.C. Smith, Jr., and K.H. Johnson, Phys. Rev. Lett. 22, 1168 (1969).

50. K.H. Johnson and F.C. Smith, Jr., Phys. Rev. Lett. 24, 139 (1970).

51. K.H. Johnson and F.C. Smith, Jr., Chem. Phys. Lett. 7, 541 (1970).

52. K.H. Johnson and F.C. Smith, Jr., Chem. Phys. Lett. 10, 219 (1971).

53. J.W. Davenport, Ph.D. Thesis, University of Pennsylvania (1976).

54. J.W. Davenport, Phys. Rev. Lett. 36, 945 (1976).

55. J. Kreile, A. Schweig, and W. Thiel, Chem. Phys. Lett. 108, 259 (1984).

56. F.A. Grimm, Chem. Phys. 81, 315 (1983).

57. T.A. Carlson, M.O. Krause, F.A. Grimm, P. Keller, and J.W. Taylor, J. Chem. Phys. 77, 5340 (1982).

58. T.A. Carlson, M.O. Krause, D. Mehaffy, J.W. Taylor, F.A. Grimm, and J.D. Allen, Jr., J. Chem. Phys. 73, 6056 (1980).

59. D. Mehaffy, P.R. Keller, J.W. Taylor, T.A. Carlson, M.O. Krause, F.A. Grimm, and J.D. Allen, Jr., J. Electron Spectrosc. Relat. Phenom. 26, 213 (1982).

60. F.A. Grimm, J.D. Allen, Jr., T.A. Carlson, M.O. Krause, D. Mehaffy, P.R. Keller, and J.W. Taylor, J. Chem. Phys. 75, 92 (1981).

61. T.A. Carlson, A. Fahlman, W.A. Svensson, M.O. Krause, T.A. Whitley, F.A. Grimm, M.N. Piancastelli, and J.W. Taylor, J. Chem. Phys. 81, 3828 (1984).

62. E.W. Plummer, T. Gustafsson, W. Gudat, and D.E. Eastman, Phys. Rev. A 15, 2339 (1977).

63. T. Gustafsson, Phys. Rev. A 18, 1481 (1978).

64. H.J. Levinson, T. Gustafsson, and P. Soven, Phys. Rev. A 19, 1089 (1979).

65. J.L. Dehmer, A.C. Parr, S.H. Southworth, and D.M.P. Holland, Phys. Rev. A 30, 1783 (1984).

66. M. Roche, D.R. Salahub, and R.P. Messmer, J. Electron Spectrosc. Relat. Phenom. 19, 273 (1980).

67. G.M. Bancroft, E. Pellach, and J.S. Tse, Inorg. Chem. 21, 2950 (1982).

68. B.W. Yates, K.H. Tan, G.M. Bancroft, L.L. Coatsworth, and J.S. Tse, J. Chem. Phys. 83, 4906 (1985).

69. B.W. Yates, K.H. Tan, G.M. Bancroft, L.L. Coatsworth, J.S. Tse, and G.J. Schrobilgen, J. Chem. Phys., in press (1986).

70. N. Rosch, W.G. Klemperer, and K.H. Johnson, Chem. Phys. Lett. 23, 149 (1973).

71. U. Scherz, J. Chem. Phys. 56, 1315 (1972).

72. J.C. Slater, "The Calculation of Molecular Orbitals", (John Wiley, New York, 1979).

73. J.C. Slater, "The Self-Consistent Field for Molecules and Solids: Quantum Theory of Molecules and Solids", Volume 4, (McGraw-Hill, New York, 1974).

74. R. Latter, Phys. Rev. 99, 510 (1955).

75. K.H. Tan, G.M. Bancroft, L.L. Coatsworth, and B.W. Yates, Can. J. Phys. 60, 131 (1982).

76. B.W. Yates, K.H. Tan, L.L. Coatsworth, and G.M. Bancroft, Phys. Rev. A 31, 1529 (1985).

77. J.A.R. Samson, Phil. Trans. Roy. Soc. London A 268, 141 (1970).

78. S. Aksela, K.H. Tan, G.M. Bancroft, H. Aksela, B.W. Yates, and L.L. Coatsworth, Phys. Rev. A 32, 1219 (1985).

79. G.M. Bancroft, I. Adams, L.L. Coatsworth, C.D. Bennewitz, J.D. Brown, and W.D. Westwood, Anal. Chem. 47, 586 (1975).

80. L.C. Lee, E. Phillips, and D.L. Judge, J. Chem. Phys. 67, 1237 (1977).

81. K. Schwarz, Phys. Rev. B 5, 2466 (1972).

82. C.R. Brundle, M.B. Robin, and H. Basch, J. Chem. Phys. 53, 2196 (1970).

83. K. Hagen and K. Hedberg, J. Chem. Phys. 59, 1549 (1973).

84. A.P. Cox, G. Duxbury, J.A. Hardy, Y. Kawashima, J.C.S. Faraday II 76, 339 (1980).

85. F.A. Grimm, T.A. Carlson, W.B. Dress, P. Agron, J.O. Thomson, and J.W. Davenport, J. Chem. Phys. 72, 3041 (1978).

86. M. Piancastelli, P.R. Keller, J.W. Taylor, F. Grimm, T.A. Carlson, M.O. Krause, and D. Lichtenberger, J. Electron Spectrosc. Relat. Phenom. 34, 205 (1984), and references therein.

87. T.A. Carlson, A. Fahlman, M.O. Krause, P.R. Keller, J.W. Taylor, T. Whitley, and F.A. Grimm, J. Chem. Phys. 80, 3521 (1984).

88. G.M. Bancroft, B.W. Yates, K.H. Tan, and L.L. Coatsworth, J. Chem. Soc. Chem. Commun., 1613 (1984).

89. T.M. Zimkina and A.S. Vinogradov, J. Phys. (Paris) 32, C43 (1971); A.S. Vinogradov and T.M. Zimkina, Opt. Spectrosc. (USSR) 31, 288 (1971).

90. W. Hayes and F.C. Brown, Phys. Rev. A 6, 21 (1972).

91. H. Friedrich, B. Pittel, P. Rabe, W.H.E. Schwarz, and B. Sonntag, J. Phys. B 13, 25 (1980).

92. R.N.S. Sodhi, S. Daviel, C.E. Brion, and C.G.B. de Souza, J. Electron Spectrosc. Relat. Phenom. 35, 45 (1985), and references therein.

93. A.A. Pavlychev, A.S. Vinogradov, T.M. Zimkina, D.E. Onopko, and S.A. Titov, Opt. Spectrosc. (USSR) 47, 40 (1979).

94. A.A. Pavlychev, A.S. Vinogradov, and T.M. Zimkina, Opt. Spectrosc. (USSR) 52, 139 (1982).

95. M. Ya. Amusia, A.A. Pavlychev, A.S. Vinogradov, D.E. Onopko, and S.A. Titov, Opt. Spectrosc. (USSR) 53, 91 (1983).

96. P.J. Basset and D.R. Lloyd, J. Chem. Soc. A, 641 (1971).

97. A.E. Jonas, G.K. Schweitzer, F.A. Grimm, and T.A. Carlson, J. Electron Spectrosc. Relat. Phenom. 1, 29 (1972/73).

98. M.B. Hall, M.F. Guest, I.H. Hillier, D.R. Lloyd, A.F. Orchard, and A.W. Potts, J. Electron Spectrosc. Relat. Phenom. 1, 497 (1972/73).

99. D.R. Lloyd and P.J. Roberts, J. Electron Spectrosc. Relat. Phenom. 7, 325 (1975).

100. R. Jadrny, L. Karlsson, L. Mattson, and K. Siegbahn, Chem. Phys. Lett. 49, 203 (1977).

101. F.C. Brown, R.Z. Bachrach, and A. Bianconi, Chem. Phys. Lett. 54, 425 (1978).

102. T. Cvitaš, H. Gusten, L. Klasinc, I. Novadj, and H. Vančik, Z. Naturforsch. 33A, 1528 (1978).

103. D.W. Lindle, P.H. Kobrin, C.M. Truesdale, T.A. Ferrett, P.A. Heimann, H.G. Kerkhoff, U. Becker, and D.A. Shirley, Phys. Rev. A 30, 239 (1984).

104. A.P. Hitchcock and C.E. Brion, J. Electron Spectrosc. Relat. Phenom. 13, 219 (1978).

105. J. Stephens, D. Dill, and J.L. Dehmer, J. Chem. Phys. (in press).

106. S.T. Mason, Phys. Rev. A 31, 3698 (1985).

107. T.A. Carlson, M.O. Krause, A. Fahlman, P.R. Keller, J.W. Taylor, T. Whitley, and F.A. Grimm, J. Chem. Phys. 79, 2157 (1983).

108. R.G. Newton, "Scattering Theory of Particles and Waves", (Springer, Berlin, 1982).

109. J. Macek, Phys. Rev. A 2, 1101 (1970).

110. A.U. Hazi, Phys. Rev. A 19, 920 (1979).

111. R.R. Lucchese, G. Raseev, and V. McKoy, Phys. Rev. A 25, 2572 (1982).

112. R.R. Lucchese and V. McKoy, J. Chem. Phys. 85, 2166 (1981).

113. T. Cvitaš, H. Gusten, L. Klasinc, J. Chem. Phys. 67, 2687 (1977).

114. A.W. Potts, H.J. Lempka, D.G. Streets, and W.C. Price, Phil. Trans. Roy. Soc. London A 268, 59 (1970).

115. R. Jadrny, L. Karlsson, L. Mattsson, and K. Siegbahn, Physica Scripta 16, 235 (1977).

116. J. Doucet, P. Sauvageau, and C. Sandorfy, J. Chem. Phys. 58, 3708 (1973).

117. H.J.T. Preston and J.J. Kaufman, Chem. Phys. Lett. 50, 157 (1977).

118. A.W. Potts, I. Novak, F. Quinn, G.V. Marr, B. Dobson, I.H. Hillier, and J.B. West, J. Phys. B 18, 3177 (1985).

119. W. Lotz, J. Opt. Soc. Am. 60, 206 (1970).

120. F.A. Cotton, "Chemical Applications of Group Theory", (Wiley-Interscience, New York, 1971), p. 289.

121. R.A.A. Boschi and D.R. Salahub, Can. J. Chem. 52, 1217 (1974).

122. J.W. Rabalais, "Principles of Ultraviolet Photoelectron Spectroscopy", (Wiley-Interscience, New York, 1977), p. 43.

123. R. Cambi, G. Ciullo, A. Sgamellotti, F. Tarantelli, R. Fantoni, A. Giardini-Guidoni, M. Rosi, and R. Tiribelli, Chem. Phys. Lett. 90, 445 (1982).

124. M.B. Robin, Chem. Phys. Lett. 119, 33 (1985).

125. F. Sette, J. Stohr, and A.P. Hitchcock, Chem. Phys. Lett. 110, 517 (1984).

126. F. Sette, J. Stohr, and A.P. Hitchcock, J. Chem. Phys. 81, 4906 (1984).

127. T.A. Carlson, A. Fahlman, M.O. Krause, T.A. Whitley, F.A. Grimm, M.N. Piancastelli, and J.W. Taylor, J. Chem. Phys. 84, 641 (1986).

CHAPTER 5

PHOTOELECTRON STUDY OF THE VALENCE BAND PARTIAL CROSS SECTIONS OF XeF_2

5.1.1 Introduction

In recent years there has been a continuing interest in theoretical and spectroscopic studies of the xenon fluorides, in the far UV and soft X-ray regions. Photoelectron spectra of the XeF_2 core[1-5] and valence[3,6,7] levels have been obtained by several workers. The core level work has been important for determining atomic charges,[1,2,4] studying the large ligand field splitting on the Xe 4d levels,[3] and correlation satellites (shakeup) on the core levels.[3] After a number of problems with the valence band assignment,[3,6,7] there is general agreement on the valence band assignment[3,8,9] despite large discrepancies between ab initio[10,11] and Xα calculations.[4,8,9,12] In addition, there have been a number of absorption cross section measurements in the far UV and soft X-ray regions[13-16] covering both the valence band and Xe 4d levels

In this chapter, the first five valence band partial cross sections for gas phase XeF_2 are reported over the photon energy range 20-50 eV Detailed theoretical partial cross sections and branching ratios obtained from

MS-Xα calculations are compared with experiment. The interest in studying XeF_2 stems firstly from the fact that it is a linear triatomic molecule containing Xe as the central atom. As discussed by Sette et al.,[17] shape resonance positions in linear triatomic molecules such as N_2O, CO_2 and COS do not correlate with their bond lengths because multiple scattering interference effects are extremely important.[18] In such linear cases, outgoing photoelectrons are strongly forward scattered.[18] This effect is expected to be even larger in XeF_2 since the central Xe atom is of much higher atomic number (Z = 54), resulting in a very large electron-atomic scattering factor.[19] Secondly, the bond length in XeF_2 (r_{Xe-F} = 2.00 Å[10]) is certainly one of the longest studied for a polyatomic molecule. Comparison of the partial cross sections obtained for XeF_2 with those of the well-studied analogues (e.g. CO_2) should shed some light on the relative importance of bond length on resonance position in linear triatomic molecules. Thirdly, due to the valence band assignment problems and theoretical calculation problems mentioned previously, the generally accepted valence band assignment should be confirmed finally, based on their experimental partial cross section behavior.

5.2.1 Experimental

XeF_2 crystals were prepared using a previously reported method[20] and used without further purification.

Samples of XeF_2 were kindly supplied by G.J. Schrobilgen. Gas phase photoelectron spectra of XeF_2 were obtained, once again, with photons from the Canadian Synchrotron Radiation Facility (CSRF)[21,22] at Tantalus I and the Leybold-Heraeus LHS-11 photoelectron spectrometer in conjunction with a multicapillary array gas probe. The experimental arrangement has been described elsewhere in the literature[23] and in Chapter 2 of this thesis. It was found that heating a small teflon sample container of solid XeF_2 behind the multicapillary array to ~50°C generated sufficient vapor pressure to collect spectra. Decomposition of XeF_2 was minimal, as evidenced by the absence of atomic Xe 5p spin-orbit peaks in the spectra. A 600 lines/mm holographic grating from JY Inc. was used in a Mark IV Grasshopper monochromator, limiting our minimum photon energy to ~21 eV. Spectra of the valence region were recorded at ~~2.5~~ Å monochromator band width, and 50 eV electron analyzer pass energy (0.4 eV electron resolution) from 21-50 eV photon energy. Representative spectra at 21, 24, and 33 eV photon energies are shown in Figure 5.2.1-1. There are striking intensity changes between these spectra, particularly on the $3\pi_g$ and $10\sigma_g$ orbitals. As discussed in section 3.2.1, the transmission function of the electron spectrometer has been found to be constant to within 20% for kinetic energies between 2-60 eV.[23,25] We have obtained very good agreement down to ~2 eV kinetic energy

Figure 5.2.1-1

Photoelectron spectra of XeF_2 at 21 eV, 24 eV, and 33 eV photon energies. The molecular orbital assignment is given in the bottom plot.

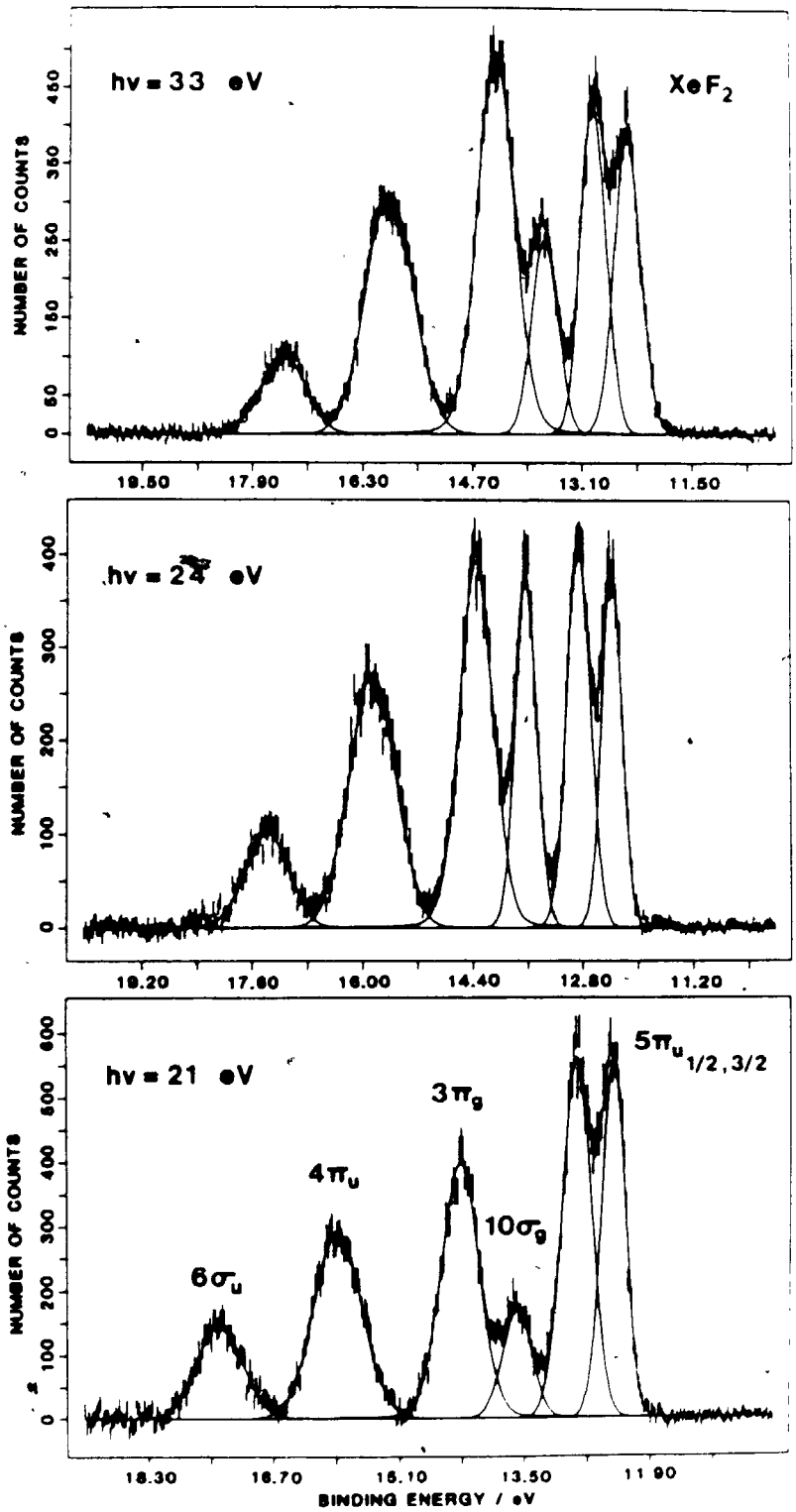
hv = 33 eV
XeF2
NUMBER OF COUNTS
0
50
150
250
350
450
19.50
17.90
16.30
14.70
13.10
11.50
hv = 24 eV
NUMBER OF COUNTS
0
100
200
300
400
19.20
17.60
16.00
14.40
12.80
11.20
hv = 21 eV
6σu
4πu
3πg
10σg
5πu1/2,3/2
NUMBER OF COUNTS
0
100
200
300
400
500
600
18.30
16.70
15.10
13.50
11.90
BINDING ENERGY / eV

between our partial cross sections for CF_4[26] and those of Carlson et al.[27]

All of the photoelectron spectra were computer-fitted using an iterative procedure described previously in the literature.[28] Voigt functions simulated by a linear combination of Lorentzian-Gaussian line shapes were used in this fitting procedure. Accurate branching ratios could be readily obtained from the fitted peak areas. The weak and broad F 2s orbitals $(5\sigma_u, 8\sigma_g)^4$ and weak Xe 5s orbital $(9\sigma_g)^4$ were neglected in the branching ratio determination. Even at 50 eV photon energy, the combined contributions from the F 2s and Xe 5s orbitals is less than ~8%. The experimental branching ratios were then converted to partial cross sections, using the total photoabsorption data of Nielsen and Schwarz[14,15] (measured in arbitrary units) and assuming the photoionization yield to be unity over the photon energy range investigated. The photoabsorption data of Nielsen and Schwarz was converted to absolute cross section using Black et al.'s photoabsorption value of 59 ± 5 Mb at 158 nm (7.85 eV).[16]

5.3.1 Theory

Theoretical partial cross sections were obtained for the valence molecular orbitals of XeF_2 as a function of photon energy, using the MS-Xα cross section program of Davenport.[29] The parameters employed in the calculation are shown in Table 5.3.1-1. The atomic exchange parameters

Table 5.3.1-1

Parameters used in the MS-Xα Calculation

Region	X	Y	Z[a)]	R[a)]	α	Initial State ℓ_{max}	Final State ℓ_{max}
Outersphere	0.0	0.0	0.0	5.6480	0.72369	5	14
Xe	0.0	0.0	0.0	2.6670	0.69984	4	4
F_1	0.0	0.0	3.7795	1.8685	0.73732	3	3
F_2	0.0	0.0	-3.7795	1.8685	0.73732	3	3

a) Coordinates and sphere radii in atomic units, 20% overlapping spheres used.

α_{HF} are those of Schwarz.[30] For the outersphere and intersphere regions a weighted average of the atomic exchange parameters was used, based on the number of valence electrons. The calculation was performed in $D_{\infty h}$ symmetry, using a Xe-F bond distance of 2.00 Å[10] and 20% overlapping spheres. A kinetic energy mesh size of 1.36 eV was used in the calculation of the photoionization cross sections.

The photoionization cross section was calculated using the converged SCF ground state potential, modified with a Latter tail potential[31] in order to account for the proper large r behavior. Since previous studies[32,33] have shown that the calculations are sensitive to the number of partial waves used, the spherical harmonics were extended to higher azimuthal ℓ quantum numbers, as shown in Table 5.3.1-1. This choice of maximum ℓ values should provide convergence in σ to better than a few percent over the entire photon energy range. All symmetry-allowed photoionization processes based on the dipolar selection rule were included in the calculations (i.e. $\Delta\Lambda = 0, \pm 1$; u $\leftrightarrow$ g).[29]

Initially a similar calculation was attempted on XeF_2 using touching spheres. Although most of the cross section results were very similar to the 20% overlapping spheres case, small discontinuities and oscillatory behavior were observed in the cross sections and the eigenphase sums at specific kinetic energies. Since it was

suspected that this additional structure in the touching spheres calculation was due to some numerical problem, the calculation was repeated using 20% overlapping spheres. The overlapping spheres calculation gave continuous cross sections and eigenphase sums over the entire photon energy range. It is suspected that the touching spheres calculation introduced larger than normal discontinuities in the molecular potential at the sphere edges. Since other touching sphere calculations[26,29] have shown no such problems (e.g. CF_4, SiF_4, and CF_3I results in Chapter 4), it may be due to the very large bond distance in XeF_2 (r_{Xe-F} = 2.00 Å[10]) and subsequently the poorer muffin-tin potential generated by touching spheres, due to the larger interatomic region created. Since only a constant potential is used in the interatomic region, overlapping the spheres reduces the charge in the interatomic region, giving a better approximation to the molecular potential.

5.4.1 Results and Discussion

The overall valence bonding in XeF_2 is relatively simple.[4,10] In terms of ionization potential, the generally accepted ordering of the five outermost valence levels (Figure 5.2.1-1) is $5\pi_u < 10\sigma_g < 3\pi_g < 4\pi_u < 6\sigma_u$. The Xe-F antibonding $5\pi_u$ MO is spin-orbit split into $^2\Pi_{3/2}$ and $^2\Pi_{1/2}$ terms due to the high Xe 5p character. The $10\sigma_g$ and $3\pi_g$ are nonbonding fluorine 2p orbitals. The only bonding levels are the $4\pi_u$ and $6\sigma_u$ molecular orbitals,

derived primarily from the Xe 5p and F 2p orbitals. Below the diffuse Rydberg-like orbitals, XeF_2 has only one empty valence orbital. This $7\sigma_u^*$ orbital is strongly antibonding and corresponds to the antibonding partner of the $6\sigma_u$ orbital. DV-Xα and Xα-SW calculations[4,9] have placed the $7\sigma_u^*$ orbital ~4 eV above the highest occupied $5\pi_u$ orbital, and appear to give UV transition energies[4] involving this orbital that are in good agreement with experiment.[10] For the benefit of the ensuing discussion, it is important to note that the $6\sigma_u$, $4\pi_u$, $5\pi_u$, and $7\sigma_u^*$ orbitals have substantial Xe 5p character.[4,10]

The theoretical and experimental partial photoionization cross sections (σ) and branching ratios (BR) are shown in Figures 5.4.1-(1-5). The theoretical results are based on MS-Xα calculations using overlapping spheres. In general, there is good agreement between the theoretical MS-Xα and experimental partial cross sections and branching ratios (Figure 5.4.1-(1-5)). Owing to experimental limitations, the partial cross sections could not be measured lower than 21 eV photon energy. The major discrepancy in MO assignment between ab initio[10,11] and Xα calculations[4,8,9,12] has been in the reversal of the highest occupied $10\sigma_g$ and $5\pi_u$ orbitals. Basch et al.[10] noted this reversal in their ab initio calculation and assigned the first valence band in the photoelectron spectrum as $5\pi_u$, based on the spin-orbit splitting present in the first valence band. The $10\sigma_g$ orbital cannot be

Figure 5.4.1-1

The upper plot shows the experimental and theoretical MS-Xα (——) photoionization cross section (in Mb) of the $5\pi_u$ valence orbital of XeF_2; plus the partial-channel cross sections for $5\pi_u \rightarrow k\sigma_g$ (– –), $5\pi_u \rightarrow k\pi_g$ (· · · ·), and $5\pi_u \rightarrow k\delta_g$ (----). The bottom plot gives the theoretical MS-Xα (——) and experimental branching ratios.

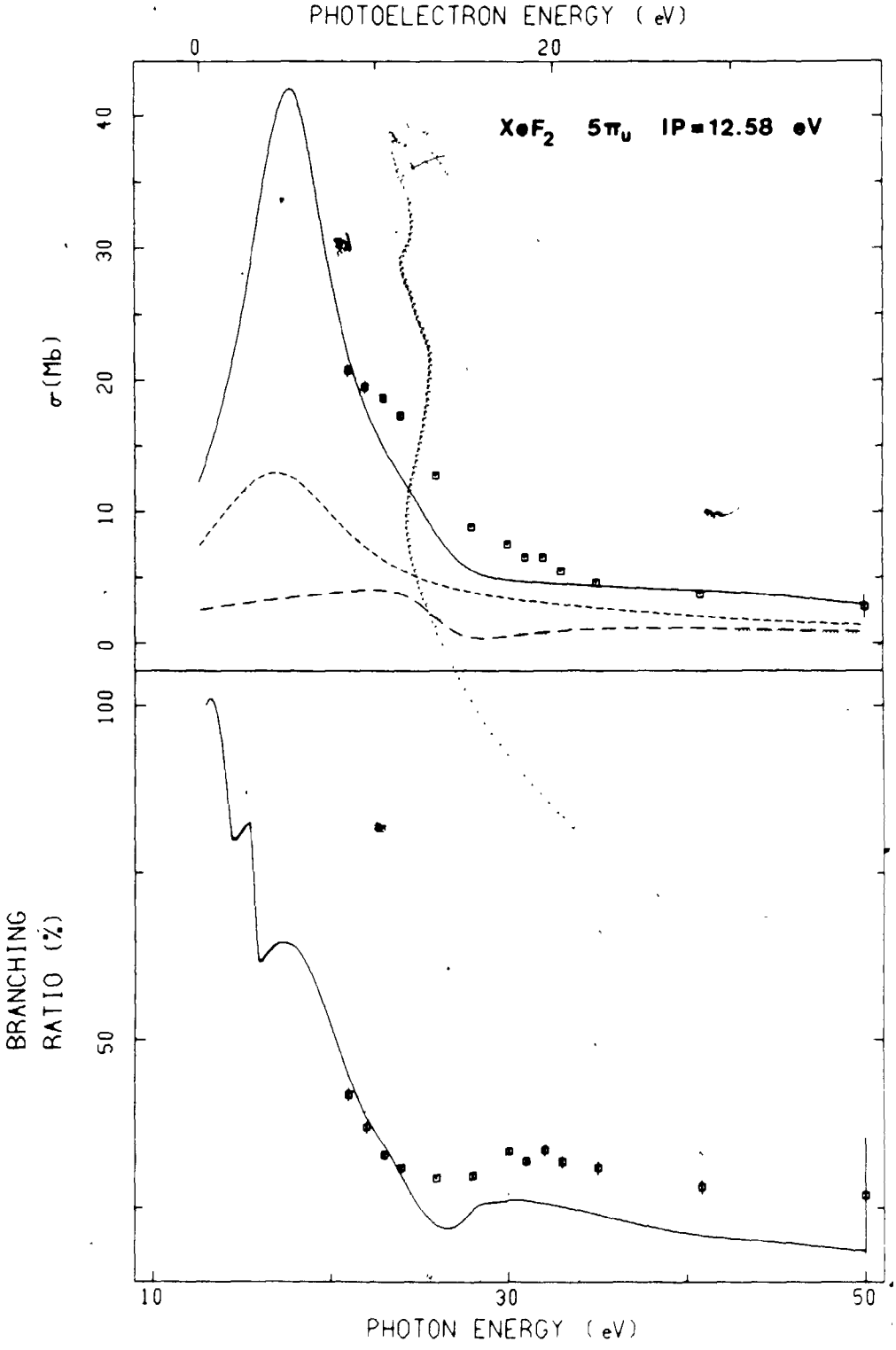
PHOTOELECTRON ENERGY (eV)
0
20
XeF2 5πu IP=12.58 eV
σ(Mb)
40
30
20
10
0
100
50
BRANCHING RATIO (%)
10
30
50
PHOTON ENERGY (eV)

Figure 5.4.1-2

The upper plot shows the experimental and theoretical MS-Xα (——) photoionization cross section (in Mb) of the $10\sigma_g$ valence orbital of XeF_2; plus the partial-channel cross sections for $10\sigma_g \rightarrow k\sigma_u$ (– –) and $10\sigma_g \rightarrow k\pi_u$ (·····). The bottom plot gives the theoretical MS-Xα (——) and experimental branching ratios.

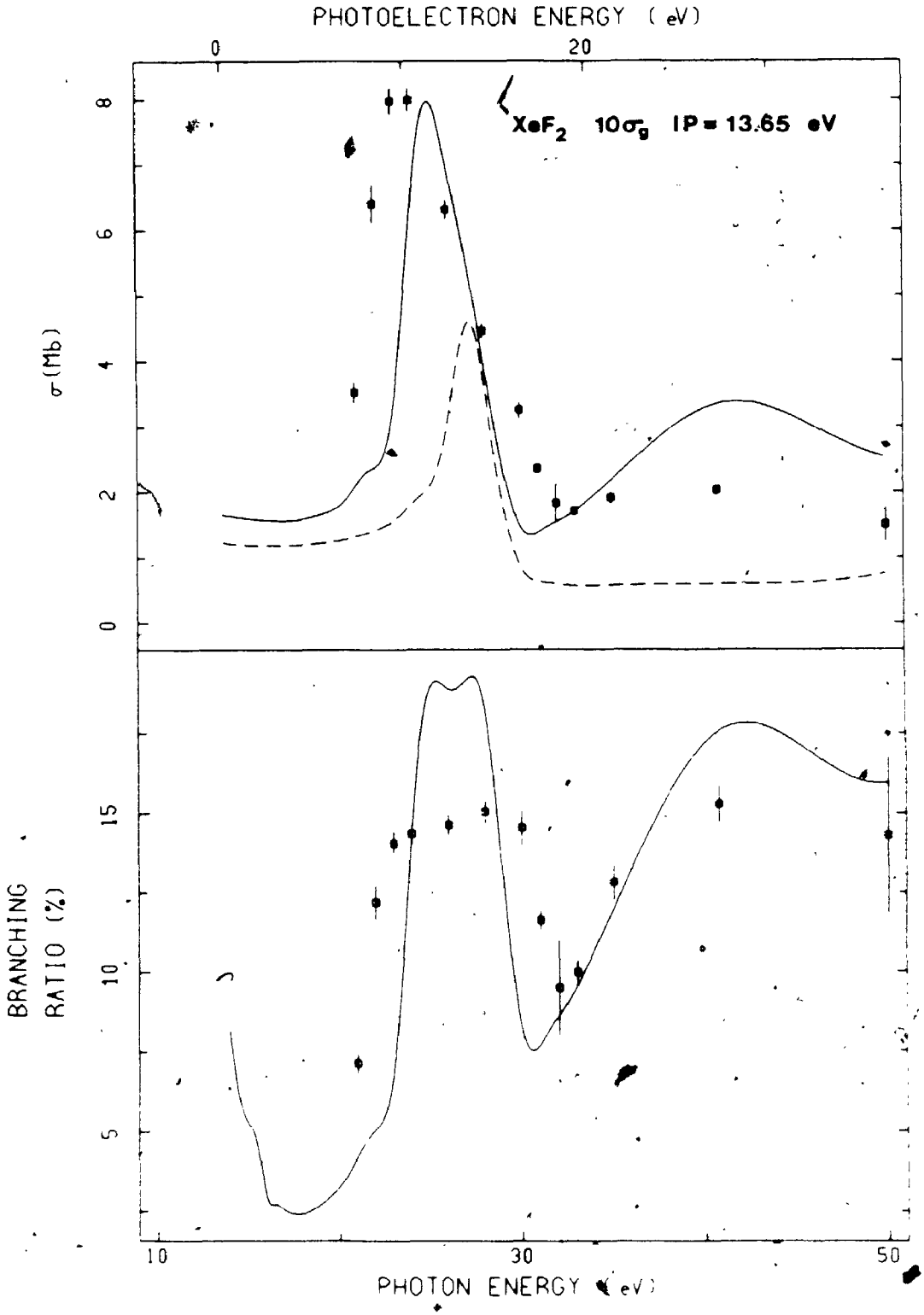
PHOTOELECTRON ENERGY (eV)
0
20
XeF_2 $10\sigma_g$ IP = 13.65 eV
σ(Mb)
0
2
4
6
8
BRANCHING RATIO (%)
5
10
15
10
30
50
PHOTON ENERGY (eV)

Figure 5 4 1-3

The upper plot shows the experimental and theoretical MS-Xα (———) photoionization cross section (in Mb) of the $3\pi_g$ valence orbital of XeF_2, plus the partial-channel cross sections for $3\pi_g \rightarrow k\sigma_u$ (– –), $3\pi_g \rightarrow k\pi_u$ ( ), and $3\pi_g \rightarrow k\delta_u$ (----). The bottom plot gives the theoretical MS-Xα (———) and experimental branching ratios

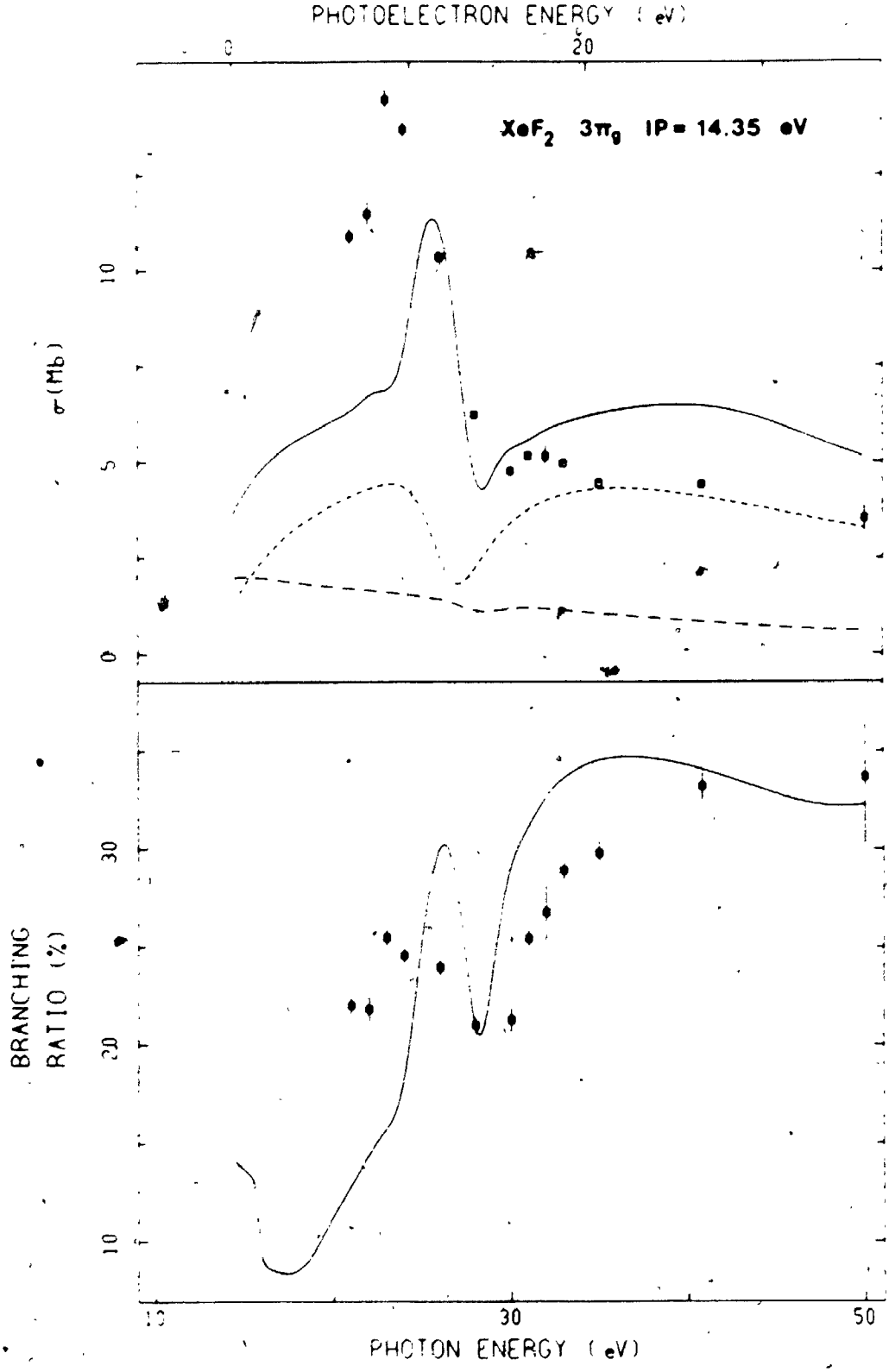
PHOTOELECTRON ENERGY (eV)
0
20
XeF2 3πg IP = 14.35 eV
σ (Mb)
10
5
0
BRANCHING RATIO (%)
30
20
10
10
30
50
PHOTON ENERGY (eV)

Figure 5.4.1-4

The upper plot shows the experimental and theoretical MS-Xα (——) photoionization cross section (in Mb) of the $4\pi_u$ valence orbital of XeF_2; plus the partial-channel cross sections for $4\pi_u \rightarrow k\sigma_g$ (– –), $4\pi_u \rightarrow k\pi_g$ (· · · ·), and $4\pi_u \rightarrow k\delta_g$ (----). The bottom plot gives the theoretical MS-Xα (——) and experimental branching ratios.

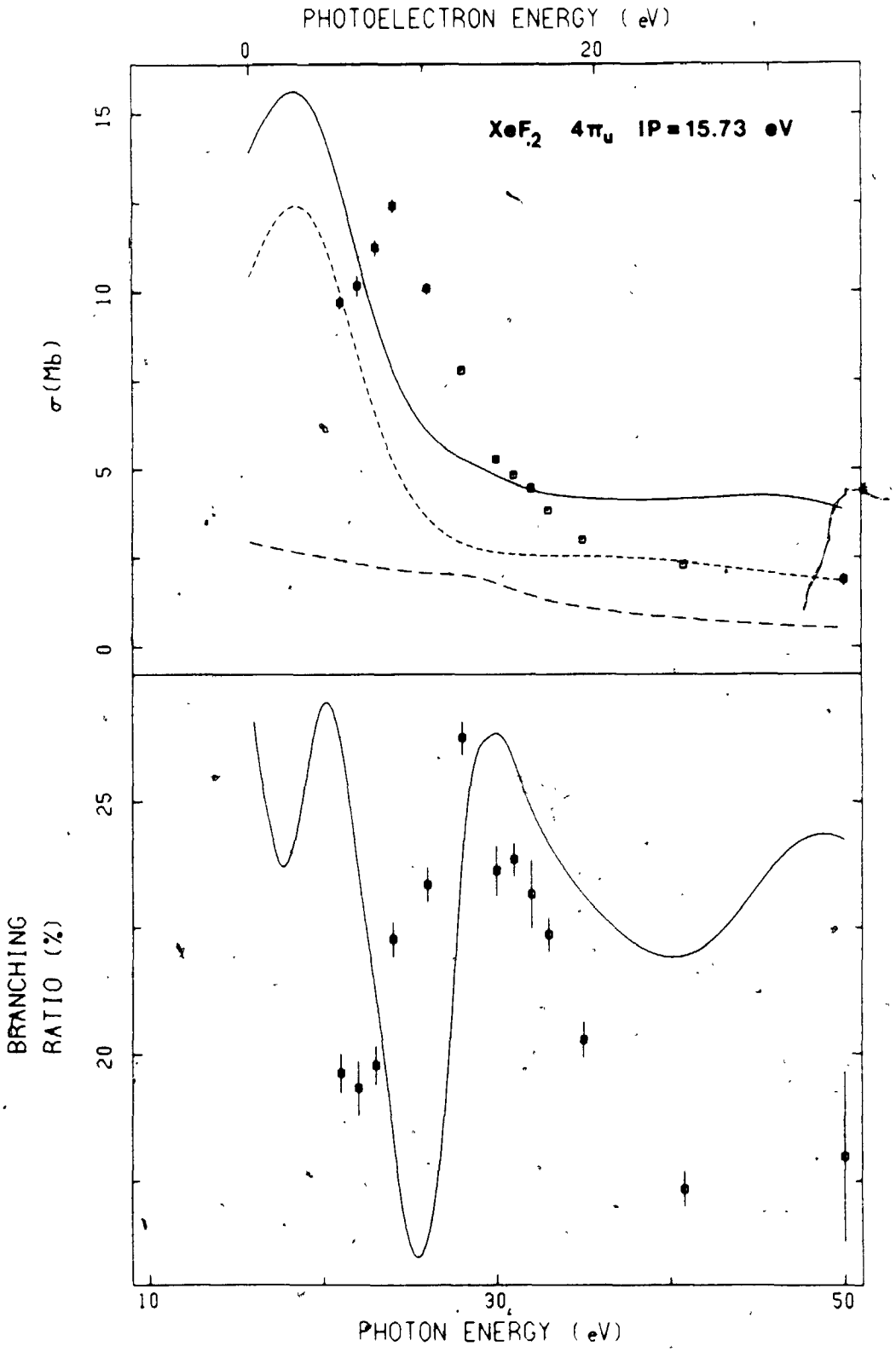
PHOTOELECTRON ENERGY (eV)
0
20
XeF_2 $4\pi_u$ IP = 15.73 eV
σ(Mb)
15
10
5
0
BRANCHING RATIO (%)
25
20
10
30
50
PHOTON ENERGY (eV)

Figure 5.4.1-5

The upper plot shows the experimental and theoretical MS-Xα (——) photoionization cross section (in Mb) of the $6\sigma_u$ valence orbital of XeF_2; plus the partial-channel cross sections for $6\sigma_u \rightarrow k\sigma_g$ (– –) and $6\sigma_u \rightarrow k\pi_g$ (· · · ·). The bottom plot gives the theoretical MS-Xα (——) and experimental branching ratios.

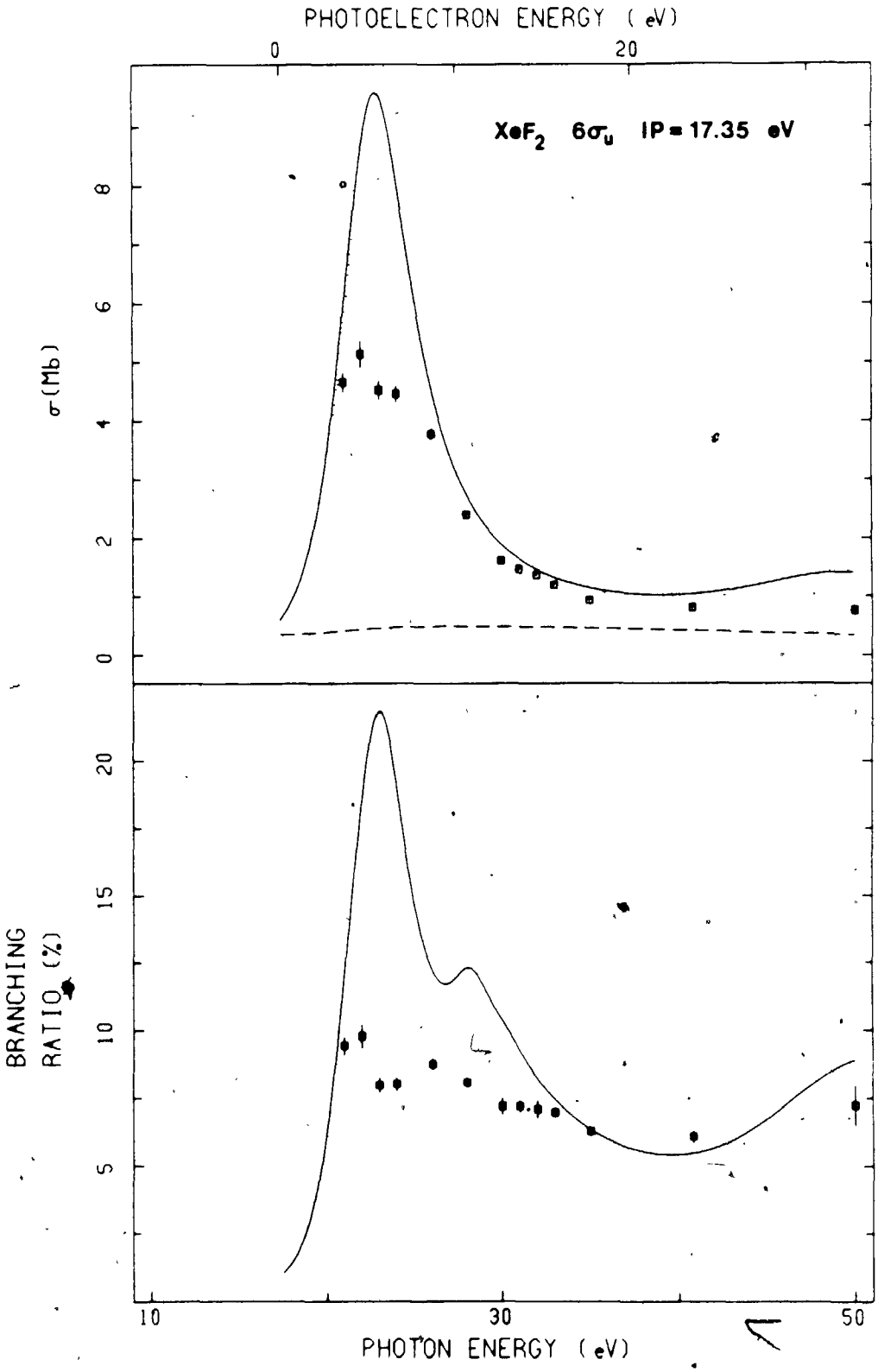
PHOTOELECTRON ENERGY (eV)
0
20
XeF2 6σu IP = 17.35 eV
σ(Mb)
0
2
4
6
8
BRANCHING RATIO (%)
5
10
15
20
10
30
50
PHOTON ENERGY (eV)

spin-orbit split since the ion formed has zero orbital momentum ($\Lambda = 0$). The good agreement found in Figures 5.4.1-1 and 5.4.1-2 between theory and experiment enables us to confirm, on a cross section basis, that the highest occupied MO is indeed $5\pi_u$. The most distinctive difference in the $5\pi_u$ partial cross section is that it decreases monotonically from ~21 Mb at 21 eV photon energy to ~3 Mb at 50 eV photon energy, whereas the nonbonding $10\sigma_g$ partial cross section exhibits a strong resonance feature of ~8 Mb at ~23.5 eV photon energy. The present assignment is in agreement with previous experimental assignments based on photoelectron spectra,[3,6,10] and theoretical Xα results.[4,8,9,12]

A summary by outgoing channel of the theoretical MS-Xα eigenphase sum features is shown in Table 5.4.1-1, while Table 5.4.1-2 compares the theoretical and experimental resonance positions for XeF_2. The kinetic energy positions labelled E_{phase} in Table 5.4.1-1 indicate possible resonance positions. According to Kreile's first criterion for a resonance,[34] the eigenphase sum must change by $\gtrsim 0.3\pi$ over an energy range $\Delta E \lesssim 6$ eV. Based on this, the σ_g and δ_g channels exhibit only very weak resonance behavior. This leaves four resonant channels - one of even parity (π_g) at ~4.8 eV kinetic energy and three of odd parity (π_u, δ_u, σ_u) at ~11.6, ~11.6, and ~14.3 eV kinetic energies, respectively.

Table 5.4.1-1

Theoretical MS-Xα Eigenphase Sum Features

Channel Symmetry	MS-Xα Results		
	E_{phase}(eV)[a]	Δ(Eigenphase Sum)[b]	Partial-Wave[c]
π_g	4.8	0.34π	2
δ_g	4.8	0.21π[d]	2
π_u	11.6	0.68π	3
δ_u	11.6	0.62π	3
σ_g	12.9	0.28π[d]	2
σ_u	14.3	0.55π	1

a) The resonance energy E_{phase} is given by the inflection point in the plot of the eigenphase sum versus photoelectron kinetic energy.
b) According to Kreile's[34] first resonance criteria, the eigenphase must change by $\geq 0.3\pi$ over an energy range $\Delta E \leq 6$ eV.
c) Predominant asymptotic partial-wave components are shown.
d) Since the change in eigenphase sum is $<0.3\pi$, only very weak resonance behavior is predicted.

Table 5.4.1-2

Resonance Positions[a] from MS-Xα and Experiment for XeF_2

MO	Channel Symmetry	Ms-Xα Results[b] E_{phase} (eV)	Experimental Results $E_{resonance}$ (eV)
$5\pi_u$	π_g	4.8 s	
	δ_g	4.8 m	
	σ_g	12.9 w	~11.4 (shoulder)
$10\sigma_g$	π_u	11.6 s	10.4 s
	σ_u	14.3 s	~14.4 (shoulder)
$3\pi_g$	π_u	11.6 s	8.7 s
	δ_u	11.6 w	
	σ_u	14.3 w	
$4\pi_u$	π_g	4.8 w	
	δ_g	4.8 s	8.3 s[c]
	σ_g	12.9 w	
$6\sigma_u$	π_g	4.8 s	4.7 s
	σ_g	12.9 w	

a) All resonance positions expressed in terms of photoelectron kinetic energy.

b) Classification: strong (s), medium (m), weak (w).

c) Coupling of the δ_g and δ_u scattering channels is proposed (see text).

The experimental and theoretical partial photoionization cross sections and branching ratios (BR) for the $5\pi_u$ MO are shown in Figure 5.4.1-1. Although the theoretical BR tends to be smaller than experiment by ~8% at higher photon energies, the overall agreement between theory and experiment for both partial cross section and BR is very good. The BR minimum at ~26 eV photon energy and weak maximum at ~31 eV photon energy are reproduced well theoretically. At photon energies <21 eV, the spectral variation of the $5\pi_u$ partial cross section is dominated by the resonance in the $5\pi_u \rightarrow k\pi_g$, which maximizes at ~18 eV photon energy. Analysis of the asymptotic partial waves shows that the π_g resonance is due to resonant trapping by the molecular potential barrier of the d-wave component ($\ell = 2$) of the continuum molecular wavefunction. This resonance could not be probed experimentally, however, due to limitations in photon energy range caused by the monochromator. The broader σ_g channel contributes significantly above 21 eV photon energy, again with the d-wave component dominating. Experimentally, the $5\pi_u$ partial cross section decreases monotonically above 21 eV photon energy, in good agreement with theory.

The variation of the $10\sigma_g$ photoionization cross section shown in Figure 5.4.1-2, clearly illustrates the π_u and σ_u resonances predicted at 11.6 and 14.3 eV kinetic energies. These two resonances dominate between 20-30 eV photon energy. The overall theoretical BR shape agrees

well with experiment, although the theoretical BR values are higher by ~4% in the resonance region. The broad feature at ~26 eV photon energy in the theoretical BR is caused by overlap of the two resonances. Both this and the broad maximum which follows at higher photon energy are reproduced very nicely theoretically. Agreement between experiment and theory for the partial cross section is equally good, but a much weaker maximum is observed experimentally at ~41 eV photon energy. The asymmetric feature centered at ~10 eV kinetic energy appears to be slightly broader and shifted ~1.2 eV to lower kinetic energy than predicted by theory. Partial wave analysis indicates that the π_u resonance is due to resonant f-wave trapping, whereas the σ_u resonance is due to resonant p-wave trapping (Table 5.4.1-1).

A similar situation occurs in Figure 5.4.1-3 for the $3\pi_g$ orbital, which consists also of nonbonding fluorine 2p orbitals. A single resonance of π_u symmetry is predicted to occur at 11.6 eV kinetic energy. Experimentally, a resonance is found at ~8.7 eV kinetic energy, shifted lower some 2.9 eV kinetic energy from theory. Reasonable agreement is found for the branching ratio, with the pronounced dip at ~28 eV photon energy being well reproduced theoretically. As for the $10\sigma_g$ orbital, it was found that this π_u resonance is also due to resonant f-wave trapping. Clearly, both of these nonbonding orbitals of XeF_2 can support resonances.

The three photoionization channels of the $3\pi_g$ orbital in Figure 5.4.1-3 are qualitatively similar to the $1\pi_g \rightarrow k\sigma_u$, $k\pi_u$, and $k\delta_u$ profiles in O_2, F_2, and CO_2.[35-38] With the exception of the resonance contributions from the δ_u, π_u, and σ_u channels near 11.6 eV, 11.6 eV, and 14.3 eV kinetic energy respectively, these channels are similar to the atomic fluorine 2p cross sections.[38] The $3\pi_g \rightarrow k\delta_u$ component resembles the 2p → kd atomic-like cross section, with which it corresponds presumably in the separated-atom limit. The $3\pi_g \rightarrow k\sigma_u$ component is similar to a 2p → ks atomic cross section, while the weak $3\pi_g \rightarrow k\pi_u$ component corresponds to the dipole forbidden 2p → kp atomic cross section. The nonbonding nature of the $3\pi_g$ orbital results in substantial atomic fluorine 2p character appearing in the photoionization cross section. However, near the resonances the photoionization cross section can deviate considerably from this atomic behavior due to multiple scattering effects, as evidenced by the substantial increase in cross section that occurs at resonance in the π_u channel. A similar type of behavior occurs on the $1\pi_g$ orbital of CO_2 in the σ_u channel at ~17.5 eV kinetic energy,[39] but the resonance is experimentally barely detectable in this case.

It is evident from Figure 5.4.1-4 that the $4\pi_u$ theoretical photoionization cross section is primarily due to the d-wave component of the δ_g channel. The σ_g and π_g channels are relatively small and structureless, although

there is evidence of an extremely weak maximum at 12.9 eV kinetic energy in the σ_g channel. The three $4\pi_u$ components are qualitatively similar to the corresponding channels for the $1\pi_u$ orbital in O_2,[37] F_2,[35] and CO_2.[38,39] Based on Padial et al.'s[38] assignment for the analogous $1\pi_u$ orbital of CO_2, the $4\pi_u \rightarrow k\delta_g$ component in XeF_2 is largely fluorine 2p → kd atomic-like in nature, and the $4\pi_u \rightarrow k\sigma_g$ and $k\pi_g$ channels resemble fluorine 2p → ks and dipole forbidden 2p → kp, respectively.

The agreement between theory and experiment for the $4\pi_u$ photoionization cross section is not very satisfactory. It is clear from the structure which is observed experimentally at ~8.3 eV kinetic energy that some other process unaccounted for in the calculations is occurring. The position of the maximum is almost identical to the π_u resonance observed for the $3\pi_g$ orbital at ~8.7 eV kinetic energy (Table 5.4.1-2). Since the π_u and δ_u resonances are predicted theoretically at virtually the same kinetic energy, a δ_u resonance would also be expected in this general vicinity. It is possible that this structure is due to dipole forbidden coupling of the $4\pi_u$ orbital to the $k\delta_u$ channel. A similar argument has been proposed by Padial et al.[38] to explain a discrepancy on the analogous $1\pi_u$ orbital of CO_2 in the ~20-25 eV photon energy range. They propose that due to the oxygen-atom 2p character of the $1\pi_g$ and $1\pi_u$ orbitals in CO_2, that the $1\pi_g^{-1}\ k\delta_u$ and $1\pi_u^{-1}\ k\delta_g$ configurations mix due to

significant spatial overlap, causing coupling of the δ_u and δ_g scattering states.

In Figure 5.4.1-5, it is evident that the $6\sigma_u$ theoretical photoionization cross section is almost exclusively dominated by the d-wave component of the π_g channel resonance at ~4.8 eV kinetic energy. The experimental maximum at ~4.7 eV kinetic energy is in good agreement with the theoretical value (Table 5.4.1-2). The σ_g channel is virtually flat and contributes less than 0.5 Mb to the total. A resonance is also predicted at 4.7 eV kinetic energy for the analogous $3\sigma_u$ orbital in CO_2, using the multiple scattering method.[39] Although this resonance in CO_2 occurs instead in the σ_g channel, it is also caused by resonant d-wave trapping and assigned as the intravalence transition $3\sigma_u \rightarrow 5\sigma_g^*(\sigma^*)$.[38,39] This type of assignment cannot be applied to XeF_2, however, since there are no virtual valence orbitals of gerade symmetry. Unlike CO_2 which has three valence virtual orbitals ($2\pi_u^*(\pi^*)$, $5\sigma_g^*(\sigma^*)$, $4\sigma_u^*(\sigma^*)$), XeF_2 has only the $7\sigma_u^*(\sigma^*)$, and this is clearly bound.[4,9,10] The π_g resonance on the $6\sigma_u$ orbital in XeF_2 is therefore not due to an intravalence transition. This would presumably imply that higher virtual orbitals than these are responsible for this feature. Such higher virtual orbitals would tend to be more atomic-like, and possibly of mixed valence-Rydberg character.

At higher photon energies the agreement on the $6\sigma_u$ orbital (Figure 5.4.1-5) between theory and experiment is quite good, for both σ and BR. Since the experimental cross section is beginning to decrease at 21 eV photon energy, it is consistent with the existence of this π_g resonance. The theoretical cross section here is narrower and more intense than experiment. This is due to the neglect of vibration, which usually causes the multiple scattering method to exaggerate resonance intensities and underestimate widths.[40,41]

5.5.1 Conclusions

Experimental branching ratios and partial cross sections have been determined for the first five valence band orbitals of XeF_2 as a function of photon energy. Comparison of the experimental results with MS-Xα calculations show generally good agreement with regards to the overall cross section and branching ratio behavior. The two nonbonding orbitals involving fluorine 2p orbitals ($10\sigma_g$, $3\pi_g$) display a total of three resonances, illustrating that these molecular orbitals located at the periphery of the molecule can exhibit intense resonances, and do so in spite of the large bond length involved and lack of appropriate virtual valence orbitals above threshold.

Certain of the partial-channel cross sections contain profiles that appear atomic in origin, presumably

correlating with strongly allowed transitions in the separated-atom limit. The $4\pi_u \rightarrow k\sigma_g$, $4\pi_u \rightarrow k\pi_g$, and $4\pi_u \rightarrow k\delta_g$ partial-channel cross sections resemble atomic fluorine $2p \rightarrow ks$, $2p \rightarrow kp$ (dipole forbidden) and $2p \rightarrow kd$ atomic-like cross sections,[42] respectively. Similarly, if one ignores the σ_u, π_u, and δ_u resonance contributions, the $3\pi_g \rightarrow k\sigma_u$, $3\pi_g \rightarrow k\pi_u$, and $3\pi_g \rightarrow k\delta_u$ partial-channel cross sections also resemble atomic fluorine $2p \rightarrow ks$, $2p \rightarrow kp$ (dipole forbidden) and $2p \rightarrow kd$ atomic-like cross sections, respectively. This behavior is also similar to the $1\pi_u$ and $1\pi_g$ cross sections of O_2, F_2, and CO_2,[35-38] and due apparently to the largely atomic 2p nature of these molecular orbitals. There is evidence that coupling occurs between $3\pi_g^{-1}\, k\delta_u$ and $4\pi_u^{-1}\, k\delta_g$ configurations, causing discrepancies between experiment and theory to occur around ~8.3 eV kinetic energy. A similar case of coupling occurs on the $1\pi_g$ and $1\pi_u$ orbitals of O_2 and CO_2.[36-38]

With the exception of the $4\pi_u$ orbital, the other valence orbitals exhibit at least one resonance in their photoionization continua. The u-symmetry orbitals ($5\pi_u$, $6\sigma_u$) display resonances in the π_g channel due to d-wave trapping. Since both of these orbitals are Xe-F antibonding/bonding in character, this tends to suggest that the outgoing channel may also carry significant Xe and F character. As the xenon Rydberg orbitals, with the exception of the d-type orbitals, are bound in the ground state of XeF_2,[4] this further implies that the π_g outgoing

channel in these two instances are of mixed valence-Rydberg orbital character The most likely candidate for the π_g outgoing channel appears to be the $5\pi_g^*$ orbital. The previous calculation of Tse et al.[4] on XeF_2^+ places the $5\pi_g^*$ orbital at ~5 eV above threshold, and is of predominantly mixed valence(Xe d)-Rydberg(d) orbital character

The g-symmetry orbitals ($10\sigma_g$, $3\pi_g$) both display resonances in the π_u channel due to f-wave trapping, while the $10\sigma_g$ orbital also resonates in the σ_u channel due to p-wave trapping. Since XeF_2 has only one valence virtual orbital ($7\sigma_u^*(\sigma^*)$), and this is bound,[4,9,10] these resonances are not due to an intravalence transition. One can only speculate that mixed valence-Rydberg orbitals involving atomic F 3d orbitals[35] may be responsible for these features. Nielsen et al.[15] have measured the VUV spectra of XeF_n (n = 2,4,6) and found that a broad maximum centered at ~23.5 eV photon energy occurred in each, with the maximum becoming more intense as the number of fluorines increased in the series. Since this is the photon energy region where these resonances lie, this implies that these features have substantial atom-like fluorine character. Additional experimental and theoretical work on the XeF_n series (n = 2,4,6) is now needed to interpret further the actual nature of these resonances observed in XeF_2.

5.6.1 References

1. S.E. Karlsson, K. Siegbahn, and N. Bartlett, "ESCA Applied to Free Molecules", (North-Holland, Amsterdam, 1969), p. 132.

2. T.X. Carroll, R.W. Shaw, Jr., T.D. Thomas, C. Kindle, and N. Bartlett, J. Am. Chem. Soc. 96, 1989 (1974).

3. G.M. Bancroft, P.A. Malmquist, S. Svensson, E. Basilier, U. Gelius, and K. Siegbahn, Inorg. Chem. 17, 1595 (1978).

4. J.S. Tse, D.J. Bristow, G.M. Bancroft, and G.J. Schrobilgen, Inorg. Chem. 18, 1766 (1979).

5. S. Aksela, H. Aksela, G.M. Bancroft, D.J. Bristow, and G.J. Schrobilgen, J. Chem. Phys. 82, 4809 (1985).

6. C.R. Brundle, M.B. Robin, and G.R. Jones, J. Chem. Phys. 52, 3383 (1970).

7. C.R. Brundle, G.R. Jones, and H. Basch, J. Chem. Phys. 55, 1098 (1971).

8. L. Scheire, P. Phariseau, R. Nuyts, A.E. Foti, V.H. Smith, Jr., Physica 101A, 22 (1980).

9. G.L. Gutsev and A.E. Smoljar, Chem. Phys. 56, 189 (1981).

10. H. Basch, J.W. Moskowitz, C. Hollister, and D. Hankin, J. Chem. Phys. 55, 1922 (1971).

11. L.S. Bartell, M.J. Rothman, C.S. Ewig, and J.R. Van Wazer, J. Chem. Phys. 73, 367 (1980).

12. A. Rosén and D.E. Ellis, Chem. Phys. Lett. 27, 595 (1974).

13. J. Jortner, E.G. Wilson, and S.A. Rice, "Noble Gas Compounds", edited by H.H. Hyman, (University of Chicago Press, Chicago, 1963), p. 358.

14. F.J. Comes, R. Haensel, U. Nielsen, and W.H.E. Schwarz, J. Chem. Phys. 58, 516 (1973).

15. U. Nielsen and W.H.E. Schwarz, Chem. Phys. 13, 195 (1976).

16. G. Black, R.L. Sharpless, D.C. Lorents, D.L. Huestis, R.A. Gutcheck, T.D. Bonifield, D.A. Helms, and G.K. Walters, J. Chem. Phys. 75, 4840 (1981).

17. F. Sette, J. Stohr, and A.P. Hitchcock, J. Chem. Phys. 81, 4906 (1984).

18. B.-K. Teo, J. Am. Chem. Soc. 103, 3990 (1981).

19. W.H. Flygare, "Molecular Structure and Dynamics", (Prentice-Hall, Englewood Cliffs, N.J., 1978), p. 611.

20. R. Gillespie, A. Netzer, and G.J. Schrobilgen, Inorg. Chem. 13, 1458 (1975).

21. K.H. Tan, G.M. Bancroft, L.L. Coatsworth, and B.W. Yates, Can. J. Phys. 60, 131 (1982).

22. K.H. Tan, P.C. Cheng, G.M. Bancroft, and J. Wm. McGowan, Can. J. Spectrosc. 29, 134 (1984).

23. B.W. Yates, K.H. Tan, L.L. Coatsworth, and G.M. Bancroft, Phys. Rev. A 31, 1529 (1985).

24. J.A.R. Samson, Philos. Trans. Roy. Soc. London A 268, 141 (1970).

25. S. Aksela, K.H. Tan, G.M. Bancroft, H. Aksela, B.W. Yates, and L.L. Coatsworth, Phys. Rev. A 32, 1219 (1985).

26. B.W. Yates, K.H. Tan, G.M. Bancroft, L.L. Coatsworth, and J.S. Tse, J. Chem. Phys. 83, 4906 (1985).

27. T.A. Carlson, A. Fahlman, W.A. Svensson, M.O. Krause, T.A. Whitley, F.A. Grimm, M.N. Piancastelli, and J.W. Taylor, J. Chem. Phys. 81, 3828 (1984).

28. G.M. Bancroft, I. Adams, L.L. Coatsworth, C.D. Bennewitz, J.D. Brown, and W.D. Westwood, Anal. Chem. 47, 586 (1975).

29. J.W. Davenport, Ph.D. Thesis, University of Pennsylvania (1976).

30. K. Schwarz, Phys. Rev. B 5, 2466 (1972).

31. R. Latter, Phys. Rev. 99, 510 (1955).

32. M. Roche, D.R. Salahub, and R.P. Messmer, J. Electron Spectrosc. Relat. Phenom. 19, 273 (1980).

33. F.A. Grimm, T.A. Carlson, W.B. Dress, P. Agron, J.O. Thomson, and J.W. Davenport, J. Chem. Phys. 72, 3041 (1978).

34. J. Kreile, A. Schweig, and W. Thiel, Chem. Phys. Lett. 108, 259 (1984).

35. A.E. Orel, T.N. Rescigno, B.V. McKoy, and P.W. Langhoff, J. Chem. Phys. 72, 1265 (1980).

36. A. Gerwer, C. Asaro, B.V. McKoy, and P.W. Langhoff, J. Chem. Phys. 72, 713 (1980).

37. P.W. Langhoff, A. Gerwer, C. Asaro, and B.V. McKoy, Int. J. Quantum Chem. S13, 645 (1979).

38. N. Padial, G. Csanak, B.V. McKoy, and P.W. Langhoff, Phys. Rev. 23, 218 (1981).

39. P.M. Dittman, D. Dill, and J.L. Dehmer, Chem. Phys. 78, 405 (1983).

40. R.R. Lucchese, G. Raseev, and V. McKoy, Phys. Rev. A 25, 2572 (1982).

41. R.R. Lucchese and V. McKoy, J. Chem. Phys. 85, 2166 (1981).

42. D.A.L. Kilcoyne, C.M. McCarthy, S. Nordholm, N.S. Hush, and P.R. Hilton, J. Electron Spectrosc. Relat. Phenom. 36, 153 (1985).

END

210487

FIN